
Calum Crake

*Lady Margaret Hall*

Supervisors

Constantin-C. Coussios

Eleanor Stride

# Targeting and Characterisation of Magnetic Microbubbles for Drug Delivery using Passive Acoustic Mapping

**A thesis submitted for the degree of Doctor of Philosophy**

October 2015

# Abstract

Passive acoustic mapping (PAM) is a versatile technique for monitoring of therapeutic ultrasound, in particular the generation of cavitation and subsequent bubble dynamics. The objective of this thesis was to apply PAM to investigate the activity of different types of cavitation agent and any correlation to therapeutic effects. The work focuses particularly on a new type of agent in the form of microbubbles that can be magnetically targeted, which have shown great potential for localised drug delivery.

In this thesis PAM was used to study the behaviour of magnetic microbubbles (MMB) in tissue phantoms, *in vitro* cell experiments and *in vivo* mouse models. In tissue phantoms magnetic localisation of microbubble-induced cavitation activity was demonstrated and resolved using PAM. Under clinically relevant flow conditions an increase in the energy of cavitation on the order of 2-5 times was observed using PAM, which was similar to doubling the injected microbubble dose.

To facilitate cell experiments a novel chamber system was used with improved variants of MMB as well as condensed magnetic nanodroplets which were shown to enhance uptake of fluorescent small interfering RNA (siRNA), transfection of knock-down siRNA and paclitaxel-induced cell kill. Magnetic targeting was associated with increased cavitation power in PAM as well as increased treatment efficacy measured by biological methods including fluorescence microscopy and flow cytometry.

Finally, improved MMB were tested for the first time *in vivo* under real-time B-mode imaging and PAM, followed by fluorescence and MR imaging to assess distribution. MMB cavitation activity was of similar magnitude to the commercial contrast agent SonoVue®. Cavitation induced by the microbubbles and magnetic targeting were both associated with increases in fluorescence and MRI contrast in tumours. The therapeutic potential of MMB and monitoring power of PAM were thus demonstrated.

# Statement of Originality

I hereby declare that this submission is my own work and, to the best of my knowledge, it contains no materials previously published or written by another person, or substantial proportions of material which have been accepted for the award of any other degree or diploma at the University of Oxford or any other educational institution, except where due acknowledgement is made in the thesis.

Any contribution made to the research by others, with whom I have worked at the University of Oxford or elsewhere, is explicitly acknowledged in the thesis.

I also declare that the intellectual content of this thesis is the product of my own work, except to the extent that assistance from others in the project's design and conception or in style, presentation and linguistic expression is acknowledged.

Calum Crake

October 2015

# Acknowledgements

It has been a privilege to work under the supervision of Professors Constantin-C. Coussios and Eleanor Stride. Their complementary advice, expertise and enthusiasm were vital for the success of my research.

The work in this thesis is built upon that of many others. In particular I would like to thank all of my colleagues in the BUBBL group for their various contributions over the past three years: perhaps most notably Christian Coviello and Jamie Collin for their endless patience and advice on all things acoustics. I would also like to thank Dario Carugo, Joshua Owen and Jeong Yu Lee for their invaluable contributions to the *in vitro* experiments, and Robert Carlisle and Apurva Shah for their assistance with the *in vivo* work.

Finally, I would like to like to acknowledge the support of my family, without whom none of this research could have been completed. In particular I would like to thank my parents – to whom this thesis is dedicated – for their unceasing support, and my wife Alessandra.

I would also like to gratefully acknowledge financial support from the Engineering and Physical Sciences Research Council, as part of the Oxford Centre for Doctoral Training in Healthcare Innovation (EP/G036861/1).

# Dissemination

## Peer-Reviewed Journal Publications

**C. Crake**, R. Carlisle, J. Owen, S. Smart, C. Coviello, C.-C. Coussios, E. Stride, '*In vivo biodistribution of fluorescently tagged magnetic microbubbles for cavitation enhancement with real time passive acoustic mapping*' (in preparation)

J. Owen, **C. Crake**, R. Browning, J. Lee, D. Carugo, P. Jakeman, P. Rademeyer, E. Stride, '*A versatile method for the production of magnetic microbubbles for targeted drug delivery*' (in preparation)

J. Y. Lee, **C. Crake**, B. Teo, D. Carugo, M. de Saint Victor, A. Seth, E. Stride, '*Magnetic Nanoparticle-loaded Chitosan-deoxycholic acid Nanodroplets for Ultrasound-enhanced siRNA Delivery*' (in preparation)

J. Y. Lee, D. Carugo, **C. Crake**, J. Owen, M. de Saint Victor, A. Seth, C.-C. Coussios, E. Stride, '*Nanoparticle-loaded Protein-Polymer Nanodroplets for Improved Stability and Conversion Efficiency in Ultrasound Imaging and Drug Delivery*,' Advanced Materials, vol. 27, pp. 5484-5492, Oct 2015

D. Carugo, J. Owen, **C. Crake**, J. Y. Lee, E. Stride, '*Biologically and acoustically compatible chamber for studying ultrasound-mediated delivery of therapeutic compounds*,' Ultrasound in Medicine and Biology, vol. 41, pp. 1927-1937, Jul 2015

**C. Crake**, M. de Saint Victor, J. Owen, C. Coviello, J. Collin, C.-C. Coussios, E. Stride, '*Passive Acoustic Mapping of Magnetic Microbubbles for Cavitation Enhancement and Localization*,' Physics in Medicine and Biology, vol. 60, pp. 785-806, Jan 2015

M. de Saint Victor, **C. Crake**, C.-C. Coussios, E. Stride, '*Properties, characteristics and applications of microbubbles for sonothrombolysis*,' Expert Opinion on Drug Delivery, vol. 11, pp. 187-209, Feb 2014

**Conference Proceedings**

**C. Crake**, M. de Saint Victor, C. Coviello, J. Owen, C. C. Coussios, E. Stride, '*Passive acoustic mapping of magnetic microbubbles in an in vitro flow model*,' Proceedings of Meetings on Acoustics, vol. 19, p. 075025, Jun 2013

**Conference Presentations**

C. Coviello, **C. Crake**, R. Myers, S. Graham, J. Kwan, R. Carlisle, C. Coussios, '*Characterization of cavitation dynamics from nano-scale cavitation agents during drug delivery in-vivo using combined B-mode guidance and real-time passive acoustic mapping*,' 15th International Symposium on Therapeutic Ultrasound, Utrecht, The Netherlands, Apr 2015

J. Y. Lee, D. Carugo, **C. Crake**, J. Owen, E. Stride, '*Phase-Shift Protein-Polymer Nanodroplets for Targeted Drug Delivery and Ultrasound Imaging*,' 20th European symposium on Ultrasound Contrast Imaging, Rotterdam, The Netherlands, Jan 2015

**C. Crake,** C. C. Coussios, E. Stride, '*Cavitation dynamics of magnetic microbubbles using passive acoustic mapping (poster)*,' 14th International Symposium on Therapeutic Ultrasound, Las Vegas, USA, Apr 2014

M. de Saint Victor, **C. Crake**, C. C. Coussios, E. Stride, '*Targeted sonothrombolysis with magnetic microbubbles*,' 14th International Symposium on Therapeutic Ultrasound, Las Vegas, USA, Apr 2014

# CONTENTS

# LIST OF FIGURES

# LIST OF TABLES

# ACRONYMS

| | |
|---|---|
| AU | Arbitrary Units |
| *bis*-NHS-PEG | O,O′-Bis(2-(N-Succinimidyl-succinylamino)ethyl) polyethylene glycol |
| BUBBL | Biomedical Ultrasonics, Biotherapy and Biopharmaceuticals Laboratory |
| CB | Capon Beamformer |
| CT | Computed Tomography |
| DDFP | Dodecafluoropentane |
| DMEM | Dulbecco's Modified Eagle Medium |
| DNA | Deoxyribonucleic Acid |
| DOPE | 1,2-Dioleoyl-Sn-Glycero-3-Phosphoethanolamine |
| DOTMA | N-(1-(2,3-Dioleyloxy)Propyl)-N,N,N-Trimethylammonium Chloride |
| DPPC | Dipalmitoylphosphatidylcholine |
| DSEPC | 1,2-Distearoyl-Sn-Glycero-3-Ethylphosphocholine |
| DSPC | 1,2-Distearoyl-Sn-Glycero-3-Phosphocholine |
| DSPE | 1,2-Distearoyl-Sn-Glycero-3-Phosphoethanolamine |
| FCS | Fetal Calf Serum |
| FDA | Food and Drug Administration (USA) |
| FF | Ferrofluid |
| FFT | Fast Fourier Transform |
| FITC | Fluorescein Isothiocyanate |
| F-MMB | Fluorescent siRNA MMB |
| FWHM | Full Width at Half Maximum |

| | |
|---|---|
| GPU | Graphics Processing Unit |
| GUI | Graphical User Interface |
| HIFU | High Intensity Focused Ultrasound |
| HSA | Human Serum Albumin |
| IONP / IONC | Iron Oxide Nanoparticles / Nanocrystals |
| K-MMB | Knockdown siRNA MMB |
| MMB / MMBs | Magnetic Microbubbles |
| MND / MNDs | Magnetic Nanodroplets |
| MNP | Magnetic Nanoparticles |
| MR / MRI | Magnetic Resonance / Magnetic Resonance Imaging |
| MTS | 3-(4,5-Dimethylthiazol-2-Yl)-5-(3-Carboxymethoxyphenyl)-2-(4-Sulfophenyl)-2H-Tetrazolium |
| MVB | Minimum Variance Beamformer |
| NA | Nucleic Acid |
| PAM | Passive Acoustic Mapping |
| PBS | Phosphate Buffered Saline |
| PDMS | Polydimethylsiloxane |
| PEEK | Polyether Ether Ketone |
| PEG | Polyethylene Glycol, Polyoxyethylene-40-stearate |
| PFC | Perfluorocarbon |
| PFH | Perfluorohexane |
| PFM | Perfluoromethylcyclohexane |
| PFP | Perfluoropentane |
| PI | Propidium Iodide |
| PMMA | Poly(Methyl Methacrylate) |
| PRF | Pulse Repetition Frequency |
| PSF | Point Spread Function |
| PTFE | Polytetrafluoroethylene |
| PTX | Paclitaxel |
| PTX-MND | Paclitaxel-Loaded Magnetic Nanodroplets |

| | |
|---|---|
| PTX-MNP | Paclitaxel-Loaded Magnetic Nanoparticles |
| PVA | Poly(Vinyl Alcohol) |
| RCB | Robust Capon Beamformer |
| RF | Radio Frequency |
| RISC | RNA-Induced Silencing Complex |
| RMS | Root Mean Square |
| RNA | Ribonucleic Acid |
| ROI | Region of Interest |
| RPM | Revolutions per Minute |
| RX | Receive |
| SDS | Sodium Dodecyl Sulphate |
| siRNA | Small Interfering Ribonucleic Acid |
| S-MMB | Scrambled siRNA MMB |
| SONAR | Sound Navigation and Ranging |
| SPIO | Superparamagnetic Iron Oxide |
| TE | Echo Time (MRI) |
| TEA | Time Exposure Acoustics |
| TEMED | Tetramethylethylenediamine |
| TIFF | Tagged Image File Format |
| TM | Trade Mark |
| TR | Repetition Time (MRI) |
| TRITC | Tetramethylrhodamine |
| TX | Transmit |
| US | Ultrasound |

CHAPTER 1

# INTRODUCTION

Passive acoustic mapping (PAM) is a versatile technique for monitoring of therapeutic ultrasound, in particular the generation of cavitation and subsequent bubble dynamics. The overall objective of this thesis is to apply PAM to investigate the activity generated by different types of cavitation agent and any correlation to therapeutic effects. The work will focus particularly on a new type of agent in the form of microbubbles that can be magnetically targeted and which have shown great promise as a means of facilitating localised drug delivery. In this chapter[1] PAM and magnetic microbubbles (MMB) are introduced and set within their wider historical and technical context in the fields of medical ultrasound and targeted drug delivery. The key aims of the project, and structure of the thesis are then introduced.

[1] Portions of this chapter have been previously published (Crake *et al.*, 2015)

## 1.1. DIAGNOSTIC ULTRASOUND

The *Oxford English Dictionary* defines 'ultrasound' as '*Sound or other vibrations having an ultrasonic frequency*[2]*, particularly as used in medical imaging*' (OUP, 2015). As an imaging modality ultrasound offers numerous advantages over alternative methods of 'seeing within the body' such as x-ray, CT and MRI, including safety, low cost, portability and 'real-time' image formation. These characteristics make ultrasound imaging an ideal candidate for applications such as obstetrics, in which it has been routinely used for over 30 years (Campbell *et al.*, 1985). The widespread adoption of ultrasound imaging followed the development of array-based scanners in the 1980s, the technology having evolved throughout the 20th century from its roots in WWII-era sonar and radar (Szabo, 2004).

## 1.2. THERAPEUTIC ULTRASOUND

In addition to its use in imaging, as a *therapeutic* modality ultrasound has an equally long history. The biological effects of intense high frequency sound were noted as early as the 1920s (Wood and Loomis, 1927), with the first clinical reports of ultrasound-based physiotherapy appearing in the 1930s and of cancer treatment in the 1940s (see Kremkau, 1979; original papers in German). Major progress including clinical trials demonstrating the utility of high intensity ultrasound for cancer treatment and functional neurosurgery was made by the Fry brothers beginning in the 1950s (Fry and Fry, 1960), and later by Fry and Heimburger (Heimburger *et al.*, 1975), however, these early developments were hampered by poor focusing control, a lack of real-time feedback and in many cases the retained need for craniotomy, which negated many of the potential advantages of such an inherently non-invasive technique (Jagannathan *et al.*, 2009). Advances in electronics, computing power and

[2] i.e. above 20 kHz, the nominal upper threshold of human hearing

transducer technology in the intervening decades have since addressed most of these limitations. Therapeutic ultrasound has since been applied to a diverse range of applications in the fields of minimally invasive surgery and targeted drug delivery such as thermal ablation (Illing *et al.*, 2005), mechanical tissue fractionation (Roberts *et al.*, 2006), breakdown of blood clots (Alexandrov *et al.*, 2008), delivery of genes (Newman *et al.*, 2001), chemotherapeutic agents (Unger *et al.*, 1998) and oncolytic viruses (Carlisle *et al.*, 2013) and enhancing transport of drugs across the blood-brain barrier (Hynynen *et al.*, 2001). For both imaging and therapy the effects of ultrasound may be enhanced in many applications by the use of acoustically active microbubbles.

## 1.3. MICROBUBBLE CONTRAST AGENTS

The benefits of microbubbles in ultrasound imaging were discovered by chance in the 1960s when it was found that rapid injection of a range of substances (including dyes, saline and patient's blood) through a catheter placed in the heart resulted in increased imaging contrast (Gramiak *et al.*, 1969). Subsequent research established that this was due to generation of microbubbles and enhanced when the solutions were agitated (Meltzer *et al.*, 1980). The duration of this effect was found to increase when the solutions were mixed with a quantity of the patient's blood due to the albumin content forming a stabilising shell around the air core of the bubbles: this led to the development of Albunex®, the first commercial ultrasound contrast agent (Feinstein *et al.*, 1990). Similar microbubble suspensions are now routinely used to improve contrast in conventional diagnostic imaging (Al-Mansour *et al.*, 2000). Microbubbles may also act as adjuvants for higher intensity therapeutic regimes, in particular those involving acoustic cavitation (Coussios and Roy, 2008). However, current microbubble agents are subject to their own inherent limitations for therapeutic applications: in particular the microbubbles need to be very close to their target (on the order of 10s of

micrometres) in order to have an effect (Ward *et al.*, 2000) and an injected dose of microbubbles will be cleared from the circulation within minutes (Klibanov, 2005). Both of these limitations are compounded if the treatment mechanism requires another species (e.g. therapeutic drug) to be present simultaneously at the intended site. A possible solution involves *targeting* of microbubbles to maximise their effect by increasing the local concentration of bubbles at the treatment site: this may also provide the additional benefit of reducing systemic drug toxicity by enabling localised release of therapeutics attached to or encapsulated within the bubble (Hua *et al.*, 2010).

## 1.4. TARGETING OF MICROBUBBLES

Drug targeting is a broad field which has undergone rapid growth in recent years, with a particular focus on the delivery of chemotherapeutics to tumours (Lammers *et al.*, 2012) and on traversing the blood-brain-barrier to target the central nervous system (de Boer and Gaillard, 2007). Numerous potential 'vehicles' for drug transport have been developed, including those based on liposomes, polymers, micelles, nanoparticles and antibodies. The methods used to target them range from passive accumulation to ligand-based active targeting or externally triggered release (such as by temperature or some other external force) (Lammers *et al.*, 2012). Biological targeting methods such as antibody binding (Villanueva *et al.*, 1998) benefit from excellent specificity, and could potentially be used to 'seek' targets for treatment without prior knowledge of their location (Kaufmann and Lindner, 2007). However, their performance *in vivo* is often less from ideal, resulting in low targeting efficiency (Thurber *et al.*, 2008), strong dependence on flow conditions (Takalkar *et al.*, 2004), and even stimulation of an immunogenic response (Wang *et al.*, 2012). In the present work an alternative physical method of microbubble targeting was explored using an externally applied magnetic field.

## 1.5. MAGNETIC TARGETING

Magnetic targeting for drug delivery was first demonstrated *in vitro* in the 1970s using solid microspheres (Senyei *et al.*, 1978) and in human trials using a drug-carrying ferrofluid in the 1990s (Lübbe *et al.*, 1996). By association of magnetic nanoparticles with gene vectors, magnetic forces can be used to enhance transfection directly even in the absence of ultrasound (magnetofection) (Scherer *et al.*, 2002); alternatively, ultrasound may be used to induce acoustic cavitation, the physical effects of which may induce transient opening of cellular membranes (sonoporation) (Miller *et al.*, 2002). Magnetic microbubbles (MMB) respond both acoustically and to a magnetic field so may be used to combine the advantages of both effects: such microbubbles have been shown to enhance gene delivery both *in vitro* (Stride *et al.*, 2009; Mannell *et al.*, 2012; Vlaskou *et al.*, 2010b) and *in vivo* (Mulvana *et al.*, 2010). Previous work has shown that magnetic microbubbles may be simultaneously retained against flow and imaged using conventional ultrasound imaging techniques (Owen *et al.*, 2012b), and could also be used to provide contrast under MRI (Yang *et al.*, 2009; Liu *et al.*, 2011). In related work the filling gas was replaced by a volatile liquid forming magnetic nanodroplets that vaporise into microbubbles upon ultrasound exposure (Lee *et al.*, 2015). These will be described in more detail in subsequent chapters.

The ability to manipulate the location and concentration of microbubbles using an externally applied magnetic field has numerous potential advantages for ultrasound-mediated therapies, particularly those involving cavitation. The acoustic response of the bubbles enables them to be imaged and promotes cavitation under therapeutic excitation, while their magnetic response may facilitate more targeted initiation of this cavitation activity in space, a more sustained supply of cavitation nuclei over time, and subsequently greater energy deposition for a given dose of microbubbles or ultra-

sound intensity. This, in turn should lead to an improvement in treatment localisation thereby reducing the injected dose required.

With further development, additional co-injection or modification of the microbubbles to carry a drug has the potential to allow simultaneous imaging, targeting, release and enhanced delivery using a single vehicle. However, for such translation to be realised, improved understanding of magnetic microbubble behaviour is required: in particular evaluation of any changes in their response as a result of the increased proximity of microbubbles under magnetic confinement, and whether this can be maintained under clinically relevant conditions and treatment durations both *in vitro* and *in vivo*. In addition, the optimal exposure conditions for different therapeutic applications vary greatly, from relatively low amplitude stable cavitation to promote thrombolysis (Datta *et al.*, 2008) to more violent cavitation-enhanced heating for ablative treatment (Jensen *et al.*, 2012). There is thus an equally strong need for effective treatment monitoring methods.

## 1.6. TREATMENT MONITORING

Existing monitoring methods for therapeutic ultrasound include conventional active ultrasound imaging (e.g. B-mode hyperecho (Rabkin *et al.*, 2005)), ultrasound elastography (Kallel *et al.*, 1999), MRI thermometry (Rivens *et al.*, 2007), CT (Wood *et al.*, 2006) and more invasive methods such as embedded thermocouples (Hynynen *et al.*, 1993). However, most of these techniques rely on secondary effects such as macroscopic changes in tissue structure or temperature so are generally limited to high-intensity ablative treatments, suffer from poor spatial and temporal resolution (Jensen *et al.*, 2013), and may not be possible in real-time during ultrasound exposure. In many cases cavitation has been shown to play a key role (Coussios *et al.*, 2007). Passive recording of the acoustic emissions from cavitation – passive cavitation detec-

tion (Neppiras and Coakley, 1976) – provides a more direct method of monitoring cavitation-induced bioeffects, and may be extended to map cavitation in two (Gyöngy and Coussios, 2010b) or three dimensions (Collin *et al.*, 2013), then termed passive acoustic mapping.

## 1.7. PASSIVE ACOUSTIC MAPPING

Passive acoustic mapping (PAM) utilises an array of receivers to record the acoustic emissions from a tissue volume followed by beamforming of the recordings to reconstruct the distribution of sources. As such, it enables real-time spatiotemporal monitoring of cavitation activity in the field of view of an ultrasound probe. The technique was initially demonstrated as a means of tracking bubble activity in agar phantoms (Gyöngy *et al.*, 2008), while related work (without parallel channel recording) used similar methods to image cavitation in saline and *ex vivo* liver (Salgaonkar *et al.*, 2009). PAM has subsequently been used to investigate the activity of flowing commercial microbubbles (Choi and Coussios, 2012), echogenic liposomes (Haworth *et al.*, 2012), monitoring of bubble activity in the brain through the skull (Arvanitis *et al.*, 2013; Jones *et al.*, 2013) and to predict lesioning in *ex vivo* liver (Jensen *et al.*, 2013; Jensen *et al.*, 2012). For short (1-2 cycle) pulse excitation, synchronisation of passive data acquisition with the high-intensity pulses may be used to improve the axial resolution of mapping, and combined with high-speed active imaging (Gateau *et al.*, 2011b). Prior to the present work PAM has not been applied to targeted microbubbles.

## 1.8. AIMS AND OBJECTIVES

### 1.8.1. Statement of problem

It is clear that therapeutic ultrasound is a powerful treatment modality which has great potential for the non-invasive treatment of tissues deep within the body. Cavitation phenomena have been found to play a key role in many such applications and may be greatly enhanced by the addition of exogenous nuclei such as microbubbles. By appropriate agent design these may facilitate additional benefits allowing combined imaging, targeting, payload release and enhanced drug delivery using a single vehicle. Magnetic microbubbles are one such agent which has shown promise in early *in vitro* and *in vivo* trials.

However, in previous targeted microbubble experiments – with magnetic targeting or otherwise – acoustic monitoring was typically limited or absent completely. As a result the effect of targeting on the acoustic response of the microbubbles was not evaluated. Similarly, the potential effects of magnetic targeting on cavitation behaviour and whether this could be correlated to a therapeutic effect, were unknown. In addition, as the 50 years of prior work in the field has shown, the provision of reliable real-time monitoring is vital for the adoption of any new medical intervention.

### 1.8.2. Aims

The overall aim of the work described in this thesis was to address these challenges. PAM was applied to magnetic microbubbles to investigate both basic scientific questions – such as whether any influence of microbubble targeting could be observed in their acoustic emissions – as well as in a more applied manner using *in vitro* and *in vivo* models with a view to developing the technique from the laboratory into a clinical tool. In particular, the key objectives of the present work include investigation of the following:

1) Whether or not magnetic localisation of microbubble-induced cavitation could be achieved under focused ultrasound excitation and detected using PAM.

2) The effects of magnetic confinement on the characteristics of the resulting cavitation activity (spatial distribution, total energy, sustainability, etc.).

3) Whether these effects could still be observed under physiologically relevant flow conditions.

4) Whether or not enhanced cavitation activity produced therapeutically relevant bioeffects in *in vitro* models, and if these can be correlated with PAM.

5) Finally, whether these effects could be observed in *in vivo* models.

### 1.8.3. Thesis outline

In Chapter 2 a detailed review of previous work in the fields of passive acoustic mapping and magnetic microbubbles is presented, covering the background material relevant to understanding of the techniques and methods used in the experiments. The experimental work is described in Chapters 3, 4 and 5, and is divided between that conducted in tissue phantoms, *in vitro* (cell) and *in vivo* (mouse) models respectively. Chapter 3 investigates whether PAM could be a useful technique for monitoring of magnetic microbubbles by studying the behaviour of bubble samples under controlled laboratory conditions in tissue phantoms. In Chapter 4 these methods are applied to a number of different cell models for drug delivery applications and the correlation between acoustic emissions and drug uptake and/or cell viability examined. In Chapter 5 these investigations are extended to *in vivo* models. Finally, the overall conclusions of the work are presented in Chapter 6 together with suggestions for future work.

CHAPTER 2

# BACKGROUND & LITERATURE REVIEW

In this chapter a more detailed review is conducted of those areas most relevant to the project. The chapter is organised into four main sections:

1) Clinical background and motivation

2) Passive acoustic mapping – the acoustic monitoring technique used in this thesis

3) Magnetic microbubbles – the targeted cavitation nuclei whose performance was investigated and

4) Therapeutic applications – the biological targets to which 1) and 2) were applied, and biological techniques used to assess their success

Finally, the chapter is summarised in Section 2.5.

## 2.1. CLINICAL BACKGROUND & MOTIVATION

Therapeutic ultrasound is a versatile technique which offers great promise for the non-invasive treatment of a wide variety of conditions deep within the body. The effects of ultrasound may be significantly enhanced by the use of acoustically-active microbubbles, which may also be used to impart additional functionality such as delivery of a payload (e.g. therapeutic drug). Microbubbles may also be designed in such a way that they may be selectively targeted to the location of interest, which could be of great benefit in the case of toxic drugs such as chemotherapeutics. One such targeting mechanism which was employed in this thesis uses magnetic nanoparticles, such that the microbubbles may be localised using a magnetic field.

A significant barrier to the widespread adoption of therapeutic ultrasound for clinical use concerns the provision of adequate real-time treatment monitoring. This is vital both to maximise the efficacy of treatment and to ensure patient safety. Current clinical monitoring methods such as B-mode hyperecho are clearly inadequate for this purpose. A promising alternative technique which has been employed for monitoring of acoustic emissions in previous *in vitro* and *in vivo* studies is passive acoustic mapping (PAM). In this thesis PAM was used to study the behaviour of magnetic microbubbles in a variety of settings, as well as for real-time monitoring of their response both *in vitro* and *in vivo*.

In the following sections PAM and magnetic microbubbles are reviewed in more detail, followed by an introduction of the biological targets to which they were applied in this thesis.

## 2.2. PASSIVE ACOUSTIC MAPPING

Passive acoustic mapping (PAM) refers to the use of passively recorded acoustic data – in particular the acoustic emissions from cavitation – to produce maps showing an estimate of the distribution of acoustic sources that generated these emissions. In the experimental configuration used for the work in this thesis this typically involves cavitation induced by a therapeutic ultrasound transducer with the acoustic emissions received by an imaging array (Figure 2.1).

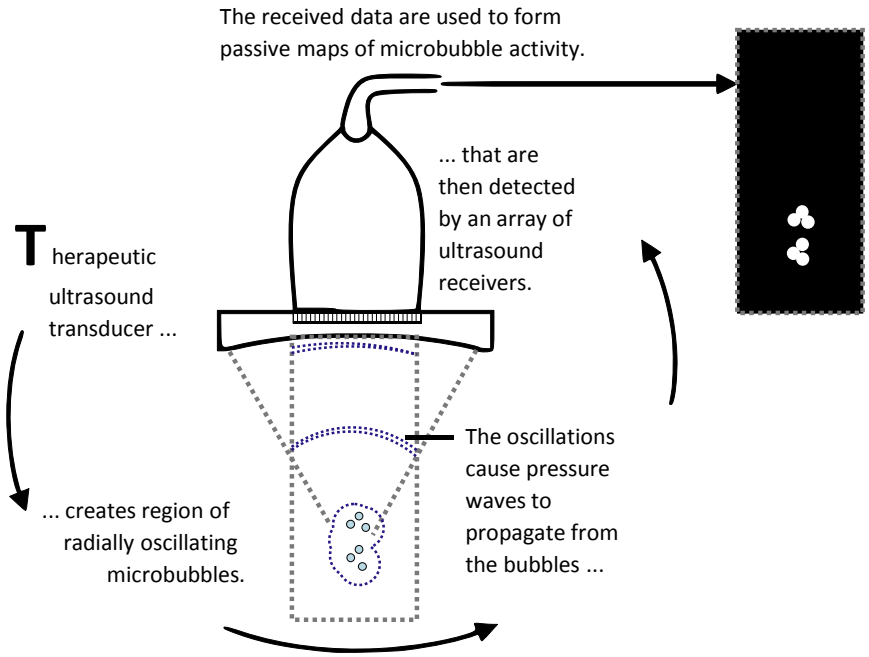


Figure 2.1: Monitoring of therapeutic ultrasound with passive acoustic mapping, reproduced from (Gyöngy, 2010).

The implementation of PAM used in this thesis is based on that described in the D.Phil. thesis of (Gyöngy, 2010) and subsequent development by members of the BUBBL group – in particular Christian Coviello, Carl Jensen, Jamie Collin and James Choi – whose contributions are expressly acknowledged.

### 2.2.1. Historical background

Acoustic imaging can be broadly split into active techniques – primarily 'pulse echo' in which a pulse is transmitted and the image constructed from the received echoes[3] – and passive methods, in which no outgoing pulse is used. Active methods range from SONAR (sound navigation and ranging) developed towards the end of WWI, through to modern diagnostic ultrasound imaging (Szabo, 2004). These are not discussed in detail here however as the work described in this thesis focuses on the use of passive methods.

Passive acoustic imaging may be further subdivided into techniques in which noise is generated within a target and those in which sound from some other source is merely scattered by the target (Buckingham *et al.*, 1992; Potter, 1994). The former includes use of engine/propeller noise for passive SONAR (Hahn, 1975) and various methods for localisation and mapping of animal calls both in air and under water (Walker, 1963; Watkins and Schevill, 1971; Clark, 1980; Magyar *et al.*, 1978; Chen *et al.*, 2006; Spiesberger and Fristrup, 1990); while the latter includes mapping of underground seismic features (Norton and Won, 2000) or structures in the ocean (Buckingham *et al.*, 1992) using ambient noise.

The use of passive arrays for mapping of cavitation during High Intensity Focused Ultrasound (HIFU) exposure in a manner similar to this thesis was initially described by (Gyöngy *et al.*, 2008; Gyöngy, 2010), in which a coaxial HIFU transducer and linear array assembly was used to induce cavitation in agar phantoms and produce maps of the resulting cavitation activity. Similar techniques have also been demonstrated elsewhere for monitoring of cavitation activity (Salgaonkar *et al.*, 2009; Gateau *et al.*,

[3] Other active ultrasonic imaging methods include 'pitch catch' (Delrue *et al.*, 2010) in which the pulse is reflected between transducers positioned at an angle, and acoustic tomography (Greenleaf and Bahn, 1981) in which an image is reconstructed from recordings taken at multiple angles, but these are not commonly used for modern medical imaging.

2011b; Jones *et al.*, 2013). The method used was based on a technique from seismology known as Time Exposure Acoustics (TEA) in which ambient seismic noise is used for mapping of underground acoustic sources (Norton *et al.*, 2006; Norton and Won, 2000), which itself was built upon proof-of-concept studies for imaging of underwater structures using ocean noise (Buckingham, 1993; Buckingham *et al.*, 1992).

### 2.2.2. Basic acoustics and wave propagation

In order to explain the theory of passive acoustic mapping it is useful to review a few basic elements of acoustics. Below expressions for the pressure radiated from a point source and corresponding source power are derived. In PAM the inverse problem of estimating source strength and hence source power from pressure recordings is considered.

Sound is a perturbation in pressure which propagates as a longitudinal wave. When these perturbations are small, their propagation can be described mathematically by the linear wave equation (Dowling and Ffowcs Williams, 1983):

$$\frac{1}{c^2}\frac{\partial^2 p'}{\partial t^2} - \nabla^2 p' = 0 \tag{2.1}$$

where $p'$ is pressure perturbation, and $\nabla$ the Laplacian operator. The speed of sound $c$ varies from around 340 m/s in air to 1500 m/s in water (Dowling and Ffowcs Williams, 1983) or ~1540 m/s in soft tissue (Ludwig, 1950). D'Alembert's solution to this equation in spherical polar form may be written:

$$p'(r,t) = \frac{f(r-ct)}{r} + \frac{g(r+ct)}{r} \tag{2.2}$$

where $f$ and $g$ are arbitrary functions. So from the wave equation, taking $g = 0$:

$$\left(\frac{1}{c^2}\frac{\partial^2}{\partial t^2} - \nabla^2\right)\frac{f(t-r/c)}{r} = 0 \tag{2.3}$$

This function is undefined at the origin due to the $1/r$ term. Close to the origin, as $r \to 0$ the $\nabla^2$ term becomes dominant, leaving a form of Laplace's equation:

$$\nabla^2 \frac{f(t-r/c)}{r} = 0 \tag{2.4}$$

The integral of this function over a small spherical volume with surface area $4\pi\epsilon^2$ tends to $-4\pi f(t)$ as $\epsilon \to 0$ (Dowling and Ffowcs Williams, 1983). This result can be incorporated into the wave equation so that it is only active at the origin (and zero elsewhere) using a 3-dimensional Dirac delta function $\delta(\mathbf{x})$, i.e.:

$$\left(\frac{1}{c^2}\frac{\partial^2}{\partial t^2} - \nabla^2\right)\frac{f(t - r/c)}{r} = 4\pi f(t)\delta(\mathbf{x}) \tag{2.5}$$

For which the solution for $p'$ may be written as (Dowling and Ffowcs Williams, 1983):

$$p'(\mathbf{x}, t) = \frac{\tilde{q}(t - r/c)}{4\pi r} \tag{2.6}$$

where $\tilde{q}(t)$ is the *source strength* of a source of sound defined such as it is active only at the origin and zero elsewhere using a Dirac delta function, known as a *mono-pole point source*, and $r = |\mathbf{x}|$. Equation 2.6 is an important result which describes the pressure received at a remote point $\mathbf{x}$ radiated from a point source of strength $\tilde{q}$. The emissions from the source spread out spherically and arrive at the remote point after a time $r/c$. The units of $\tilde{q}$ are evidently Pascal-metres as expressed above, which can be shown to be equivalent to $kg/s^2$; i.e. mass acceleration, or rate of change of mass outflow from the source. A similar expression for the inverse problem of reconstructing the source strength from pressure readings is found in the PAM algorithm below (Section 2.2.4).

The source strength can be converted to more useful units of power and energy by considering the acoustic intensity. The instantaneous acoustic intensity[4] $I$ is defined as

[4] Practical measurements of acoustic intensity (e.g. using a hydrophone) are not instantaneous due to finite temporal resolution, and are subject to spatial averaging over the size of the detector. Such measurements are typically specified as peak or average values in space and over time, e.g. spatial peak temporal peak ($I_{SPTP}$).

the power per unit area, and may be found from the product of pressure and particle velocity $u$. For a plane wave the particle velocity $u$ is given by the pressure divided by acoustic impedance $\rho_0 c$, i.e. (Dowling and Ffowcs Williams, 1983):

$$I = p'u = p'^2/\rho_0 c \tag{2.7}$$

Substituting for $p'$ from Equation 2.6 gives:

$$I = \frac{\left(\tilde{q}\left(t - \frac{r}{c}\right)\right)^2}{16\pi^2 r^2 \rho_0 c} \tag{2.8}$$

This expression represents the instantaneous acoustic intensity a distance $r$ away from a point source of strength $\tilde{q}$. Assuming $\rho_0$ and $c$ are constant[5] the acoustic wave spreads out spherically from the source, so crosses a surface area $4\pi r^2$. The product of intensity and the surface area it crosses must equal therefore equal the source power $P$, i.e. (Lighthill, 2003):

$$P = \frac{\left(\tilde{q}\left(t - \frac{r}{c}\right)\right)^2}{4\pi \rho_0 c} \tag{2.9}$$

This expression could be considered analogous to the familiar expression $P = V^2/Z$ for electrical power, where $V$ is the source strength (voltage) and $Z$ the (electrical) impedance; the extra $4\pi$ scaling term results from the use of spherical polar coordinates. The result of Equation 2.9 is used to convert the source strength of Equation 2.6 into units of power, which is then integrated to give source energy in the PAM algorithm below (Section 2.2.4).

[5] If $\rho_0 c$ is not constant then a portion of the wave will be reflected (and a portion transmitted) due to the impedance change, expressed as the coefficients of reflection and transmission respectively. In addition, if the speed of sound $c$ is not constant then a wave arriving at the boundary at an angle will be refracted in accordance with Snell's law. These effects may cause aberration (blurring) of the PAM images and reduce the signal-to-noise if there are materials with significantly different acoustic properties (e.g. bone/air) in the ultrasound field.

### 2.2.3. Principles of passive acoustic mapping

The basic method by which the recordings of acoustic emissions received on an array can be used to reconstruct the distribution of sources which produced them is perhaps best understood with the aid of a diagram (Figure 2.2) and consists of 5 steps:

1) The acoustic emissions from a source such as a bubble undergoing acoustic cavitation propagate spherically outwards from their source as a pressure wave. From the point of view of a linear array (as in Figure 2.1) this spherical wave appears as a section of a circle (Figure 2.2, top left).

2) If the position of the array elements is known then the distance from each of them to a point of interest may be calculated. Assuming the speed of sound of the medium is known this can be converted to differences in propagation time from the chosen point to each of the elements, and hence used to time shift the recordings as if the receivers were equidistant from the chosen point (Figure 2.2, mid left). In beamforming terminology (see below) this is known as 'steering' the data (Coviello *et al.*, 2015).

3) By averaging the set of delayed recordings it can be reduced to a single trace corresponding to an estimate of the source strength over time from that point (Figure 2.2, bottom left). In principle this could be found using a simple average, however it is more accurate to first multiply each of the recordings by a term which compensates for the differences in distance (and hence size of the sphere over which the pressure wave has spread) for each element.

4) By appropriate calculation (described in detail later) the source strength can be reduced to a single value representing the strength of acoustic emissions from the chosen point. By taking the mean-squared source strength and dividing by

acoustic impedance (which may be considered analogous to the expression $P = V^2/Z$ for electrical power) a value of the power of cavitation from that point in Watts is obtained. Likewise, integration over time gives units of energy in Joules.

5) Finally, to obtain a *map* of cavitation power, steps 2-4 are repeated over a range of locations (and hence time delays), and the resulting power values recorded. Plotting of source power as a function of position gives the resulting map (Figure 2.2, right). The whole process may then be repeated (at a frame rate set by the memory and speed limitations of the recording system) to allow spatiotemporal monitoring of cavitation activity.

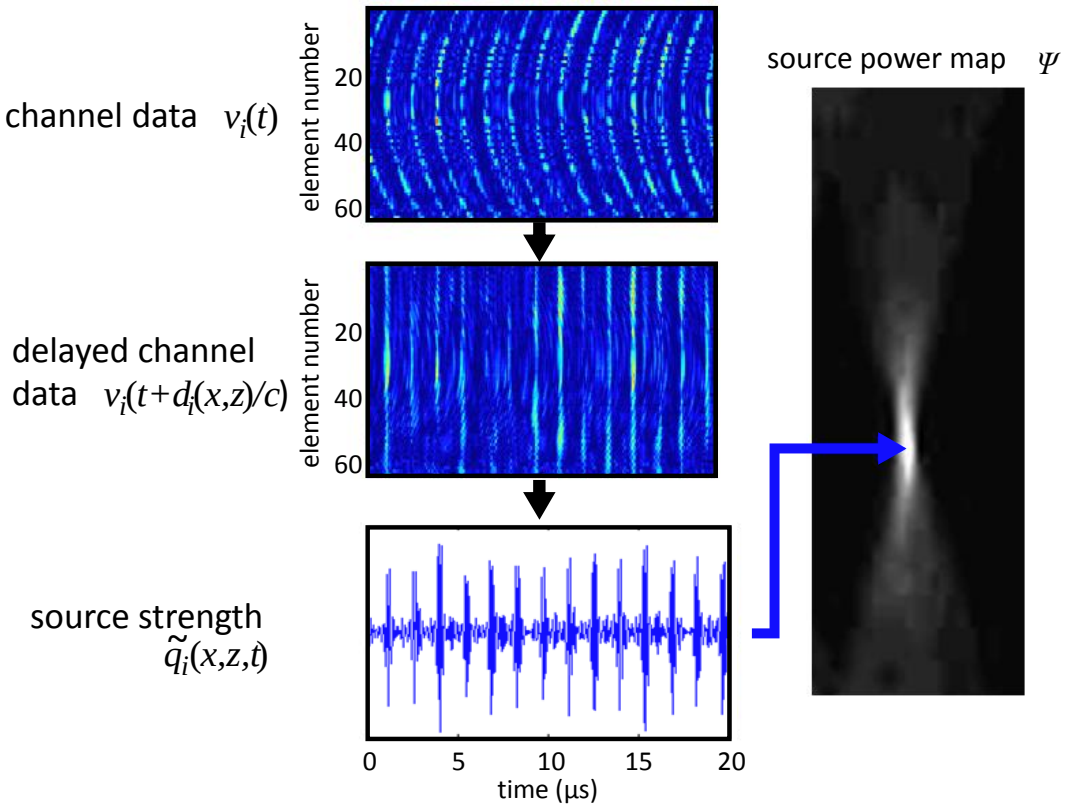


Figure 2.2: The basic passive acoustic mapping algorithm, reproduced from (Gyöngy, 2010). Channel data shows emissions from a single bubble cavitating periodically. For each location in the map the channel data is appropriately delayed and averaged, and the mean-square value taken to give the resulting power value for that pixel in the map.

### 2.2.4. Time exposure acoustics

Mathematically the delay, weighting and averaging process outlined above can be represented by the following concise pair of equations.

The source strength $\tilde{q}$ at a remote point $\mathbf{r}$ is found from a weighted average of pressure recordings $\tilde{p}$ from a set of $N$ sensors located at positions $\mathbf{r}_i$, each of which is delayed to account for propagation time to that sensor (assuming a speed of sound $c$) and scaled to account for spherical spreading (Gyöngy and Coussios, 2010a):

$$\tilde{q}(\mathbf{r},t) = \frac{1}{N}\sum_{i=1}^{N} 4\pi|\mathbf{r}_i - \mathbf{r}|\tilde{p}\,(\mathbf{r}_i, t + |\mathbf{r}_i - \mathbf{r}|/c) \tag{2.10}$$

This expression is essentially a rearrangement of the pressure field radiating from a point source of strength $\tilde{q}$ kg/s$^2$ (Equation 2.6). The source power may likewise be calculated by taking the square of the source strength divided by acoustic impedance as in Equation 2.9, where $\rho_0$ is the undisturbed density of the medium (Gyöngy and Coussios, 2010a). Integration of the source power over time gives units of energy.

$$\tilde{E}(\mathbf{r}) = \int \frac{\tilde{q}^2(\mathbf{r},t)}{4\pi\rho_0 c}\,dt \tag{2.11}$$

Equations 2.10 and 2.11 are based on an imaging technique from seismology known as *Time Exposure Acoustics* (TEA), so called as the energy map is obtained by integration of the data received over a period of time (typically based on the frame rate), by analogy to long exposure photography (Norton and Won, 2000; Norton *et al.*, 2006). The formulation above adds scaling terms to put the source power and energy in units of Watts or Joules respectively.

## 2.2.5. Resolution limits

Diffraction refers to the process by which waves spread out as a result of interference effects (OUP, 2015). In any classical system based on waves (sound, light, radio, x-ray, etc.) this places a limit on the maximum resolution which may be achieved on the order of a wavelength. For a given system this process may be described by the point spread function (PSF), which essentially describes how a point source appears after broadening as a result of diffraction, and hence defines the resolution limit for that system. The width of the PSF at half its peak value defines the minimum distance between sources which can be separated according to the Rayleigh criterion (Borgiotti and Kaplan, 1979), and hence the maximum resolving power of the system.

The theoretical resolution limit for PAM using a linear array is based on the size of the focal region for such an array, expressions for which may be found in the literature and are noted below (Graham, 1983; Sherman, 1962; Kino, 1987). These expressions were re-derived in the context of PAM in a similar manner by (Gyöngy, 2010).

In the context of this thesis cavitation was induced using a 500 kHz HIFU transducer, so for PAM to be useful as a monitoring tool it is desirable for the resolution to be smaller than the focal region of this transducer. For the transducer used in this thesis the focal region measured 3 mm (transverse) by 25 mm (axial) (Appendix A).

### 2.2.5.1. Transverse resolution

In the transverse direction (across the array) the resolution is given by (Gyöngy and Coussios, 2010a; Gyöngy, 2010; Sherman, 1962):

$$\Delta x = 0.89\,\frac{F\lambda}{D} \tag{2.12}$$

Where $F$ is the axial distance from the source to the array (effective focal length), $D$ is the size of the array aperture, and $\lambda$ wavelength of the source. For the setup of Chapter 3 $F$ = 73 mm, $D$ = 38.4 mm and $\lambda$ = 0.22 mm (assuming a source at the 7.14 MHz centre frequency of the array, speed of sound for tissue of 1,540 m/s (Ludwig, 1950)), so $\Delta x$ = 0.36 mm. This is smaller than the HIFU transducer focus.

#### 2.2.5.2. Axial resolution

In the axial direction (outwards from the array) the resolution is given by (Gyöngy and Coussios, 2010a; Graham, 1983; Gyöngy, 2010):

$$\Delta z = 6.95 \left(\frac{F}{D}\right)^2 \lambda \tag{2.13}$$

Which for the setup of Chapter 3 yields $\Delta z$ = 5.4 mm. While this is larger than the transverse resolution it is still a factor of 4 smaller than the length of the focal region of the HIFU transducer, so should still be able to accurately assess cavitation in this region. Due to the squared dependence on $F/D$ increasing the size of the aperture or reducing depth can greatly increase the resolution.

To improve the resolution of PAM alternative algorithms such as optimal beam-forming methods may be employed, as discussed below. Such algorithms can achieve resolution closer to the diffraction limits than simple methods such as TEA, and under certain circumstances (e.g. assuming uncorrelated sources) can exceed these limits (i.e. super resolution imaging) (Borgiotti and Kaplan, 1979).

### 2.2.6. Beamforming

The delay-and-sum approach of Equation 2.10 in the TEA algorithm is an example of a versatile array processing technique known as *beamforming* or spatial filtering (Van Veen and Buckley, 1988). A more general representation of such a delay-and-sum beamformer is shown in Figure 2.2 (Mucci, 1984).

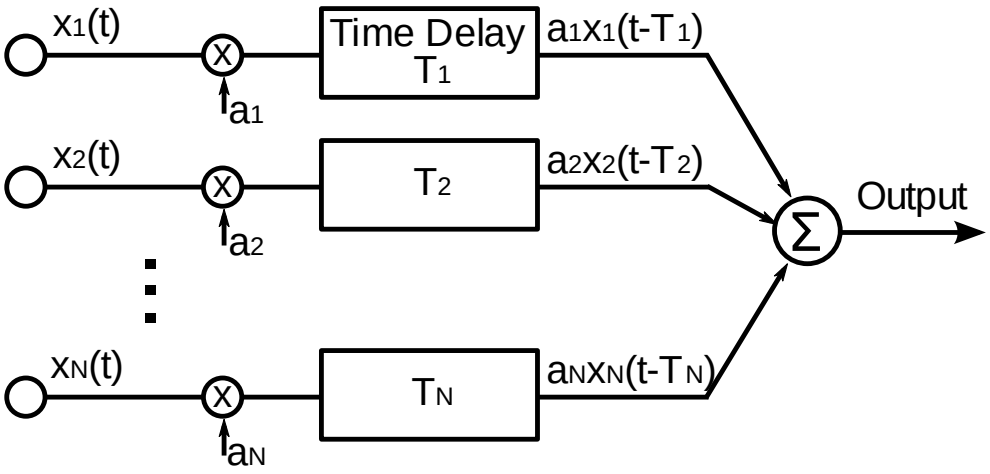


Figure 2.3: General representation of a beamformer, based on (Mucci, 1984), © 1984 IEEE. The output is formed from a weighted sum of the delayed input signals.

For the delay-and-sum beamformer shown above the output is formed from a weighted sum of the delayed input signals, thus the output $b(t)$ may be written in terms of the weighting coefficients $a_n$, input signals $x_n$and time delays $T_n$ as (Mucci, 1984):

$$b(t) = \sum_{n=1}^{N} a_n \, x_n(t - T_n) \tag{2.14}$$

By comparison with Equation 2.10 it is evident that the TEA algorithm follows this configuration, where the $1/N$ and spherical spreading terms are combined into the weighting coefficients $a_n$, and $|\mathbf{r}_i - \mathbf{r}|/c$ time delay terms given by $T_n$. More generally, a beamformer may consist of several delay and sum stages in order to sample the signal both in space and over time (Van Veen and Buckley, 1988).

### 2.2.7. Optimal beamforming

The method used to calculate weighting coefficients may be used to classify a beamformer as either 'data independent' or 'statistically optimal' (Van Veen and Buckley, 1988). In a data independent beamformer the weighting coefficients do not depend on the signal received, while for a statistically optimal beamformer the weights are varied based on the data itself in order to optimise the response. The TEA algorithm as outlined above is evidently data independent, as the weighting terms depend only on the region of interest selected and array geometry. Statistically optimal beamforming algorithms such as the Capon beamformer (Capon, 1969) described below can be used to improve the performance of beamforming, and reduce artefacts that occur from simple algorithms such as TEA (Coviello *et al.*, 2015).

In order to compare such improved algorithms to TEA Equations 2.10 and 2.11 are re-expressed using the more general terminology of (Coviello *et al.*, 2015), under which the source strength is given by:

$$\tilde{q}(x,t) = \frac{4\pi}{\alpha}\mathbf{w}^T\mathbf{D}(\mathbf{x})\mathbf{s}(\mathbf{x},t) = \frac{4\pi}{\alpha}\sum_{j=1}^{N} w_j d_j(\mathbf{x}) s_j\left(t + \tau_j(\mathbf{x})\right) \qquad (2.15)$$

Here $\mathbf{w}$ is a vector of beamforming weights, $\mathbf{D}(\mathbf{x})$ a (diagonal) matrix which holds the distance from each sensor to the location of interest $\mathbf{x}$, and $\mathbf{s}(\mathbf{x},t)$ is the pre-steered set of recordings from the array (i.e. after time delays, as in Equation 2.10). The term $\alpha$ represents the sensitivity of the sensors, i.e. converts the units of $\mathbf{s}$ to pressure. This may equivalently be written as a sum over the $N$ sensors, where $j$ is the current element. The source energy is then given (as in Equation 2.11) by:

$$\Psi(\mathbf{x}) = \frac{1}{4\pi\rho_0 c}\int_{t_0}^{t_0+t'} \tilde{q}(\mathbf{x},t)^2 dt \qquad (2.16)$$

Defining a correlation matrix $\mathbf{R}_s(\mathbf{x})$ – which essentially represents how similar the signal on one element is to each of the others over a time period $t'$ – for the set of recordings from the array as:

$$\mathbf{R}_s(\mathbf{x}) = \int_{t_0}^{t_0+t'} \mathbf{s}(\mathbf{x},t)\mathbf{s}(\mathbf{x},t)^{\boldsymbol{T}} dt \tag{2.17}$$

Then after substitution the source energy may be written as:

$$\Psi(\mathbf{x}) = \frac{4\pi}{\alpha^2 \rho_0 c} \mathbf{w}^T \mathbf{D}(\mathbf{x}) \mathbf{R}_s(\mathbf{x}) \mathbf{D}(\mathbf{x}) \mathbf{w} \tag{2.18}$$

For the TEA algorithm the weight vector is uniform across the array and is simply the $1/N$ term in Equation 2.10, i.e. $\mathbf{w}_{\mathrm{TEA}} = (1/N)\mathbf{1}$, where $\mathbf{1}$ is a $N \times 1$ vector of ones. For optimal beamforming algorithms the weights are calculated based on the statistics of the data. Two such algorithms are discussed below.

### 2.2.8. The Capon beamformer

The Capon beamformer (CB) (Capon, 1969), also known as the minimum variance beamformer (MVB), is an example of a statistically optimal beamformer in which the weights **w** are varied based on statistics of the data in order to improve performance. The beamformer is designed to vary the weights such that it passes the signal undisturbed from the current position of interest, while rejecting interference from other locations (Coviello *et al.*, 2015).

The process by which varying the weights can reduce interference is illustrated in Figure 2.4. The pressure waves from two cavitating sources – one at the current point of interest, the other an interfering source at some other location – are received by an array. To recover the signal from the point of interest the data are first steered (i.e. time delays are applied) as explained above (step 1). In TEA an average is then taken using equal weights which are fixed regardless of the signal received (steps 2-4, top row of figure). Since the signal from the point of interest is in phase after the time delays (while that from the interfering source is not) it appears more strongly in the output signal, but the signal from the interfering source may not be removed completely.

Using optimal beamforming (steps 2-4, bottom row of figure) the weights are modified to reduce the magnitude of the interfering source while not affecting that from the point of interest. Since the signal from the point of interest is in phase it will be unaffected by varying the weights provided the sum of weights remains the same (i.e. equal to 1). This is not true for the signal from the interfering source, so by appropriate weight selection its magnitude can be reduced in the output. In this example the elements where the interference is most out of phase were assigned larger weights, so that the interfering signal is reduced in the output after averaging. As a result the total power of the output signal (e.g. mean-square) will be reduced.

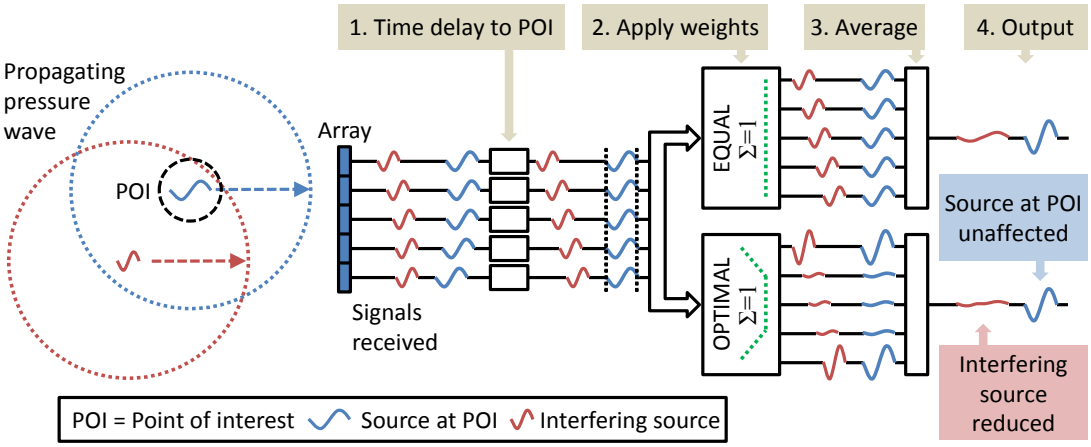


Figure 2.4: Reduction of interference using optimal beamforming. Using equal weights (as in TEA) the interfering source is reduced in amplitude to some degree since it is out of phase after the time delays to the point of interest, but not removed entirely. In optimal beamforming (e.g. CB) the weights are modified to attenuate the interfering source further. In this simplified example the elements where the interference is most out of phase were assigned larger weights, so the interfering signal is reduced after averaging. The signal from the point of interest is unaffected since it is in phase after the time delays and sum of weights is the same.

In practice the presence or location of interfering sources is typically unknown. However, if by varying the weights (subject to the constraint that their sum remains equal to 1) the output power is reduced, this implies that the excess power was from interference from outside the current point of interest. This essentially describes the Capon beamformer, the purpose of which is to select weights which minimise the output power[6], subject to the constraint that the sum of weights remains equal to 1. Mathematically this may be expressed using the previous expression for output power (from Equation 2.18) as (Coviello *et al.*, 2015):

$$\min_{\mathbf{w}} \mathbf{w}^T \mathbf{D}(\mathbf{x}) \mathbf{R}_s(\mathbf{x}) \mathbf{D}(\mathbf{x}) \mathbf{w} \quad \text{subject to} \quad \mathbf{w}^T \mathbf{a_0} = 1 \tag{2.19}$$

Where $\mathbf{a_0}$ is a *steering vector* whose elements are based on the delays due to propagation to each receiver (Van Veen and Buckley, 1988). In the form presented here the array data $\mathbf{D}(\mathbf{x})\mathbf{s}(\mathbf{x}, t)$ has already been distance compensated so the corresponding steering vector $\mathbf{a_0}$ for the Capon beamformer is simply a vector of ones. The con-

[6] For a signal with zero mean the variance is equal to power, hence Capon's method is also known as minimum variance beamforming

strained optimisation problem expressed in Equation 2.19 may be solved analytically to find the optimal weights (Appendix D) (Coviello *et al.*, 2015; Stoica and Moses, 2005) and hence maps produced.

However, in practice the conventional Capon beamformer outlined here may actually result in *worse* performance than data-independent beamforming methods such as TEA due to even modest uncertainty in the steering vector $\mathbf{a_0}$ (Lorenz and Boyd, 2005; Vorobyov *et al.*, 2003) which may occur due to array imperfections (e.g. cross-coupling between elements, variation in element position), gain mismatch, or other physical effects such as variation of speed of sound in the sample under test (Coviello *et al.*, 2015). This effect is illustrated in Figure 2.5 which shows PAMs produced from an experiment in which microbubbles were excited at a known location and monitored using an array with uneven element sensitivity. TEA (left image) shows the peak in energy correctly co-located with the channel (but with substantial artefacts outside of it due to multi-bubble interactions), while the CB (middle) image is completely inaccurate. The robust Capon beamformer (RCB) algorithm discussed below allows the steering vector to vary to compensate for these uncertainties and alleviate these effects.

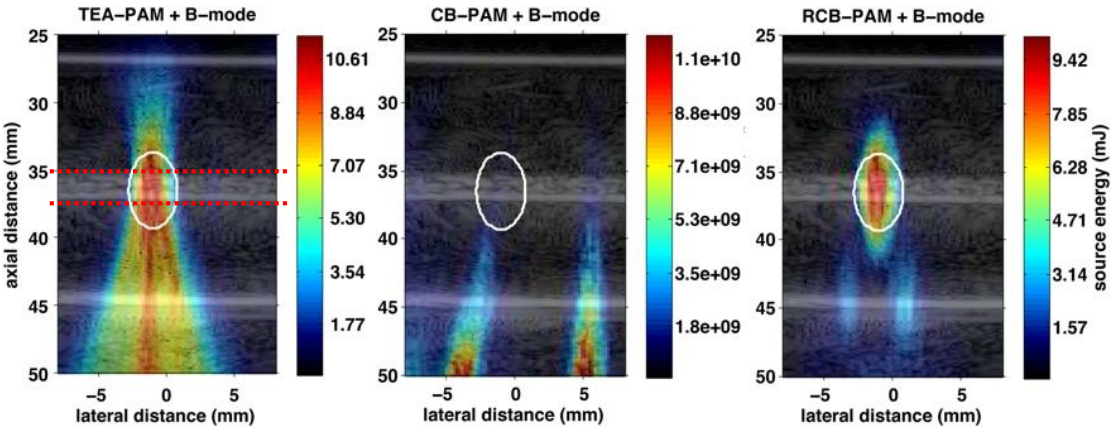


Figure 2.5: Comparison of PAM beamformer performance, reprinted with permission from (Coviello *et al.*, 2015). Copyright 2015 Acoustical Society of America. PAMs produced from the same data using (a) TEA, (b) CB and (c) RCB ($\epsilon$ = 8.45) beamformers are overlaid on B-mode images. Microbubbles were made to flow through a channel (outlined with the red dotted lines in left image) and excited using a HIFU transducer.

### 2.2.9. The Robust Capon beamformer (RCB)

In assuming a steering vector equal to 1 the Capon beamformer effectively implies that the pre-steered data $\mathbf{D}(\mathbf{x})\mathbf{s}(\mathbf{x},t)$ is already perfectly compensated for distance and time delays. For various physical reasons – such as variations in element positions, unequal gain or cross-coupling between elements (Coviello *et al.*, 2015) – the real steering vector may be different to the assumed value, which can lead to sub-optimal selection of weights and the severe performance degradation illustrated in Figure 2.5.

The RCB instead makes the steering vector a variable, allowing it to vary within a range set by an overall uncertainty parameter $\epsilon$ to compensate for these effects. The constrained optimisation may be written (after some simplifying assumptions) as (Coviello *et al.*, 2015):

$$\min_{\mathbf{a}} \mathbf{a}^T \mathbf{R}_s(\mathbf{x})^{-1}\mathbf{a} \quad \text{subject to} \quad \|\mathbf{a}-\bar{\mathbf{a}}\|^2 \leq \epsilon \tag{2.20}$$

Where $\mathbf{a}$ is the new steering vector, $\bar{\mathbf{a}} = \mathbf{1}$ the initial steering vector and $\epsilon$ the uncertainty parameter by which $\mathbf{a}$ is allowed to vary. The constrained optimisation problem of Equation 2.20 may be solved using the Lagrange multiplier method analytically (Li *et al.*, 2003; Stoica and Moses, 2005). The solution is more complex than the standard Capon beamformer (Section 2.2.8) as the resulting expression is nonlinear, but may be readily solved by numerical methods (Coviello *et al.*, 2015). Using the RCB formulation of (Li *et al.*, 2003) allows calculation of energy values directly without explicit weight calculation.

The RCB algorithm can be used to obtain superior mapping performance compared to the TEA and CB algorithms, as shown in Figure 2.5 (right image) where the indicated cavitation is more tightly contained within its (known) location. However, care must be taken in selection of an appropriate value of the tolerance parameter $\epsilon$ to

produce meaningful results. Figure 2.6 shows PAMs produced using the RCB algorithm for the same data using three different values of $\epsilon$ – at too low a value (left image) the post-focal artefact was not completely supressed, while at too high a value (right image) the artefact was accentuated.

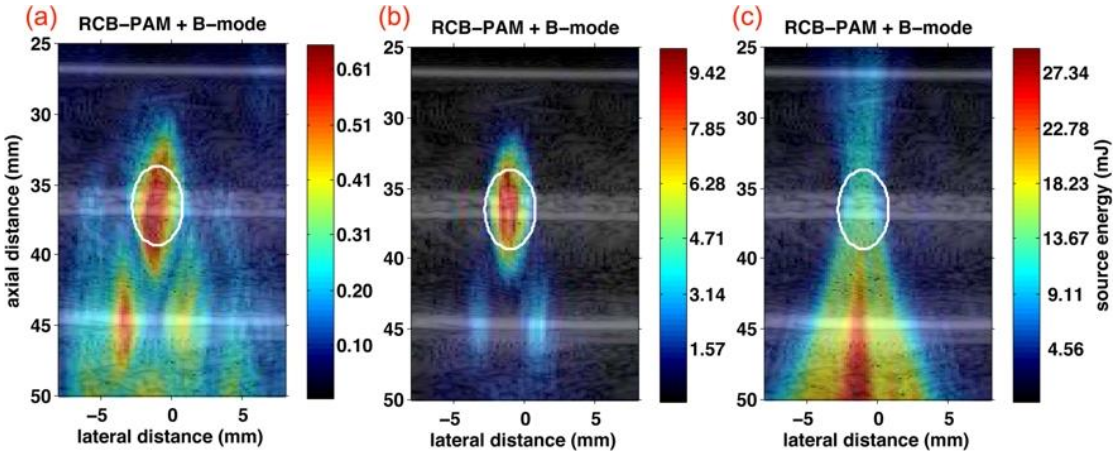


Figure 2.6: Effect of tolerance parameter $\epsilon$ on PAM using RCB, reprinted with permission from (Coviello *et al.*, 2015). Copyright 2015 Acoustical Society of America. PAMs produced from the same data with $\epsilon =$ (a) 0.05, (b) 8.39 and (c) 64 are overlaid on B-mode images. Microbubbles were made to flow through a channel in the centre of the image and excited using a HIFU transducer.

The best value of $\epsilon$ in a particular case will depend on the data under consideration. In cases such as the *in vitro* setup of Figure 2.6 where the expected region of cavitation is known, the optimal value of $\epsilon$ can be determined experimentally, for instance by comparing the energy in the focal and post-focal regions (indicating interference suppression), or comparing the energy at the focus compared to a reference algorithm such as TEA (indicating preservation of focal energy estimate). For the data above using these metrics an optimal value for $\epsilon$ of 8.39 was determined (as in Figure 2.6 (b)) (Coviello *et al.*, 2015).

Aside from the need for an appropriate value of $\epsilon$ the main disadvantage of the RCB algorithm is increased computational complexity. For an array with $N$ elements the number of operations required for a conventional delay-and-sum beamformer such as TEA is proportional to the number of elements $N$ (Asl and Mahloojifar, 2012),

while for the RCB algorithm it is on the order of $N^3$ (Li *et al.*, 2003). For a typical ultrasound imaging array with 128 elements RCB therefore requires $128^2 = 16{,}384$ times as many operations, which poses a considerable challenge. Development of parallel-processing methods to improve the speed of execution of Capon beamforming methods is ongoing (Asen *et al.*, 2014).

For these reasons, the data in this thesis was all initially processed using the TEA algorithm, including during the *in vivo* experiments of Chapter 5 where TEA-based PAM images were shown in real time during experiments. A sub-set of the *in vivo* data from Chapter 5 was subsequently post-processed using a provisional Graphics Processing Unit (GPU)-based parallel RCB implementation by Erasmia Lyka whose contribution is expressly acknowledged.

### 2.2.10. Artefacts and limitations

A common artefact which is particularly pronounced using simpler PAM implementations such as the TEA algorithm is a post-focus 'tail' in which activity is shown at a range beyond the actual region of cavitation (e.g. Figure 2.5a). Simulations suggest that this is likely due to interference of the emissions from multiple bubbles (Coviello *et al.*, 2015) combined with the worsening resolution at increasing depth (Section 2.2.5.2). Robust beamforming methods such as the RCB algorithm discussed above were specifically designed to reject interference between sources so can alleviate these effects (Figure 2.5c).

Other major limitations of PAM are typically specific to a given practical implementation, including bandwidth and sensitivity limits of the array and signal processing chain, or memory, processing and transfer delays in the data storage system. For a given application these may be optimised to make best use of the equipment available within the constraints of the experiment.

### 2.2.11. Biological relevance and interpretation of PAM data

PAM is a versatile method for monitoring cavitation activity, the data from which may be analysed in numerous ways. However, a major limitation of the technique to which there is no universal answer concerns the correct interpretation of the data. This is subject to several conditions, including:

1) Processing of the data in an appropriate manner for the effect being studied. This may include analysis of maps in space, over time, defining regions of interest, calculation of metrics etc., as employed in the following chapters.

2) Where a biological effect is to be monitored, establishment of appropriate metrics from the PAM data which may be related to the bioeffect measured by independent means. Depending on the bioeffect being studied it may not be possible to measure in real time simultaneous with PAM acquisition (e.g. organ samples taken after *in vivo* experiments). For example, previous studies in the literature have compared the position of lesions in *ex vivo* liver with the focus of activity in PAM (Jensen *et al.*, 2012). In later chapters of this thesis metrics from PAM data are compared to fluorescence readings and flow cytometry.

3) Establishment of the limits under which the correlation in (2) fails to hold. For example, increasing the microbubble concentration above some saturation point may increase the magnitude of cavitation, but not give rise to increased bioeffect (or even introduce undesired effects such as cell death). Such limitations are encountered in Chapter 4.

### 2.2.12. Applications of PAM

Finally, before proceeding to review the development of the magnetic microbubbles it is useful to briefly summarise the sort of problems to which PAM has been applied.

PAM and related methods have been used for a wide range of applications including tracking of cavitation activity in phantoms during HIFU exposure (Gyöngy *et al.*, 2008; Gyöngy and Coussios, 2010a; Gyöngy and Coussios, 2010b) and analysis of cavitation behaviour of microbubbles (Choi and Coussios, 2012; Haworth *et al.*, 2012; Crake *et al.*, 2013; Crake *et al.*, 2015).

In tissue, PAM has also been used for acoustic monitoring (Salgaonkar *et al.*, 2009), lesion prediction (Jensen *et al.*, 2012; Haworth *et al.*, 2015) and prediction of temperature (Jensen *et al.*, 2013) in *ex vivo* liver. Elsewhere, PAM has been used to map cavitation through the intact primate skull (Arvanitis *et al.*, 2013; Arvanitis and McDannold, 2013), while the effects of the human skull on PAM image aberration have also been simulated (Jones *et al.*, 2013; O'Reilly *et al.*, 2014) and corrected (Arvanitis *et al.*, 2015). PAM has also been used for monitoring of *in vivo* extravasation experiments, and correlated with viral delivery (Choi *et al.*, 2014).

Finally, in addition to the optimal beamforming techniques outlined previously, modification of the algorithm under certain experimental conditions may be able to improve the resolution of PAM, such as by synchronisation of data acquisition with very short high-intensity cavitation-initiating pulses (Gateau *et al.*, 2011b).

In this thesis PAM was used for investigation and monitoring of the behaviour of magnetic microbubbles in various experimental scenarios. Magnetic microbubbles are reviewed in the following section.

## 2.3. MAGNETIC MICROBUBBLES

The term ‘magnetic microbubbles’ (MMB) in this thesis refers in the most general sense to any micrometre-scale bubbles containing gas (or liquid which can be vaporised to become a gas) encapsulated by some form of stabilising shell, and containing some form of magnetically responsive particles such that the resulting bubbles may be affected by a magnetic field, but are not permanently magnetised. The latter point is important to stress, as permanently magnetic microbubbles would be of limited use due to aggregation. Figure 2.7 illustrates this effect in practice: when a magnet is applied, MMBs form chains which align themselves with the magnetic field; these chains rapidly break apart when the magnetic force is removed. This behaviour is similar to that of macro-scale magnetic objects such as paperclips or iron filings.

The definition above encompasses the simplest phospholipid + ferrofluid MMB formulations found in the literature, as well as the various improved variants described in this thesis including those containing additional emulsifiers such as polyethyleneglycol (PEG) derivatives, high molecular weight gas or liquid cores, fluorescent markers and/or therapeutic molecules. Further background detail on each of these is included below. First the underlying mechanisms by which magnetic microbubbles are used to provide enhanced drug delivery in this thesis are reviewed, in particular sonoporation and magnetofection.

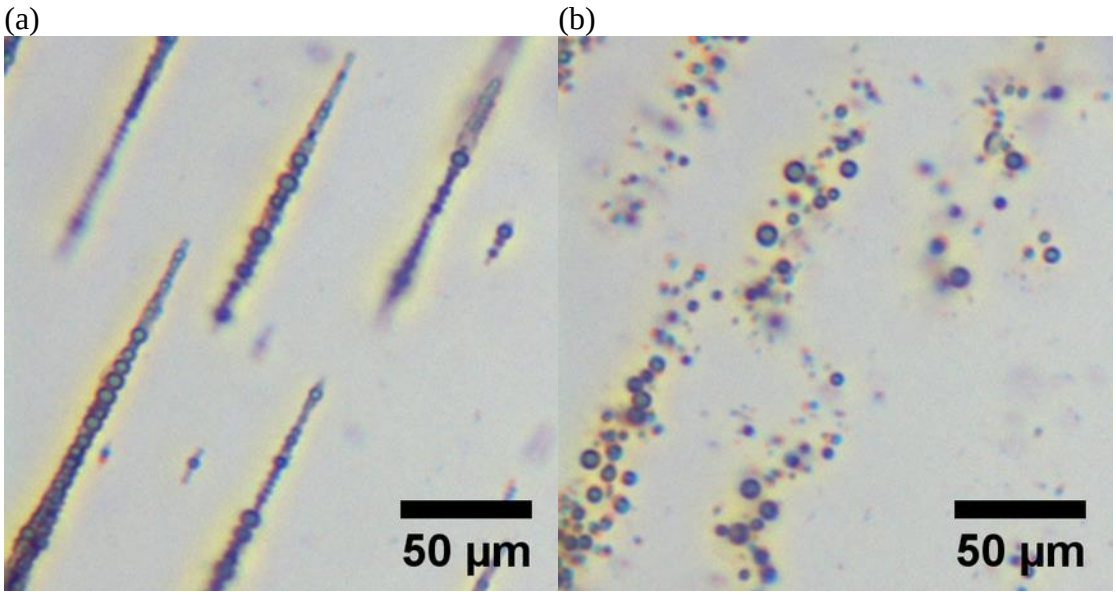


Figure 2.7: Microscope images showing chaining and dissolution of MMB. Microscope images taken using 10 × objective with (a) magnet applied: chains of MMBs aligned with the magnetic field; (b) immediately after magnet removed

### 2.3.1. Cell transfection and sonoporation

Nucleic acids (NA) such as ribonucleic acid (RNA), small interfering RNA (siRNA), double-stranded RNA (dsRNA) or deoxyribonucleic acid (DNA) are large, charged molecules (Wang *et al.*, 2010; Miller *et al.*, 2002) which severely limits their uptake by cells. In addition, NA may be broken down by enzymes in plasma such as nuclease (Layzer *et al.*, 2004), as well as within the cells by lysosomes (Wang *et al.*, 2010). Consequently a number of methods of protecting NA and facilitating their transport into cells (termed *transfection*) have been developed, the effects of which may be either stable or transient in nature. In stable transfection the transferred gene is incorporated into the genome of the cell, so will be passed on following cell division, while in transient transfection the nucleic acids may result in protein expression temporarily before being cleared from the cell (Miller *et al.*, 2002).

The methods by which transfection is achieved may be broadly categorised as either viral or non-viral. Non-viral methods include the use of chemicals containing charged ions such as calcium phosphate or cationic polymers and physical techniques

such as microinjection or application of an electric field, while viral methods include delivery via specially engineered retroviruses (Felgner *et al.*, 1987) and adenoviruses (Carlisle *et al.*, 2013). However, many of these techniques are plagued by issues related to toxicity and/or inefficiency which make them unsuitable for *in vivo* or clinical use. For example, the initial popularity of viral methods was heavily impacted (Ginn *et al.*, 2013) by severe adverse effects (including deaths and leukaemia-like illness) observed in early gene therapy clinical trials (Edelstein *et al.*, 2007).

One of the most widely used non-viral methods for transfection (Miller *et al.*, 2002) is lipofection: encapsulation of NA into liposomes using a positively charged lipid such as N-(1-(2,3-Dioleyloxy)Propyl)-N,N,N-Trimethylammonium Chloride (DOTMA). The positive charge of the lipid first binds to negatively charged phosphate groups on the NA to be transfected, and then to the (lipid bilayer) cellular membrane, thereby enabling transport of the NA into cells (Felgner *et al.*, 1987). The popularity of this technique is reflected in the widespread use of the commercial product Lipofectamine® (Dalby *et al.*, 2004)

However, a major limitation of both lipofection and viral methods is that any exposed cells may be affected, leading to limited control over their distribution and therefore poor spatial and temporal specificity (Miller *et al.*, 2002). Application of physical stimuli can greatly improve spatial targeting, for instance by electroporation (opening of membrane pores to admit DNA by high-voltage electric fields) (Aihara and Miyazaki, 1998) or particle bombardment (attachment of DNA to metal projectiles, which are physically fired at the cells at high velocity using a ‘gene gun’) (Uchida *et al.*, 2009). However, electroporation requires invasive electrode placement while particle bombardment is only suitable for surface targets (Miller *et al.*, 2002).

A more recent development – which is the focus of the current work – is the use of ultrasound to enhance cell membrane permeability, termed *sonoporation*, in which ultrasound-induced cavitation is used to open transient pores in the cell membrane (Miller *et al.*, 2002). Because ultrasound can be tightly focused extracorporeally these effects can be concentrated in a specific volume even at considerable tissue depths, thereby reducing off-target effects. Cavitation nuclei can be used to reduce the acoustic pressure required for cavitation to occur, as well as providing additional functionality such as attachment of therapeutic agents or targeting ligands, increasing the localisation and efficiency of treatment (Miller *et al.*, 2002). By selection of appropriate acoustic conditions (such that negligible cavitation occurs in absence of nuclei) they may also be used to influence the timing of treatment.

In the work described in this thesis sonoporation was induced using focused ultrasound with two different types of cavitation nuclei – improved formulations of magnetic microbubbles, and magnetic nanodroplets. These are used to improve the delivery of two therapeutic agents: siRNA, which was attached to the magnetic microbubbles; and paclitaxel, which was encapsulated into the magnetic nanodroplets. Background details on these two agents and the methods used to assess efficacy are included in the following sections. First the second underlying mechanism involved in these experiments, termed magnetofection, is reviewed.

### 2.3.2. Magnetic drug targeting and magnetofection

The term ‘magnetofection’ first appeared in the literature in the early 2000s (Plank *et al.*, 2002; Scherer *et al.*, 2002) and refers to the association of nucleic acids with magnetic particles to enhance their transport into cells under the effect of a magnetic field (Plank *et al.*, 2011).

A detailed review on the subject of magnetofection was conducted by (Plank *et al.*, 2011). Typically the process uses iron oxide nanoparticles which are associated directly with nucleic acid or a carrier (commonly a virus) using e.g. ligand binding or electrostatic attraction. Variants of the technique have been used for a range of gene therapy applications both *in vitro* and *in vivo* (Plank *et al.*, 2011).

The feasibility of magnetofection (and magnetic drug targeting in general) is limited by the small size of the nano-scale magnetic carriers. This limits the force which may be exerted by the magnetic field, such that it may be insufficient to counteract forces such as blood flow in the body. This problem may be solved by incorporating the magnetic particles into an object which appears larger with respect to the magnetic field but is still small enough to pass through capillaries, such as a magnetic microbubble (Plank *et al.*, 2011) or phase-change nanodroplet (Lee *et al.*, 2015). An additional major benefit of both methods is that the resulting carriers are also acoustically responsive, so can combine the effects of sonoporation (discussed above) with magnetofection.

### 2.3.3. Magnetic microbubbles

A number of variants of magnetic microbubbles may be found in the literature. The main developments are summarised below, followed by discussion of the key factors in microbubble formulation.

In an early example (Soetanto and Watarai, 2000) two formulations of magnetic microbubble were prepared using either 300 nm iron oxide particles or 1 μm 'magnetic carbons' (iron particles coated with carbon). Microbubbles were formed by stirring a solution containing sodium stearate (common soap) and then filtered to obtain an average bubble size of around 10 μm. The attenuation of ultrasound was found to be similar to nonmagnetic microbubbles, while the resonant frequency decreased due to the increased effective density of the microbubble shell. However, these formulations were not suitable for *in vivo* use: injection of even low concentrations (0.1 %) of sodium stearate results in thrombus formation (Hoak, 1964), while the calcium ions used in the first formulation could also result in cardiotoxicity (Zaloga *et al.*, 1987). Other early examples of magnetic microbubbles may be found in the patent literature, for example (D'arrigo, 1993; Dharmakumar *et al.*, 2003), however these were intended to facilitate MRI contrast and not active magnetic targeting.

The issue of suitable materials for formation of magnetic microbubbles is discussed by (Plank *et al.*, 2007) who chose to focus on albumin- and cationic lipid-based formulations due to their proven history for gene delivery applications. Indeed, both albumin (Albunex®, Optison®) and phospholipid (Definity®) (Gormley and Wu, 1998; Main *et al.*, 2009) conventional microbubbles have been approved by the Food and Drug Administration (FDA) for clinical use for imaging contrast. Plank *et al.* (2007) comment that albumin-based magnetic microbubbles could be produced either by sonication, or with better results by mixing a commercial agent such as Optison®

with magnetic nanoparticles; however cationic lipid-based formulations gave the best results. A simple cationic lipid-based formulation based on the nonmagnetic lipospheres of (Unger *et al.*, 1998) was described, using soybean oil (a mixture of fatty acids), a commercial cationic lipid preparation (Metafectene), surfactant coated magnetic nanoparticles and a buffer supplemented with glycerol and propylene glycol (Plank *et al.*, 2005; Plank *et al.*, 2007). The components were mixed in a vial filled with perfluoropropane ($C_3F_8$) gas which was then shaken for 1 min at 2500 revolutions per minute (RPM) using an automated agitator. Due to the use of a positively charged lipid nucleic acids can also be electrostatically attached to the bubbles; transfection of cells with a luciferase reporter showed increased uptake under the effect of a magnet which was further enhanced by simultaneous exposure to ultrasound (Plank *et al.*, 2007). Particular variants of this formulation are described in (Vlaskou *et al.*, 2010a; Holzbach *et al.*, 2010; del Pino *et al.*, 2010) which used the transfection reagent Metafectene, 1,2-Dioleoyl-Sn-Glycero-3-Phosphoethanolamine (DOPE) lipid and fluidMAG-Tween-60 magnetic nanoparticles to produce magnetic microbubbles which were retained against flow, observed under B-mode ultrasound and used for *in vitro* siRNA delivery and *in vivo* gene delivery experiments. The simple production method of this formulation is an advantage however as noted in (Vlaskou *et al.*, 2010a) does require careful control as numerous factors such as shaking time and frequency can affect the resulting bubble population.

In (Stride *et al.*, 2009) magnetic microbubbles were produced using a formulation consisting of a single phospholipid (L-α-phosphatidylcholine), oil-based ferrofluid (iron oxide nanoparticles in isoparaffin) and phosphate buffered saline (PBS) by a combination of sonication and manual shaking. The microbubbles were shown to enhance delivery of luciferase to Chinese hamster ovary cells under combined ultra-

sound exposure (1 MHz, 1 MPa p-p) and magnetic field. In (Mulvana *et al.*, 2010) the same microbubbles were used for preliminary *in vivo* luciferase transfection experiments in a mouse model: the original target of the heart proved difficult to access experimentally. However, some spatial selectivity of transfection was demonstrated between the two lungs. The authors noted that improvements in the stability, concentration and homogeneity of the microbubbles would be required in future work. The behaviour of this microbubble formulation was simulated numerically by (Lind, 2014) as well as in related work by (Mulvana *et al.*, 2012), while the effects of blood on targeting efficacy of similar microbubbles (based on 1,2-Distearoyl-Sn-Glycero-3-Phosphocholine (DSPC)) were studied by (Owen *et al.*, 2014) and compared to biotin targeting.

In Vlaskou *et al.* (2010b) two formulations are described based on the lipids Dipalmitoylphosphatidylcholine (DPPC) and 1,2-Distearoyl-Sn-Glycero-3-Phosphoethanolamine(DSPE)-PEG-biotin which were suspended in water and sonicated into liposomes which were extruded through a membrane. Lipid stock and one of two different iron oxide nanoparticle preparations (fluidMAG-UC/C-11 and fluidMAG-UC/C-H) were shaken in a mixture of PBS, glycerol and propylene glycol in a vial filled with perfluoropropane. The microbubbles showed enhanced luciferase transfection to HeLa cells *in vitro* under the combined effects of ultrasound and a magnetic field, however this was correlated with reduced cell viability. Similarly, a more comprehensive MMB formulation (including synthesis of the magnetic nanoparticles) was described by (Mannell *et al.*, 2012) in which viral particles were attached to the microbubbles and used to target endothelial cells with combined biological, magnetic and ultrasonic techniques.

Several groups have investigated the potential of magnetic microbubbles for imaging purposes, including (Wu *et al.*, 2011) which used a similar formulation to (Vlaskou *et al.*, 2010b) with the addition of a vascular cell adhesion antibody to establish whether combined biological and magnetic targeting could be used for diagnosis of atherosclerotic plaques. Similarly the use of MMB for combined MR and ultrasound imaging have been explored using various formulations based on albumin (Liao *et al.*, 2012), poly(vinyl alcohol) (PVA) (Barrefelt *et al.*, 2013) or other polymer (Liu *et al.*, 2011) bubbles.

## 2.3.4. Effects of microbubble formulation

The review of magnetic microbubble formulations above provides important context for the current work and a rich source of potential variants for use in experiments, however, the rationale behind a particular composition is not always obvious. Below the effects of the 4 key components of a formulation – the shell material, core gas, magnetic material and suspending medium – and the manufacturing method are discussed. Alternative functionalisation methods (e.g. biological targeting) are not discussed here as these are not directly relevant to the present work and tend to be highly application-specific.

### 2.3.4.1. Shell material

The excess pressure within the bubble due to surface tension (known as the Laplace pressure) is given by $\Delta p = 2\sigma/r$ where $\sigma$ is the interfacial tension and $r$ the radius of the bubble (Stride, 2009). This pressure can be on the order of 0.1 MPa for a micron-scale air bubble in water. If the pressure within the bubble exceeds the gas pressure in the blood then the gas will begin to dissolve: as the bubble shrinks the surface tension will increase further, accelerating bubble loss (Schutt *et al.*, 2003). The addition of a surfactant – typically molecules with a hydrophilic 'head' and hydrophobic 'tail' – can be used to reduce the surface tension $\sigma$, and also provide a physical barrier to gas diffusion to reduce this effect (Stride, 2009).

Various surfactants can be used. The two early commercial agents Echovist and Levovist were both based on the release of air bubbles from dissolving galactose microparticles: in Levovist palmitic acid was added to coat the resulting microbubbles in an attempt to increase their stability (Schutt *et al.*, 2003). More recent commercial agents such as SonoVue®, Definity® and Albunex® as well as the experimental agents outlined in Section 2.3.3 make use of primarily phospholipid or albumin shells to sta-

bilise the microbubbles. Increasing lipid chain length has been shown to increase the resistance of the shell to air permeation, increasing microbubble stability (Borden and Longo, 2002). Addition of a surface 'brush' layer of hydrophilic polymer such as PEG to the microbubbles reduces contact between microbubbles (and hence coalescence), and increases circulation time *in vivo* by reducing uptake (e.g. by macrophages) (Klibanov, 2005). PEG may be incorporated either as a separate emulsifier such as Polyethylene-40-Stearate, or grafted directly to the phospholipid (e.g. DSPE-PEG2000) (Borden *et al.*, 2005; Zhao *et al.*, 2004). Increasing the PEG to lipid ratio has been shown to reduce the viscosity of the microbubble shell (Hosny *et al.*, 2013): in this thesis a low PEG:DPSC ratio of 1:9 was used.

#### 2.3.4.2. Core gas

Early contrast agents such as free gas bubbles (Ophir and Parker, 1989) or first-generation commercial agents such as Echovist (Smith *et al.*, 1984) were based on air, and as a result were not sufficiently stable to pass the lungs and so were only used in limited applications such as right-heart imaging (Schutt *et al.*, 2003). Second generation commercial products including Optison®, Definity® and SonoVue® all make use of high molecular weight, low solubility gases to improve the stability and circulation time of the microbubbles.

A detailed review of the effects of microbubble core gas on bubble stability was conducted by (Schutt *et al.*, 2003). The rate of bubble shrinkage as a result of gas diffusion depends upon the solubility of the gas in the surrounding liquid (often expressed as the Ostwald coefficient). An ideal gas for microbubbles must therefore be as insoluble in water as possible, while remaining sufficiently volatile as to be in the gas phase under biologically relevant conditions (an exception to the latter rule is for production of nanodroplets, discussed below). Perfluorocarbon gases (PFC, of the

general chemical form $C_xF_y$) are the least water-soluble yet volatile compounds known (Schutt *et al.*, 2003) so are an ideal candidate for this purpose, and can increase the lifetime of an air bubble in blood from a few seconds to several minutes. In blood a bubble containing PFC may initially swell as it takes up dissolved air gases, before slowly shrinking as the PFC diffuses out. When injected into the circulation the microbubbles come into close contact with air in the lungs resulting in gas exchange: the PFC is exhaled and replaced with air (Schutt *et al.*, 2003).

#### 2.3.4.3. Magnetic material

The magnetic particles used in the microbubble formulations outlined in Section 2.3.3 are invariably based on iron oxide. Often the particles are sufficiently small (< 50 nm) such that they can be considered single magnetic domains, then termed superparamagnetic iron oxide (SPIO) nanoparticles. SPIO particles have been FDA-approved as contrast agents for MRI as commercial products such as Feridex® (Bulte and Kraitchman, 2004) so their inclusion in magnetic microbubbles should not raise safety concerns.

The way in which magnetic particles are incorporated into the microbubbles varies significantly between formulations. The soap or calcium-based methods of early examples were clearly not suitable for clinical use (Soetanto and Watarai, 2000). In (Stride *et al.*, 2009) and Chapter 3 of this thesis the particles were suspended in an oil-based ferrofluid which may also raise safety concerns. More recent variants in the literature make use of water-based ferrofluids, in particular the fluidMAG range produced by Chemicell (Berlin, Germany), which allow direct incorporation without the use of an oil layer. The iron oxide nanoparticles are available coated with a range of hydrophilic polymers to prevent aggregation and allow binding to other components such as the shell of a microbubble. In the case of the microbubbles used later in this

thesis the nanoparticles were coated with a lipid to allow direct incorporation into the lipid bubble shell.

#### 2.3.4.4. Media and method of manufacture

The media in which microbubbles are produced may also affect their performance. In particular, the addition of chemicals to increase the viscosity of the (typically water or PBS) carrier solution can reduce coalescence and improve stability (Rasor and Tickner, 1984): a common example in the literature being addition of 10 % each by volume of glycerol and propylene glycol (Talu *et al.*, 2006; Unger *et al.*, 1998; Vlaskou *et al.*, 2010a) which are common biologically compatible additives (Gad, 2002).

The method by which microbubbles are produced has a profound effect on the resulting product. A number of preparation techniques for microbubbles in general may be found in the literature, including sonication (most common), high shear emulsification (rapid stirring), membrane emulsification (forcing the components through a porous membrane), ink-jet printing, electrohydrodynamic atomisation (drawing through a narrow jet under the influence of an electric field) and microfluidic devices such as T-junctions (Stride and Edirisinghe, 2008). For the magnetic microbubble formulations discussed in Section 2.3.3 the most common production methods were sonication and simple shaking. Alternative magnetic microbubble production methods such as microfluidic devices may be found in the literature, but these tend to be slower or have lower yield compared to sonication (e.g. $10^4$ microbubbles/mL (Park *et al.*, 2010) compared to $10^7$ microbubbles/mL or higher using sonication (Owen *et al.*, 2012b)) for equivalent processing times.

Further factors such as the ratio and total quantities of materials used, size and material of vial and sonication parameters (where used) may also affect the properties of

the resulting microbubble suspension. As a result comparison of results using different formulations must be done with care, and detailed protocols are critical for repeatability of experiments. A summary of the microbubble formulations used in this thesis is given in Section 2.3.6 and detailed protocols are included in Appendix E.

Before concluding this section with a summary of the microbubble formulations used in this thesis, below a variant in which the filling gas is replaced with a substance which is initially in the liquid phase is introduced – magnetic nanodroplets.

### 2.3.5. Magnetic nanodroplets

Nanodroplets are emulsions formed by dispersion of immiscible liquids in a carrier, such as that formed by shaking oil and water. If the liquid chosen has a boiling point close to body temperature then the droplets will convert into bubbles either spontaneously upon injection into the blood stream or in response to some energy input (e.g. increased temperature or reduced pressure; i.e. ultrasound pulse). The droplets may then be used in the same way as conventional microbubble agents, but as a result of their initial state may achieve advantages of longer circulation times and better penetration into tissue (Sheeran and Dayton, 2014). Such products are referred to under various names in the literature including nanodroplets (Lee *et al.*, 2015), phase-change droplets (Sheeran and Dayton, 2014) phase-change nanoemulsions (Sheeran *et al.*, 2013) and phase-shift nanoemulsions (Kopechek *et al.*, 2013). For simplicity in this thesis the term 'nanodroplets' is used.

An early commercial example of such a nanodroplet product was EchoGen® (Grayburn *et al.*, 1995), which consisted of liquid dodecafluoropentane (boiling point 29 °C) in water with a stabilising surfactant. Upon injection the nanodroplets (c. 0.3 µm diameter) were expected to nucleate into gas bubbles of 2-5 µm in size (Schutt *et al.*, 2003). However, the bubbles formed by spontaneous nucleation were found to be much larger than this (c. 14 µm) (Grayburn, 1997) raising concerns about coalescence (Lin and Pitt, 2013), while high-dose animal studies resulted in severe respiratory distress (Grayburn *et al.*, 1995). The product never recovered from these safety concerns and was subsequently withdrawn from consideration by the FDA (Schutt *et al.*, 2003).

While EchoGen® was intended to nucleate spontaneously by thermal expansion, a more controlled alternative method uses ultrasonic pulses to vaporise the droplets, known as acoustic droplet vaporisation. Early examples of nanodroplets designed for

acoustic vaporisation may be found in the patent literature (Apfel, 1998) and in papers from various groups over the previous 15 years using a range of perfluorocarbons including dodecafluoropentane (DDFP) (Kripfgans *et al.*, 2000), Perfluoropropane ($C_3F_8$), Perfluoropentane (PFP), Perfluorohexane (PFH) and Perfluoromethylcyclohexane (PFM) (Giesecke and Hynynen, 2003).

In addition to varying the volatile liquid used to cause phase transition, stabilising coatings such as albumin or polyethyleneglycol (PEG) may also be incorporated into the formulation to improve the stability of the nanodroplets. Finally, solid particles may also be incorporated which act as nucleation sites for phase transition, improving conversion efficiency. If magnetic nanoparticles such as iron oxide are used then the nanodroplets may be made to respond to a magnetic field (Lee *et al.*, 2015).

## 2.3.6. Microbubble formulations in this thesis

The magnetic microbubbles used in this thesis are based on the formulation described by Stride *et al.* (2009) and subsequent developments particularly by Joshua Owen (Owen, 2015) in view of the potential formulation improvements discussed in Section 2.3.4. The magnetic nanodroplet variant was developed by Jeong Yu Lee (Lee *et al.*, 2015).

The various formulations employed in this thesis are summarised in Table 2.1. Detailed protocols for the production of each are included in Appendix E.

| **Acronym** | **DSPC-MMB** | **F-MMB**<br>**K-MMB**<br>**S-MMB** | **PTX-MND** | **DiI-MMB** |
|---|---|---|---|---|
| **Description** | Air-cored lipid microbubbles with oil-based ferrofluid | $SF_6$-cored PEG/lipid microbubbles with lipid-coated nanoparticles and siRNA | Paclitaxel loaded PFP-cored magnetic nanodroplets | $SF_6$-cored PEG/lipid microbubbles with lipid-coated nanoparticles and DiI |
| **Chapter** | 3 (phantoms) | 4 (*in vitro*) | 4 (*in vitro*) | 5 (*in vivo*) |
| **Reference** | (Crake *et al.*, 2015) | (Owen, 2015) | (Lee *et al.*, 2015) | (Owen, 2015) |
| **Core** | Air | $SF_6$ | PFP | $SF_6$ |
| **Shell** | DSPC | DSPC/ DSEPC/PEG | HSA/*bis*-NHS-PEG | DSPC/ PEG |
| **Magnetic** | Oil-based FF (15 nm) | Lipid-MNP (50 nm) | IONC (5 nm) | Lipid-MNP (50 nm) |
| **Payload** | None | siRNA: ‘F’luorescent, ‘K’nockdown, ‘S’crambled | Paclitaxel | DiI dye |

Table 2.1: Magnetic microbubble and nanodroplet formulations used in this thesis. Chemical acronyms are defined in the table on page x.

### 2.3.7. Challenges & limitations of magnetic targeting

The ability to achieve sufficient magnetic field strength and gradient are undoubtedly the most significant obstacles for translation of magnetic targeting for clinical use, particularly when deep targets are concerned. Rare-earth permanent magnets such as the neodymium iron boron (NdFeB) magnets employed later in this thesis can achieve surface magnetic flux density on the order of 1.5 T, but this decays rapidly with distance (Appendix C). Such magnets are therefore only suitable for targets at limited depth (<10mm) such as the skin or surface tumours. Nonetheless, targeting was demonstrated using such magnets in this thesis. Similar magnets (and/or arrangement of several) have also been used for clinical trials in which drugs were delivered in a ferrofluid (Lübbe *et al.*, 1996).

By incorporation of several magnet elements into an array they may be used to allow targeting over a larger area – a linear Halbach array constructed from 5 magnet elements was used for cell experiments in this thesis for such a purpose (Chapter 4). More advanced magnet array designs may be used to increase the depth at which useful magnetic forces can be achieved (i.e. those that may facilitate targeting) beyond 20 mm (Barnsley *et al.*, 2015). Single electromagnets could be used to target at greater depths (>30 mm) (Alexiou *et al.*, 2006), while arrangements of several electromagnets may be used to allow concentration of particles at a point (Nacev *et al.*, 2014) as well as arbitrary 'steering' of magnetic particles (Probst *et al.*, 2011) within a plane. Selective steering of magnetic particles confined to a flow channel has also been demonstrated by retrofitting stronger gradient coils to an MRI scanner (Mathieu and Martel, 2010). While achieving deep magnetic targeting on a human scale remains a significant challenge, such previous work suggests it should be possible.

## 2.4. THERAPEUTIC APPLICATIONS

In this section the two therapeutic agents used in this thesis (siRNA and Paclitaxel) and analysis methods used to assess their delivery are described.

### 2.4.1. Small interfering ribonucleic acid (siRNA)

siRNA refers to short (< 30 base pairs) fragments of double-stranded RNA, also known as oligonucleotides, which interfere with (i.e. reduce the expression of) specific genes in cells (Xia *et al.*, 2002). siRNA can be used to silence disease-causing genes (Soutschek *et al.*, 2004) and is a good candidate for ultrasound-enhanced delivery due to the poor uptake typically observed for such nucleic acids *in vitro* and *in vivo* (Section 2.3.1).

siRNA may be produced within cells from longer strands of double-stranded RNA (dsRNA) by the Dicer enzyme (Bernstein *et al.*, 2001), or by direct introduction of siRNA. Once within cells siRNA causes gene silencing by the RNA interference (RNAi) mechanism (Figure 2.8). siRNA is incorporated into an RNA-induced silencing complex (RISC) (Schwarz *et al.*, 2004) in which the protein Argonaute 2 (AGO2) (Rand *et al.*, 2004) unwinds the siRNA strands and discards the 'sense' or 'passenger' strand (Rand *et al.*, 2005). The activated RISC-siRNA complex (which contains the single 'antisense' or 'guide' strand of the siRNA) binds to and cleaves the complimentary sequence of messenger RNA (mRNA) within the cell – its target – therefore reducing expression of the corresponding gene (Sachs, 1993).

In this thesis the delivery of siRNA to cells was assessed using fluorescence imaging and viability assays which are discussed in the methods section for the appropriate experiments (Section 4.2.6). In addition flow cytometry was performed for a subset of the experiments, further background on which is included below (Section 2.4.3).

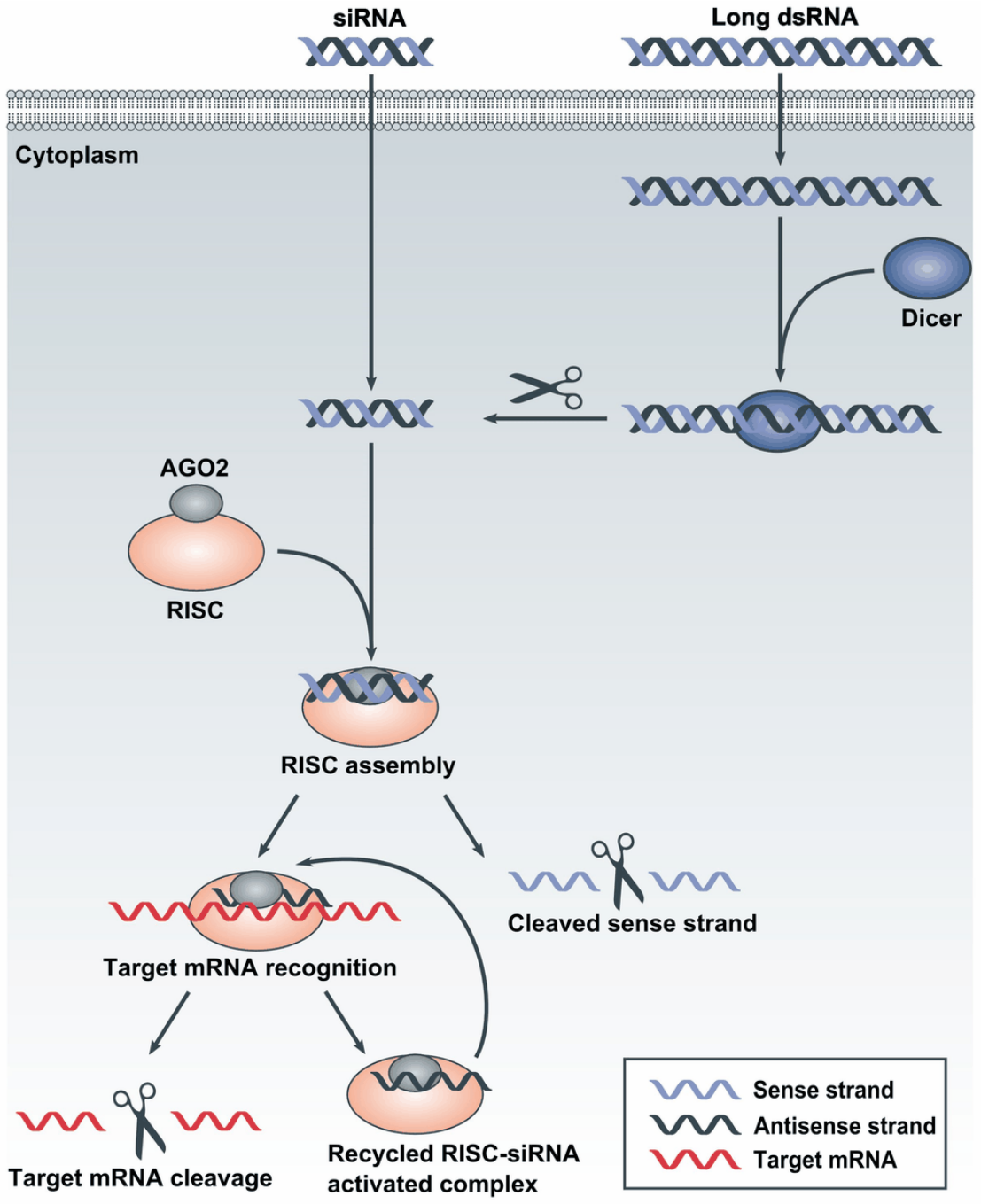


Figure 2.8: The mechanism of RNA interference, adapted by permission from Macmillan Publishers Ltd: Nature Reviews Drug Discovery (Whitehead *et al.*, 2009), copyright 2009. siRNA is introduced to the cell directly or via long double-stranded RNA (dsRNA) cleaved by the Dicer enzyme. siRNA is incorporated into an RNA-induced silencing complex (RISC), unwound by the protein Argonaute 2 (AGO2) and the 'sense' strand discarded. The activated RISC-siRNA complex (which contains the 'antisense' strand of the siRNA) cleaves the complimentary strand of messenger RNA (mRNA), therefore reducing expression of the corresponding gene.

### 2.4.2. Paclitaxel

Paclitaxel (PTX) is a drug with anti-tumour properties (Wani *et al.*, 1971) which is believed to induce apoptotic (programmed) cell death by binding to the microtubules responsible for nuclear division during the M phase (mitosis, i.e. cell division) of the cell cycle (Wang *et al.*, 2000). As a result the effects of PTX treatment are not seen for 24 hours as the cells must complete one full cycle (Section 2.4.3.1). Due to the systemic side effects of Paclitaxel (Cella *et al.*, 2003) it is a good candidate for targeted delivery.

### 2.4.3. Principles of flow cytometry

In this thesis siRNA- and PTX-treated cells were analysed using flow cytometry. A diagram showing the basic principles of flow cytometry is shown in Figure 2.9. A suspension of fluorescently stained cells is made to flow through a nozzle and past a laser, the forward- and side-scattered laser light is collected, and used to count and characterise the cells based on the measured fluorescence intensity. By appropriate staining (see below) the method may be used to identify cells of different sizes, or containing different amounts of fluorescent material as a result of biological differences between them such as their stage within the cell cycle (Steinkamp, 1984).

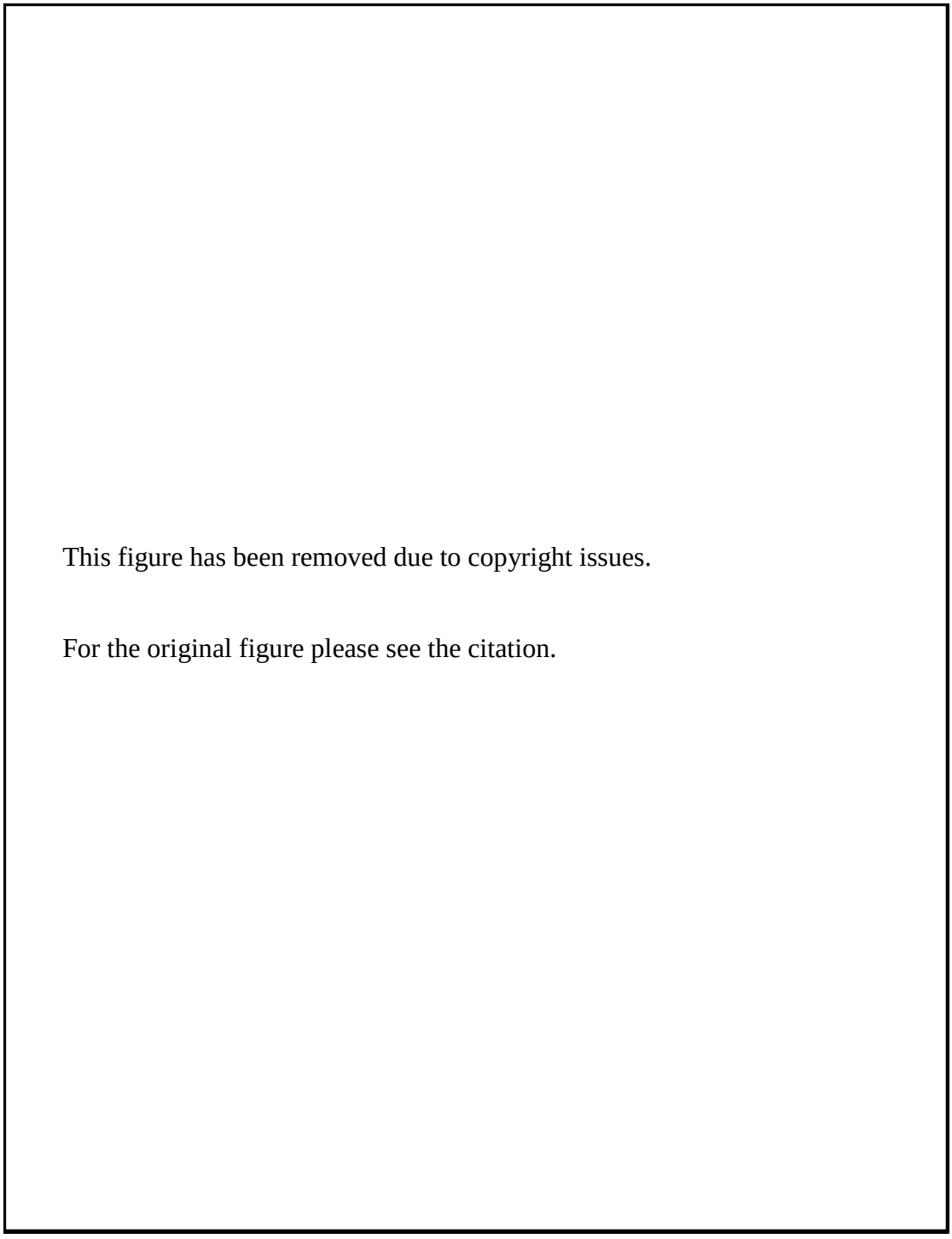


Figure 2.9: Principles of flow cytometry, reproduced from (Herzenberg *et al.*, 1976). Cells are labelled with fluorescent dye, suspended and made to flow past a laser. The scattered light is measured and used to count and characterise the cells. Optionally the measurements may be used to automatically sort the cells based on their fluorescence intensity, then known as fluorescence-activated cell sorting (Herzenberg *et al.*, 1976).

### 2.4.3.1. Propidium iodide (PI) staining and the cell cycle

By staining cells with propidium iodide (PI; a common stain for nuclear DNA) before flow cytometry the quantity of nuclear DNA within the cells is indicated by their fluorescence intensity. During the cell replication cycle (Figure 2.10) the quantity of DNA within each cell varies – a cell in the $G_2$ phase will contain twice the DNA of one in the $G_1$ phase as DNA replication has occurred – so these measurements in turn indicate the stage within the cell replication cycle of the cells. Commonly cells are fixed before analysis such that the readings represent their state at a defined time point. They will also indicate cells which contain an abnormal quantity of DNA, which may indicate that they are in the process of cell death. Successful treatment by PTX leads to a sub-$G_1$ peak: i.e. cells which contain less than the normal (pre replication) quantity of DNA observed in the $G_1$ phase.

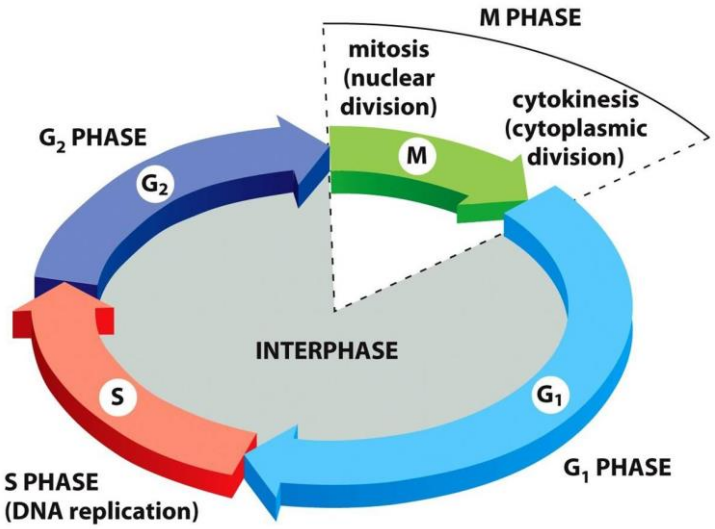


Figure 2.10: Phases of the cell cycle, reproduced from (Alberts *et al.*, 2002). DNA replication occurs during the S (synthesis) phase, and cell division during the M (mitosis) phase, during which the nucleus and then cytoplasm divide. Between these phases are two gap phases termed $G_1$ and $G_2$ during which cell growth and replication of other organelles and proteins occur. $G_1$, S and $G_2$ are collectively termed *interphase*, which might occupy typically 23 out of 24 hours for human cells in culture. Copyright © 2002, Bruce Alberts, Alexander Johnson, Julian Lewis, Martin Raff, Keith Roberts, and Peter Walter; Copyright © 1983, 1989, 1994, Bruce Alberts, Dennis Bray, Julian Lewis, Martin Raff, Keith Roberts, and James D. Watson. Reproduced with permission from Garland Science.

## 2.5. SUMMARY

siRNA and Paclitaxel are two therapeutic molecules which could benefit from microbubble-enhanced delivery due to their poor uptake and systemic side effects respectively. Their effects may be quantified biologically using methods such as fluorescence labelling and flow cytometry.

Magnetic microbubbles may be used to enhance delivery of drugs or genes to cells through a combination of ultrasonic (sonoporation) and magnetic (magnetofection) effects. Microbubble formulation depends on several key parameters which define the chemical composition as well as secondary effects such as the method of manufacture. The gas core of a microbubble may be replaced with a volatile liquids to create phase-change agents (nanodroplets) which are subsequently vaporised into microbubbles. However, the effect of the concentration of cavitation nuclei on cavitation activity and the resulting efficiency of transfection or delivery has not been previously investigated.

Passive acoustic mapping (PAM) is a versatile technique which has been employed for a range of therapeutic ultrasound applications and enables real-time spatio-temporal quantification and classification of cavitation activity. Recent improvements in the beamforming algorithms used, including the robust Capon beamformer, have made it possible to improve the spatial resolution of cavitation maps and to remove artefacts relating to multi-bubble interactions and differences in array element sensitivities.

In the following three chapters, PAM was applied to both magnetic microbubbles and nanodroplets in tissue phantoms, *in vitro* and *in vivo* models respectively.

CHAPTER 3

# PASSIVE ACOUSTIC MAPPING OF MAGNETIC MICROBUBBLES IN TISSUE PHANTOMS

## 3.1. INTRODUCTION

In this chapter the behaviour of magnetic microbubbles was investigated using passive acoustic mapping under controlled laboratory conditions in tissue phantoms. The objective of this chapter was to address aims 1-3 of the thesis (Section 1.8.2), i.e. to establish whether magnetic localisation of the bubbles could be detected using PAM; to investigate the effects of magnetic confinement on the resulting cavitation activity, and test whether this could translate to therapeutically relevant benefits (e.g. enhanced cavitation).

The magnetic microbubbles used in this chapter consisted of 1,2-distearoyl-sn-glycero-3-phosphocholine (DSPC), air and an oil-based ferrofluid containing 15 nm diameter iron oxide nanoparticles, and are referred to by the acronym DSPC-MMB to distinguish them from other formulations used elsewhere in the thesis (Section 2.3.6). DSPC-MMB were injected into a tissue mimicking phantom at different flow veloci-

ties (0 to 50 mm/s) with or without an applied magnetic field. The microbubbles were excited using a 500 kHz single element focused transducer at peak negative focal pressures of 0.1-1.0 MPa, while a 64 channel imaging array passively recorded their acoustic emissions. The recordings were used for mapping of the cavitation activity using PAM and subsequently analysed with respect to the different experimental conditions.

The results in this chapter have been previously presented (Crake *et al.*, 2014; Crake *et al.*, 2013) and published (Crake *et al.*, 2015)[7].

[7] The experiments in this chapter were designed and conducted by the author. The assistance of co-authors to the associated publications is gratefully acknowledged; in particular Joshua Owen regarding development of the microbubble formulation, and Marie de Saint Victor, Christian Coviello and Jamie Collin for advice and helpful discussions.

## 3.2. METHODS

### 3.2.1. Experimental setup

An overview of the experimental setup is given in Figure 3.1. Ultrasound was generated using a 500 kHz single-element high intensity focused ultrasound (HIFU) transducer (model H-107B-10; Sonic Concepts, Inc., Bothell, WA, USA) with an outer diameter of 64 mm, focal length 63 mm, and featuring a 45 × 18 mm rectangular cutout through which a linear imaging array probe (model L10-5; Zonare Medical Systems, Mountain View, CA, USA) with 128 elements, 38 mm aperture and 5-10 MHz bandwidth was aligned such that the focus of the HIFU transducer was within the imaging plane. Driving waveforms were generated using a function generator (model 33250A; Agilent, Wokingham, Berkshire, UK) synchronised to the ultrasound engine (model z.one; Zonare Medical Systems, Mountain View, CA, USA) using a trigger output signal from the imaging engine which was amplified using a pulser-receiver (model DPR300; JSR Ultrasonics, Pittsford, NY, USA). The imaging engine was used to passively record 64 channels of acoustic emissions from every second element of the array (elements 2-64 and 65-127) during exposures. The driving signal was applied to the HIFU transducer via a 55 dB power amplifier (model A300; Electronics and Innovation, Rochester, NY, USA) and impedance matching network supplied by the transducer manufacturer. Both the function generator and ultrasound imaging engine were connected to a desktop PC running MATLAB (The MathWorks, Natick, MA, USA) which was used to control and synchronise exposures.

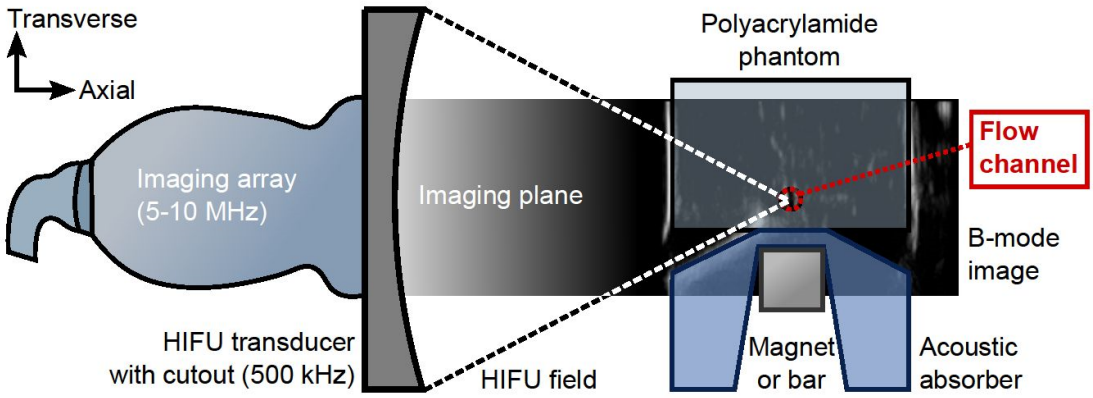


Figure 3.1: Experimental setup for *in vitro* testing of DSPC-MMB using passive acoustic mapping. Microbubbles flow through a channel formed in a polyacrylamide tissue phantom, aligned with the focus of a 500 kHz HIFU transducer. A 5-10 MHz imaging array is aligned through a cutout in the HIFU transducer for B-mode imaging and to passively record acoustic emissions simultaneously over 64 channels. Transverse and axial orientations are defined relative to the centre of the front face of the imaging array.

A 7 % polyacrylamide tissue phantom containing a 1.6 mm diameter flow channel was prepared according to established protocols (Khokhlova *et al.*, 2006) by mixing 26 mL of 40 % acrylamide suspension, 15 mL tris(hydroxymethyl)-aminomethane buffer, 126 mg of ammonium persulfate, and 107 mL deionised water (chemicals purchased from Sigma Aldrich, Poole, Dorset, UK). The mixture was degassed at 0.1 bar for 10 minutes using a vacuum pump (model MZ 2; Vacuubrand, Wertheim, Germany). 75 mL of the solution was measured into a poly(methyl methacrylate) holder with inner dimensions 40 × 40 × 74 mm fitted with a removable stainless steel mandrel. The volume of solution used was determined experimentally in order to minimise the thickness of the layer of hydrogel covering the mandrel while still allowing sufficient rigidity for its removal. 75 µL of tetramethylethylenediamine (TEMED; Sigma Aldrich, Poole, Dorset, UK) was then added to catalyse the polymerisation reaction and the phantom allowed to set. Before commencing the experiments, the top and sides of the phantom holder were removed and the assembly inverted.

A single rectangular permanent magnet (N52 grade NdFeB, 10 × 10 × 25 mm; NeoTexx, Berlin, Germany) with transversal magnetisation 1.5 T was positioned be-

low the flow channel and replaced with a nonmagnetic stainless steel bar of the same dimensions in control runs. The magnet or nonmagnetic bar was placed within an acoustic absorber cast from polyurethane rubber (Aptflex F36; Precision Acoustics, Dorset, UK) with angled sides in order to reduce surface reflections. The magnetic field at the location of the channel was measured in air using a Hall-effect sensor (model A1302; Allegro MicroSystems, Worcester, MA, USA), indicating that the magnetic flux density at the channel (8 mm away from the magnet surface) was approximately 0.1 T.

The acoustic absorber, magnet and phantom holder assembly were aligned with the focus of the HIFU transducer using the mandrel as a pulse-echo target in a 50 × 80 × 55 cm tank filled with degassed, deionised water. The mandrel was subsequently removed and the two ends of the channel connected to a flow loop. The air within the channel was then used as a pulse-echo target to confirm alignment and subsequently replaced with water using the flow loop.

Deionised water and magnetic microbubbles (DSPC-MMB) were maintained in suspension using an overhead stirrer (model WZ-50006; Cole-Parmer, Hanwell, London, UK) set at a low speed to avoid entraining gas, and drawn through the phantom by a variable-speed peristaltic pump (model Minipuls Evolution; Gilson, Middleton, WI, USA). The pump speed was calibrated to the flow rate by measuring the flow through the phantom and tubing system over the speed range of the pump (0.1-60 RPM), and corresponding average flow velocity in the phantom calculated based on the 1.6 mm diameter of the channel. In the experiments involving flow, a flow rate of 2.4 mL/min was used, corresponding to an average fluid velocity of 20 mm/s or shear rate (assuming Poiseuille flow) of 100 $s^{-1}$, which is within the range of human veins (Whitmore, 1967; Loncar *et al.*, 2007). In further experiments the flow rate was var-

ied from 1.8-6 mL/min, corresponding to an average fluid velocity of 15-50 mm/s or shear rate of 75-250 $s^{-1}$. In all cases the total circulating volume in the reservoir, tubing and phantom was 50 mL.

### 3.2.2. Magnetic microbubbles (DSPC-MMB)

The magnetic microbubbles used in this chapter (DSPC-MMB) were prepared by sonication as described in previous studies using a single phospholipid and an oil-based ferrofluid (Owen *et al.*, 2012b; Stride *et al.*, 2009). 15 mg of 1,2-distearoyl-sn-glycero-3-phosphocholine (DSPC; Avanti Polar Lipids, Inc., Alabaster, Alabama, USA) in powder form was weighed into a 25 mL plastic vial previously rinsed with surgical spirit (Boots Pharmaceuticals, Nottingham, UK). 15 mL of deionised water was added to the vial following which the phospholipid was dispersed by sonication using an ultrasonic cell disruptor (3 mm probe diameter, model XL2000; Misonix, Farmingdale, New York, USA) operating at 22.5 kHz and 8 W root-mean-square (RMS) output power with the probe tip placed deep within the liquid for 30 seconds. The probe was then moved to the air-liquid interface and the vial tilted to entrain gas and sonicated for a further 30 seconds, after which the mixture was vigorously manually shaken for a final 30 seconds. To produce magnetic microbubbles, 15 µL of a magnetic nanoparticle suspension (10 % by volume 10 nm spherical iron oxide in iso-paraffin; Liquids Research, Bangor, UK) was added to the mixture and the sonication procedure repeated.

For control experiments, the magnetic microbubble suspension was replaced with an equal volume of water or with water containing 15 µL of the magnetic nanoparticle suspension that was sonicated prior to use.

Microbubbles were examined using an optical microscope (model DM500; Leica Microsystems, Wetzlar, Germany) fitted with a digital camera (model MicroPublisher

3.3; QImaging, Surrey, BC, Canada) and operated at 400 × magnification. 10 µL samples were taken from each batch of microbubbles, and 30 images taken from each sample. The particle size distribution and concentration were then obtained using purpose-written software in MATLAB (The MathWorks, Natick, MA, USA) (Sennoga *et al.*, 2010). Figure 3.2 shows a typical microscope image of a sample of magnetic microbubbles together with the corresponding size distribution which is similar to that reported in previous work (Owen *et al.*, 2012b; Stride *et al.*, 2009).

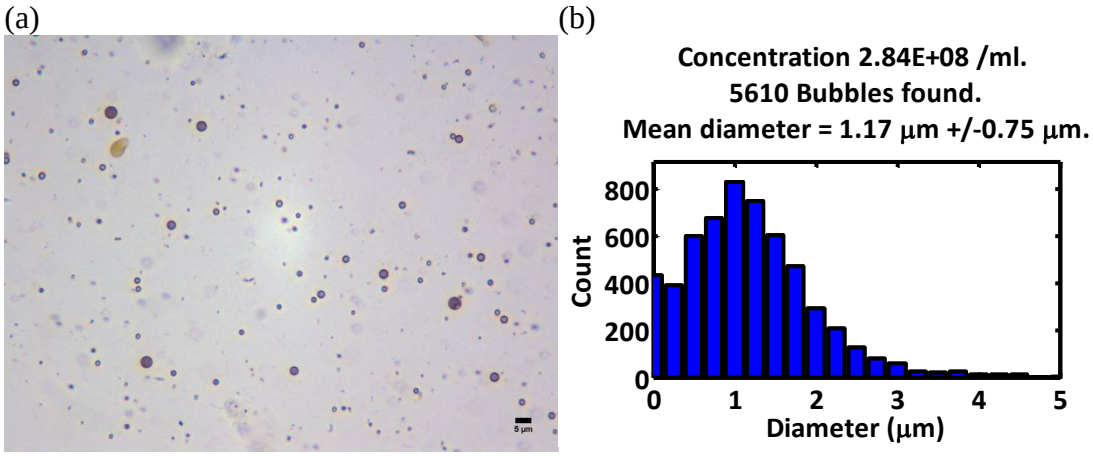


Figure 3.2: Optical characterisation of magnetic microbubbles (DSPC-MMB). (a) Bright field microscope image of a sample of magnetic microbubbles (scale bar represents 5 µm) and (b) Size distribution plot obtained from 30 images of magnetic microbubbles using image processing software (Sennoga *et al.*, 2010).

### 3.2.3. Passive acoustic mapping

Cavitation activity was characterised using passive acoustic mapping as previously described using the time exposure acoustics algorithm (Section 2.2.4).

Using the experimental setup described in Section 3.2.1 the centre of the flow channel appeared under B-mode imaging at 0 mm transverse, 73 mm axial relative to the midpoint of the imaging array. Passive acoustic maps of 201 × 41 pixels were therefore produced using this method over a region of interest of ±5 mm transverse and 50-90 mm axial measured from the midpoint of the imaging array, corresponding to a pixel size of 0.05 × 0.5 mm. This exceeds the theoretical -3 dB transverse and axial resolutions of the maps, which for a source at the 7.14 MHz centre frequency of the array, at the HIFU focal distance of 73 mm and array aperture size of 38 mm, are 0.36 mm transverse and 5 mm axially (Section 2.2.5).

### 3.2.4. Experimental protocol

The free-field focal pressure and beam profile of the HIFU transducer were calibrated in water using a 400 μm diameter needle hydrophone (model Onda HNA-0400; Onda Corporation, Sunnyvale, CA, USA) (Appendix A). Pressure values referred to subsequently are peak negative focal pressure.

The microbubble suspension was injected into or drawn through the phantom and excited using the HIFU transducer, while the imaging array passively recorded 64 channels of their acoustic emissions. In each case the imaging frame rate was used to trigger the function generator and therefore define the pulse repetition frequency of HIFU excitation. To prevent temporal aliasing short pulses of 25 cycles (50 μs) were used such that the propagation delay and duration of each pulse was shorter than the

137 μs recording length (equivalent to 10 cm pulse-echo imaging depth) in each frame captured by the imaging engine.

To obtain consistent samples, the magnetic microbubbles were made on the same day as each set of experiments and stored in a refrigerator until required. Before each experimental run the microbubbles were resuspended by manual shaking and the required volume immediately drawn into a syringe, avoiding any foam, before injection. The timing of each run was monitored to improve consistency and reduce effects such as resettling of the microbubbles.

#### 3.2.4.1. Cavitation threshold of magnetic microbubbles

To establish the cavitation threshold of magnetic microbubbles, 1 mL of the magnetic microbubble suspension was injected into the stirred reservoir to give a total circulating volume of 50 mL (2 % DSPC-MMB suspension by volume) and drawn through the phantom using the peristaltic pump. The flow rate was set to give an average flow velocity in the channel of 20 mm/s based on previous work and under which magnetic targeting has been demonstrated (Choi and Coussios, 2012; Owen *et al.*, 2012b).

The flowing microbubble suspension was excited with 25 pulses of 25 cycles at a pulse repetition frequency (PRF) of 1 Hz at peak negative focal pressures of 0.1 to 1 MPa in steps of 0.1 MPa. To establish baseline values the procedure was also performed using water and sonicated ferrofluid; the cavitation threshold of microbubbles was defined as the point at which the energy of cavitation emissions was at least 6 standard deviations above that of water. Three repeats using new samples of microbubble suspension, sonicated ferrofluid or water were performed in each case. In all cases the nonmagnetic bar was installed in the acoustic absorber close to the channel.

### 3.2.4.2. Effect of a magnetic field on cavitation of DSPC-MMB without flow

To investigate the effects of magnetic targeting on the spatial distribution, intensity and sustainability of magnetic microbubble induced cavitation under static conditions (i.e. without replenishment from flow), 1 mL samples of diluted DSPC-MMB suspension (50 % DSPC-MMB suspension by volume) were directly injected into the channel in the phantom and subsequently isolated by closing a three-way tap at each end of the phantom.

The microbubble suspension was excited with 25 pulses of 25 cycles at a pulse repetition frequency of 1 Hz and a peak negative focal pressure of 0.5 MPa, beginning 1 minute after sample injection. Either the magnet or nonmagnetic bar was installed in the acoustic absorber close to the channel. Five repeats using new samples of microbubble suspension were conducted for each experimental condition.

### 3.2.4.3. Effect of a magnetic field on cavitation of flowing DSPC-MMB

To investigate the effects of flow, replenishment and retention of magnetic microbubbles on their cavitation response, 0.5 or 1 mL of the magnetic microbubble suspension was injected into the stirred reservoir to give a total circulating volume of 50 mL (1 % or 2 % DSPC-MMB suspension by volume) and drawn through the phantom using the peristaltic pump to give an average flow velocity in the channel of 15-50 mm/s. This volume fraction of microbubble suspension is well within *in vivo* guidelines (Hedrich, 2012) but is higher than that typically used clinically for imaging (e.g. a 2.4 mL bolus of SonoVue® (European Medicines Agency, 2014) injected into the human blood volume of around 5 litres (Feldschuh and Enson, 1977)). However, doses of microbubbles over 50 mL have been tolerated clinically (Bokor *et al.*, 2001; European Medicines Agency, 2014), representing a similar volume fraction of the human circulation to that used in these experiments. With further development it may

also be possible to concentrate the microbubble suspension and reduce the injection volume required for a given microbubble number density.

The microbubble suspension was excited with pulses of 25 cycles at a pulse repetition frequency of 0.1 Hz and a peak negative focal pressure of 0.5 MPa, for a total duration of 15 minutes. In order to obtain baseline measurements and ensure the system was clean for each run, exposures were started before injection of the microbubble suspension, which reached the focal region approximately 1 minute into each experiment. Either the magnet or nonmagnetic bar was installed in the acoustic absorber close to the channel. Three repeats using new samples of microbubble suspension were conducted for each experimental condition. The flow loop was rinsed and drained between experimental runs.

### 3.2.5. Data analysis

Following the experiments, the raw data files from the ultrasound imaging engine were converted to MATLAB-readable files, upsampled to increase the accuracy of the time delays applied in beamforming (Section 3.2.3), and comb filtered in the frequency domain with a comb width of 300 kHz to separate the harmonic (multiples of the 0.5 MHz HIFU excitation frequency) and broadband components, before being processed using the PAM algorithm described above. The resulting passive acoustic maps, each corresponding to one pulse of HIFU excitation, were subsequently analysed in space and over time in a similar manner to previous work (Choi and Coussios, 2012) by extracting the energy values of regions of interest within the maps.

To produce spectra for analysis of pressure ramp experiments the comb filter step was omitted and the time-domain source strength at the focus subject to a Fourier transform (MATLAB function *fft*); the spectra were subsequently averaged over each

set of 25 pulses and scaled as per Section 3.2.3 such that the total energy was equal to that displayed in the maps.

Shifts in the spatial distribution of cavitation were assessed using the spatial energy ratio (Choi and Coussios, 2012) calculated by taking the sum of energy in a 1 × 1 $mm^2$ area at the bottom of the channel divided by the sum of energy in a 1 × 1 $mm^2$ area at the top of the channel, such that a value greater than 1 would indicate a shift towards the magnet. The relative intensity of cavitation was assessed by finding the width (in mm) at which the peak in energy in the row of pixels at the focal depth fell to 75 % of its maximum value, and the total energy contained in a 2 × 2 $mm^2$ area encompassing the whole of the channel. These parameters were calculated for each pulse individually except in the case of static microbubbles without replenishment (Section 3.2.4.2) where the maps were first summed over the 25 pulses. The resulting parameters were used to calculate a mean and standard deviation over the repeats (n = 3-5) for each set of experimental conditions, following which statistical testing in the form of a two-sample t-test (MATLAB function *ttest2*) was applied.

## 3.3. RESULTS

### 3.3.1. Cavitation threshold of magnetic microbubbles

The response of magnetic microbubbles to a pressure ramp is illustrated in Figure 3.3. Across the whole of the pressure range tested, the resolved source energy was significantly higher ($p < 0.01$) for magnetic microbubbles than either sonicated ferrofluid or water (Figure 3.3(a)). The result for water was, as expected, indistinguishable from the baseline noise level of the system. Previous work has shown that similar hydrogels have a higher cavitation threshold at this frequency than the maximum peak negative pressure used here in the absence of cavitation nuclei (1.7 MPa at 0.5 MHz in polyacrylamide gel, (Rifai *et al.*, 2010); 3 MPa at 1 MHz in agar gel, (Gateau *et al.*, 2010)), while related studies have shown that thresholds can be as high as tens of megapascals for gelatin gels (27 MPa at 1.1 MHz (Maxwell *et al.*, 2013)), *ex-vivo* blood (27 MPa at 1.1 MHz (Maxwell *et al.*, 2013); 10 MPa at 0.7 MHz (Gateau *et al.*, 2013)), and *in-vivo* brain tissue (17 MPa at 0.7 MHz (Gateau *et al.*, 2011a)). Some increase in the signal when sonicated ferrofluid was used was anticipated due to the possibility of coherent reflections occurring from oil droplets and increased gas content in the suspension due to the sonication step used for dispersion, and may be considered a proxy for the conditions after ferrofluid-containing microbubbles have been destroyed. With magnetic microbubbles the source energy rose rapidly with increasing peak negative pressure until reaching a plateau at approximately 500 kPa. These results are very similar to those observed in a similar setup with the lipid-based non-magnetic commercial ultrasound contrast agent SonoVue®, suggesting that the ferrofluid has minimal impact on bubble acoustic response under these conditions (Choi and Coussios, 2012).

The frequency spectra obtained at the lower peak negative pressure steps (Figure 3.3(b)) indicated the expected bubble response, with clear harmonics at the lowest pressure, higher amplitude harmonics and introduction of ultraharmonic components at the intermediate pressures, and increasing broadband noise (indicative of inertial cavitation) at higher pressures (Leighton, 1994). Again, this behaviour mirrors that of commercial ultrasound contrast agents (Choi and Coussios, 2012; Arvanitis *et al.*, 2011) and suggests cavitation thresholds associated with detection of harmonics and broadband noise in this system of 100 kPa and 400 kPa respectively, similar to those of SonoVue® (Choi and Coussios, 2012).

In order to maximise the signal-to-noise ratio, a peak negative focal pressure of 500 kPa was selected for use in subsequent experiments. Under these conditions the source energy for the magnetic microbubbles suspension was close to its peak value (while in the absence of microbubbles it remained minimal), with a frequency spectrum dominated by broadband noise.

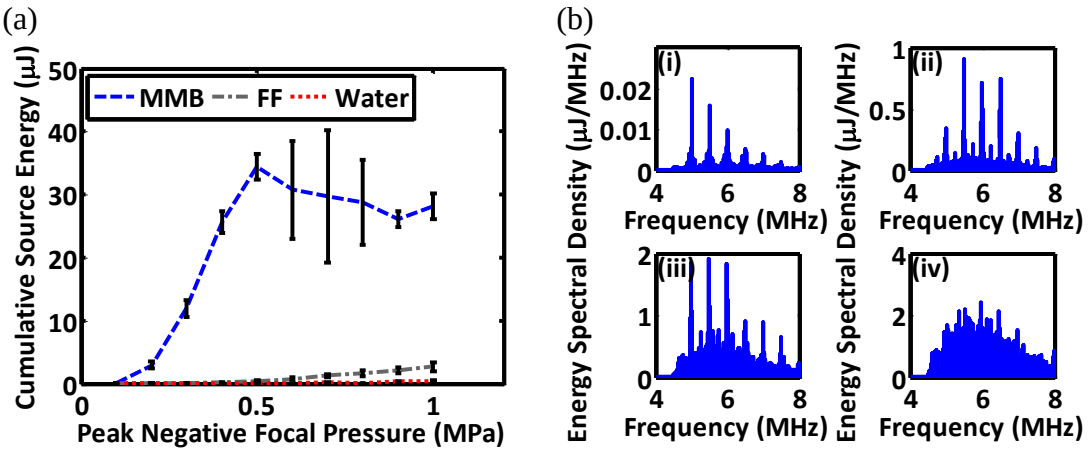


Figure 3.3: Effect of peak negative pressure ramp on cavitation source energy assessed using PAM for DSPC magnetic microbubbles (MMB) vs. sonicated ferrofluid (FF) and water. (a) Total energy in the focal region over 25 pulses at 1 Hz pulse repetition frequency (PRF) (n = 3). (b) Sample spectra at (i) 0.1, (ii) 0.2, (iii) 0.3 and (iv) 0.5 MPa peak negative focal pressure show harmonics followed by ultraharmonic components at lower pressures and increasing broadband noise at higher pressures.

## 3.3.2. Effect of a magnetic field on cavitation of static DSPC-MMB

### 3.3.2.1. Spatial distribution of cavitation activity

Passive acoustic maps showing the response of static samples of magnetic microbubbles with and without application of a magnetic field are shown in Figure 3.4. In the absence of a magnetic field, the cavitation activity was strongest towards the upper half of the channel due to the buoyancy of the gas-filled microbubbles (Figure 3.4(a)). When the magnet was placed below the channel, the cavitation activity shifted towards the lower half (Figure 3.4(b)) due to attraction of microbubbles towards the magnet. The presence of non-magnetic bubbles in the sample is indicated by the separate smaller peak in intensity towards the top of the channel. The amplitude (peak energy) of cavitation emissions also increased with magnetic targeting, most likely due to retention of a larger number of bubbles within the focal region during and after bolus injection, which would otherwise have been equally distributed along the channel.

Passive acoustic maps for 5 repeats of each set of experimental conditions were analysed in MATLAB (Section 3.2.5). Figure 3.5 shows the results in terms of the spatial energy ratio (ratio of energy in an area on the lower half of the channel divided by equal area on the upper half) and the width in the transverse direction at which energy falls to 75 % of the peak value in each run. These results show a statistically significant ($p < 0.001$) change in the spatial distribution of cavitation activity, which is both shifted in space towards the magnet (spatial energy ratio increases by a factor of 3 towards the magnet) and spread over a smaller area (peak width at 75 % energy is reduced by half) due to magnetic attraction of the microbubbles. These results suggest that microbubbles are attracted towards the magnet and in doing so were also pulled closer together than they would be under buoyancy.

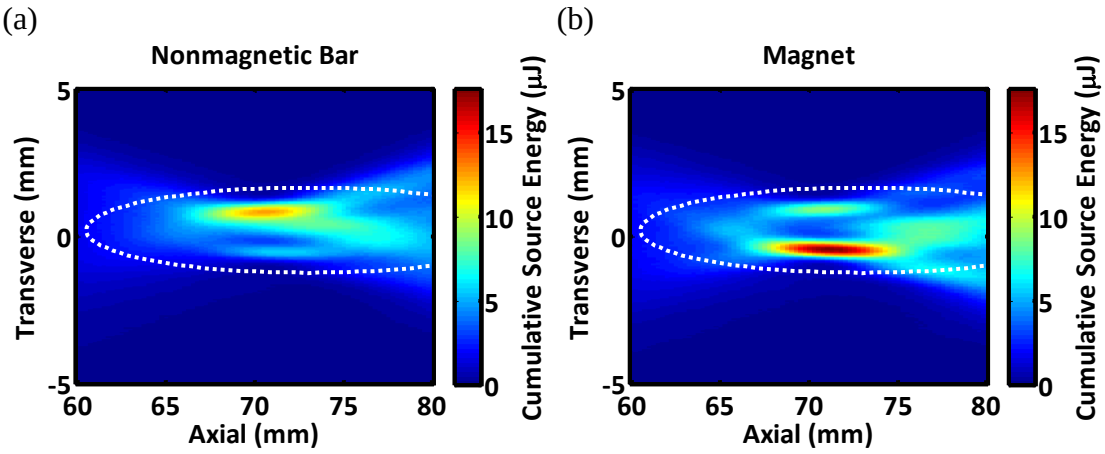


Figure 3.4: Examples of passive acoustic maps for magnetic microbubbles excited with 25 × 25 cycle pulses at 500 kHz, 0.5 MPa peak negative focal pressure. The dotted ellipse shows the -3 dB focal region of the HIFU transducer. A nonmagnetic bar or magnet was placed below the channel. (a) Control experiment without magnetic field shows DSPC-MMB float to the top of the channel. (b) Placement of a magnet below the channel resulted in a shift in location and increase in energy of cavitation activity. Transverse and axial orientations are defined relative to the centre of the front face of the imaging array.

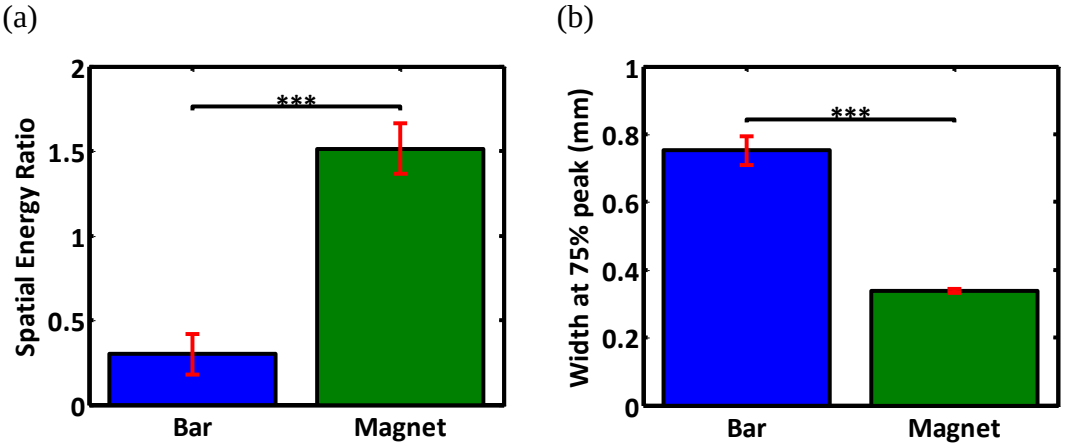


Figure 3.5: Effect of a magnetic field on spatial distribution of cavitation activity produced by magnetic microbubbles excited with 25 × 25 cycle pulses at 500 kHz, 0.5 MPa peak negative focal pressure. (a) Ratio of energy of acoustic emission from lower and upper halves of the channel increases from < 1 (due to buoyancy) to > 1 due to attraction towards the magnet. (b) Width in transverse direction (relative to imaging array) at which energy falls to 75 % of its peak value is reduced, suggesting higher local bubble concentration (***$p < 0.001$, $n = 5$).

### 3.3.2.2. Total energy of cavitation activity

Analysis of the cumulative sum of each 25 pulse exposure is shown in Figure 3.6 in terms of the overall peak source energy (maximum pixel value at the HIFU transducer focal depth) and the average source energy over a 2 × 2 $mm^2$ area around the focus. The peak source energy shows a statistically significant ($p < 0.01$) mean increase of 69 % over the baseline value without magnetic targeting. This may be explained partially by microbubbles being pulled closer together (Section 3.3.2.1), however the average source energy over a broader area also shows a smaller but significant ($p < 0.05$) mean increase of 53 %. Combined, these two results suggest that the increase in source energy was due to a combination of spatial shift of magnetic microbubbles already at the focus, as well as retention of those which would otherwise be located elsewhere in the channel and outside of the imaging plane (either during or after injection of the microbubble bolus).

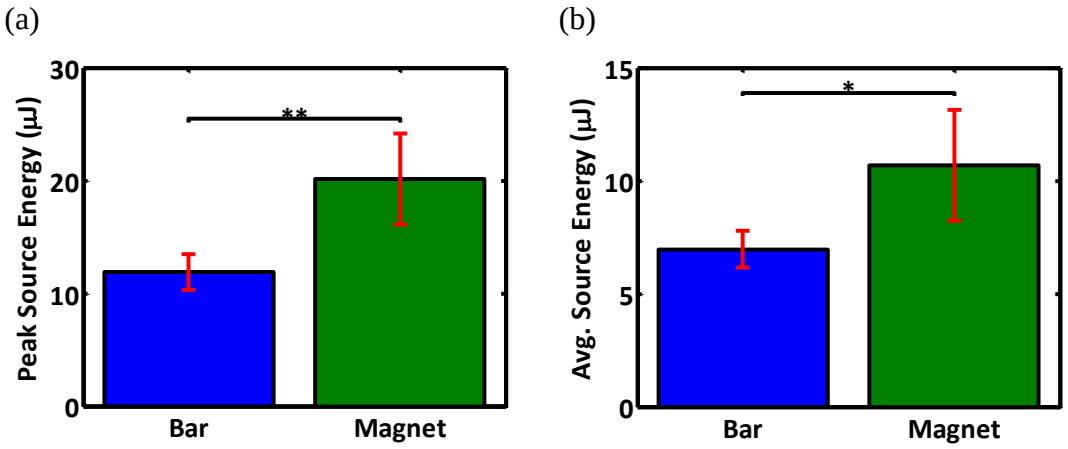


Figure 3.6: (a) Spatial peak at focal depth and (b) spatial average (over a 2 × 2 mm area about the focus) source energy of cavitation emissions for magnetic microbubbles excited with 25 × 25 cycle pulses at 500 kHz, 0.5 MPa peak negative focal pressure with and without a magnetic field. Both variables are increased under the influence of a magnet (**$p < 0.01$, *$p < 0.05$, $n = 5$).

### 3.3.2.3. Sustainability of cavitation activity

Analysis of the response of magnetic microbubbles to individual excitation pulses is summarised in Figure 3.7 as a time series for each individual run (n = 5 in each case). Where the average source energy in a 2 × 2 $mm^2$ area about the focus was considered (as in Section 3.3.2.2 but for individual frames) a statistically significant ($p < 0.05$) increase in energy of approximately 50 % was observed in the response to the first two bursts of HIFU excitation where magnetic targeting was applied compared to the baseline case without targeting. When the results were normalised relative to the amplitude of the first frame in each experimental run no significant difference was observed, suggesting that this change was primarily due to a greater number of cavitation nuclei being present at the start of the run, with little change thereafter. In all cases the response decayed towards zero after the first few frames of ultrasound data due to lack of microbubble replenishment under these static conditions: longer term analysis which includes microbubble replenishment under flow may be found in Section 3.3.3.

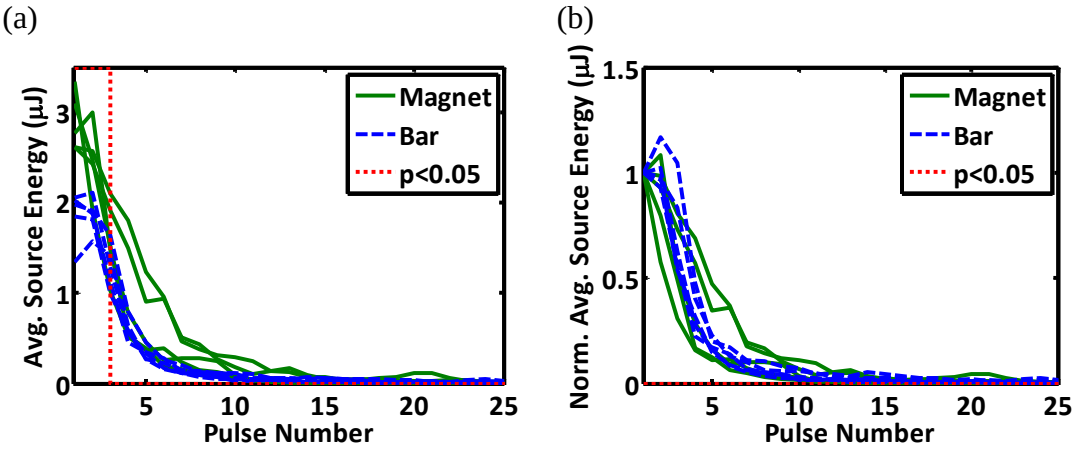


Figure 3.7: Change in average source energy from magnetic microbubbles over 25 pulses at 500 kHz, 0.5 MPa peak negative focal pressure (n = 5). (a) A statistically significant increase in energy ($p < 0.05$) is present in the first two pulses in the presence of an applied magnetic field. (b) Normalisation with respect to the first pulse in each case results in similar decay profiles (no significant difference).

## 3.3.3. Effect of a magnetic field on cavitation of flowing DSPC-MMB

### 3.3.3.1. Effect of magnetic retention on cavitation activity

The response of flowing magnetic microbubbles under conditions for which retention has previously been shown to occur is summarised in Figure 3.8. The microbubble suspension was injected into the reservoir immediately prior to the first pulse of HIFU excitation, and arrived at the focus at approximately t = 1 minute. In all cases the source energy of individual pulses rose rapidly upon arrival of microbubbles at the focus (Figure 3.8(a)), before reaching a peak value which then decayed over the following 10-15 minutes due to microbubble destruction. For the first few pulses the rise in source energy followed a similar profile with and without targeting. Over the following pulses, however, the source energy with magnetic targeting became dominant and continued to rise. The source energy using magnetic targeting reached a peak value of approximately 2.5 times the baseline case without targeting and this was maintained for the remainder of the experiments.

Overall, the cumulative sum of the source energy over 15 minutes was significantly increased ($p < 0.001$) with magnetic targeting, by a factor of approximately 2.5 times (Figure 3.8(b)) compared to the baseline case without targeting. Under flow conditions, passive acoustic maps summed over the duration of exposures show greater energy using magnetic targeting, but with no obvious spatial bias (Figure 3.8(c)). Analysis of the profile of emissions transverse to the array did however show a greater increase in energy at the lower side of the channel which was closer to the magnet (Figure 3.8(d)) when magnetic targeting was used. Under flow conditions it was no longer possible to separately discern buoyant/retained or magnetic/nonmagnetic bubble populations within the channel, as observed in the static case (Figure 3.4), and the peak in emissions was located close to the centre of the channel in all runs.

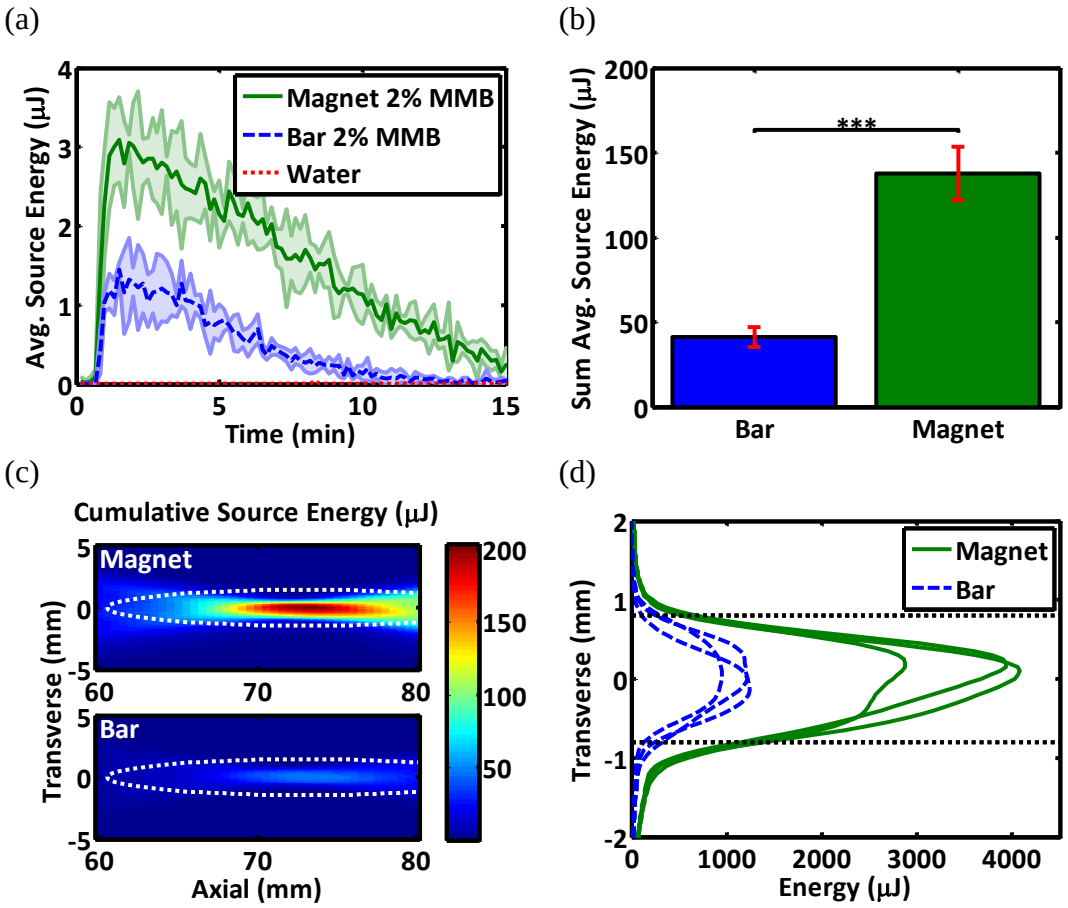


Figure 3.8: Effect of magnetic retention on cavitation response of flowing magnetic microbubbles. DSPC-MMB were injected at t = 0 and arrived at the focus at approximately t = 1 min. (n = 3). (a) Average source energy in a 2 × 2 mm area about the focus was higher in the presence of a magnetic field due to retention of microbubbles against flow. (b) Total source energy over the duration of exposure shows a significant increase using magnetic targeting (n = 3, ***=p < 0.001). (c) Examples of passive acoustic maps summed over the duration of exposures show greater energy using magnetic targeting, but with no detectable spatial bias. Transverse and axial orientations are defined relative to the centre of the imaging array. The dotted ellipse shows the -3 dB focal region of the HIFU transducer. (d) The profile of emissions transverse to the array showed greater increase in energy at the lower side of the channel which was closer to the magnet (n = 3). The approximate position of the 1.6 mm diameter channel walls as measured on B-mode imaging prior to experiments is shown by the dotted lines.

These results suggest that magnetic targeting is effective in increasing the local concentration of microbubbles against flow, under clinically relevant flow conditions and treatment durations. This effect is manifest as a higher source energy in the resulting passive acoustic maps, which (with further development) could be monitored in real-time during ultrasound exposure and used to improve ultrasound-mediated therapies. Such a real-time system is developed in later chapters. Under flow the spatial

bias introduced by magnetic targeting was less pronounced on a sub-vessel scale than it was in the static case evaluated previously, and the distribution of cavitation activity was more symmetrical about the centre of the channel. This is to be expected given the fluid velocity profile (see Discussion, Section 3.4).

The effect of varying the microbubble dose under flow is shown in Figure 3.9. The magnetic microbubble suspension (0.5 mL or 1 mL) was injected to give a total circulating volume of 50 mL (1 % or 2 % concentration by volume) at t = 0, and reached the focus at approximately t = 1 minute. At 2 % concentration by volume (Figure 3.9(a), as per Section 3.3.3.1) the mean energy ratio with magnetic targeting compared to the baseline case without targeting was approximately 2.5 (Figure 3.9(c)) at the point at which microbubbles began to arrive at the focus, and rose thereafter as the energy from non-targeted runs fell towards zero. When the microbubble concentration was halved to 1 % the source energy in both experimental conditions fell, however it remained consistently higher with magnetic targeting than without (Figure 3.9(b)). The decline in source energy when the microbubble concentration was reduced was more pronounced without targeting than with it; as a consequence the mean energy ratio at the point at which microbubbles began to arrive was roughly double that observed at the higher microbubble concentration (Figure 3.9(d)).

Comparison of the source energy over time for the two concentrations (Figure 3.9(a) vs. (b)) suggests that application of magnetic targeting has a similar effect to doubling the injected microbubble concentration.

These results suggest that magnetic targeting is effective at increasing the local microbubble concentration over a range of microbubble doses, which manifests as an increase in the cavitation source energy over time when observed using passive acoustic mapping. The effect of magnetic targeting is increasingly pronounced under mi-

crobubble-scarce conditions where there is greater potential for benefit. Clinically, these effects may allow greater local cavitation response (and thus treatment efficacy) for a given dose of microbubbles; conversely this could allow reduced dosage of microbubbles and thus reduce the risk of adverse effects.

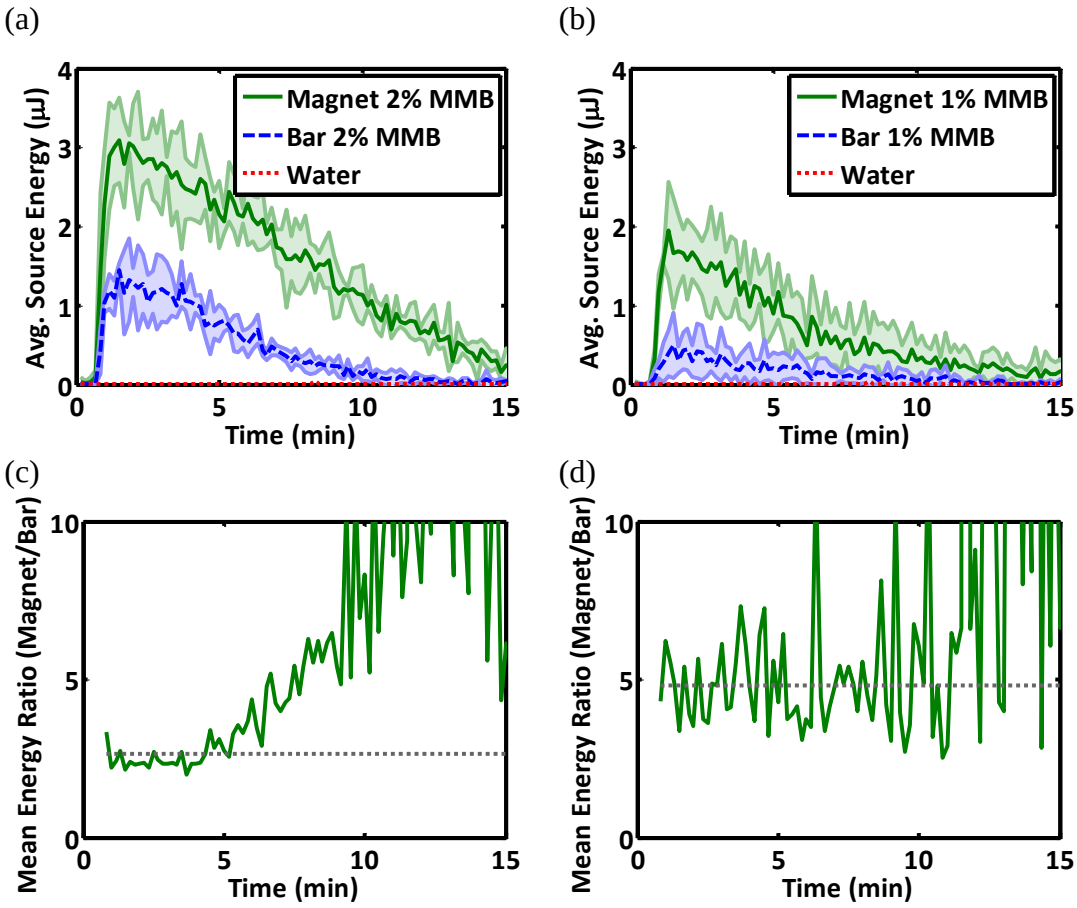


Figure 3.9: Effect of variation of microbubble dose on cavitation response of flowing magnetic microbubbles with and without magnetic targeting. Average source energy in a 2 × 2 mm area about the focus at (a) 2 % and (b) 1 % microbubble concentration by volume were both higher in the presence of a magnetic field due to retention of microbubbles against flow. Comparison of the two cases shows that magnetic retention had similar effect as doubling the microbubble dose (n = 3). (c,d) Mean energy ratio (magnet/bar) over the 3 repeats in each condition was approximately 2.5 × and 5 × at the start of microbubble arrival at 2 % and 1 % DSPC-MMB volume concentration respectively. The mean of the first 5 minutes in each case (t = 1-6 minutes) is shown by the dotted line; the y-axis scale is capped at 10 × as the ratio becomes non-meaningful as the source energy from non-targeted runs approaches zero.

#### 3.3.3.2. Effect of flow rate

The effect of varying the flow rate is shown in Figure 3.10. As the flow velocity was reduced from 20 mm/s to 15 mm/s (Figure 3.10 (b-a)) the source energy both with and without magnetic targeting fell due to the reduced rate of microbubble replenishment at the focus during and between HIFU pulses. However, the decline in the case without targeting was more pronounced: at a flow velocity of 15 mm/s the mean energy ratio with magnetic targeting compared to the baseline case without targeting was approximately 5 times, compared to a ratio of 2.5 times at a flow velocity of 20 mm/s. As the flow rate was increased from 20 mm/s to 50 mm/s (Figure 3.10 (b-c)) the replenishment rate of microbubbles was so great that there was no further benefit to be gained by targeting of the microbubbles under these particular conditions.

As was shown under variation of microbubble dose (Section 3.3.3.1) these results imply that the effects of magnetic targeting are greatest under microbubble-scarce conditions, where there is greater potential for benefit. It is important to note that while these results illustrate the effect of varying key parameters such as the dose of microbubble suspension or flow rate, other parameters which were held constant here (such as magnitude or gradient of magnetic field, or relative position of the magnet and focus of the HIFU transducer in the direction of flow) may increase the effectiveness of magnetic targeting.

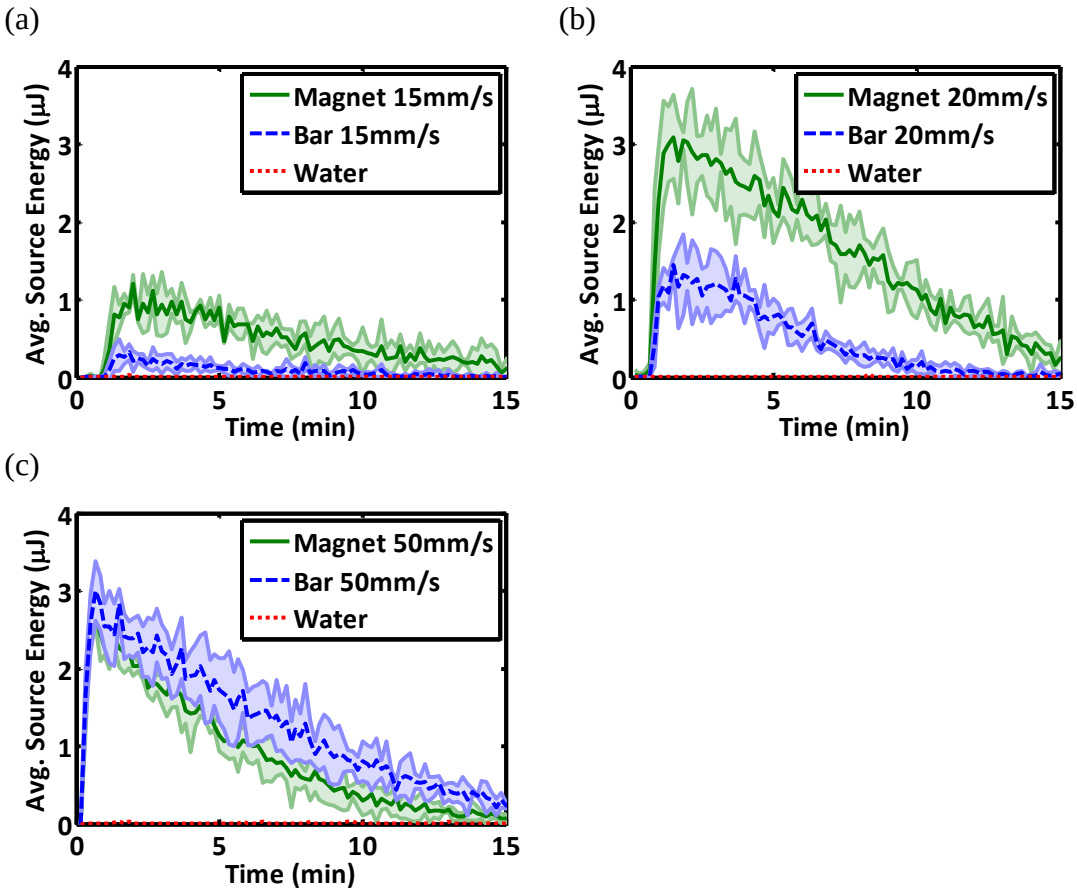


Figure 3.10: Effect of variation of microbubble flow rate on cavitation response of flowing magnetic microbubbles (2 % concentration by volume) with and without magnetic targeting. Average source energy in a 2 × 2 mm area about the focus at (a) 15 mm/s, (b) 20 mm/s and (c) 50 mm/s flow velocity (n = 3 in each case). The corresponding flow rates were 1.8 mL/min, 2.4 mL/min and 6 ml/min; shear rates were 75 $s^{-1}$, 100 $s^{-1}$ and 250 $s^{-1}$ respectively.

## 3.4. DISCUSSION

Although the size distribution (Owen *et al.*, 2012a) and scattering cross section at the fundamental of the magnetic microbubbles has been shown to be similar to that of SonoVue®, previous work has indicated that their nonlinear response is less pronounced (Mulvana *et al.*, 2012). It is therefore encouraging that the cavitation threshold and evolution of cavitation source energy and corresponding frequency spectra with increasing peak negative focal pressure illustrate typical microbubble behaviour (Leighton, 1994) and were very similar to those encountered with commercial agents in previous work (Choi and Coussios, 2012; Arvanitis *et al.*, 2011) under close experimental conditions. These results imply that the presence of the oil layer has minimal effect on bulk bubble behaviour, and so even without their interaction with a magnetic field being used for targeting, such a bubble formulation could be clinically useful both as contrast agents and for therapy. Indeed, these and similar formulations have previously been studied under B-mode ultrasound (without therapeutic excitation) (Owen *et al.*, 2012a) and demonstrated to enhance gene delivery both *in vitro* (Stride *et al.*, 2009) and *in vivo* (Mulvana *et al.*, 2010) (without acoustic monitoring). The stability of such microbubbles could be improved for *in vivo* use by replacement of the filling gas with lower-solubility, higher molecular-weight compounds such as the sulphur hexafluoride used in SonoVue® (Schneider, 1999). The microbubble formulation could be further developed for clinical use by co-administration or attachment (e.g. to the shell or by encapsulation) of active therapeutics, which could then be simultaneously targeted, imaged and delivered with real-time monitoring in a complete ultrasound-enhanced drug delivery system. Such improvements to the microbubble formulation and real-time monitoring system are included in later chapters.

For evaluation of the effects of magnetic targeting on microbubble behaviour under focused ultrasound excitation, passive acoustic mapping proved to be an effective technique which was able to discern sub-millimetric changes in the spatial distribution of cavitation activity as well as tracking of the evolution of bubble behaviour over time. Under static conditions both a shift in the location of maximum cavitation energy and an increase in amplitude were observed. These changes suggest that acoustically active magnetic microbubbles were indeed attracted towards the magnet and in doing so achieved a greater number density than would otherwise have occurred under steady-state conditions without targeting. Non-magnetic microbubbles present in the sample as a result of the sonication process used to produce them manifested as separate and lower amplitude local maxima in the maps, and reduce the apparent effect of targeting to some degree (refined microbubble production techniques could eliminate this issue). Nonetheless, statistically significant changes in the spatial energy ratio, peak width and total (average or peak) source energy were observed. These observations suggest targeting was successful and sufficient to counter possible negative effects such as closer proximity of bubbles to other bubbles or surfaces. The response of single boluses of microbubbles to multiple excitation pulses suggests a front-loaded effect in which the source energy decay profile is largely a function of the number density of microbubbles present at the beginning of a pulse sequence, with (in the absence of microbubble replenishment from flow) little further effect of targeting thereafter.

Under flow conditions magnetic targeting was shown to consistently increase the cavitation energy emitted from magnetic microbubbles under focused ultrasound excitation, which was maintained over timescales on the order of minutes and monitored over the duration of exposures using PAM. Over time the cavitation energy both with

and without magnetic targeting declined due to progressive destruction of microbubbles by the ultrasound pulses and physical effects of the flow loop. However, the cavitation energy with targeting was consistently higher than that without targeting, due to local enhancement of the microbubble concentration. While in the absence of targeting, microbubbles should be approximately evenly distributed throughout the circulating volume, with targeting the region close to the magnet will contain both free-circulating microbubbles and those which were retained out of flow by the magnet in-between excitation pulses. Variation of the microbubble dose showed that the effect of magnetic targeting was particularly pronounced at lower microbubble concentrations, which presented greatest opportunity for benefit due to the limited steady-state number density of cavitation nuclei. Similarly, variation of the flow rate showed that the effects of targeting were greatest at lower flow rates where replenishment of microbubbles during and between pulses was more limited. Broadly speaking, magnetic targeting was found to increase the source energy of emissions by 2-5 times at a given microbubble concentration, and produced comparable effect to that of doubling the microbubble dose without targeting.

Spatial analysis of individual passive acoustic maps under flow did not show as clear-cut changes in response to magnetic targeting as was seen in the static case: this is understandable as the response to each excitation was now confounded by spatial and temporal averaging in which a changing population of nuclei moved into and out of the focal region during each pulse. The influence of flow may be expected to be most pronounced in the centre of the channel where (assuming a Poiseuille profile) the fluid velocity would be highest, and indeed, the peak in energy observed in passive acoustic maps under flow conditions was in all cases close to the centre of the channel, in contrast to the static case where it was close to the walls as a result of mi-

crobubble buoyancy or magnetic targeting. A possible explanation for this discrepancy is that microbubbles arriving at the focus during a pulse cavitated before they could be significantly diverted by the magnetic field. The overall increase in cavitation source energy suggests that over the focal region as a whole a higher number density of microbubbles was achieved. A small shift in the profile of activity in the plane of the magnetic field was however observed: whether this would be visible on such a sub-vessel scale clinically (or if only an overall increase in cavitation energy over the vessel could be resolved) depends primarily on the length scales of the vessel under consideration, magnetic field gradient, and on other geometric considerations such as depth within tissue, vessel branching and proximity to other vessels.

The work in this chapter has several limitations which will be improved upon in subsequent chapters. Firstly, while the passive acoustic mapping technique itself may readily be applied in real-time during exposures, this was not possible in the setup used here due to limitations of the clinical ultrasound engine which was used to record acoustic emissions. In later chapters the Verasonics programmable ultrasound platform (Kaczkowski and Daigle, 2011) was used to allow real-time feedback during experiments. Secondly, the modest magnetic fields used in this study (around 0.1 T at the flow channel) limits the parameter space in terms of variables such as flow rate and microbubble concentration, and would also restrict the depth at which such techniques could be applied *in vivo*. Using a larger Halbach array magnet magnetic retention of microbubbles has been demonstrated in saline in similarly sized vessels to this chapter at shear rates up to 373 $s^{-1}$ under B-mode imaging (Owen *et al.*, 2014); in blood targeting efficiency (i.e. the number of bubbles retained by the magnet) was reduced compared to saline, but to a much lesser extent than with avidin-biotin targeting. Towards this end, magnet arrays (Owen *et al.*, 2014) were used in later *in vitro*

work (Chapter 4) (development of more advanced magnet designs for *in vivo* work is ongoing). Finally, while the results here show clear effects in terms cavitation data, for greater clinical relevance it will be necessary to relate this to biological effects, such as enhanced delivery of active therapeutics or marker molecules. This problem is addressed in the following chapters using *in vitro* and *in vivo* models.

Overall, these results show that magnetic localisation of microbubble-induced cavitation was successfully achieved under the influence of a modest magnetic flux density (0.1 T) and could be resolved using passive acoustic mapping. Under flow conditions at clinically relevant shear rates of up to 100 $s^{-1}$ targeting efficacy was maintained and was shown to consistently increase the energy of cavitation emissions by a factor of 2-5 times, which was approximately equivalent to doubling the injected microbubble dose. These results suggest that magnetic targeting could be used to localise and increase the concentration of microbubbles and hence cavitation activity for a given systemic dose of microbubbles or ultrasound intensity.

## 3.5. CONCLUSIONS

The aims of this chapter were to establish whether magnetic localisation of microbubbles could be detected using PAM; to investigate the effects of magnetic confinement on the resulting cavitation activity, and to test whether this could translate to therapeutically relevant benefits such as enhanced cavitation.

The acoustic response of the lipid-based magnetic microbubbles was found to be similar to that of commercial ultrasound contrast agents. Magnetic localisation of microbubble-induced cavitation activity was successfully achieved and could be resolved using passive acoustic mapping, manifesting as a statistically significant shift in the spatial distribution and increases in the intensity and sustainability of cavitation activity under the influence of a magnetic field. Under flow conditions at shear rates of up to 100 $s^{-1}$ targeting efficacy was maintained. Application of a magnetic field was shown to consistently increase the energy of cavitation emissions by a factor of 2-5 times over the duration of exposures compared to the case without targeting, which was approximately equivalent to doubling the injected microbubble dose. These results suggest that magnetic targeting could be used to localise and increase the concentration of microbubbles and hence cavitation activity for a given systemic dose. Particularly in the case of delivery of toxic drugs, this could be exploited to reduce the risk of adverse effects and improve the scope of patient eligibility. Towards this aim, the following two chapters focus on validation of the techniques outlined here for targeted delivery *in vitro* and *in vivo*.

CHAPTER 4

# PASSIVE ACOUSTIC MAPPING OF MAGNETIC MICROBUBBLES *IN VITRO*

## 4.1. INTRODUCTION

Having demonstrated the ability of magnetic microbubbles to enhance cavitation and of passive acoustic mapping to monitor this process in Chapter 3, the aim of this chapter was to investigate whether this enhanced activity can promote therapeutic delivery in an *in vitro* model (i.e. aim 4 of the thesis as a whole; Section 1.8.2). Two different microbubble agents were used: an improved formulation of the magnetic microbubbles, as well as magnetic liquid nanodroplets that are converted into microbubbles upon exposure to ultrasound. These agents were tested for two potential therapeutic applications: transfection of cells with siRNA, and delivery of a chemotherapeutic drug currently in clinical use (paclitaxel).

The experiments reported in this chapter were conducted in collaboration with colleagues in the BUBBL group. In particular the contributions of Dario Carugo, who designed the cell chamber; Joshua Owen, who developed the new magnetic mi-

crobubble formulation and cultured and analysed the cells for the experiments in which they were used; and Jeong Yu Lee, who developed the magnetic nanodroplets and similarly performed cell culture and analysis for the corresponding experiments are explicitly acknowledged. Parts of the cell chamber work were previously published in (Carugo *et al.*, 2015) and the work on the nanodroplets in (Lee *et al.*, 2015). Portions of the work with the fluorescent siRNA model were included in (Owen, 2015) and that with the knockdown siRNA model is under preparation for publication.

The work described in this chapter represents the culmination of several overlapping workstreams conducted in collaboration with the researchers named above, and is organised into sections accordingly. A brief introduction to the cell chamber system designed for the experiments is included below, while introductory material on the therapeutic agents, corresponding mechanisms of action and the biological analysis methods employed to assess efficacy are included in Section 2.4.

### 4.1.1. Cell chambers

A wide variety of devices for cell culture may be found in the literature, many of which have been adapted for use in studies of ultrasound-mediated therapy. Existing devices may be categorised as tubes (Ogawa *et al.*, 2002), well plates (Jackson *et al.*, 2011) or parallel-plate chambers (Rahim *et al.*, 2006). In particular, the OptiCell™ parallel plate chamber system (since discontinued; originally designed to allow cell culture in a sealed device compatible with optical microscopy) has been used in numerous ultrasound-mediated drug and gene delivery studies (e.g. Rahim *et al.*, 2006; Meijering *et al.*, 2007; Meijering *et al.*, 2009; Stride *et al.*, 2009). Despite this widespread usage, parallel plate chambers suffer from various drawbacks, chiefly as a result of their geometry: in order to present a thin volume between two flat parallel plates (ideal for culture and imaging purposes) such chambers are typically only accessible from small ports around their periphery. This leads to difficulties in loading and unloading cells or therapeutic agents, or for other purposes such as acoustic calibration. For these reasons an alternative device which was expressly designed to facilitate ultrasound exposure was utilised for the majority of the experiments The device consists of a polydimethylsiloxane (PDMS) membrane ‘lid’ designed to fit a widely available thin-bottomed cell culture dish (Carugo *et al.*, 2015). It is described in more detail in Section 4.2.1 and its acoustic characteristics outlined in Section 4.3.1.

## 4.2. METHODS

The following sections include details of the methods used for *in vitro* experiments including design and characterisation of the cell culture chamber used in the experiments, ultrasound exposure and monitoring system, microbubble agents used, cell models employed, and subsequent biological and acoustic data analysis.

### 4.2.1. Cell chamber design and fabrication

A cell chamber consisting of a commercially available cell culture dish coupled with an acoustically compatible lid was produced for use in the *in vitro* experiments[8]. The following sections include details of the acoustic characterisation of the system, which was conducted by the author and is of primary importance to the current work. For completeness this is preceded by a brief summary of the lid design process, further details of which may be found in the associated publication (Carugo *et al.*, 2015).

A lid was designed to fit a commercial cell culture dish (µ-Dish 35 mm, Ibidi GmbH, Germany) which was chosen as a readily available chamber in which cells could be cultured directly and was compatible with high resolution microscopy for examination of cells. The lid was cast from polydimethylsiloxane (PDMS), a silicon-based polymer that has previously been used for microfluidic devices in biological applications (Mata *et al.*, 2005; Sia and Whitesides, 2003). Besides biological compatibility, PDMS provides additional benefits of optical transparency, gas permeability and ease of moulding which led to its use in soft contact lenses (Nicolson and Vogt, 2001).

The lid was cast using replica moulding in a manifold assembled from three main parts machined from Teflon® and poly(methyl methacrylate) (PMMA) using a lathe,

[8] The cell chambers used in this chapter were developed and produced by Dario Carugo whose assistance is gratefully acknowledged

as summarised in Figure 4.1. Two segments of polyether ether ketone (PEEK) tubing were installed to produce holes in the lid to allow for filling and drainage of the chamber. Degassed PDMS was poured into the assembly and allowed to set on a hot-plate at 90 °C for 90 minutes. Once the PDMS had solidified the lid was removed by disassembly of the manifold and coupled with a cell culture dish.

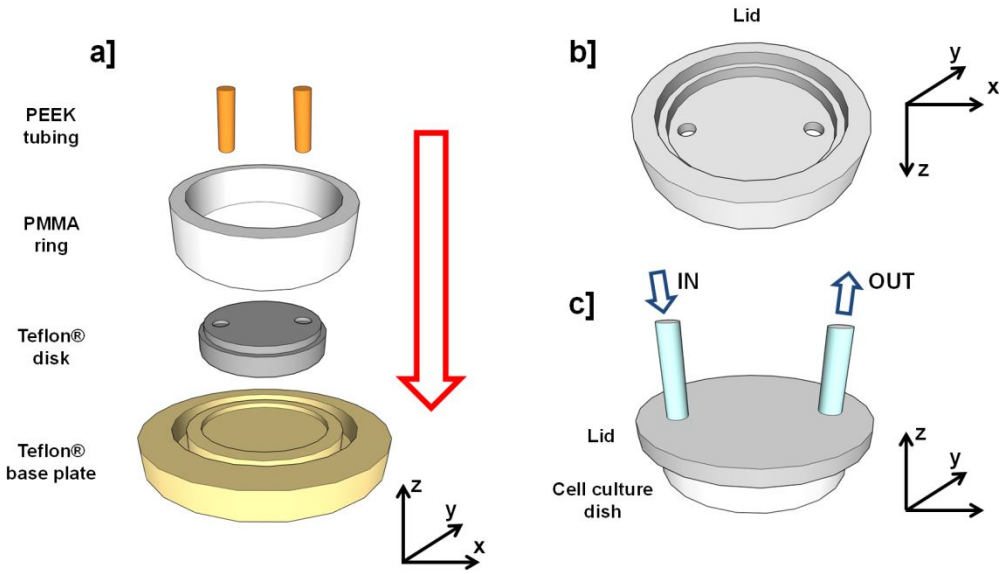


Figure 4.1: Cell chamber lid design and fabrication. (a) Components of the manifold constructed for replica moulding of the lid. These include a Teflon® base plate with recesses for coupling with a Teflon® disk and a PMMA ring, and two segments of PEEK tubing to be coupled with the top surface of the disk. The red arrow indicates the direction of assembly. (b) Schematic depiction of the obtained lid (shown inverted), with holes for fluid injection and discharge. (c) Lid coupled with a cell culture dish (white), with inlet and outlet tubing (light blue) inserted through its holes. Reproduced under Creative Commons license from (Carugo *et al.*, 2015).

Flow field simulation and sealing tests were performed to confirm that the conditions within the chamber during priming would not cause damage to the cells on the bottom surface (via excessive shear stress) and that cells would be isolated from the test tank (Carugo *et al.*, 2015)[9].

#### 4.2.1.1. Lid acoustic characterisation

In order to assess the suitability of the system for ultrasound-mediated delivery the effects of the lid on both a relatively low-frequency ultrasound signal as might be

[9] Testing and simulation conducted by Dario Carugo and not included in this thesis

used for therapy and a high-frequency signal relevant to cavitation detection were evaluated. A schematic of the experimental setup is shown in Figure 4.2. The lid was mounted in a water tank containing degassed, deionised water at 37 °C and placed between the relevant ultrasound source and a hydrophone used for measurement of the resulting acoustic field[10]. The transducer was driven (via a matching network in the case of the low frequency transducers) by a 55dB power amplifier (model A300; Electronics & Innovation, Ltd., USA) connected to a function generator. A 0.4 mm diameter needle hydrophone (model HNA-0400; Onda Corp., USA) attached to a 3-axis positioning system was used to measure the acoustic field. The hydrophone signal was recorded using a computer-controlled digital storage oscilloscope (model WaveRunner 44Xi, LeCroy, USA) which was also used to monitor the voltage waveform applied to the transducer. Data were processed following experiments using MATLAB (The MathWorks Inc., USA).

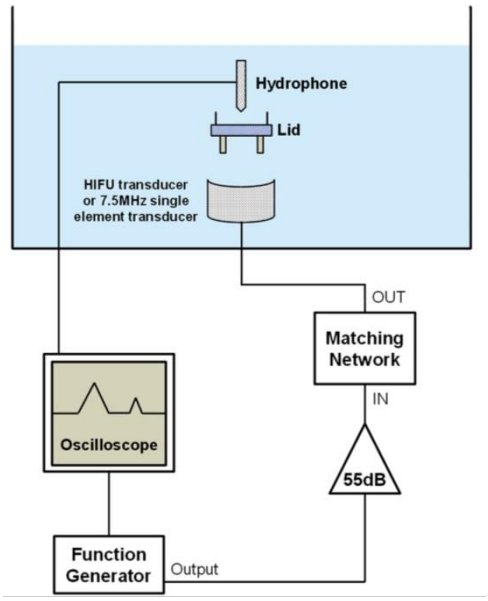


Figure 4.2: Instrumental setup for measurement of lid acoustic characteristics. The matching network was omitted for tests using the 7.5 MHz single element transducer. Adapted under Creative Commons license from (Carugo *et al.*, 2015).

[10] For the purpose of these measurements the bottom of the cell culture dish was removed to permit access of the hydrophone. The effect on acoustic calibration should be minor as the plastic membrane is very thin (180 µm).

#### 4.2.1.1.1. Low frequency acoustic performance

To evaluate the effect of the lid on ultrasound in the typical therapeutic range two single element high intensity focused ultrasound (HIFU) transducers (Sonic Concepts Inc., USA) were used. Model H-107 F-18 was employed for US frequencies of 0.5 and 1.59 MHz, and model H-107 E-35 was employed for an US frequency of 1.1 MHz. The hydrophone was aligned initially to the focus of the HIFU transducer and then scanned over a 4.8 mm × 4.8 mm area in the plane transverse to ultrasound propagation, corresponding to the plane in which cells would be located within the chamber. Such scans were obtained for lids of different thicknesses and the maximum peak-to-peak pressure extracted.

#### 4.2.1.1.2. High frequency acoustic performance

To evaluate the performance of the lid at higher ultrasound frequencies (relevant for cavitation monitoring) the 500 kHz HIFU transducer was replaced with a focused single element transducer with a 7.5 MHz centre frequency (model V320-SU; Olympus NDT, USA). The transducer was operated in burst mode (100 cycles per burst, PRF 10 Hz) at frequencies of 4-11 MHz (chosen to match a typical linear array ultrasound probe) in steps of 1 MHz. A constant excitation voltage was applied which corresponded to 0.8 MPa peak-to-peak pressure at 8 MHz, falling to approximately 0.4 MPa at the extremes of the frequency range due to the frequency response of the transducer. 32 measurements were performed at the spatial peak at each frequency for each of the lids. The same experimental setup, with minor adjustments, was used to measure the reflection coefficient of the lid and the substrate of the cell dish using the single element transducer driven by a pulser-receiver in pulse-echo mode.

### 4.2.2. Setup for *in vitro* cell transfection experiments

A schematic of the setup used for *in vitro* cell transfection is shown in Figure 4.3. Ultrasound was generated using a 500 kHz spherically focused single-element high intensity focused ultrasound (HIFU) transducer (model H-107B-10; Sonic Concepts, Inc., Bothell, WA, USA) with an outer diameter of 64 mm, focal length 63 mm, and featuring a 45 × 18 mm rectangular cutout through which an imaging linear array probe (model L11-4v; Verasonics Inc., Kirkland, WA, USA) with 128 elements, 38 mm aperture and 4-11 MHz bandwidth was aligned such that the focus of the HIFU transducer was within the imaging plane. Function generator 1 (model 33250A; Agilent, Wokingham, Berkshire, UK) was set to pulse mode and triggered from the ultrasound research platform (model Vantage 256; Verasonics Inc., Kirkland, WA, USA) using a trigger output signal. The output from function generator 1 was used to trigger the second function generator which produced the sinusoidal drive signal for the HIFU transducer. The use of two function generators allowed treatment to occur at a multiple of the imaging frame rate as each imaging frame triggered a chain of treatment pulses. The driving signal was applied to the HIFU transducer via a 55 dB power amplifier (model 1040L; Electronics and Innovation, Rochester, NY, USA) and impedance matching network supplied by the transducer manufacturer. The ultrasound research platform was connected to a host desktop PC to configure the imaging sequence, save data and provide real-time display during the experiments.

The HIFU transducer and imaging array assembly were mounted on a 3 axis positioning stage in a 60 × 57 × 25 cm Perspex tank filled with filtered, degassed, deionised water which was heated to 37 $^{o}$C using an immersion heater. Prior to commencing experiments the focus of the HIFU transducer was located using a 200 μm needle hydrophone (Precision Acoustics, Dorchester, UK). The location of the hydrophone

tip observed under B-mode imaging was recorded and used to position samples at the focus during experiments. Samples were placed in the cell chamber described in Section 4.2.1 and mounted on top of a rectangular Halbach array of permanent magnets constructed from 5 elements (N52 grade NdFeB, transversal magnetisation 1.5 T, 10 × 10 × 25 mm; NeoTexx, Berlin, Germany) or a nonmagnetic aluminium bar of the same dimensions so that any reflections of the ultrasound field would be consistent between experiments.

The magnet and chamber assembly (shown in Figure 4.4a) was attached to a 3 axis positioning stage and the samples aligned with the focus of the HIFU transducer. The ultrasound research platform was initially used to align the sample with the focus of the HIFU transducer under B-mode imaging using a script supplied by the system manufacturer; an annotated B-mode image showing the cell chamber is shown in Figure 4.4b. Based on previous transfection experiments (Stride *et al.*, 2009) the ultrasound conditions used were 1 MPa peak-to-peak, 40 cycles per burst, 1 kHz PRF for 10 seconds per treatment. The ultrasound research platform was set to passively record the acoustic emissions from cavitation (array transmit disabled; receive on 128 channels, 25 MHz sample rate, 174 µsec recording length) at a frame rate of 100 Hz for the first 1 second of each exposure during experiments; initial experiments having shown that the majority of acoustic emissions occurred during this period. In preliminary tests cells were contained in a commercial OptiCell$^{TM}$ chamber (Fisher Scientific, Loughborough, UK) instead of the dish/lid system and the Verasonics ultrasound platform was substituted with the Zonare-based system described in Chapter 3.

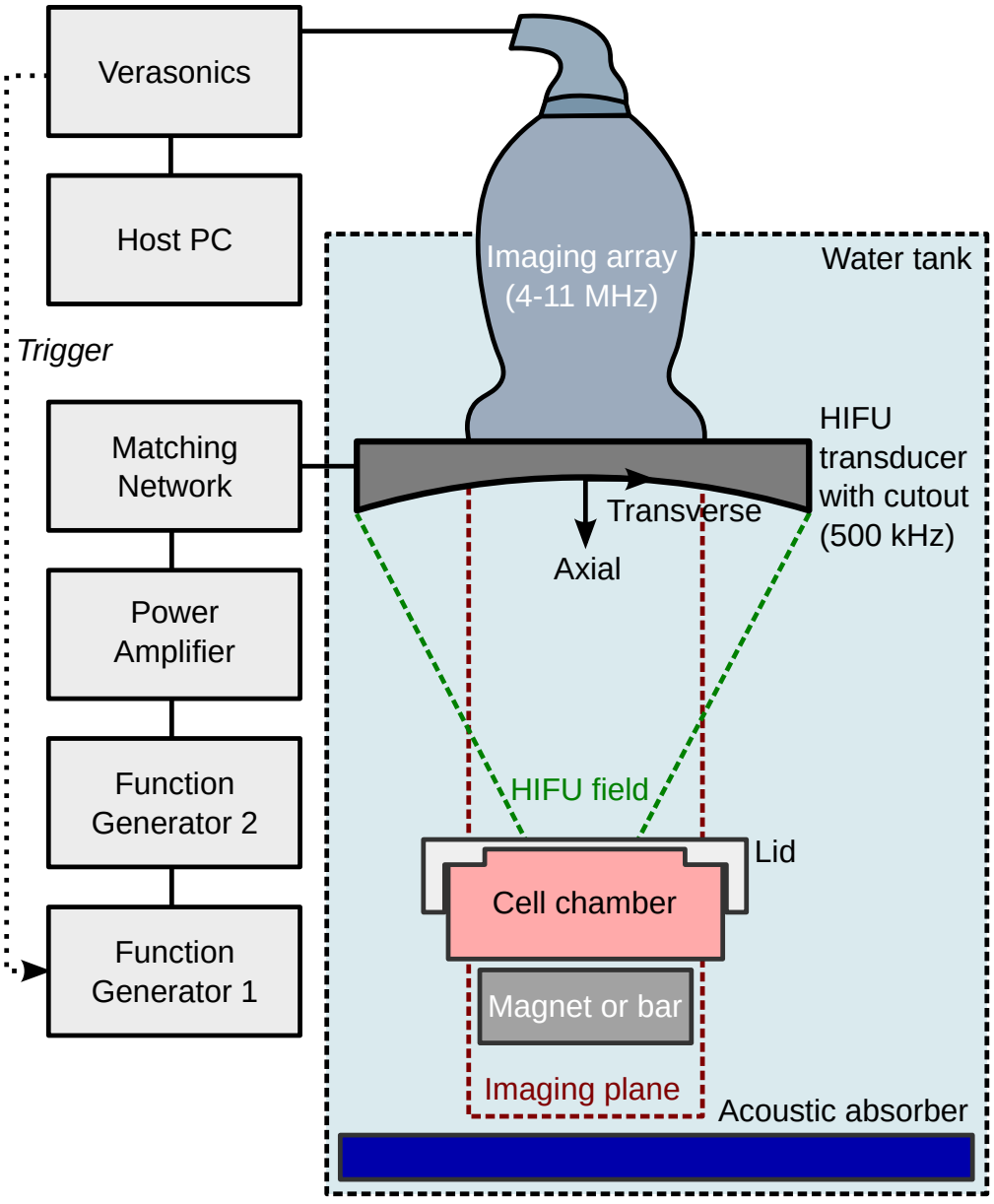


Figure 4.3: Setup for *in vitro* cell transfection experiments (not to scale). A cross-sectional view through the water tank is shown. Samples were placed in a cell chamber at the focus of a 500 kHz HIFU transducer with a rectangular cutout for an imaging array. Two function generators were used to allow treatment to take place at a multiple of the imaging frame rate. In preliminary experiments cells were contained in an OptiCell™ chamber instead of the dish/lid system and the Verasonics ultrasound platform was substituted with the Zonare-based system described in Chapter 3.

(a)

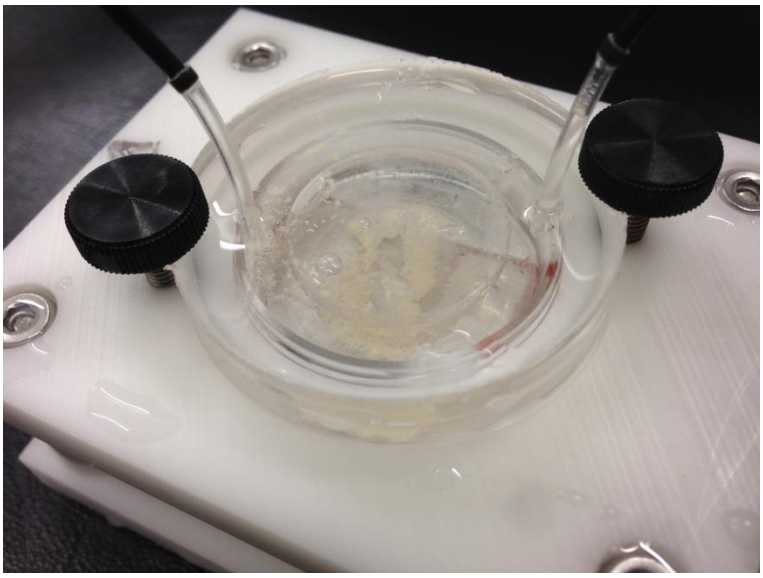

(b)

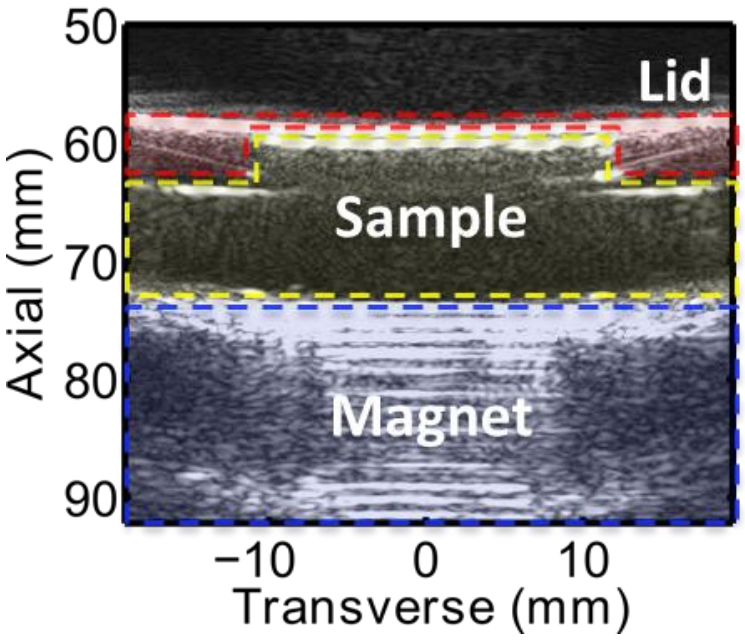


Figure 4.4: Images of setup for *in vitro* experiments. (a) Photograph of cell chamber, lid and inlet/outlet tubing installed on top of the magnet assembly. The chamber in this case contains a sample of magnetic microbubbles in water, which may be seen on the bottom of the chamber. (b) Annotated B-mode image showing the lid, sample and magnet as observed from the ultrasound imaging array; reproduced under Creative Commons licence from (Lee *et al.*, 2015).

## 4.2.3. Magnetic microbubble and nanodroplet production

As above, two variants of ultrasound-responsive magnetic agents were tested: an improved formulation of magnetic microbubbles, and magnetic liquid droplets, which are initially nano-scale but vaporise into microbubbles upon ultrasound exposure.

### 4.2.3.1. siRNA-bound MMB production (F-MMB, K-MMB, S-MMB)

The magnetic microbubbles in this chapter[11] differ from those described in Chapter 3 in a number of ways. First, the magnetic nanoparticles were incorporated directly into the coating to remove the damping effect of the carrier oil and potential toxicity. Second, polyethylene glycol-40-stearate was used as an emulsifier to improve microbubble yield and stability. Third, for the siRNA loaded microbubbles a charged lipid was used to enable attachment of the siRNA to the bubble surface.

For the microbubble preparation, 1,2-distearoyl-sn-glycero-3-phosphocholine dissolved in chloroform (DSPC; 25 mg/mL) and 1,2-distearoyl-sn-glycero-3-ethylphosphocholine (DSEPC; 25 mg/mL) were purchased from Avanti Polar Lipids Inc. (Alabaster, Alabama, USA). Polyoxyethylene-40-stearate (PEG) and chloroform were purchased from Sigma Aldrich (Gillingham, Dorset, UK). Phosphate buffered saline (PBS) and BLOCK-iT™ fluorescent siRNA oligo (lot no: 1477937; Alexa Fluorophore 647-tagged; absorption max: 650 nm, emission max: 668 nm) and GFP knockdown siRNA (Ambion® Silencer® GFP; product code AM4626; supplied with negative control siRNA) were purchased from Life Technologies (Paisley, UK). FluidMAG-Lipid (25 mg/mL 50 nm spherical phosphatidylcholine coated magnetite particles in sterile water) was purchased from Chemicell (Berlin, Germany). Sulphur Hexafluoride ($SF_6$) was purchased from BOC (Guildford, UK).

[11] The magnetic microbubbles used in this chapter were developed and produced by Joshua Owen who is gratefully acknowledged

PEG was dissolved in chloroform (10 mg/mL) using a bath sonicator. DSPC, DSEPC and PEG solutions were mixed in a 100:44:4.5 molar ratio (60 µL of 25 mg/mL DSPC solution, 29 µL of 25 mg/mL DSEPC solution, 18 µL of 10 mg/mL PEG solution) in a glass vial. Glass precision syringes (Hamilton Microliter; Sigma Aldrich, Gillingham, Dorset, UK) were used to measure solutions for chloroform resistance. The vial was left on a hotplate at 50 °C for 12 hours in a fume hood to allow the chloroform to evaporate. The resulting lipid film was resuspended in 1.5 mL filtered PBS on a hotplate at 75 °C with constant stirring for 1 hour. 15 µL of Fluid-MAG-Lipid solution and 20 µL of the relevant siRNA oligo were added to the clear lipid suspension.

Three different siRNA products were used in the experiments:

1. To produce fluorescent siRNA MMBs (F-MMB), BLOCK-iT™ siRNA was used (a generic, fluorescent tagged siRNA which does not cause knockdown of a specific gene)

2. To produce knockdown siRNA MMBs (K-MMB) Ambion® Silencer® GFP siRNA (a GFP knockdown siRNA) was used

3. As an inactive control MMBs containing scrambled siRNA (S-MMB; negative control supplied with the Ambion® Silencer® siRNA) was used

The solution was then sonicated for 90 s to disperse the components using an ultrasonic cell disruptor (tip fully immersed, power setting 2; model XL 2000, 3 mm probe diameter, 22.5 kHz, Misonix Inc., Farmingdale, NY, USA). To produce microbubbles the probe tip was moved to the air-liquid interface and sonication repeated for 10 s (power setting 15) while $SF_6$ was continuously delivered from the gas cylinder to the vial via a tube held close to the vial opening. After sonication the solution

was centrifuged to remove unbound siRNA (1000 RPM, 10 mins) in a syringe in a manner similar to that previously described (Feshitan *et al.*, 2009).

#### 4.2.3.2. Paclitaxel-loaded magnetic nanodroplet production (PTX-MND)

Paclitaxel-loaded magnetic nanodroplets (PTX-MND) were developed based on a protein-polymer shell, initially liquid perfluoropentane (PFP) core, and magnetic nanoparticles[12]. Upon exposure to ultrasound with sufficient (frequency dependent) pressure amplitude the liquid PFP core is vaporised into a gas, producing microbubbles from the initially nano-sized agent. A schematic of the MNDs is shown in Figure 4.5.

Magnetic nanodroplets based on a protein-polymer mixture were produced as described in the associated publication (Lee *et al.*, 2015). Albumin was chosen for its biocompatibility, while PEG (bound to a cross-linker) was added to improve stability. Iron oxide nanoparticles act as nucleation sites to promote phase transition of the nanodroplets into bubbles, as well as allowing magnetic targeting.

Human serum albumin (HSA), O,O′-Bis(2-(N-Succinimidyl-succinylamino)ethyl) polyethylene glycol (*bis*-NHS-PEG; molecular weight 2,000), dichloromethane, iron oxide nanoparticles (IONP; $Fe_3O_4$, 5 nm), paclitaxel (PTX) and sodium dodecyl sulphate (SDS) were purchased from Sigma-Aldrich (Dorset, UK). Perfluoropentane (PFP; 99 %) was purchased from Apollo Scientific (Cheshire, UK).

To produce the paclitaxel-loaded magnetic nanodroplets HSA was dissolved in 1 mL distilled water (4 mg/mL) and stirred for 10 minutes at room temperature. 6 mg of *bis*-NHS-PEG dissolved in 100 µL dichloromethane, 100 µL of IONP in dichloromethane (5 mg/mL; i.e. 500 µg IONP) and 500 µg PTX were mixed and added to the

[12] The magnetic nanodroplets used in this chapter were developed and produced by Jeong Yu Lee who is gratefully acknowledged

HSA solution. The mixture was sonicated using an ultrasonic cell disruptor (tip fully immersed, power setting 2; model XL 2000, 3 mm probe diameter, 22.5 kHz, Misonix Inc., Farmingdale, NY, USA) at 4 °C for 30 seconds. The resulting oil-water emulsion was transferred to a rotary evaporator and the solvent rapidly evaporated at reduced pressure at a temperature of 30 °C. The resulting solution of HSA nanoparticles was dialysed using distilled water (molecular weight cut-off 3,500 Daltons) to remove unbound PEG and stored in a 4 °C refrigerator until required. To produce nanodroplets prior to experiments 50 µL PFP was added to the vial and sonicated (power setting 1, 10 seconds) with the same ultrasonic cell disruptor. Immediately after sonication the mixture was transferred to a vial containing 0.5 % SDS solution using a Polytetrafluoroethylene (PTFE) tube (0.3 mm inner diameter) connected to a syringe followed by stirring at 4 °C for 5 minutes. The PTX concentration in the nanodroplets was determined by comparison of the absorbance of the solution at 227 nm with a standard curve using a spectrophotometer (model NanoDrop®; NanoDrop Technologies, Wilmington, Delaware, USA) following ultrasound exposure to release the PTX[13].

For control experiments magnetic nanodroplets (MND) and paclitaxel-loaded nanoparticles (PTX-MNP) were prepared by omitting either the paclitaxel or PFP steps respectively. Free paclitaxel (PTX) was used as a further control.

[13] Measurements performed by Jeong Yu Lee

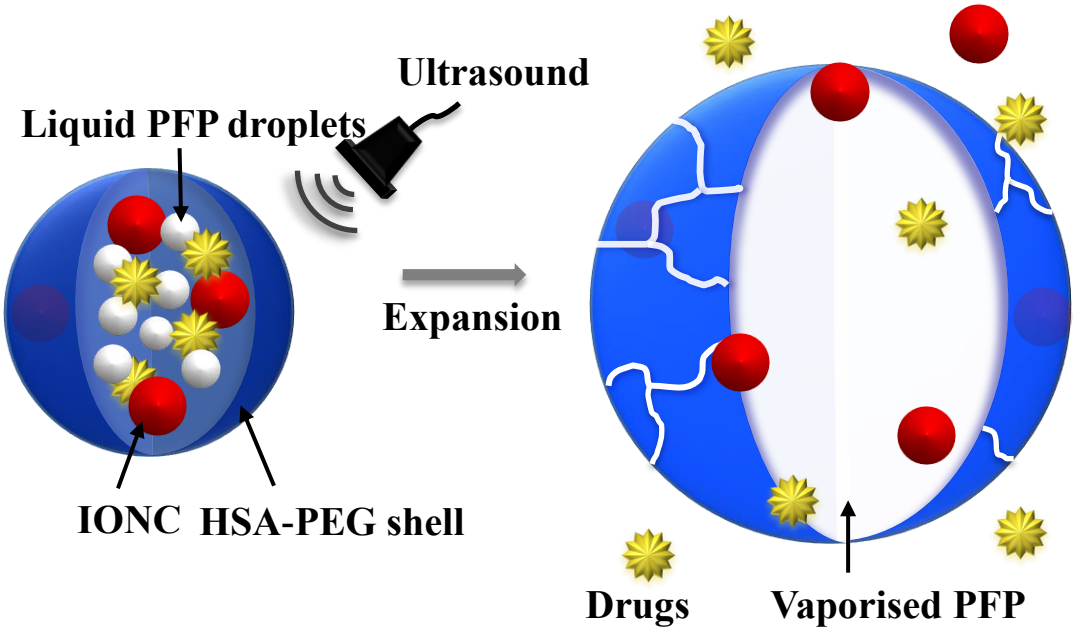


Figure 4.5: Schematic representation of magnetic nanodroplets, reproduced under Creative Commons licence from (Lee *et al.*, 2015). The droplets consist of iron oxide nanocrystals (IONC), hydrophobic drugs (Paclitaxel) and perfluoropentane (PFP). Ultrasound results in vaporisation of the liquid PFP to gas, producing microbubbles and promoting drug release.

## 4.2.4. Cell culture and preparation

### 4.2.4.1. Fluorescent siRNA MMB model

For fluorescent siRNA transfection experiments SY5Y neuroblastoma cells (ATCC; LGC Standards, Teddington, UK) were used as a model cell line due to their availability, widespread use, rapid replication rate and suitability for transfection experiments. Cells were cultured in flasks[14] using phenol-free Dulbecco's Modified Eagle Medium (DMEM) supplemented with fetal calf serum (FCS) and antibiotics. After reaching confluence the cells were released from the culture surface using Trypsin, centrifuged, mixed with further phenol-free DMEM media and divided between the cell chambers to be used in the experiments to a concentration of $1.5 \times 10^7$ cells per chamber. The prepared chambers were left overnight in an incubator at 37 $^{o}$C to allow the cells to reach confluence before commencing the experiments. Prior to each ex-

[14] Cell culture performed by Joshua Owen

periment a prepared chamber was removed from the incubator for treatment and returned to the incubator promptly after treatment.

#### 4.2.4.2. Knockdown siRNA MMB model

For testing the effect of knockdown siRNA loaded MMB, MCF7 human breast cancer cells were seeded in the cell culture dishes described in Section 4.2.1 ($5 \times 10^5$ cells/dish)[14]. The cells were grown in DMEM in an incubator at 37 $^oC$ for 24 hours prior to the experiments.

#### 4.2.4.3. Paclitaxel nanodroplets model

The effect of PTX-MND on inhibition of cancer cell growth was tested. MCF7 human breast cancer cells were seeded in the cell culture dishes described in Section 4.2.1 ($5 \times 10^4$ cells/dish)[15]. The cells were grown in DMEM in an incubator at 37 $^oC$ for 24 hours prior to the experiments.

### 4.2.5. Experimental protocol

Four sets of experiments were conducted: magnetic microbubbles to deliver siRNA (fluorescence and knockdown), magnetic nanodroplets to deliver paclitaxel, and finally magnetic nanodroplets alone to compare their response under various conditions to that of microbubbles.

#### 4.2.5.1. Fluorescent siRNA MMB model

1 mL of fluorescent siRNA loaded microbubble suspension (F-MMB) was added to the media in each of the prepared OptiCell$^{TM}$ cell chambers and the chamber placed in the 37 °C water tank at the focus of the HIFU transducer as in Figure 4.3[16]. Four samples were treated: (1) Control (no ultrasound, no magnet); (2) Magnet only (no ultrasound); (3) Ultrasound + magnet; (4) Ultrasound only (no magnet). Each sample

[15] Cell culture performed by Jeong Yu Lee
[16] Cell chambers prepared by Joshua Owen

was moved to 6 locations with respect to the focus of the HIFU transducer spaced equally in a rectangular grid over the sample. Ultrasound-treated samples were exposed to 1 MPa peak-to-peak, 500 kHz frequency, 40 cycles per burst, 1 kHz PRF for 10 seconds per exposure based on previous studies (Stride *et al.*, 2009). Following treatment the cell chambers were returned to the incubator for approximately 1 hour, following which the media (and microbubbles) were removed, 10 mL fresh media added and removed to wash the cells followed by 15 mL fresh media. The cells were then analysed within the chambers using fluorescence microscopy and a plate reader as described below.

#### 4.2.5.2. Knockdown siRNA MMB model

Each cell culture dish prepared as in Section 4.2.4.2 was removed from the incubator prior to each experiment and the media replaced with DMEM containing either knockdown siRNA MMBs (K-MMB; 200 µL or 100 µL per sample), scrambled siRNA MMBs (S-MMB 200 µL per sample), free siRNA or media only[17]. The dishes were sealed using the PDMS lids described in Section 4.2.1 and mounted on top of the magnet (or control bar) at the focus of the HIFU transducer in the setup described in Section 4.2.2. Samples were exposed to ultrasound (500 kHz, 40 cycles per burst, 1 kHz PRF, 10 seconds duration per run) at 9 locations evenly spaced 3 mm apart in a grid, while the imaging array passively recorded the acoustic emissions from every 10$^{th}$ burst for the first second of each exposure. After ultrasound exposure the cell dishes were incubated at 37 °C for 24 hours before analysis described below.

#### 4.2.5.3. Paclitaxel nanodroplets model

PTX-MND were diluted with PBS such as to achieve a final concentration of PTX of 0.5 µM in the cell chambers. Each prepared cell culture dish was removed from the

[17] Cell chambers prepared by Joshua Owen

incubator prior to each experiment and the media replaced with DMEM containing either PTX-MND, MND, PTX-MNP or free PTX[18]. The dishes were sealed using the PDMS lids described in Section 4.2.1 and mounted on top of the magnet[19] at the focus of the HIFU transducer in the setup described in Section 4.2.2. Samples were exposed to ultrasound (500 kHz, 40 cycles per burst, 1 kHz PRF, 10 seconds duration per run) at 3 locations spaced 3 mm apart along the longer axis of the magnet, while the imaging array passively recorded the acoustic emissions from every 10$^{th}$ burst for the first second of each exposure. After ultrasound exposure the cell dishes were incubated at 37 °C for 24 hours before analysis described below.

#### 4.2.5.4. Nanodroplet characterisation

To characterise the acoustic behaviour of the nanodroplets (with a view to optimising the acoustic conditions for *in vivo* experiments) nanodroplets (measured 3.5 × $10^9$ particles/mL) or SonoVue® microbubbles (quoted 1-5 × $10^8$ particles/mL) were added to cell culture dishes filled with water (total vol. ~8 mL) and exposed to ultrasound under a range of conditions (peak negative focal pressure 0-1 MPa, duty cycle 0-80 %) while the acoustic emissions were recorded. As the effective concentration of microbubbles produced by the nanodroplets (after vaporisation) was unknown, no attempt was made to 'match' the concentration with that of SonoVue®. Instead the concentrations of both agents were varied over a wide range to find that which would give comparable acoustic response in this setup. The aim of this experiment was to compare the response of the agents, not the effect of targeting, so no magnet was used[19]. Each sample was treated three times in a similar manner to the cell experiments in Section 4.2.5.3, and each experimental condition was repeated with three samples. As an additional comparison sonicated nanodroplets (i.e. nanodroplets after

[18] Cell chambers prepared by Jeong Yu Lee

[19] The response of NDs with and without a magnet was not explicitly compared in this thesis, as their small size and additional vaporisation step makes fair comparison difficult

vaporisation into microbubbles) were prepared by mixing 100 µL nanodroplet solution with 900 µL water and sonicating with an ultrasonic cell disruptor (tip fully immersed, power setting 2; model XL 2000, 3 mm probe diameter, 22.5 kHz, Misonix Inc., Farmingdale, NY, USA) for 30 seconds.

## 4.2.6. Fluorescence and flow cytometry analysis

Following the experiments, cells were analysed using fluorescence microscopy, fluorescence measurements using an automated plate reader, and flow cytometry in each of the experimental sets as detailed below.

### 4.2.6.1. Fluorescent siRNA MMB model

Cells were observed using fluorescence microscopy and an automated optical microplate reader to observe the effects of treatment with the fluorescent siRNA model[20]. In both cases the cells were retained within the OptiCell™ in which they were treated. Microscope images were taken using a fluorescence microscope (model Eclipse Ti-E; Nikon Instruments, UK) fitted with a 20 × objective (model Plan Fluor; Nikon Instruments, UK) and Fluorescein Isothiocyanate (FITC) filter cube (exposure 2 seconds, gain 1). Brightfield images were also taken (exposure 363 ms, gain 1). At each of the 6 treated locations per chamber an automated scan was conducted over a 5 × 5 mm area which was stitched together using the microscope software. The maximum fluorescence intensity was obtained from the images using ImageJ (National Institutes of Health, Bethesda, MD, USA) and the mean and standard deviation of these measurements calculated from the 6 locations per sample.

To obtain a reading of the fluorescence intensity over the full area of each sample each OptiCell™ was measured using an automated plate reader (model FLUOstar Omega; BMG LABTECH, Aylesbury, UK) with appropriate excitation/emission set-

[20] Cell analysis conducted by Joshua Owen

tings for FITC and covering the whole area of the cell growth substrate within each sample.

#### 4.2.6.2. Knockdown siRNA MMB and Paclitaxel nanodroplets model

For both the siRNA knockdown and nanodroplets/paclitaxel experiments cells were characterised after treatment using a viability assay, microscope imaging and flow cytometry[21].

The number of viable cells in each sample at 24 hours after treatment was measured using a colorimetric assay kit (Promega, Southampton, UK) based on 3-(4,5-Dimethylthiazol-2-Yl)-5-(3-Carboxymethoxyphenyl)-2-(4-Sulfophenyl)-2H-Tetrazolium (MTS) (Malich *et al.*, 1997). To further evaluate the effects of treatment cells were observed using an optical microscope following staining with propidium iodide and DNA content analysed using flow cytometry. For flow cytometry the cells were collected by centrifuging at 1100 RPM for 5 minutes, washed twice with PBS and then fixed with ice cold 70 % ethanol for 24 hours. The fixed cells were then washed with PBS and incubated with 100 µg/mL PI stain for 20 minutes and the DNA profile analysed using FACSort (BD Bioscience, Oxford, UK). The percentage of cells undergoing programmed cell death (apoptosis; an expected effect of the anticancer PTX treatment) was calculated as a percentage of the sub-$G_1$ peak determined by analysis of the flow cytometry data.

[21] Cell analysis conducted by Jeong Yu lee

### 4.2.7. PAM analysis

Following each experiment, the acoustic emissions captured by the imaging array were high-pass filtered at 1 MHz to remove the main driving signal and mapped in space to provide an estimate of the acoustic power of cavitation emissions using the reconstruction algorithm described in Section 2.2.4. To convert the arbitrary units of the signals to physical units the imaging array was calibrated as described in Appendix B. Acoustic maps over a 20 × 20 mm area about the ultrasound focus were generated for each frame of the received data. The sum of these maps from each experiment was used to estimate the total energy of acoustic emissions, and overlaid on pre-exposure B-mode images to indicate their spatial distribution. In addition, the maximum value in the maps for each individual frame was used to evaluate the evolution of cavitation activity over time. Finally, the reconstructed time-domain signal for the focal point in each frame was subject to a Fourier transform (MATLAB function *fft*) to produce spectra which were averaged over the 100 frames captured in each experiment.

## 4.3. RESULTS

### 4.3.1. Cell chamber acoustic characterisation

#### 4.3.1.1. Low frequency acoustic performance

The results of the low frequency (0.5-1.6 MHz) tests of the custom cell chamber lid are summarised in Figure 4.6 and Figure 4.7. The maximum peak-to-peak acoustic pressure was measured for different thickness values of the lid and ultrasound (US) excitation frequencies (Figure 4.6). As expected, the maximum peak-to-peak acoustic pressure reduced with increasing thickness of the lid (Figure 4.6a). At a frequency of 1.1 MHz the maximum peak-to-peak acoustic pressure reduced from 0.931 MPa for a 1.22 mm thick lid, down to 0.775 MPa for a 5.87 mm thick lid. Increasing the US excitation frequency resulted in increased attenuation of the incident field (Figure 4.6b). For an average lid thickness of 3.33 mm, the maximum peak-to-peak acoustic pressure reduced from 1 MPa to 0.913 MPa at 0.50 MHz, to 0.872 MPa at 1.10 MHz and to 0.677 MPa at 1.59 MHz.

The contours of peak-to-peak acoustic pressure at the target plane for different lid thicknesses and US excitation frequencies are shown in Figure 4.7. The spatial characteristics of the sound field were virtually undistorted under the range of experimental conditions investigated.

These results show that at therapeutically relevant US frequencies the lid had a measurable effect on the ultrasound field. As expected, attenuation of the sound field increased with both lid thickness and US frequency, and was particularly pronounced at 1.59 MHz. For monitoring of cavitation the higher frequency transmission performance is particularly of interest, and this is discussed below.

(a)

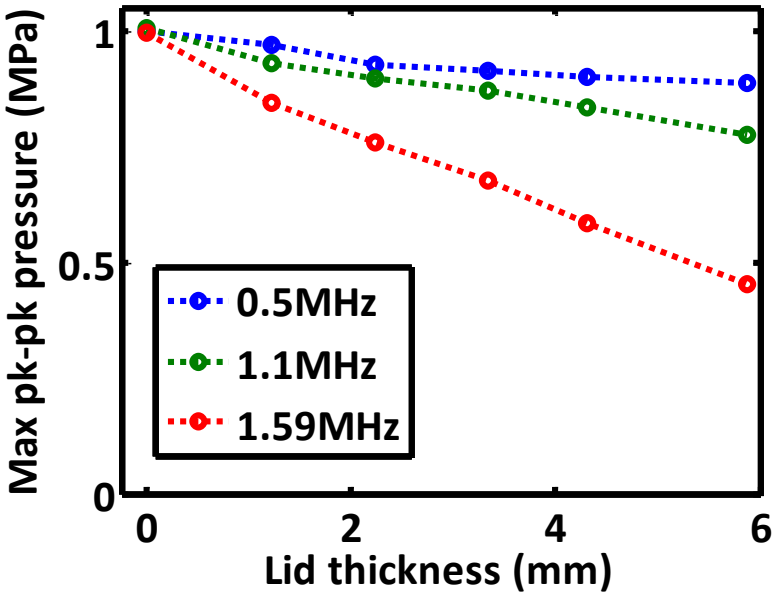


(b)

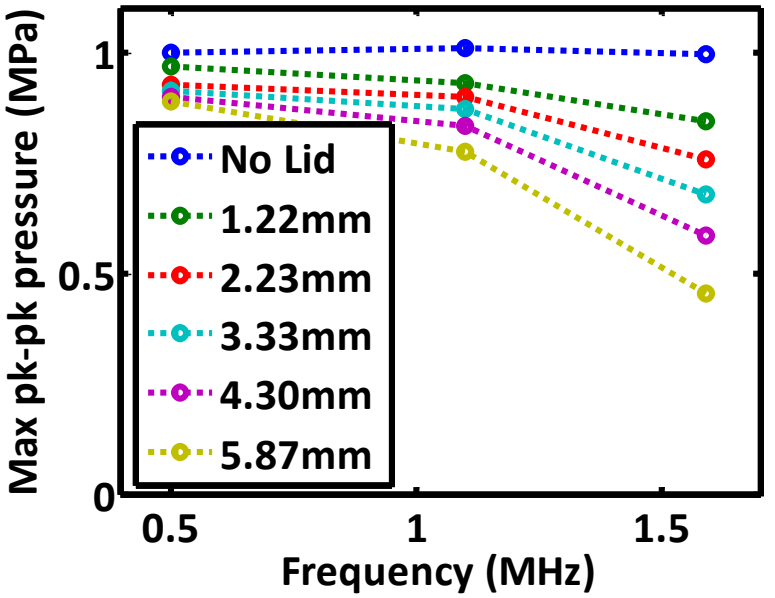


Figure 4.6: Low frequency lid transmission – peak pressure. (a) Maximum peak-to-peak pressure (in MPa) vs. lid thickness (in mm), measured at three different US frequencies (0.5, 1.1 and 1.59 MHz) which are relevant for therapeutic applications. (b) Maximum peak-to-peak pressure (in MPa) vs. frequency (in MHz), measured at different thickness values (in mm) of the lid.

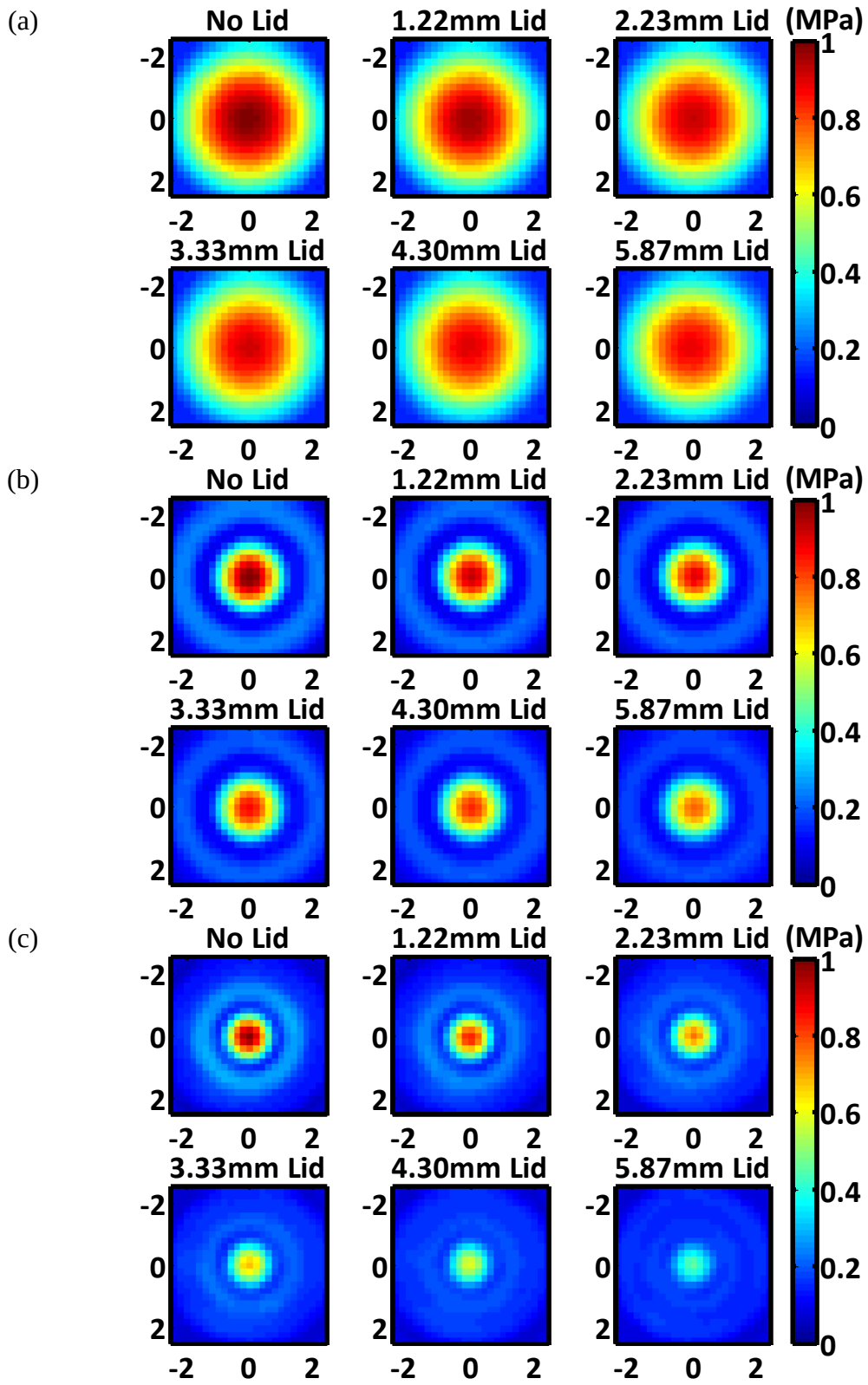


Figure 4.7: Low frequency lid transmission – spatial scans. (a-c) Contours of peak-to-peak acoustic pressure (in MPa) at the target plane (axes are in mm), measured at different thickness values of the lid, and US frequencies of 0.5 MHz (a), 1.1 MHz (b) and 1.59 MHz (c). The excitation voltage was adjusted to obtain peak-to-peak focal pressure of 1 MPa for each US frequency.

#### 4.3.1.2. High frequency acoustic performance

The results of frequency ramp experiments to evaluate the higher frequency response of the lid in the range relevant to cavitation monitoring are summarised in Figure 4.8 and Figure 4.9. As expected, the attenuation increased with lid thickness (from 20.83 % to 63.52 % for the thinnest and thickest lids at 4 MHz, respectively) as well as with ultrasound frequency.

The pulse-echo waveforms used to calculate the reflection coefficients of the thickest lid and the cell dish are shown in Figure 4.9. Each pair of waveforms shows the first and second echo of a pulse emitted from the transducer, reflected from the sample, and received by the same transducer. Dividing the peak-to-peak amplitude of the second reflection compared to the first allows an estimate of the reflection coefficient to be obtained. As expected due to the close impedance match between PDMS and water (Leibacher *et al.*, 2014) the reflection coefficient for the thickest lid was very low (0.033), whilst the reflection coefficient for the cell dish substrate was 0.078.

Results from both the sealing and acoustic characterisation tests suggest that an intermediate thickness of the lid (i.e., in the range 2 – 3 mm) represents the optimal compromise between sealing and acoustic transmission at therapeutically relevant US frequencies. However, increased attenuation of the US field was observed at higher frequencies for all thicknesses, which could potentially limit the usability of the device – in its current configuration – for applications involving detection of the higher frequency signals associated with cavitation, such as passive acoustic mapping. For this reason only the thinnest lids were deemed suitable for the following experiments.

The lid design was subsequently revised to include a ‘step’ in thickness to accommodate a thinner (100 µm) central region to improve higher frequency acoustic performance. The high frequency transmission performance of this lid is compared to

the earlier version in Figure 4.10. Using the revised 100 µm lid 92.7 % (±1.7 %) of the transmitted signal was retained over the 4-11 MHz frequency range. To maximise the signal for acoustic mapping this lid was used for subsequent experiments.

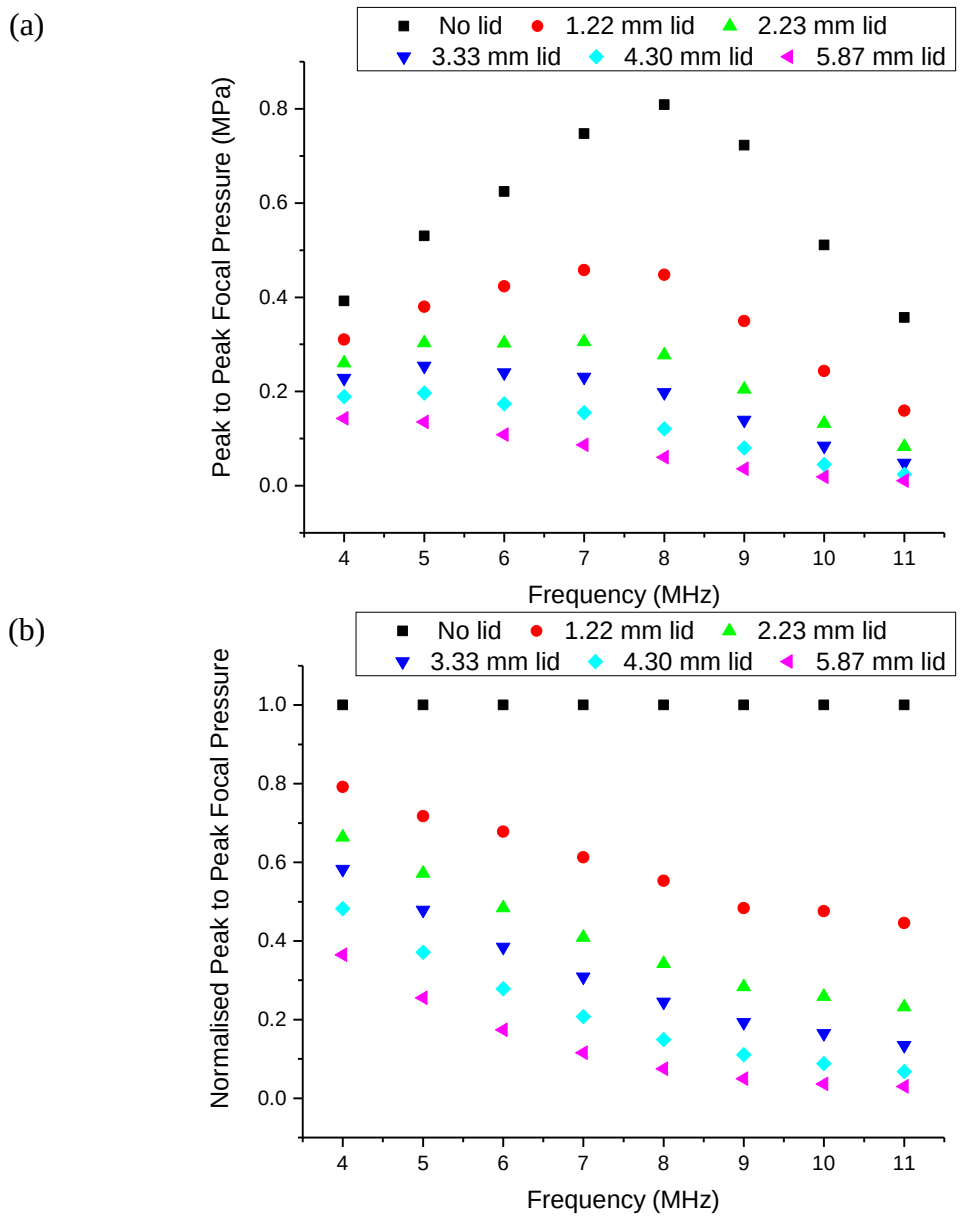


Figure 4.8: High frequency lid transmission performance. (a) Absolute and (b) normalised peak-to-peak focal pressure for different thicknesses of lid as a function of ultrasound frequency. Reproduced under Creative Commons licence from (Carugo *et al.*, 2015).

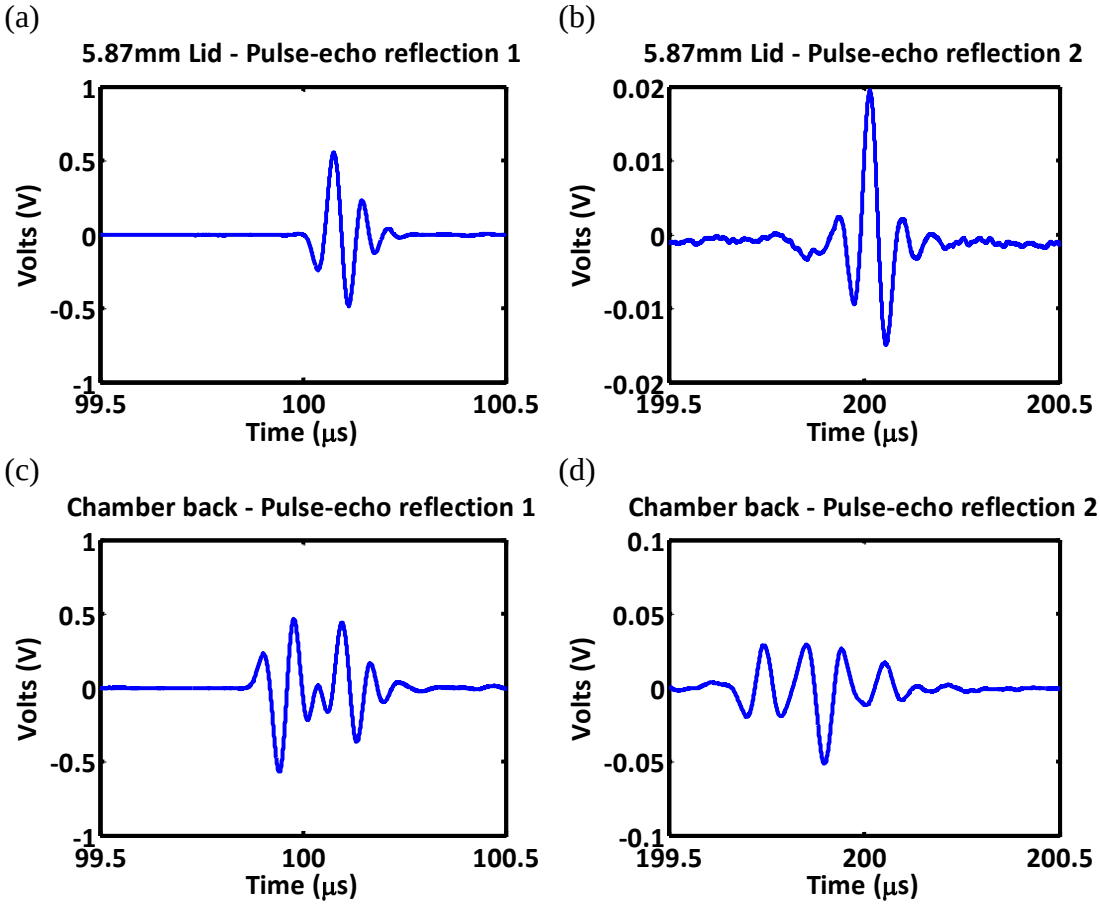


Figure 4.9: Pulse-echo waveforms used to estimate reflection coefficients (a,b) First and second reflections for a 5.87 mm thick lid. Ratio of peak-to-peak voltages gives a reflection coefficient of 0.033. (c,d) First and second reflections for the back of the cell culture chamber. Ratio of peak-to-peak voltages gives a reflection coefficient of 0.078.

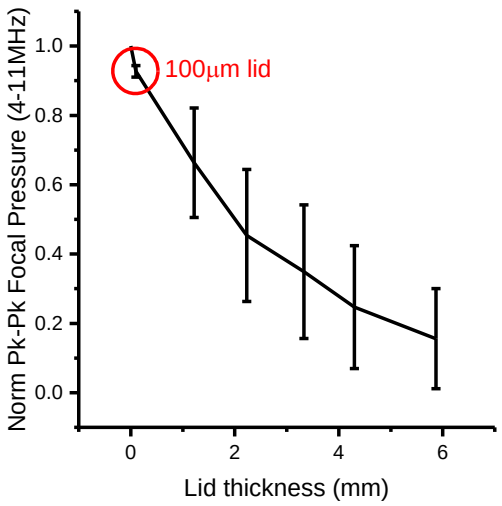


Figure 4.10: Revised 100 µm lid characterisation. Mean and standard deviation of peak-to-peak focal pressure over the 4-11 MHz frequency range are shown. Using the revised 100 µm lid design 92.7 % (±1.7 %) of the transmitted signal was retained.

## 4.3.2. Fluorescent siRNA MMB model

Fluorescence and acoustic results for fluorescent siRNA delivery experiments using magnetic microbubbles (F-MMB) are shown below.

### 4.3.2.1. Fluorescence imaging

Fluorescence measurements over the whole seeded area in the OptiCell™ chambers taken using an automated plate reader are shown in Figure 4.11. In samples treated with F-MMB without ultrasound (with or without magnet) and with F-MMB and ultrasound (without magnet) a homogeneous background fluorescence signal with low amplitude was observed. In the sample which was treated with F-MMB, ultrasound, and magnet (sample 3) discrete areas of increased fluorescence were observed, corresponding to 3 out of the 6 treated locations in the sample. These results suggest that under the combined effects of ultrasound and a magnetic field the cells were transfected with fluorescent siRNA. That only a subset of the treated locations shows transfection is likely to be due to uneven distribution of MMBs in the sample and progressive destruction of MMBs on the 6 treatments per sample.

To confirm that the fluorescence observed on the plate reader was emitted by the cells (and not due to other components such as the microbubbles) microscope images were also obtained at each of the 6 treated locations per sample. Representative images from each sample are shown in Figure 4.12. In agreement with the plate reader results, only minimal background fluorescence was observed in samples 1, 2 and 4 (the blurry, out of focus areas in sample 4 are likely to be residual buoyant microbubbles trapped within the OptiCell™), while in sample 3 (treated with F-MMB, US and magnet) fluorescence of the cells is clearly visible.

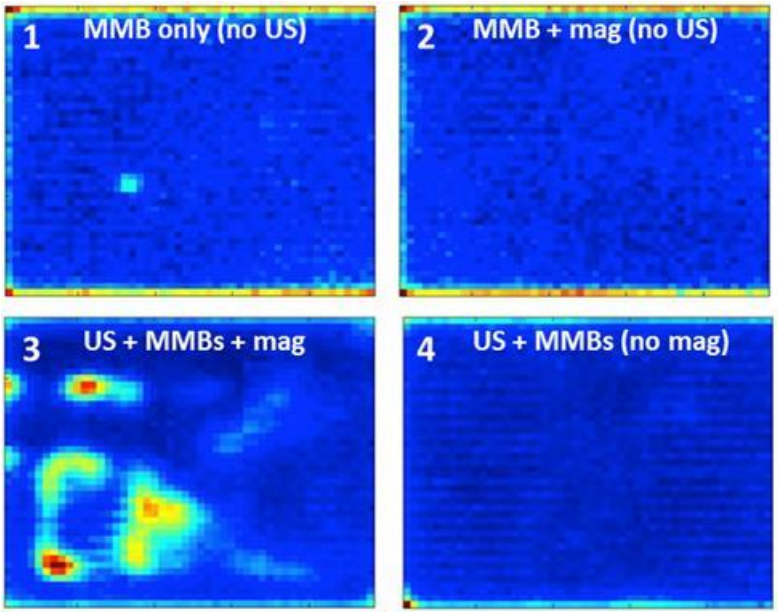


Figure 4.11: Fluorescence data for F-MMB transfection experiment using the fluorescence model, reproduced from (Owen, 2015)[22]. Scans of fluorescence intensity over the area of the cell chamber are shown. Samples 1 and 2 were treated with F-MMB (no ultrasound), without and with magnet and show negligible increase in fluorescence; 3 and 4 were treated with F-MMB and ultrasound with and without magnet.

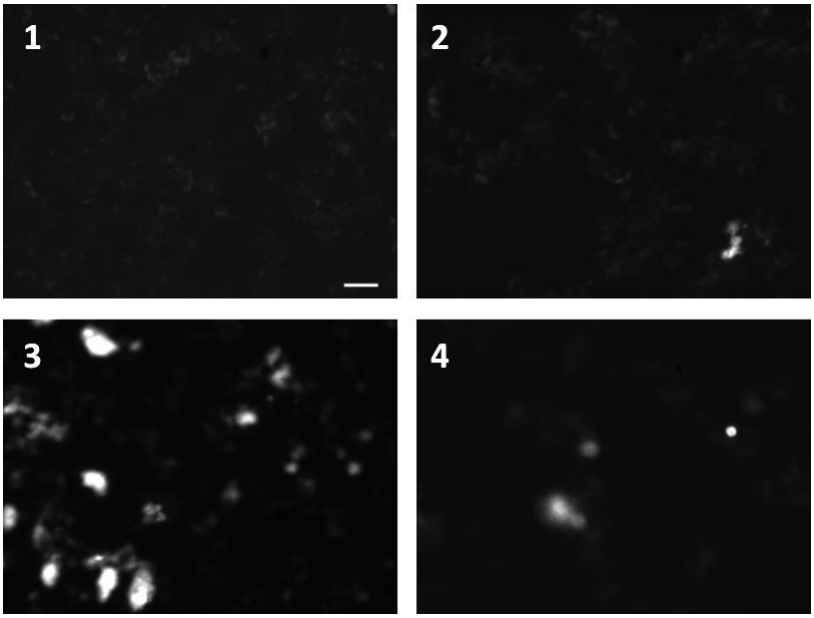


Figure 4.12: Fluorescence images for F-MMB transfection experiment using the fluorescence model, reproduced from (Owen, 2015)[22]. Fluorescence microscope images are shown using FITC filter, 2 s exposure and 10 × objective. Samples 1 and 2 were treated with F-MMB (no ultrasound), without and with magnet and show negligible increase in fluorescence; 3 and 4 were treated with F-MMB and ultrasound with and without a magnet.

[22] Fluorescence measurements and imaging conducted by Joshua Owen

The fluorescence microscope results are summarised in Figure 4.13 which shows the mean and standard deviation of the microscope images taken at each of the 6 locations per sample. An additional sample showing the fluorescence of F-MMB alone (before US treatment) is also included, and shows similar intensity to the background cell fluorescence. The mean fluorescence intensity using F-MMB, US and magnet was increased by approximately a factor of 4 compared to the control run with cells + F-MMB only. The large standard deviation on this sample is due to response only occurring in 3 out of 6 treated locations as was also observed using the plate reader. As discussed above this is likely to be due to uneven distribution of F-MMB and progressive destruction over the 6 treatments per sample. The revised cell chamber design used in later experiments aimed to eliminate some of these issues encountered with the OptiCell™.

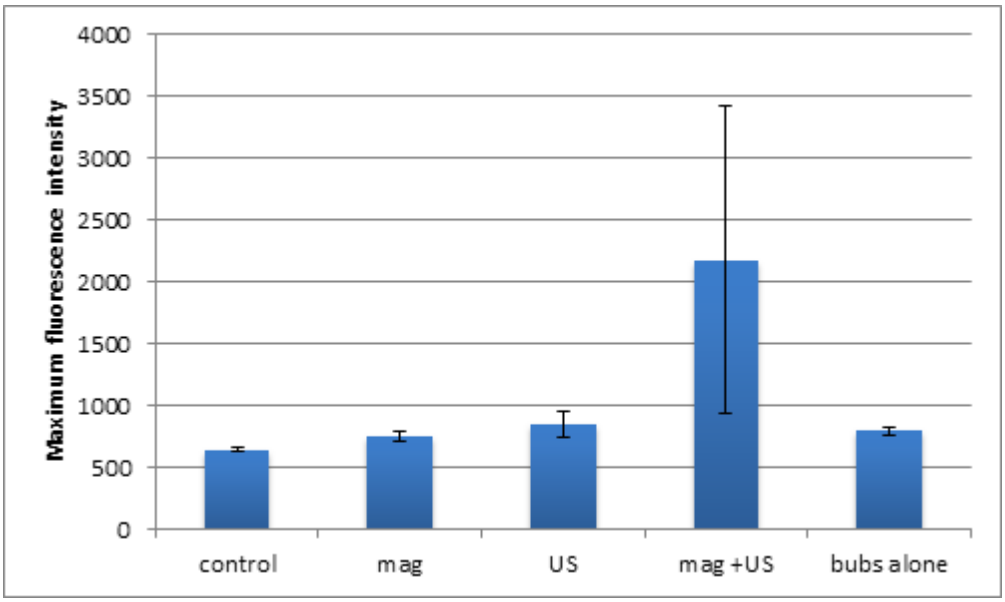


Figure 4.13: Analysis of fluorescence data for F-MMB transfection experiment using the fluorescence model, reproduced from (Owen, 2015)[23]. 'Control' represents cells treated with F-MMB only, all other samples were treated with F-MMB and magnet/US as indicated. 'Bubs alone' represents F-MMB only without cells.

[23] Fluorescence imaging conducted by Joshua Owen

#### 4.3.2.2. Passive acoustic mapping

Acoustic maps showing the emissions from each of the ultrasound-treated samples are shown Figure 4.14. An additional sample containing cells and media without F-MMB was also included. In each sample maps showing the distribution of acoustic emissions in space (summed over all of the pulses recorded per treatment) are displayed, with the 6 treatments per sample arranged corresponding to their position in the OptiCell$^{TM}$, with the order of successive treatments shown by the arrows. The focus of the HIFU transducer (and region in which cavitation is expected) is located approximately in the centre of each map.

In the sample without F-MMBs negligible cavitation was observed at all 6 locations (maximum energy 0.90 μJ), suggesting that the ultrasound pressure used here was below the cavitation threshold for cells and media in the absence of exogenous cavitation nuclei. When F-MMB were added without a magnet a large increase in cavitation was observed over all 6 of the treated locations (maximum energy 30.9 μJ), while when adding a magnet the maximum energy of cavitation more than doubled (maximum energy 67.7 μJ). Notably, in the absence of magnetic targeting cavitation appears to be relatively evenly distributed over the area of the sample, while when the magnet was added cavitation was more localised. Cavitation in the locations treated first was of greater amplitude than those without targeting and showed a pronounced decline on subsequent exposures. Comparison of the F-MMB + US + magnet run to the fluorescence readings obtained from the plate reader in the same sample (Figure 4.11) shows reasonable correlation between areas of high fluorescence and those of higher cavitation response.

These results are summarised over the 6 treatment locations per sample in Figure 4.15. In the sample without MMB cavitation energy was consistently low over the 6

exposures (mean 0.87 ± 0.02 µJ) due to the lack of cavitation nuclei. In the sample with F-MMB + US (without magnet) the energy of cavitation increased by a factor of 25 (mean 22.2 ± 5.5 µJ). In the sample with F-MMB + US + magnet the mean cavitation energy increased by a further 1.7 times (mean 38.0 ± 24.7 µJ) over the non-magnet case while the maximum energy of cavitation more than doubled (67.7 vs 30.9 µJ).

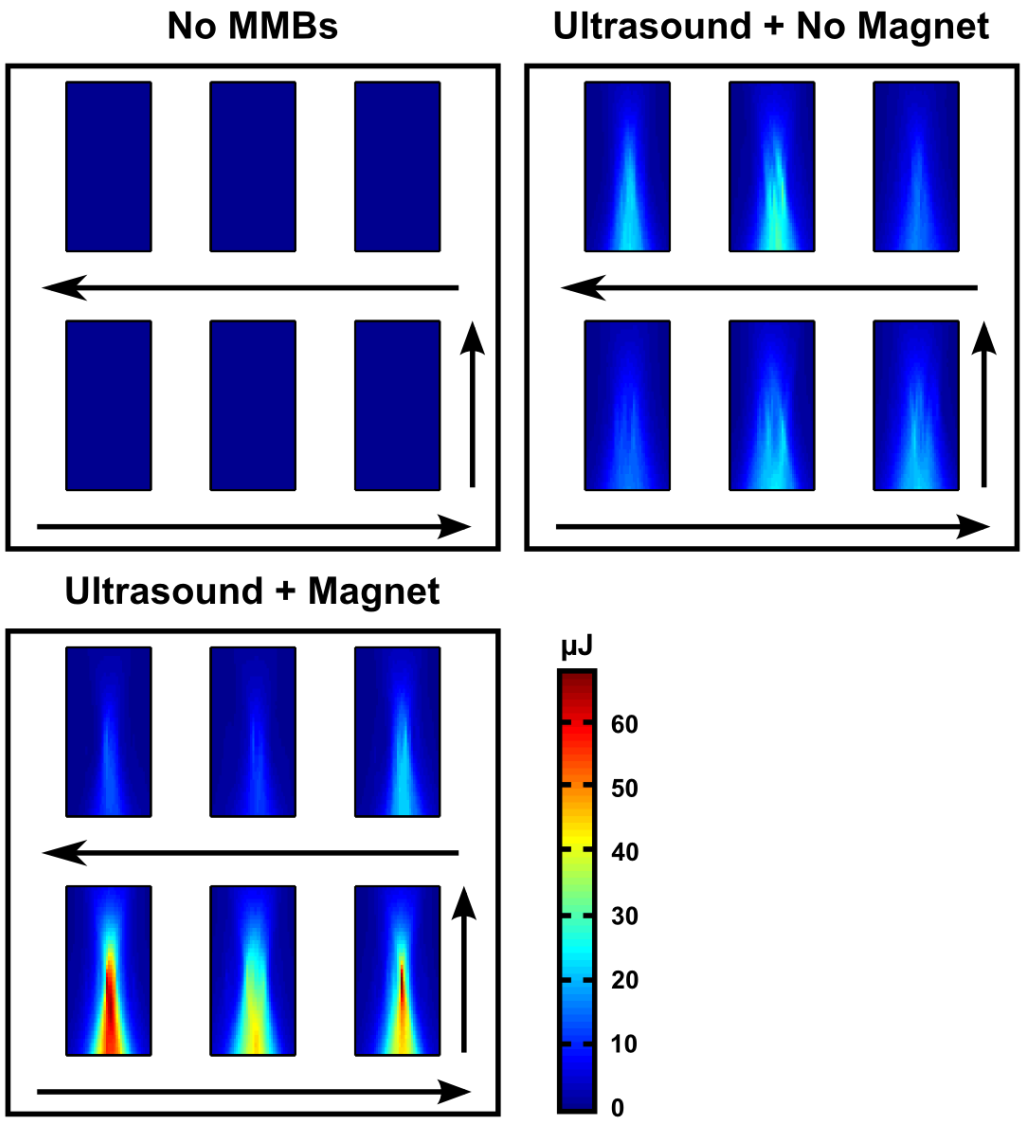


Figure 4.14: PAM data for F-MMB transfection experiment using the fluorescence model. Each sample was treated 6 times in the order indicated by the arrows, PAMs are oriented to show a cross section through the sample as indicated in Figure 4.3. Each map shows a region of interest of ±10 mm transverse and ±20 mm axial with respect to the focus of the HIFU transducer and the centre of the magnetic array (corresponding to the maximum force), which is located approximately in the middle of the maps. Colourbar represents energy.

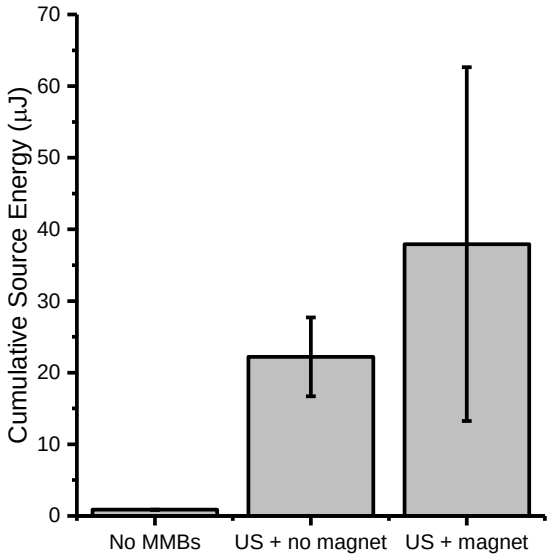


Figure 4.15: Summary of PAM data for F-MMB transfection. The mean and standard deviation of the maximum cavitation energy in each of the 6 treatment locations per sample are shown.

These results suggest that the fluorescent-tagged siRNA MMB were able to transfect cells under the influence of ultrasound and a magnetic field. Control experiments in which either of these factors were omitted showed negligible increase in fluorescence. Acoustically, PAM data from these experiments correlates well with the observed bioeffect, and helps to illustrate the synergistic effects of F-MMB, ultrasound and the magnetic field – while adding F-MMB without a magnet did result in an increase in cavitation, this was insufficient to result in transfection, most likely because F-MMB were not sufficiently close to the cells without the influence of the magnet.

Limitations in this study include the use of OptiCell$^{TM}$ chambers, the large size of which makes achieving microbubble distribution difficult and can result in cell damage or detachment during filling. The fluorescent siRNA model is also of limited clinical relevance as it only demonstrates delivery and not a therapeutic effect. In the following sections an improved cell chamber and biologically active agents are tested.

## 4.3.3. Knockdown siRNA MMB model

The results of knockdown siRNA loaded MMB experiments are shown below.

### 4.3.3.1. B-mode imaging

Representative B-mode images from each of the experimental conditions prior to treatment are shown in Figure 4.16. In the samples containing water only (Figure 4.16a) and with cells, media and free siRNA (Figure 4.16b) the PDMS lid, cell chamber and magnet surface may be seen (an annotated B-mode image is shown in Figure 4.4 for reference). When K-MMB or S-MMB were added (200 µL per sample) either with or without a magnet (Figure 4.16c, e, f) an increase in the image intensity within the sample chamber is observed due to the contrast-enhancing effect of the microbubbles, in particular towards the upper edge of the chamber just below the lid surface. This is likely to be due a subpopulation of buoyant microbubbles which were not all retained by the magnet (a layer of magnetically retained microbubbles was visually apparent on the bottom of the chamber, as in Figure 4.4b). The magnet surface towards the bottom of each image was also no longer visible due to attenuation of the ultrasound by the layer of microbubbles. When the microbubble concentration was halved (Figure 4.16d) these effects were less pronounced and the bottom of the chamber remained visible.

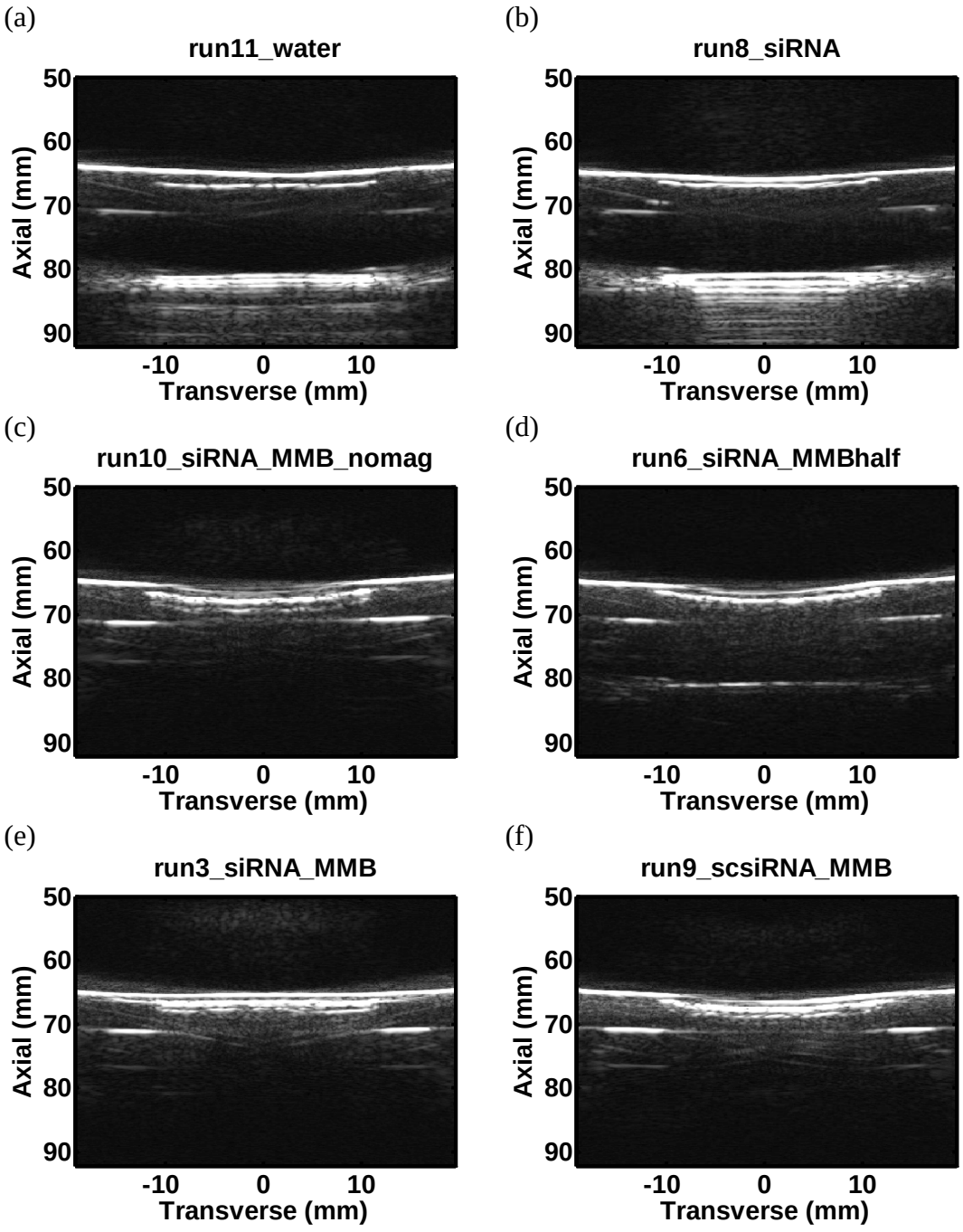


Figure 4.16: B-mode images for K-MMB experiments. Conditions are (a) Water only, (b) free siRNA, (c) K-MMB (200 µL), no magnet, (d) K-MMB (100 µL) + magnet, (e) K-MMB (200 µL) + magnet, (f) S-MMB (200 µL) + magnet

#### 4.3.3.2. Passive acoustic mapping

Passive acoustic mapping data for the various experimental conditions are shown in Figure 4.17. Passive acoustic maps summed over the duration of each experiment are shown overlaid on the pre-exposure B-mode images for each of the experimental conditions.

Using water (Figure 4.17a) or free siRNA (Figure 4.17b) negligible background cavitation was observed as expected (maximum energy 19.0 and 21.8 μJ respectively). When K-MMB were added without a magnet (Figure 4.17c) cavitation was observed with a maximum amplitude of approximately 3 times the baseline experiments (maximum energy 62.1 μJ), extending spatially in the axial (vertical) direction throughout the height of the chamber. When magnetic targeting was added using K-MMB at low or high concentration or S-MMB (Figure 4.17d-f) the amplitude of cavitation increased by approximately 3.5 times compared to the non-targeted case (maximum energy 230.7, 204.8, 201.5 μJ respectively) or around 10 times compared to the control experiments without K-MMB, with the focus of this activity located towards the bottom of the chamber close to the magnet. Notably, the amplitude of cavitation at the lower K-MMB concentration (230.7 μJ; Figure 4.17d) was actually slightly higher than that at twice the concentration (204.8 μJ; Figure 4.17e), perhaps due to the shielding effects also noted on B-mode imaging (Figure 4.16). Similar saturation/shielding effects at higher particle concentration were noted in nanodroplet characterisation experiments (Figure 4.23b). The spatial distribution and amplitude of cavitation using the control scrambled siRNA (S-MMB) (Figure 4.16f) was similar to that of the knockdown siRNA MMB (K-MMB) (maximum energy 204.8 vs. 201.5 μJ) as expected and suggests that this is a valid control in terms of acoustic behaviour.

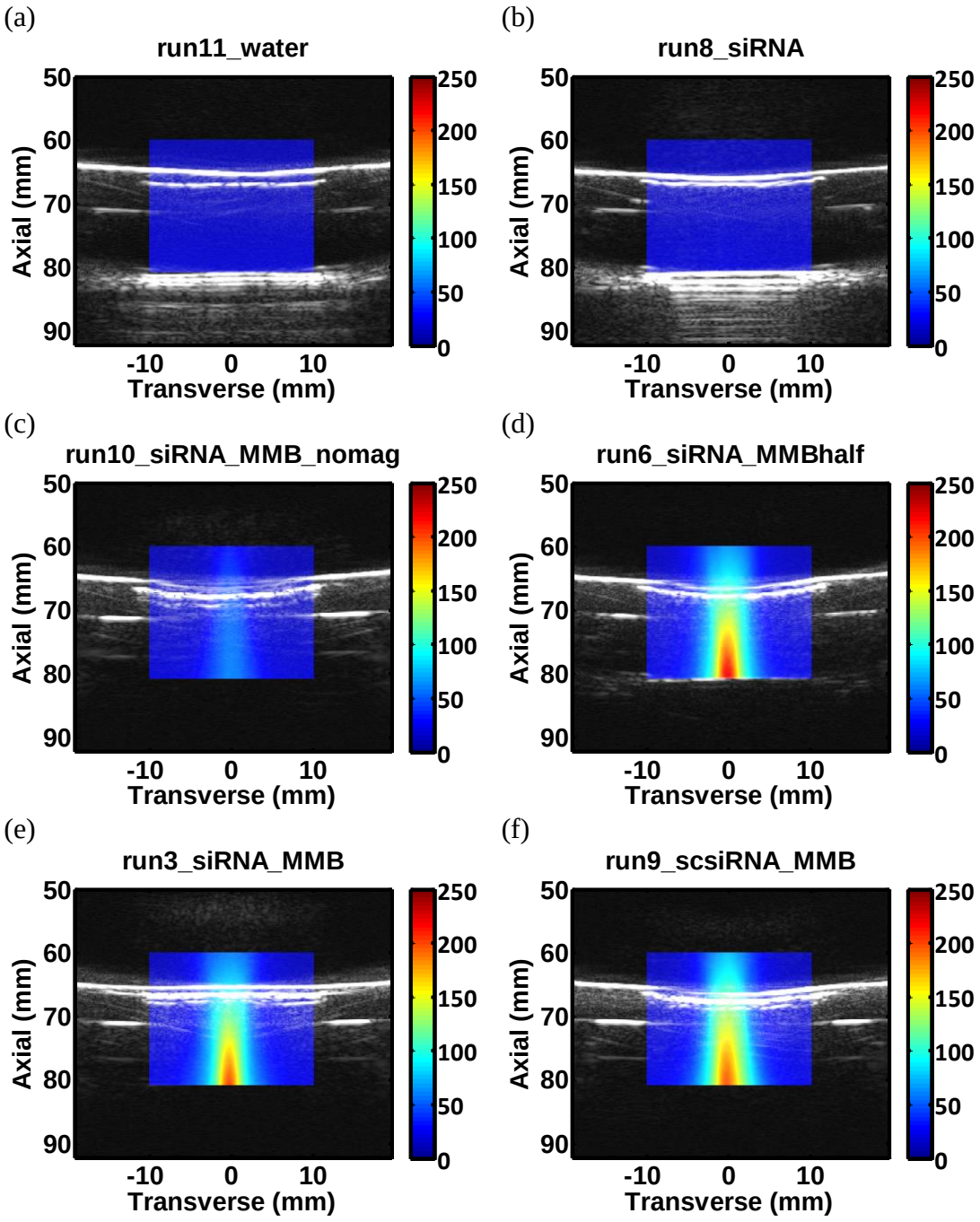


Figure 4.17: B-mode images with PAM overlay for K-MMB experiments. PAM images show sum of all 9 × 100 pulses per sample, overlaid with the B-mode image taken with the same probe prior to each experiment. Colourbars represent energy (µJ). Conditions are (a) Water only, (b) free siRNA, (c) K-MMB (200 µL), no magnet, (d) K-MMB (100 µL) + magnet, (e) K-MMB (200 µL) + magnet, (f) S-MMB (200 µL) + magnet

#### 4.3.3.3. Flow cytometry and cell viability

Flow cytometry and cell viability[24] results are shown in Figure 4.18 and Figure 4.19. Note that of the 3 repeats conducted for each experimental condition only those with the highest cell viability per condition were included for analysis (all showed viability > 70 %). The reasons for low viability (as low as 14.7 %) in the remaining runs are not yet clear, and may be due to numerous factors (besides the effects of siRNA, ultrasound and microbubbles) such as prolonged removal from the incubator during experiments, introduction of infectious agents when the cells were returned from the water tank to the incubator or other effects which might affect cell proliferation during the 24 hour delay between treatment and analysis.

The flow cytometry data in Figure 4.18 shows two peaks: the higher fluorescence intensity peak on the right corresponding to normal cells, the lower-intensity peak on the left corresponding to those with lower fluorescence (i.e. in which knockdown has occurred). Using cells only (no siRNA), free siRNA, K-MMB without a magnet, or scrambled siRNA (S-MMB) (Figure 4.18a, b, c, f respectively) negligible knockdown was observed (i.e. the right-hand peak greatly exceeds the size of the left-hand peak). When K-MMB were used with magnetic targeting at either 200 µL or 100 µL per sample fluorescence knockdown was observed, as shown by the increase in the left-hand peak of the distribution. Interestingly, the effect appeared greater in the sample treated at higher concentration, despite a slightly lower cavitation energy – this may indicate that the acoustic emissions recorded were an underestimate of the true intensity of cavitation due to shielding, or could simply be due to this sample containing twice the dose of siRNA (since this was bound to the bubbles). Future experiments could vary the siRNA dose added to the microbubbles (in addition to varying the volume of microbubble solution used in the experiments) to decouple these two effects.

[24] Flow cytometry and viability measurements performed by Jeong Yu Lee

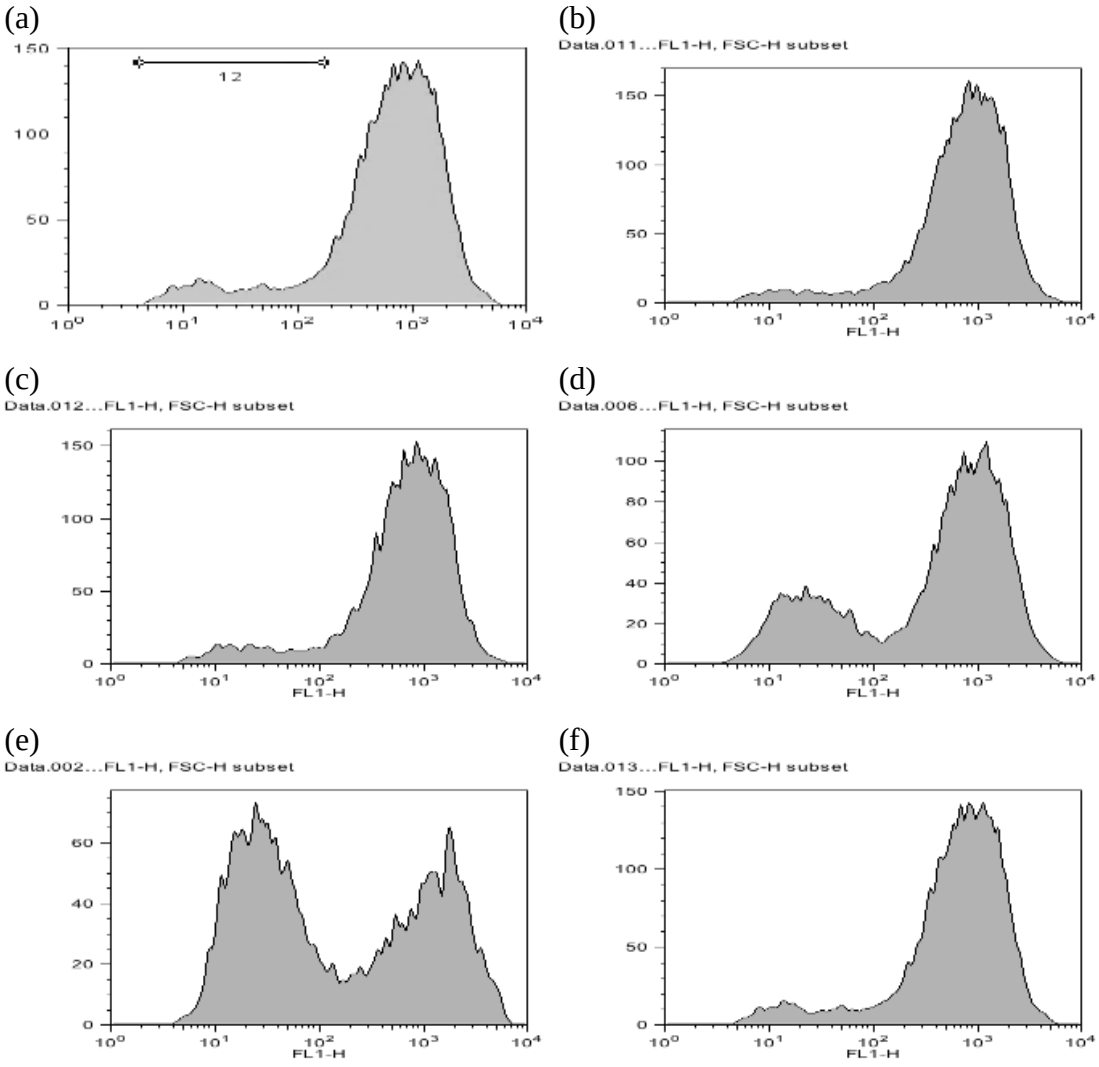


Figure 4.18: Flow cytometry data for K-MMB experiments[25]. The runs with highest cell viability from each of the 3 repeats per condition are shown. Flow cytometry data for (a) Control (cells only), (b) free siRNA, (c) K-MMB (200 µL), no magnet, (d) K-MMB (100 µL) + magnet, (e) K-MMB (200 µL) + magnet, (f) S-MMB (200 µL) + magnet. x-axis represents fluorescence intensity, y-axis represents cell count

[25] Flow cytometry and viability measurements performed by Jeong Yu Lee

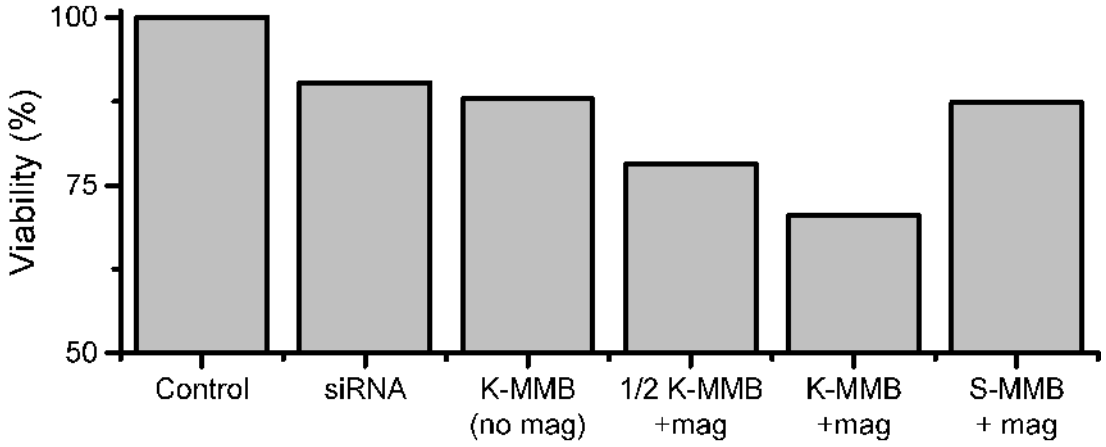


Figure 4.19: Viability data for K-MMB experiments[26]. Only runs with viability > 70 % were included for analysis. Viability measurements for the 6 cases from a colorimetric assay are shown. Results are normalised relative to the control (untreated) sample. K-MMB and S-MMB treated runs used 200 µL per sample, except '1/2 K-MMB+mag' which used 100 µL.

Viability data for the runs included for analysis are shown in Figure 4.19 and are normalised with respect to the control (untreated) sample. Using free siRNA, K-MMB without magnet or scrambled siRNA (S-MMB) viability was close to 90 % (90.3, 87.9, 87.3 % respectively). Using K-MMB with magnetic targeting at the two concentrations viability fell to 78.1 % and 70.5 % respectively.

From a biological perspective this trend in viability is of some concern, as it appears to be correlated with treatment efficacy (Figure 4.18), suggesting that the drop in viability is due to the effects of the knockdown siRNA itself. However, this thesis primarily concerns the development of magnetic targeting and passive acoustic mapping (the therapeutic agent under consideration being quite secondary). From this perspective the high viability observed using the scrambled siRNA control (S-MMB) under the same acoustic and magnetic conditions is highly encouraging as this further reinforces that the drop in viability was not primarily due to the ultrasound, magnetic field or microbubbles, but due to the therapeutic agent itself.

[26] Flow cytometry and viability measurements performed by Jeong Yu Lee

## 4.3.4. Paclitaxel nanodroplets model

In this section the cell viability, flow cytometry and acoustic mapping results from the Paclitaxel-loaded magnetic nanodroplet delivery experiments are presented.

### 4.3.4.1. Cell viability

Paclitaxel is a tumour-inhibiting drug (Wani *et al.*, 1971), so the expected effect on cancer cells is reduced viability. Due to the mechanism of action of the drug (Section 2.4.2) a 24 hour delay between treatment and measurement is required to allow for completion of the cell cycle.

Viability results measured 24 hours after PTX-MND experiments are shown in Figure 4.20. Results are normalised with respect to the mean value for the untreated control sample. Using free paclitaxel viability was not significantly reduced compared to the control sample (reduction of 9.1 ± 18.8 %, $p = 0.52$). Small increases in mean cell kill were observed using PTX-MNP and MND, of 14.5 ± 3.5 % and 18.4 ± 7.1 % respectively, perhaps due to the physical effects of the ultrasound and magnetic field, but these were not significant compared to the control sample ($p = 0.18$ and $p = 0.12$ respectively). However, using PTX-MND a large and significant ($p < 0.01$) reduction in viability of 45.7 ± 4.6 % was observed. Compared to free paclitaxel, mean cell kill at 24 hours was increased by a factor of 5 (45.7 % vs 9.1 %).

These results suggest that the synergistic effects of ultrasound, magnetic field and paclitaxel-carrying nanodroplets greatly increased the efficacy of treatment. To further evaluate the effects of treatment on the cells microscope images and flow cytometry analysis were conducted.

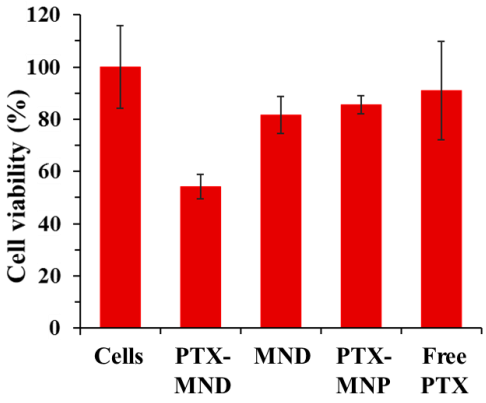


Figure 4.20: Viability results for Paclitaxel-loaded nanodroplets experiments,[27] reproduced under Creative Commons licence from (Lee *et al.*, 2015). The viability of cells 24 hours following treatment for untreated cells and those treated with US + PTX-MND, MND, PTX-MNP or free paclitaxel (at an equivalent drug concentration of 1 µg/mL) are shown.

### 4.3.4.2. Microscopic and flow cytometry analysis

Microscope image and flow cytometry data for the PTX-MND experiments are shown in Figure 4.21. Cell shrinkage and morphological (shape) changes typical of apoptosis (Taylor *et al.*, 2008) were particularly observed using PTX-MND (Figure 4.21a), in addition to reduced cell number. Some cell shrinkage was also observed using PTX-MNP, but to a lesser degree than the nanodroplets, perhaps due to the increased cavitation (discussed below). In addition using MND (no PTX) some blebbing cells and debris were observed, perhaps due to the physical effects of cavitation and accounting for the small increase in cell kill discussed above.

Flow cytometry data for the experiments are shown in Figure 4.21b, where the x-axis represents fluorescence intensity and the y-axis cell count. As the cells were stained with the (nuclear DNA) stain propidium iodide the fluorescence intensity indicates the amount of DNA in the cell. Within these plots up to three peaks are expected corresponding to different places in the cell cycle (Section 2.4.3.1): the left-most ‘sub-G1’ peak indicating cells that contain less than the normal amount of DNA

[27] Measurements performed by Jeong Yu Lee

(of cells in the G1 stage of the cell cycle); the middle ‘G1’ peak corresponding to these normal cells in the G1 stage (before DNA replication), and the rightmost ‘G2’ peak corresponding to normal cells in the G2 stage (after DNA replication). The sub-G1 population may include damaged or otherwise abnormal cells such as those undergoing cell death.

The percentage of the cell count in the sub-G1 peak therefore indicates treatment efficacy. The size of the sub-G1 peak for free PTX was similar to that of the untreated control sample (6.31 % and 6.23 % respectively), which agrees with the insignificant change in viability and microscope images discussed above. Using PTX-MNP and MND the percentage of sub-G1 cells was increased by a factor of 1.77 and 1.86 respectively compared to the control sample (to 11.0 % and 11.6 % respectively), which is in agreement with the small changes in viability and morphology discussed above. However, using PTX-MND the percentage of sub-G1 cells increased by a factor of 4.24 compared to the control sample (compared to factor of 5 increase in cell kill). This again suggests that the combined treatment greatly increased efficacy. It is important to note that the viability and flow cytometry measurements are based on analysis of each cell chamber as a whole (including cells which may not have been at the ultrasound focus), as such these results may be an underestimate of the true effect.

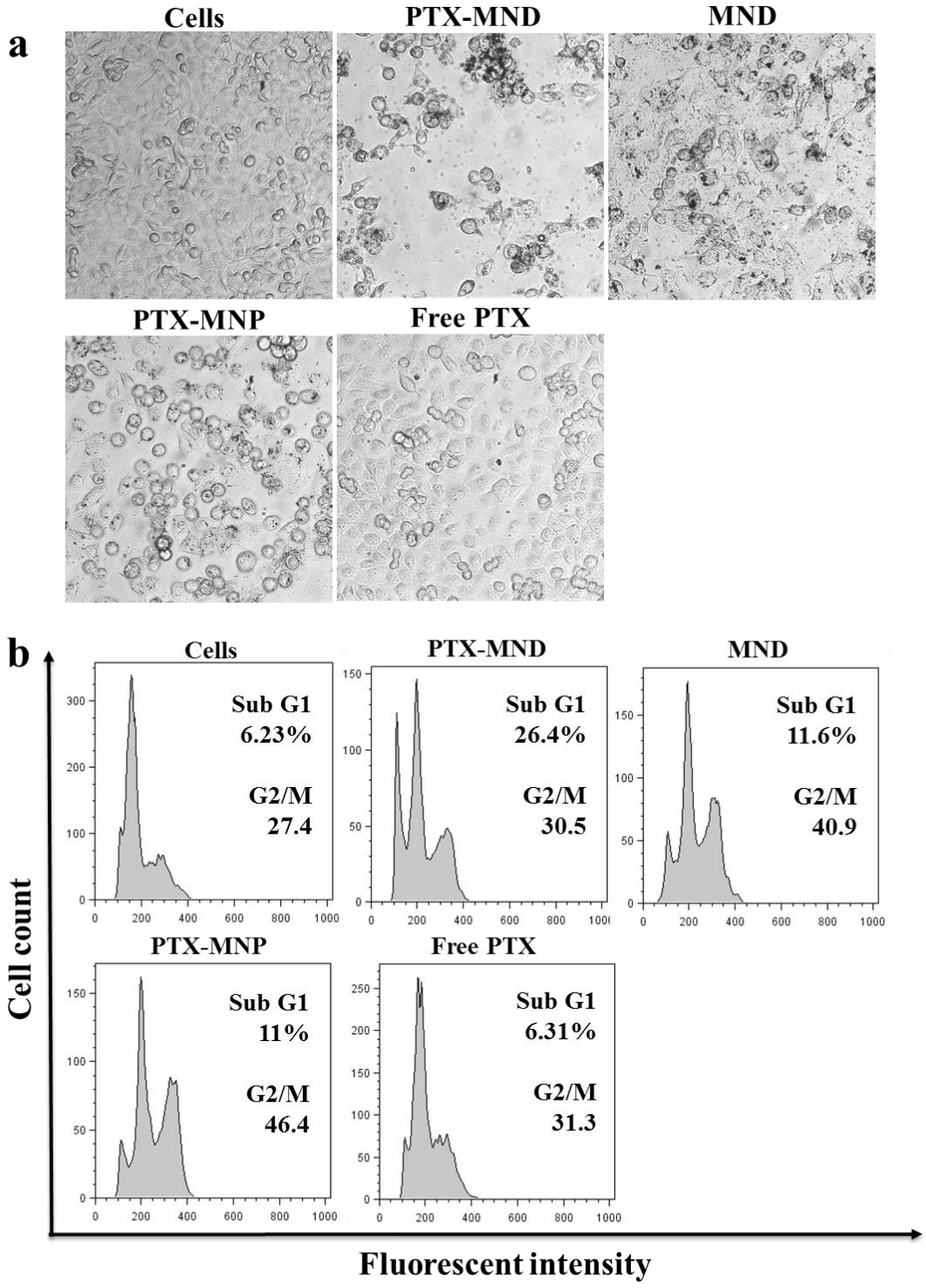


Figure 4.21: Microscope and flow cytometry results for PTX-MND experiments,[28] reproduced under Creative Commons licence from (Lee *et al.*, 2015). (a) Bright field images and (b) flow cytometric analysis of the cell cycles of untreated MCF-7 cells and those treated with US + PTX-MND, MND, PTX-MNP or free paclitaxel (at an equivalent drug concentration of 1 μg/mL).

[28] Measurements performed by Jeong Yu Lee

#### 4.3.4.3. PAM analysis

PAM data for the PTX-MND experiments are shown in Figure 4.22. The evolution of cavitation activity was measured over time, expressed as the maximum cavitation power from each recording. The averaged spectra for the emissions were also calculated in each experiment. An annotated B-mode image as seen by the monitoring probe (Figure 4.22a) shows the sample holder, magnet and PDMS lid described previously (Section 4.2.1). Passive acoustic maps showing the sum of all frames from each experiment (units of energy in μJ) for the samples with different acoustic properties (free PTX, PTX-MNP and PTX-MND) are shown, overlaid on pre-exposure B-mode images (Figure 4.22b-d). Using free PTX (no MND or MNP) the energy distribution was approximately uniform (max value 6.9 μJ) and represents the baseline signal level for the system due to background cavitation of the media, reflections from the magnet and electrical noise. As a result, the time trace and spectra within the frequency range of the probe were both approximately flat (Figure 4.22e-f, blue lines). When the cells were treated with PTX-MNP, a small increase in the PAM signal was observed. Consequently, the map was no longer uniform, with a small peak visible towards the location of the HIFU focus (max value 7.5 μJ; 8.9 % above free PTX) (Figure 4.22c). The corresponding time trace (Figure 4.22e, green line). showed that this was primarily due to increased cavitation in the first frame of ultrasound data. Finally, with PTX-MND a more pronounced increase in cavitation energy was observed (max value 10.6 μJ; 53.1 % above free PTX), which was maintained above baseline for the duration of the monitoring period (Figure 4.22e, red line). The corresponding spectra (Figure 4.22f, red line) showed the pronounced harmonic and ultraharmonic peaks suggestive of non-inertial cavitation, as well as an increase in the broadband signal level associated with inertial cavitation (Leighton, 1994). These results imply that these ultrasound conditions were sufficient to trigger vaporisation of the

nanodroplets into bubbles whose acoustic response was sufficient for them to be observed using PAM.

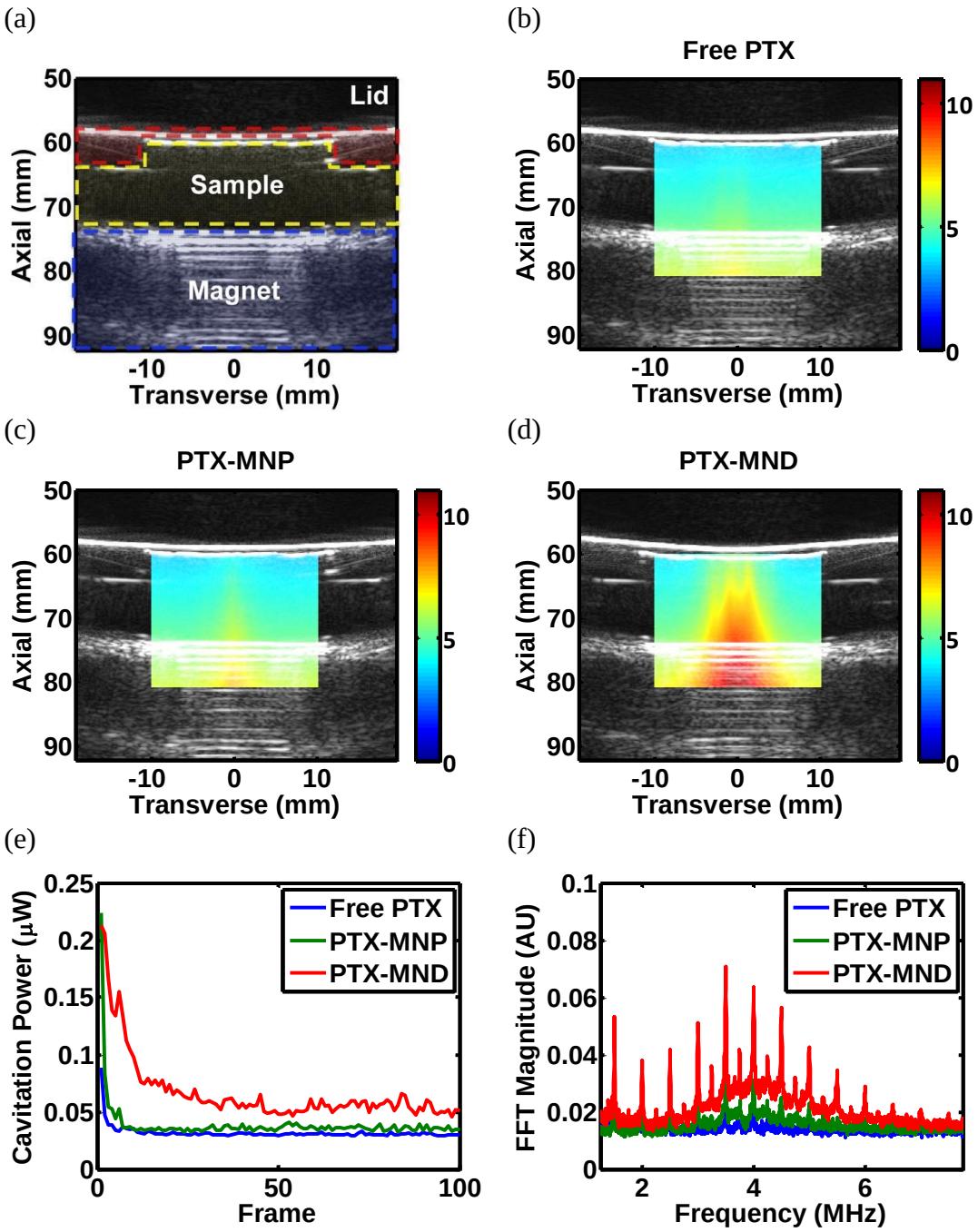


Figure 4.22: PAM results from paclitaxel loaded nanodroplet experiments, reproduced under Creative Commons licence from (Lee *et al.*, 2015). (a) Annotated B-mode image showing sample chamber, magnet and lid as seen from the imaging array. (b-d) Pre-exposure B-mode images with PAM overlay showing sum of all frames for each exposure for (b) free PTX, (c) PTX-MNP and (d) PTX-MND. Colour bars represent total cavitation energy (μJ). (e-f) Evolution of cavitation activity over time and spectra for the first exposure from each sample. (e) Maximum cavitation power (mW) from each frame of PAM data. (f) Fast Fourier transform (FFT) magnitude (arbitrary units (AU)) of the reconstructed PAM signal from the focal point.

## 4.3.5. Nanodroplet characterisation

In the previous section it was demonstrated that drug-loaded nanodroplets were able to induce bioeffects in terms of enhanced cell kill under the influence of ultrasound and a magnetic field. These experiments were conducted, however, using the same acoustic conditions used for the siRNA-loaded microbubble experiments and it was noted that the acoustic emissions from the nanodroplets were substantially lower (c.f. 10.6 μJ maximum energy in Figure 4.22d for PTX-MND, vs. 230.7 μJ in Figure 4.17 for K-MMB in the same setup). It was hypothesised that this was due to the different physical mechanisms – while the microbubbles represent gas-filled pre-existing cavitation nuclei, the droplets initially contain liquid and must first be vaporised into bubbles. To test this hypothesis (and with a view to optimising the experimental conditions for further *in vitro* and *in vivo* experiments with the nanodroplets) samples were excited under a range of acoustic conditions to characterise their response. The results are compared with those from the literature where appropriate, however previous studies typically measured only single parameters such as cavitation threshold as a function of the ultrasound conditions (Giesecke and Hynynen, 2003; Zhang and Porter, 2010) so were unable to fully capture the evolution of behaviour as a function of the acoustic conditions.

The results of the nanodroplet acoustic characterisation experiments are shown below.

### 4.3.5.1. Effect of nanodroplet concentration and comparison to SonoVue®

The effect of varying nanodroplet concentration on the resulting amplitude of cavitation activity is shown in Figure 4.23a. The cell chamber was filled with water (total volume ~8 mL) and a volume of MNDs added based on a 2-fold dilution series (100, 50, 25,… 3.12 μL; i.e. approximately 1.25, 0.6, 0.3,… 0.04 %). As expected the am-

plitude of cavitation increased with MND volume, following a linear relationship within the parameter space tested ($R^2 = 0.99$), reaching 2.5 ± 0.8 µJ at for a 100 µL sample. At the low end, using 3.12 µL MNDs the total cavitation energy of 0.77 ± 0.13 µJ (based on the sum of 300 pulses) is close to the noise floor reading for water only (0.66 ± 0.02 µJ) of the system under this configuration.

The corresponding results for different concentration suspensions of the commercial ultrasound contrast agent SonoVue® under the same conditions are shown in Figure 4.23b[29]. The range tested was extended down to 0.03 µL by pre-dilution of samples until the noise floor of the system was again reached. The amplitude of the acoustic emissions at a given concentration was found to be substantially larger using the pre-existing SonoVue® microbubbles by on average 321.1 (±162.9) times. This was as expected on account of the additional energy and hence time required to vaporise the nanodroplets. At the higher concentrations tested, the SonoVue® response appears to decline (reaching 140.4 ± 73.1 µJ at 100 µL, 55.6 × that of the 100 µL nanodroplets sample), suggesting saturation or shielding effects. At the lower-end, the response from 0.05 µL SonoVue® is within a similar range to that observed from a 100 µL sample of nanodroplets. It is important to note that these results reflect one set of exposure conditions. As discussed below, due to the need to vaporise the droplets other parameters such as the burst length have a pronounced effect on their response.

This is in agreement with previous work such as Giesecke and Hynynen (2003) which showed that the microbubble agent Optison® has a lower cavitation threshold than nanodroplet agents (albeit this was based on a threshold only; quantification of cavitation energy above the threshold was not conducted).

[29] SonoVue® was used as a comparison in these experiments instead of MMB as it is more stable over the timescale required (several hours) to conduct the numerous repeats under the different experimental conditions tested in this section

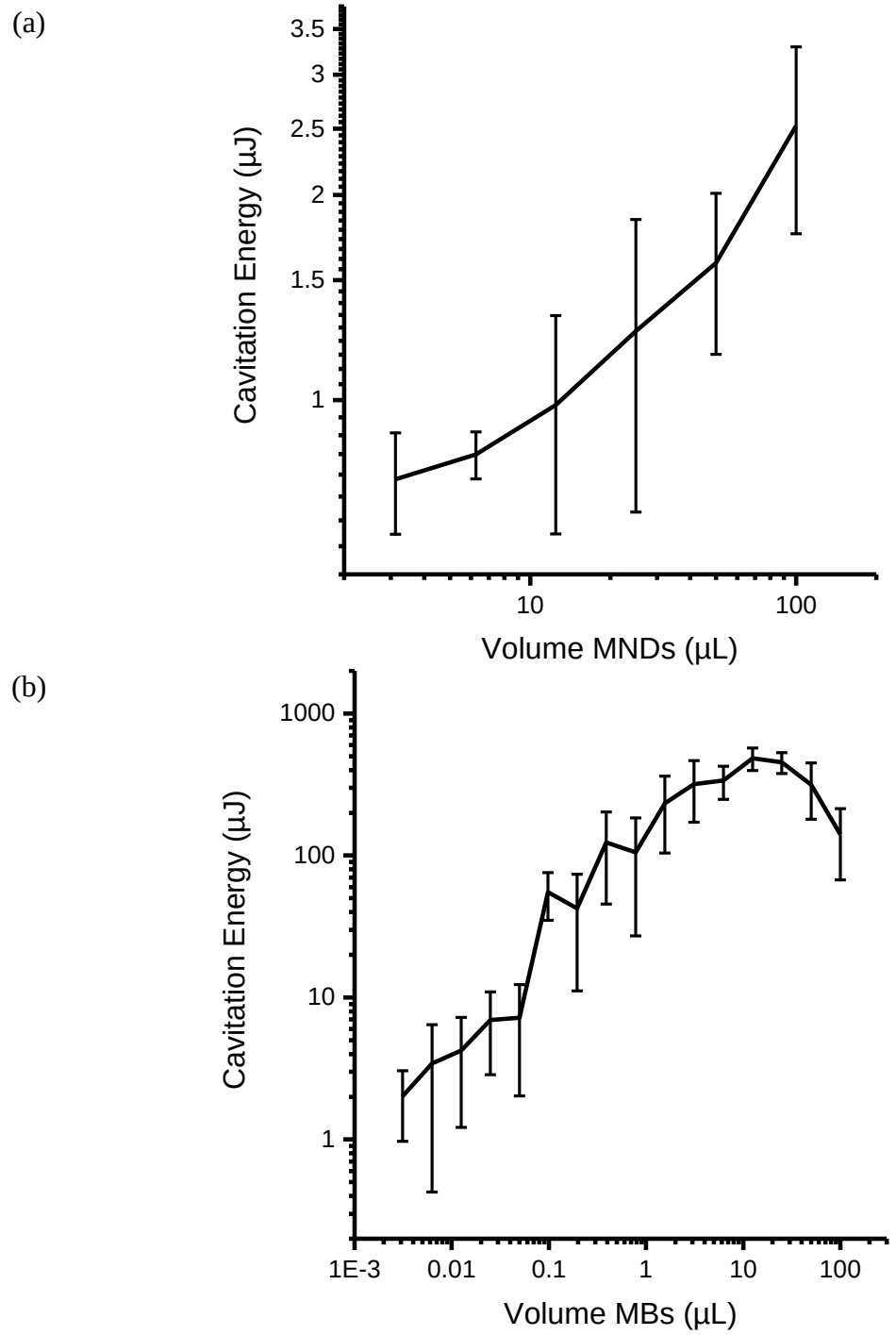


Figure 4.23: Volume ramp for (a) MNDs and (b) SonoVue® MBs. Each sample was exposed to ultrasound under the same conditions used in cell experiments (500 kHz, 1 MPa pk-pk, 40 cycles, 1 kHz PRF, 10 sec) 3 times. Error bars represent standard deviation over 3 samples per condition. In each case the volume specified was added to a cell chamber filled with water (total volume ~8 mL). Volumes less than 1 µL were measured by first diluting stock by a known factor (10 × or 100 ×).

### 4.3.5.2. Effect of prior sonication of nanodroplets

To test the hypothesis that the difference in response between nanodroplets and SonoVue® was primarily due to the presence of pre-existing microbubbles in SonoVue® (vs. only those bubbles formed during a pulse for nanodroplets), samples were tested with and without prior sonication using a low-frequency probe sonicator.

The total energy of cavitation emissions for 100 µL nanodroplets, previously sonicated nanodroplets or water control is shown in Figure 4.24. The response of the nanodroplet samples (4.6 ± 1.6 µJ) is within the range of the volume ramp experiments as expected, and is over 6.5 × the background signal for water. Using nanodroplets which had been previously sonicated the total energy of cavitation increased more than 7-fold over the un-sonicated sample (33.6 ± 14.0 µJ). The response is still lower that the 140.4 ± 73.1 µJ observed for SonoVue®, but now by a factor of 4.2 (vs. 55.6 previously); this may be due to differences in the microbubble structure or size distribution. These results are in agreement with previous work such as increased HIFU-induced temperature rise when a droplet vaporisation pulse was added (Zhang and Porter, 2010).

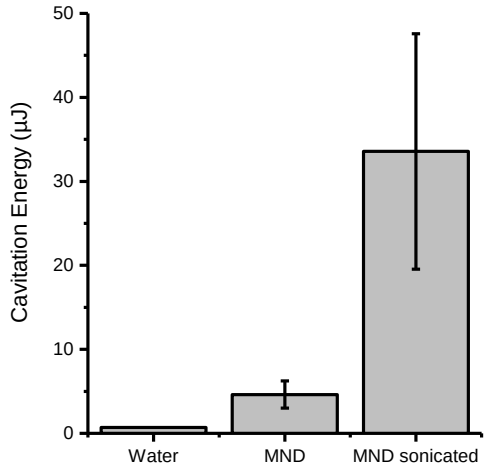


Figure 4.24: Effect of prior sonication on MNDs. Comparison between water only, MNDs and previously sonicated MNDs. Each sample (100 µL) was exposed to ultrasound under the same conditions used in cell experiments (500 kHz, 1 MPa pk-pk, 40 cycles, 1 kHz PRF, 10 sec) 3 times. Error bars represent standard deviation over 3 samples per condition.

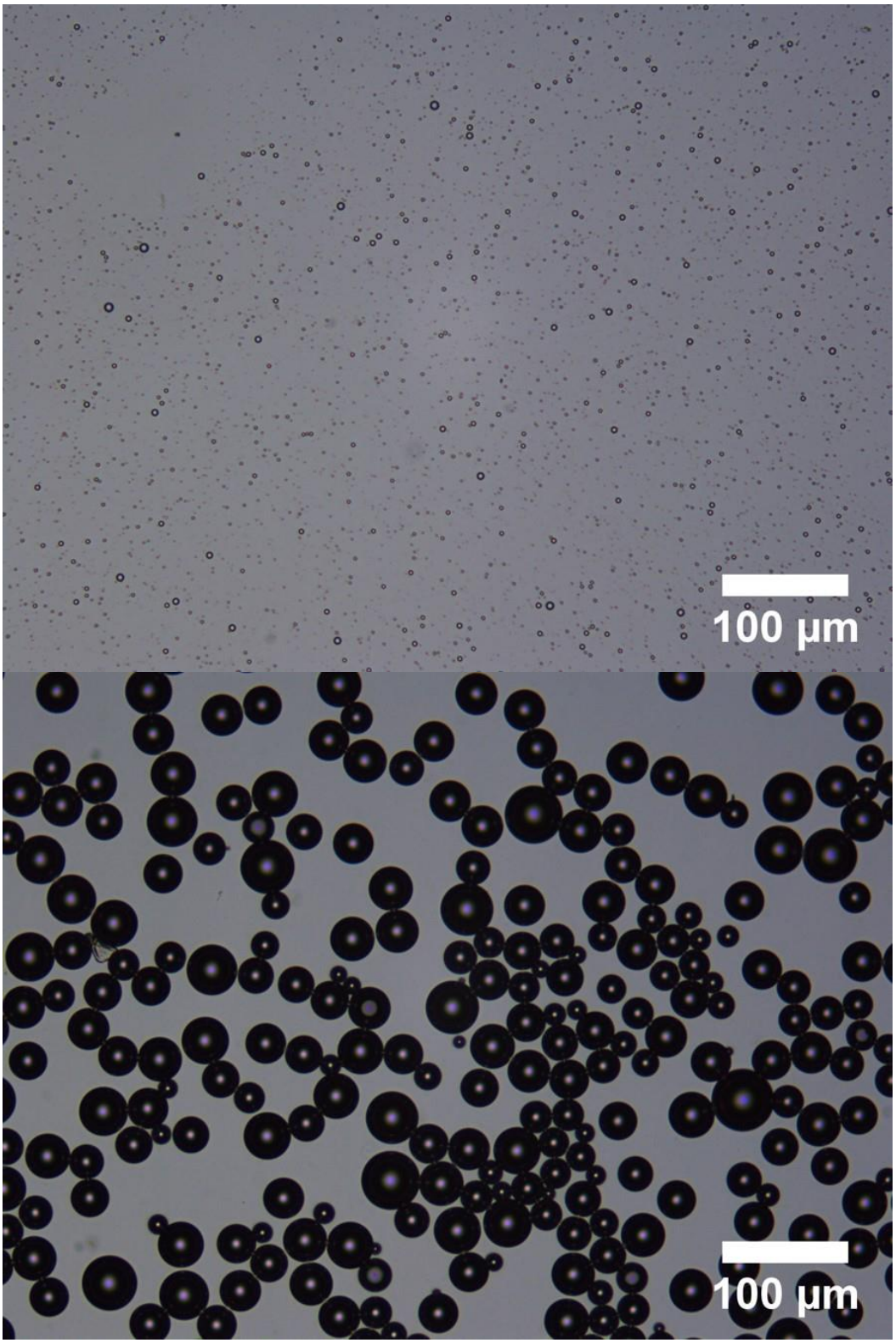


Figure 4.25: Microscope images of MNDs (a) pre and (b) post sonication. 10 % MNDs in water were sonicated for 30 seconds using the probe sonicator to vaporise the droplets into bubbles. The size distribution of the resulting microbubbles appears similar to that reported in previous work (Lee *et al.*, 2015).

To confirm that the sonicator probe did indeed result in conversion of nanodroplets into microbubbles samples were examined using an optical microscope. Images taken from samples containing 10 % MND in water without or with sonication are shown in Figure 4.25. While some larger droplets or small bubbles (maximum diameter of a few micrometres) are visible in the pre-exposure sample (Figure 4.25a), the transformation after exposure was immediately apparent by formation of visible foam which is revealed to be microbubbles in the post-exposure image (Figure 4.25b).

#### 4.3.5.3. Effect of pulse length on nanodroplets

To further investigate the hypothesis that nanodroplet vaporisation was the limiting factor in their acoustic response, the effect of pulse length was also tested. To enable comparison with previous results the length of the passively recorded samples for acoustic analysis was not varied, so increasing the burst length would not be expected to cause any increase in cavitation energy (since cavitation would merely continue after passive recording had stopped). However, increasing the burst length could cause vaporisation of a greater number of nanodroplets into microbubbles, which would then be present in the sample at the beginning of the next burst.

Figure 4.26 shows the cavitation energy recorded from a 100 µL sample of NDs (without prior sonication). To allow testing of longer bursts the pulse repetition frequency was reduced to 1 Hz. The pulse length was varied from 40 cycles (as per previous experiments, 0.008 % duty cycle at 1 Hz PRF) up to 400,000 cycles (80 % duty cycle). As expected, increasing the pulse length caused a corresponding increase in the energy of cavitation emissions, following a linear relationship ($R^2$ = 0.99). By 400,000 cycles the total energy (36.5 ± 8.6 J) was comparable to that observed using a previously sonicated sample (Figure 4.24), suggesting that most of the droplets had

been converted into microbubbles by this point. This is in agreement with previous work showing B-mode image intensity increases with burst length (Kawabata *et al.*, 2010). Other previous studies found that the *threshold* for cavitation has limited dependence on pulse length (Giesecke and Hynynen, 2003; Zhang and Porter, 2010) however these studies did not quantify cavitation energy above the threshold.

#### 4.3.5.4. Effect of ultrasound pressure on nanodroplets

Finally, it was hypothesised that vaporisation of the nanodroplets would be ultrasound pressure dependent, and so cavitation behaviour would only occur above a threshold pressure value.

The results of pressure ramp experiments are shown in Figure 4.27. At the lowest pressure tested (0.4 MPa peak-to-peak) the energy of cavitation emissions was indistinguishable from the noise floor of the system from water controls (< 0.66 μJ). At 1 MPa peak-to-peak the total energy of emissions of 6.6 ± 1.4 μJ was similar to that observed in the volume ramp experiments at this pressure. Above 1 MPa, as the pressure was increased, the total energy of cavitation emissions increased linearly ($R^2 = 0.99$). At 2 MPa, the energy of acoustic emissions was more than fifteen-fold the energy at 1 MPa (103.1 ± 33.0 μJ). Testing of higher pressures was not meaningful due to increased background cavitation observed in tests without nanodroplets.

Based on these results the cavitation threshold for nanodroplets appears to be at or below 1 MPa peak-to-peak. Using higher pressures can drastically increase the energy of cavitation, but is subject to other limitations such as those of the transducer or risk of inducing cavitation from endogenous nuclei. At higher frequencies the cavitation threshold may be higher due to the shorter time for vaporisation or bubble growth in each cycle of the ultrasound wave, as has been observed using other nanodroplet formulations in the literature (Giesecke and Hynynen, 2003). Other studies have used

droplets with high nucleation thresholds (several MPa) and found this threshold to *reduce* with ultrasound frequency, which was hypothesised to be due to nonlinear effects (higher harmonic generation) at high pressure amplitudes (Shpak *et al.*, 2014).

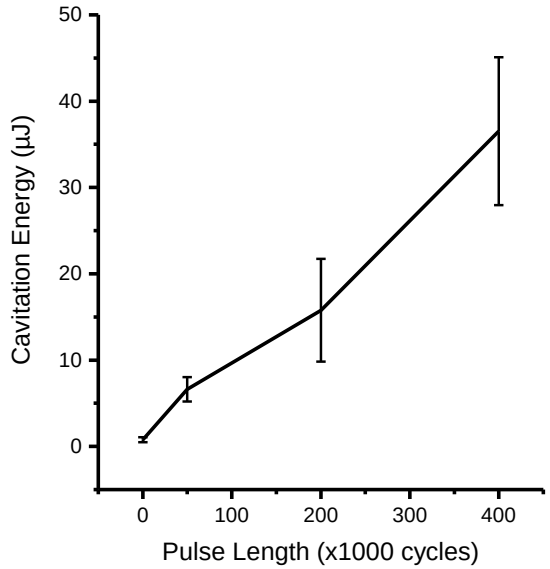


Figure 4.26: Pulse length ramp for MNDs. Pulse length was varied (40 – 400,000 cycles) for MNDs (100 µL) in water. Each sample was exposed to ultrasound under the same conditions used in cell experiments (500 kHz, 1 MPa pk-pk) 3 times. PRF was reduced to 1 Hz to allow use of longer bursts. The recording length for PAM was kept the same; longer pulses continued after recording had stopped. Error bars represent standard deviation over 3 samples per condition.

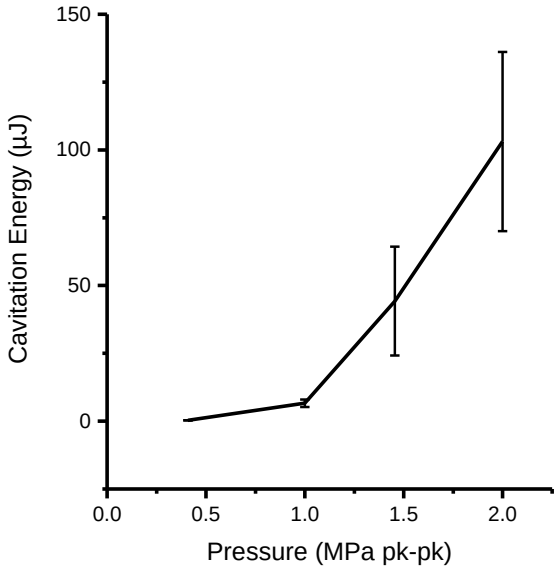


Figure 4.27: Pressure ramp for MNDs (100 µL) at 10 % duty cycle. Each sample was exposed to ultrasound (500 kHz, 50k cycles, 1 kHz PRF, 10 sec) 3 times at a pressure of 0.4, 1.0, 1.45 and 2.0 MPa pk-pk. Error bars represent standard deviation over 3 samples per condition.

## 4.4. DISCUSSION

In this chapter the techniques outlined in Chapter 3 were further developed in order to evaluate whether magnetic targeting of microbubbles could be used to enhance therapeutic effects in an *in vitro* cell model and whether passive acoustic mapping provided a useful means of treatment monitoring. To facilitate this, several improvements were made to the experimental setup including the development and testing of a biologically compatible chamber in which to grow and treat the cells, substituting the near real-time Verasonics PAM system for the previous Zonare-based setup (which required offline processing), refinement of the microbubble formulation (and introduction of novel alternative agents), and introduction of biological methods such as flow cytometry with which to assess the efficacy of treatment.

The first set of delivery experiments – using fluorescent siRNA bound to magnetic microbubbles – were carried out using OptiCell$^{TM}$ cell chambers, the Zonare-based PAM setup of Chapter 3 and a readily available cell line (Owen, 2015). While this system had numerous disadvantages compared to that used in later experiments it did however provide encouraging proof-of-concept for the work which followed, including enhanced fluorescence uptake which was well correlated with the acoustic mapping results and showed a clear benefit of magnetic targeting compared to the control experiments. However, this part of the study had several limitations. In particular, while fluorescence uptake is a commonly used marker, it can be unreliable due to effects such as cellular autofluorescence.

For this reason a more robust target was desirable. To accomplish this three key changes were made to the model, the first of which was the use of biologically active knockdown siRNA (instead of fluorescent-tagged inactive siRNA); the second being incorporation of a scrambled siRNA control (which contains the same material, but

with the bases reordered such that it should not result in the biological effect); and the third being refinement of the biological analysis procedure to include flow cytometry and viability testing to characterise the cells in addition to microscope imaging.

Using the knockdown siRNA model the results presented here are encouraging, with fluorescence knockdown being achieved in cells in the groups which were treated with K-MMB, magnet and ultrasound (and not, crucially, in the S-MMB scramble control). However, the trend in cell viability (which tended to decline with knockdown efficacy) is of some concern, as is the very low viability (~15 %) observed in some of the runs (these were considered non-meaningful so not analysed further). The acoustic data from these experiments correlate with the biological results in that cavitation was greatly increased in those experiments in which magnetic targeting, K-MMB and ultrasound were combined, and validates the S-MMB scramble control which appeared acoustically similar. However, these data also suggest that the microbubble concentration selected for these experiments may be sub-optimal, with clear shielding effects visible in B-mode images and reduced amplitude of cavitation in PAM. It is possible that this may have resulted in excessive cavitation activity and/or siRNA dose, accounting for the reduction in cell viability, but this requires further investigation. In particular, variation of the quantity of siRNA incorporated into the microbubble formulation and ultrasound conditions would allow decoupling of the effects of microbubble concentration, cavitation 'dose' and siRNA dose on the efficacy and viability results.

Drug delivery experiments using magnetic nanodroplets showed a marked reduction in cancer cell viability – indicating successful treatment – under the synergistic effects of the nanodroplets, ultrasound and magnetic field, while flow cytometry and microscopic analysis provided further evidence that this was due to the expected

mechanism of action of paclitaxel. Acoustic results for these experiments were well correlated with the biological results and showed a typical – albeit lower amplitude – bubble-like response from the droplets after undergoing phase transition, under the same ultrasound excitation conditions as were used in the previous work with microbubbles.

Finally, it was hypothesised that the lower amplitude response from the droplets was as a result of their requirement of an extra phase transition step from liquid to gas (compared to the microbubbles which already contain gas) thus presenting a lower effective microbubble concentration than the conventional microbubbles. To test this theory samples of various dilutions were tested using the same experimental setup under a range of ultrasound conditions as well as being compared to nonmagnetic commercial microbubbles. These results appeared to confirm the observations noted above: the response of a 1 % microbubble solution under the conditions used for cell experiments was around 50 times that of the droplets. Sonication of the nanodroplets prior to testing to convert them into pre-existing bubbles raised their response 7-fold and to within a range more comparable with microbubble agents, at the cost of losing the inherent advantages of the initial nano-scale agent (Section 2.3.5). Variation of the acoustic parameters (in particular burst length and pressure) using nanodroplets was able to increase the amplitude of response to that of previously sonicated samples. The results of this final part of the chapter will be used to inform the acoustic conditions chosen for future *in vitro* and *in vivo* studies using the magnetic nanodroplets.

Overall, the aim of this chapter was to establish whether cavitation induced by magnetic targeted nuclei could result in biologically relevant effects, and if this could be correlated to PAM such that this could be used for monitoring. Generally speaking, the answer to both of these questions is yes, with caveats. In each of the models tested

here (fluorescent siRNA, knockdown siRNA and PTX) enhanced bioeffects and increased cavitation in PAM were observed when magnetic targeting and ultrasound were combined. However, in the results presented here PAM was unable to account for effects such as the reduction in cell viability observed in some runs using K-MMB (discussed above). These may be due to factors which could be measured using PAM given appropriate optimisation of the treatment parameters (e.g. excessive cavitation), or may be due to secondary factors (e.g. excessive drug dose) which would not be reflected in the acoustic data. In addition, the acoustic emissions from a given agent will vary depending on numerous parameters including the nature of the therapeutic ultrasound pulses (the optimal settings for which are likely to differ between cavitation agents), characteristics of the agent and experimental setup. As such, while PAM is clearly very useful for the characterisation and monitoring purposes for which it was used here, care must be taken in comparing results between different experiments.

Generally speaking, the results in this chapter for each of the therapeutic agents and for PAM as a means of monitoring them are both promising. Further investigation of the optimal acoustic conditions and chemical formulations is warranted and would allow decoupling of effects such as microbubble concentration vs. drug dose and validation of effects such as sustainability of cavitation vs. total treatment duration.

## 4.5. CONCLUSIONS

In this chapter passive acoustic mapping with magnetic microbubbles was tested *in vitro* in several models. Following initial tests using fluorescent-tagged siRNA in a parallel-plate cell culture device an improved biologically and acoustically compatible cell chamber system was successfully designed, characterised and published and used for further experiments involving siRNA transfection and paclitaxel delivery. Using a more robust siRNA model encoding for fluorescence knockdown attached to the magnetic microbubbles – notwithstanding cell viability concerns in some of the runs, which bears further investigation – knockdown was achieved under the synergistic effects of ultrasound and the magnetic field and not in control experiments in which any of these components were omitted or using a scrambled siRNA control. Using magnetic microbubbles in which the filling gas was initially in the liquid phase – phase-change magnetic nanodroplets – improved efficacy of the chemotherapeutic drug paclitaxel was also demonstrated using the same model, while further investigation of the acoustic behaviour of the nanodroplets identified several possible avenues for improving their performance in future experiments. Increased cavitation in PAM correlated well with therapeutic effects in each of the models.

Having investigated the performance of magnetic microbubbles and demonstrated the potential for enhancement of cavitation-mediated therapies and PAM monitoring both in tissue phantoms (Chapter 3) and now *in vitro* (Chapter 4), the following chapter investigates whether these effects can be replicated *in vivo*.

CHAPTER 5

# PASSIVE ACOUSTIC MAPPING OF MAGNETIC MICROBUBBLES *IN VIVO*

## 5.1. INTRODUCTION

In the previous two chapters magnetic microbubbles were shown to enhance cavitation and therapeutic agent delivery in tissue phantom studies and *in vitro* models. A number of important questions however remain: whether or not similar phenomena can be observed *in vivo*; whether there is any correlation between cavitation activity and deposition of material in target tissue; and whether magnetic functionalisation affects the *in vivo* distribution of MMBs and their clearance mechanism(s) as compared with conventional contrast agents.

The aim of this chapter was to address these questions by conducting an *in vivo* study of MMBs in accordance with aim 5 of the thesis as a whole (Section 1.8.2). The MMB used in this chapter are labelled with the fluorescent dye DiI (DiI-MMB).

More specifically, the objectives of this chapter were to:

1) Establish whether the distribution of DiI-MMB *in vivo* could be measured after injection using fluorescent labelling and/or MRI;

2) Establish whether DiI-MMB may be used to promote cavitation activity using simultaneous B-mode imaging and passive acoustic mapping (PAM), and compare this behaviour with and without magnetic targeting and to SonoVue®; and

3) Assess whether cavitation activity may be correlated to the deposition of fluorescent and/or magnetic material in tissue.

The experiments in this chapter were conducted with the assistance of colleagues in the BUBBL group. In particular the assistance of Robert Carlisle in overall planning and conducting the experiments, Apurva Shah in preparation of mice and conducting experiments, Joshua Owen and Richard Browning for DiI-MMB manufacture, Rachel Myers for advice on sample processing, Sandra Nwokeoha for cell culture, Sean Smart (of the Gray Institute for Radiation Oncology and Biology) for MR imaging and Christian Coviello for assistance in the development of the ultrasound research platform software configuration is expressly acknowledged.

## 5.2. METHODS

### 5.2.1. Fluorescent magnetic microbubble production

The magnetic microbubbles in this chapter[30] (DiI-MMB) use a lipid supplied in chloroform, PEG stabiliser, lipophilic dye (DiI) and lipid-coated magnetic nanoparticles supplied in water (Owen, 2015). 1,2-distearoyl-sn-glycero-3-phosphocholine dissolved in chloroform (DSPC; 25 mg/mL) was purchased from Avanti Polar Lipids Inc. (Alabaster, Alabama, USA). Polyoxyethylene-40-stearate (PEG), chloroform, glycerol and propylene glycol were purchased from Sigma Aldrich (Gillingham, Dorset, UK). 1,1'-Dioctadecyl-3,3,3',3'-Tetramethylindocarbocyanine Perchlorate (DiI) stain and phosphate buffered saline (PBS) were purchased from Life Technologies (Paisley, UK). FluidMAG-Lipid (25 mg/mL 50 nm spherical phosphatidylcholine coated magnetite particles in sterile water) was purchased from Chemicell (Berlin, Germany). Sulphur Hexafluoride ($SF_6$) was purchased from BOC (Guildford, UK).

PEG was dissolved in chloroform (10 mg/mL) using a bath sonicator. DiI was dissolved in chloroform (2.5 mg/mL). DSPC and PEG solutions were mixed in a 9:1 molar ratio (61 µL of 25 mg/mL DSPC solution, 44 µL of 10 mg/mL PEG solution) in a glass vial. Glass precision syringes (Hamilton Microliter; Sigma Aldrich, Gillingham, Dorset, UK) were used to measure solutions for chloroform resistance. The addition of lipophilic dyes can be used to render microbubbles fluorescent (Lum *et al.*, 2006; Patil *et al.*, 2011) to aid with tracking *in vivo*. For fluorescent labelling of DiI-MMB 20 µL of DiI solution was added to the mixture and the vial left on a hotplate at 50 °C for 12 hours in a fume hood to allow the chloroform to evaporate. The resulting lipid film was resuspended in 1.5 mL of a solution consisting of 80 % PBS, 10 % glycerol and 10 % propylene glycol on a hotplate at 70 °C with constant stirring for 20

[30] The magnetic microbubbles used in this chapter were developed by Joshua Owen and produced by Joshua Owen and Richard Browning who are gratefully acknowledged

minutes. The solution was then sonicated for 60 s to disperse the lipids using an ultrasonic cell disruptor (tip fully immersed, power setting 2; model XL 2000, 3 mm probe diameter, 22.5 kHz, Misonix Inc., Farmingdale, NY, USA). 15 µL of FluidMAG-Lipid solution was added to the vial and sonication repeated for 10 s. To produce microbubbles the probe tip was moved to the air-liquid interface and sonication repeated for 10 s (power setting 15) while $SF_6$ was continuously delivered from the gas cylinder to the vial via a tube held close to the vial opening. After sonication the vial was immediately sealed using a pierceable stopper and stored on ice until used. Experiments were commenced within 1 hour of sonication.

## 5.2.2. *In vitro* microbubble characterisation

To characterise the magnetic microbubbles microscope images were taken in order for sizing and concentration analysis. Subsequently, *in vitro* tests were performed to confirm that microbubbles were fluorescent, responded to a magnet and were acoustically active. Finally, fluorescence measurements were taken at various microbubble concentrations in blood to confirm the feasibility of this aspect of the *in vivo* protocol.

### 5.2.2.1. Sizing

To obtain an estimate of the sizing and concentration of microbubbles, images were taken using an optical microscope (model Eclipse Ti-E; Nikon Instruments, UK) fitted with a 20 × objective (model Plan Fluor; Nikon Instruments, UK). 20 µL samples of microbubbles were taken, and 30 images taken from each sample. The particle size distribution and concentration were then obtained using purpose-written software (Sennoga *et al.*, 2010) in MATLAB (The MathWorks, Natick, MA, USA).

#### 5.2.2.2. Fluorescent labelling

To confirm that the lipophilic dye DiI could fluorescently label the microbubbles, samples were examined using a fluorescence microscope (model Eclipse Ti-E; Nikon Instruments, UK) fitted with a 20 × objective (model Plan Fluor; Nikon Instruments, UK), mercury arc light source and Tetramethylrhodamine (TRITC) filter cube. Brightfield and fluorescence images were taken of the same fields of view.

#### 5.2.2.3. Magnetic response

To confirm that microbubbles were magnetically responsive samples were pipetted onto a slide without a coverslip (the buoyancy of the microbubbles against the coverslip was found to impede motion when a coverslip was used) and examined using a 4 × objective (model Plan Fluor; Nikon Instruments, UK). The field of view was positioned towards one edge of the sample while a magnet was held above the side of the slide. Images of the same field of view were taken in both brightfield and fluorescence modes.

#### 5.2.2.4. Acoustic response and stability testing

To confirm that the microbubbles were responsive under B-mode and focused ultrasound excitation a simplified version of the experimental setup for the *in vivo* work was used (see below). 10 % by volume microbubble suspension or water was placed in a cylindrical sample holder (internal dimensions approx 20 mm diameter × 20 mm depth) with acoustically transparent Mylar windows on both ends to allow for ultrasound propagation. The central volume of the sample chamber was aligned with the focus of the HIFU transducer in a water tank. B-mode images were recorded (with the HIFU transducer disabled) for 10 seconds over a range of transmit amplitudes (transmit voltage 1.6, 4.0, 6.5, 8.8, 11.3 V). B-mode (6.5 V transmit voltage) and PAM data

were then recorded for 30 seconds with focused ultrasound excitation over a range of amplitudes (0, 1.2, 1.6, 2.0 MPa peak negative focal pressure, 100 cycles per burst).

To compare a sample with the same chemical composition but lower acoustic response the experiment was repeated with a sample of microbubbles which had been produced 24 hours previously and stored in a refrigerator and which therefore contained fewer bubbles.

#### 5.2.2.5. Fluorescence in blood

To establish whether the fluorescence of microbubbles could be observed in blood a standard curve was prepared using samples consisting of 160 µL PBS, 20 µL mouse blood and 20 µL of a 5-fold serial dilution of microbubbles (100, 20, 4, 0.8, 0.16, 0 % v/v). Samples were mixed by pipetting and then centrifuged at 3000 RPM for 2 minutes to separate plasma from insoluble components, which were resuspended in 190 µL additional PBS. Plasma samples and resuspended pellets were analysed in a black 96-well plate using a plate reader (excitation 544 nm, emission 590 nm, gain 2,000; model FLUOstar Omega; BMG LABTECH, Aylesbury, UK). Data were analysed in Microsoft Excel (Microsoft Corp., Redmond, WA) and plotted in Origin (OriginLab Corp., Northampton, MA, USA).

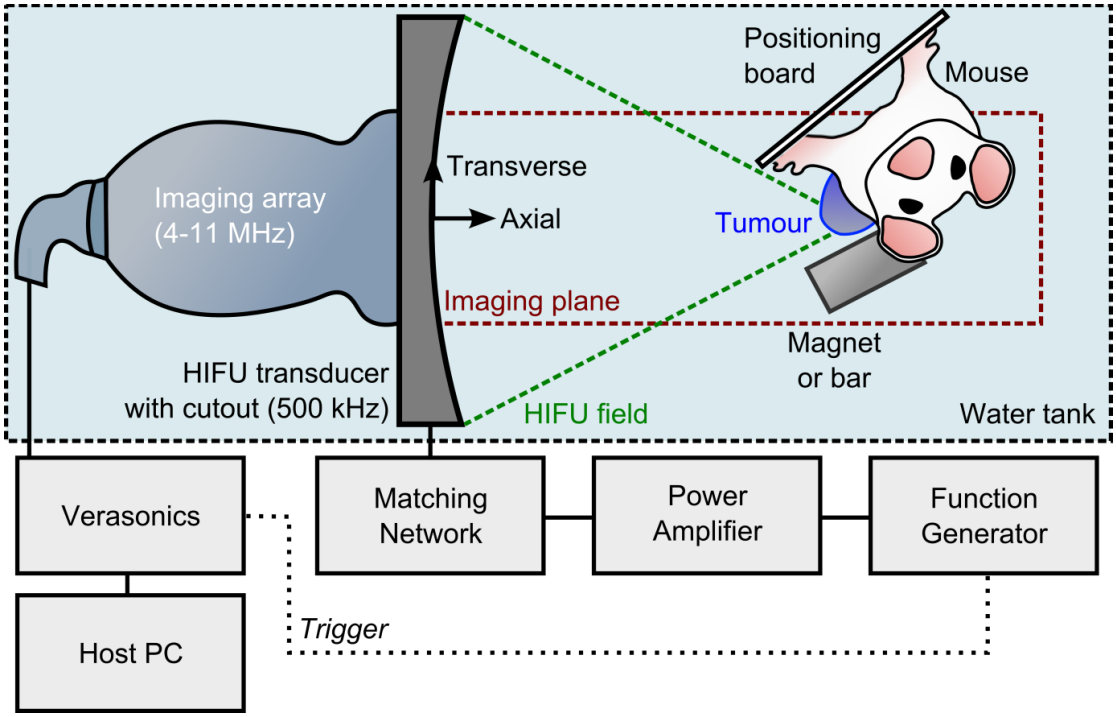


Figure 5.1: Overview of the setup for *in vivo* experiments (plan view - not to scale). Tumours were aligned with the focus of a 500 kHz HIFU transducer with a rectangular cutout for a 4-11 MHz imaging array. B-mode imaging was interspersed with passive acoustic recording of the emissions from cavitation during HIFU transducer pulses. Transverse and axial directions are defined relative to the centre of the front face of the imaging array.

### 5.2.3. Experimental setup for *in vivo* work

An overview of the experimental setup is given in Figure 5.1. Ultrasound was generated using a 500 kHz spherically focused single-element high intensity focused ultrasound (HIFU) transducer (model H-107B-10; Sonic Concepts, Inc., Bothell, WA, USA) with an outer diameter of 64 mm, focal length 63 mm, and featuring a 45 × 18 mm rectangular cutout through which an imaging linear array probe (model L11-4v; Verasonics Inc., Kirkland, WA, USA) with 128 elements, 38 mm aperture and 4-11 MHz bandwidth was aligned such that the focus of the HIFU transducer was within the imaging plane. Driving waveforms were generated using a function generator (model 33250A; Agilent, Wokingham, Berkshire, UK) synchronised to the ultrasound research platform (model Vantage 256; Verasonics Inc., Kirkland, WA, USA) using a trigger output signal. The driving signal was applied to the HIFU transducer via a 55 dB power amplifier (model 1040L; Electronics and Innovation, Rochester, NY, USA)

and impedance matching network supplied by the transducer manufacturer. The ultrasound research platform was connected to a host desktop PC to configure the imaging sequence, save data and provide real-time display during experiments.

The HIFU transducer and imaging array assembly were mounted using a 3 axis positioning stage in a 40 × 40 × 17 cm Perspex tank filled with filtered, degassed, deionised water which was heated to 37 °C using an immersion heater. Water quality was maintained during experiments by continuous flow through a loop consisting of a centrifugal pump, deionisation column, 10 µm filter and vacuum degassing membrane. Prior to commencing experiments the focus of the HIFU transducer was located using a 200 µm needle hydrophone (Precision Acoustics, Dorchester, UK). The location of the hydrophone tip observed under B-mode imaging was recorded for display as an overlay on the B-mode image after the hydrophone was removed, and used to position tumours at the focus during experiments. A single rectangular permanent magnet (N52 grade NdFeB, 10 × 10 × 25 mm; NeoTexx, Berlin, Germany) with transversal magnetisation 1.5 T or nonmagnetic stainless steel bar of the same dimensions was held in a clamp attached to a 3 axis positioning stage and placed close to the focus of the HIFU transducer. The magnet or bar was placed at an angle with respect to the ultrasound array to reduce direct reflection of the ultrasound or creation of standing waves. A Perspex board attached to a 3 axis positioning stage was used to secure mice and align tumours with the focus of the HIFU transducer under B-mode guidance. A nosepiece attached to the positioning board was used for delivery of anaesthetic during the experiments.

### 5.2.4. Ultrasound research platform configuration

An outline of the ultrasound research platform configuration script is shown in Table 5.1[31]. The ultrasound research platform was configured to provide B-mode imaging (4.5 MHz transmit centre frequency, 9 MHz receive centre frequency, 48 pulse-inversion pairs per frame, 48 active elements per transmit, 10 cm imaging depth) interleaved with passive recording of the acoustic emissions from cavitation (array transmit disabled; receive on 128 channels, 35 MHz sample rate, 250 μsec recording length). Pulse inversion was used to improve the quality of B-mode imaging for tissue (Tranquart *et al.*, 1999). The overall sequence repetition rate was set to 0.5 Hz to allow for processing and saving data between pulses. A trigger output signal was sent at the beginning of passive recording to the function generator for focused ultrasound excitation at the same pulse repetition frequency. Data were transferred during experiments from the research platform over a PCI-express bus to a host PC running MATLAB (The MathWorks, Natick, MA, USA) which was used to configure the imaging sequence, save data to disk and provide real-time display.

B-mode image reconstruction and processing were accomplished using compounding of the 96 receives per frame with built-in routines supplied by the system manufacturer. Passively recorded data was processed using an external function which included a 1 MHz high-pass digital filter (to attenuate any bleed-though of the 0.5 MHz HIFU drive signal picked up by the 4-11 MHz array) and implementation of the time exposure acoustics algorithm as previously described (Section 2.2.4). Passive maps of 20 × 24 pixels were produced over a 10 mm (transverse) × 20 mm (axial) region centred on the focus of the HIFU transducer.

[31] The assistance of Christian Coviello in development of the ultrasound research platform configuration and setup scripts is gratefully acknowledged

An example of the real-time display used for experiments is shown in Figure 5.2. B-mode images, passive acoustic maps and radio frequency (RF) data (post filter) for selected elements were shown. For alignment purposes the focus of the HIFU transducer was overlaid on the B-mode image. For display purposes PAM data were thresholded to remove the baseline electrical signal in absence of cavitation (HIFU off) and overlaid on the B-mode image with a split colourmap to provide registration of the PAM and B-mode data. Graphical User Interface (GUI) controls provided control over the beginning and end of the treatment sequence and enabled saving of the images from each frame and raw RF channel data for PAM to disk.

| | |
|---|---|
| * (Events 1-194) B-mode imaging<br>- Loop over 2 frames<br>+ Loop over 48 rays<br>* B-mode, normal<br>TX on 48 elements, RX on 128<br>250 µsec to next TX/RX<br>* B-mode, inverted<br>inverted TX 48 elements, RX on 128<br>250 µsec/15 ms (final) to next TX/RX<br>+ Step elements along array, next ray<br>+ Reconstruct and display B-mode image<br>- Next frame | * (Event 195) PAM RX<br>- Send trigger out<br>- No TX, RX on 128 elements, 250 µsec recording, 35 MHz sample rate<br>- 1.92 sec to next TX/RX<br>* (Event 196) Transfer PAM data<br>* (Event 197) Process PAM data in external function<br>* (Event 198) Overlay PAM on B-mode<br>* (Event 199) Save B-mode<br>* (Event 200) Save PAM<br>* (Event 201) Jump back to Event 1 |

Table 5.1: Pseudocode description of the US research platform imaging sequence. TX = transmit; RX = receive.

## 5.2.5. Animal model

Animal experiments were conducted in accordance with UK Home Office guidelines. Balb/c mice (female, 6-8 week old, mass 20.0 ± 1.3g; Harlan, UK) were injected subcutaneously with CT26 cells ($2 \times 10^5$ per mouse; supplier ATCC; LGC Standards, Teddington, UK) and allowed to form tumours of approximately 100-200 $mm^3$ in size before commencing experiments[32].

[32] The assistance of Robert Carlisle and Apurva Shah in preparation of mice and Sandra Nwokeoha for performing cell culture is gratefully acknowledged

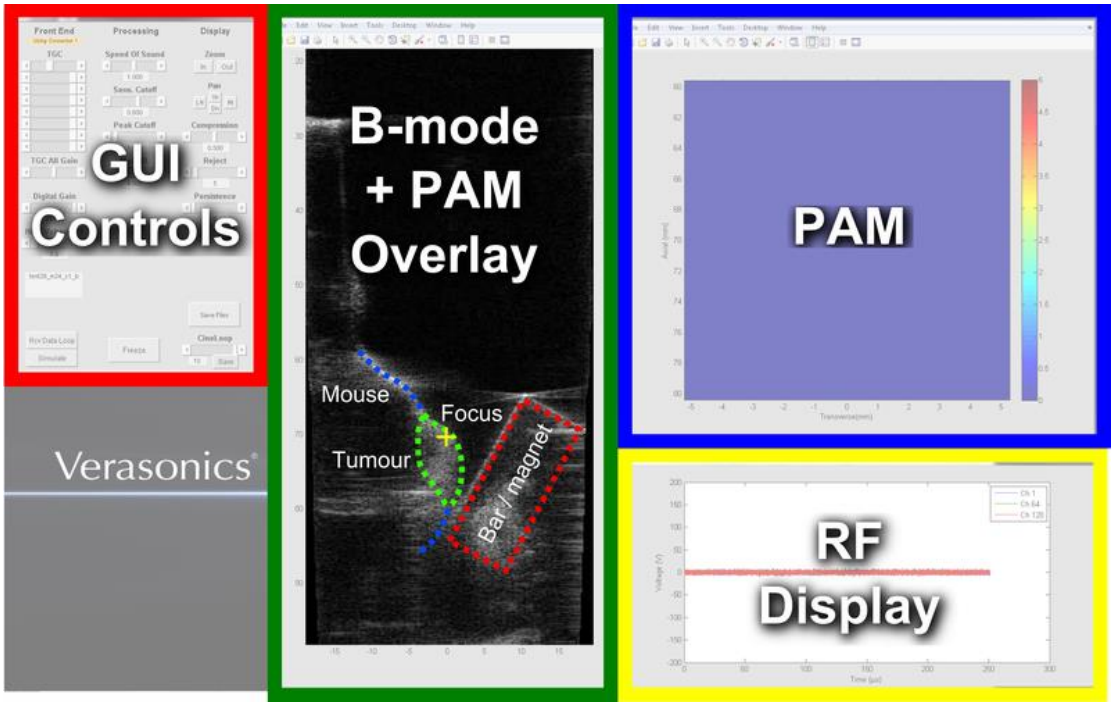


Figure 5.2: Ultrasound research platform real-time display for *in vivo* experiments (prior to activation of HIFU transducer) showing GUI controls, B-mode ultrasound image (annotated to show features), PAM standalone display (colourbar in units of power (AU)), and filtered RF data for selected channels (units in volts).

### 5.2.6. *In vivo* experimental protocol

Tumours were depilated to prevent trapping of air and outlined with a marker pen to aid in visual alignment[33]. Mice were anaesthetised using 5 % isoflurane, attached to the positioning board with tape, and maintained under anaesthesia using a nosepiece connected to the positioning board delivering 2 % isoflurane. Tail veins were cannulated using a 29 gauge needle attached to an insulin syringe via a short length of 0.3 mm inner diameter plastic tubing primed with PBS, such that the syringe could remain outside of the tank during experiments. Mice were placed vertically in the water tank (head and ears above water surface) and tumours aligned with the previously identified HIFU transducer focus under B-mode guidance. The magnet or nonmagnetic bar was aligned close to the focus, positioned at an angle to minimise disruption of the ultrasound field. 150 µL samples of magnetic microbubbles were drawn through

[33] The assistance of Robert Carlisle and Apurva Shah in conducting animal experiments is gratefully acknowledged

the pierceable lid of the vial into an insulin syringe shortly before the start of each run. Each mouse was treated with 3 × 50 µL injections at 3 locations 3 mm apart in the vertical direction (out of plane with respect to the imaging array).

A timeline for each experimental run is shown in Figure 5.3. To begin the procedure the ultrasound platform was unfrozen to simultaneously initiate saving of B-mode and passive data and focused ultrasound excitation (where applicable). After 1 minute the first 50 µL dose of microbubbles was injected. After a further 2 minutes the mouse was moved 3 mm in the vertical direction. The procedure was then repeated twice giving a total treatment time of 9 minutes. The ultrasound platform was then frozen to stop treatment, the mice were promptly removed from the tank, the cannulae were removed, and the mice were allowed to recover in a warm box. At 15 minutes from the first injection mice were sacrificed by cervical dislocation and 20 µL blood drawn from the tail vein, which was made up to 200 µL with PBS and centrifuged for 2 minutes at 3000 RPM. Plasma and insoluble components were frozen separately at -20 °C. Tumours were harvested and frozen at -20 °C.

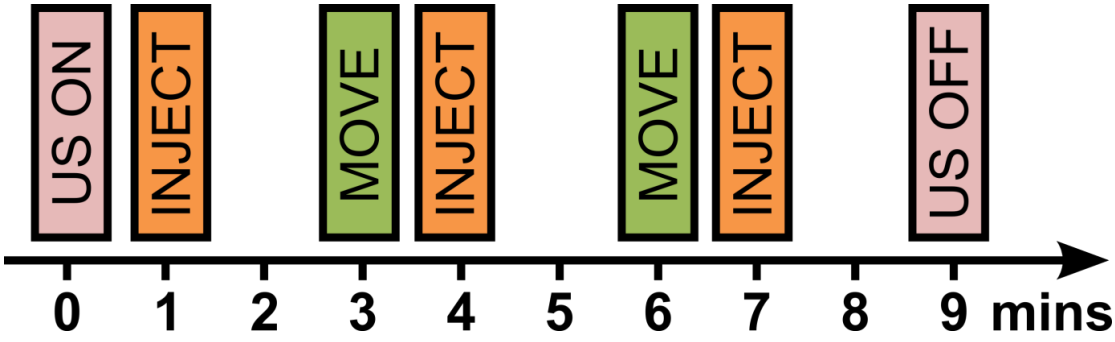


Figure 5.3: Timeline for *in vivo* experiments. Each mouse was injected with 3 samples of microbubbles and treated in 3 locations. B-mode and therapeutic ultrasound were applied for the duration of each run.

Four sets of experiments were conducted:

1) For analysis of the distribution of magnetic microbubbles 6 mice were treated with DiI-MMB (3 with magnet, 3 with nonmagnetic control) under B-mode imaging only (i.e. HIFU transducer disabled). From these mice the liver, spleen, lungs and kidneys were also harvested (in addition to tumour and blood samples) and frozen at -20 °C. Blood and organ samples from an additional untreated mouse were used to create standard curves for the fluorescence measurements by addition of known dilutions of magnetic microbubbles.

2) To establish the *in vivo* cavitation threshold for magnetic microbubbles 3 mice were treated with DiI-MMB and focused ultrasound excitation (frequency: 500 kHz, 100 cycles per burst, 0.5 Hz pulse repetition frequency) at peak negative focal pressures of 1.2, 1.6 and 2.0 MPa respectively. B-mode and PAM data were displayed during experiments and recorded.

3) For comparison of the acoustic response of magnetic microbubbles under the effect of a magnet, 3 mice were treated with either DiI-MMB + magnet, DiI-MMB + nonmagnetic control or nonmagnetic bubbles + magnet using the ultrasound conditions above (peak negative focal pressure 1.6 MPa). A new batch of DiI-MMB was used and the commercial ultrasound contrast agent SonoVue® (Bracco, Milan, Italy) made up according to the manufacturer's instructions was used as a nonmagnetic control treatment in the presence of the magnet. As an additional comparison with similar chemical composition but depleted bubble concentration one further mouse was treated using a sample of DiI-MMB taken from a vial which had been produced the previous day and then stored in a refrigerator for at least 24 hours.

4) To test whether the iron oxide content of the magnetic microbubbles could be detected under MRI, 2 additional mice were used (1 treated, 1 untreated control). The treated mouse was injected with DiI-MMB (1.6 MPa peak negative focal pressure, magnet installed) while the untreated mouse was injected with saline as a sham control. Both mice were frozen whole at -20 °C after sacrifice without removal of blood or organs for subsequent whole-body MR imaging.

### 5.2.7. Biological sample processing

The diluted plasma samples were defrosted, stored on ice and protected from light. The fluorescence of 100 µL samples was measured compared to a standard curve containing known quantities of microbubbles in plasma using the plate reader as described for the *in vitro* tests above[34]. Tissue samples were defrosted, weighed using a balance with 0.1 mg precision (model: Explorer Pro; OHAUS, Nänikon, Switzerland) and homogenised in PBS using a rotary homogeniser (model T10 basic; IKA, Staufen, Germany) to a concentration of 200 mg organ / mL buffer. Samples were stored on ice and protected from light during the procedure. The fluorescence of 100 µL samples was measured compared to standard samples containing known quantities of microbubbles homogenised in tissue using the plate reader as described for the *in vitro* tests above.

[34] The advice and assistance of Robert Carlisle, Apurva Shah and Rachel Myers in processing the biological samples is gratefully acknowledged

## 5.2.8. Magnetic resonance imaging

MRI was performed at 4.7 T (VNMRS, Varian Inc., Palo Alto, CA, USA) using a whole mouse body quadrature birdcage transmit-receive coil (Rapid Biomedical, Germany)[35].

Progressively T2* weighted imaging was performed using a 3D multiple gradient echo scan with echo time (TE) = 3.65, 9.78, 15.91 and 22.04 ms, repetition time (TR) = 50 ms and flip angle = 30 °, at an isotropic resolution of ca. 211 µm covering a field of view of 108 × 27 × 27 mm in a scan time of 14 minutes.

Images were exported to Tagged Image File Format (TIFF) files (512 × 128 × 128 pixels × 4 echo times; 32 bits per pixel; 128 MB per file) for analysis in ImageJ (National Institutes of Health, Bethesda, MD, USA). Slices showing the liver and tumour in each mouse were selected and the borders of these regions outlined manually using the freehand selection tool and saved as regions of interest using the region of interest (ROI) manager feature. The mean and standard deviation of image intensity in each region of interest were measured at each of the four echo times. To account for intensity inhomogeneity (Vovk *et al.*, 2007) the results for liver and tumour were normalised using the mean image intensities in nearby areas of muscle at the same echo times.

## 5.2.9. PAM post processing

After the experiments, the passively recorded data were reprocessed over a larger grid (40 × 36 pixels; 20 × 30 mm) using the RCB algorithm (Section 2.2.9; tolerance parameter $\varepsilon = 6.0$ was selected experimentally to give satisfactory image quality and found to be relatively insensitive to small changes) to improve the resolution of map-

[35] MR imaging was conducted by Sean Smart whose assistance in conducting imaging and advice on subsequent processing is gratefully acknowledged

ping and ensure all cavitation activity was captured in the region of interest. The maximum value in each pixel over the duration of the experiments (indicating maximum cavitation power) was overlaid in the corresponding location on the B-mode images to produce representative spatial maps of cavitation for each experiment. Note that due to unavoidable breathing motion and presence of endogenous cavitation nuclei in the *in vivo* experiments the maps were not summed over the duration of experiments (to give units of energy) as in the previous chapters, since this would introduce motion artefacts and incorporate background cavitation which is not relevant to the experiment. The maximum cavitation power was extracted from each frame of data to show the evolution of cavitation behaviour over time (in particular the effects of microbubble injection and destruction). To produce spectra of the emissions during pressure ramp experiments the passively recorded data from the 128 channels in each frame were beamformed to obtain a time trace corresponding to the focal point (i.e. steps 1-3 of the algorithm outlined in Section 2.2.3), and then subject to a Fourier transform (MATLAB function *fft*). The spectra were averaged over the duration of the experiments and plotted over a 0-10 MHz range (towards the upper end of the frequency response of the ultrasound array, and corresponding to 20 harmonics of the focused ultrasound excitation frequency).

## 5.3. RESULTS AND DISCUSSION

### 5.3.1. *In vitro* DiI-MMB characterisation

#### 5.3.1.1. Sizing

The results of microbubble sizing are shown in Figure 5.4. The measured microbubble concentration of $1.8 \times 10^8$ microbubbles/mL and mean diameter of 3.1 µm were both similar to those of commercial clinically approved contrast agents (e.g. 1-5 $\times 10^8$ microbubbles/mL and 2.5 µm mean diameter for SonoVue®; (Schneider, 1999)).

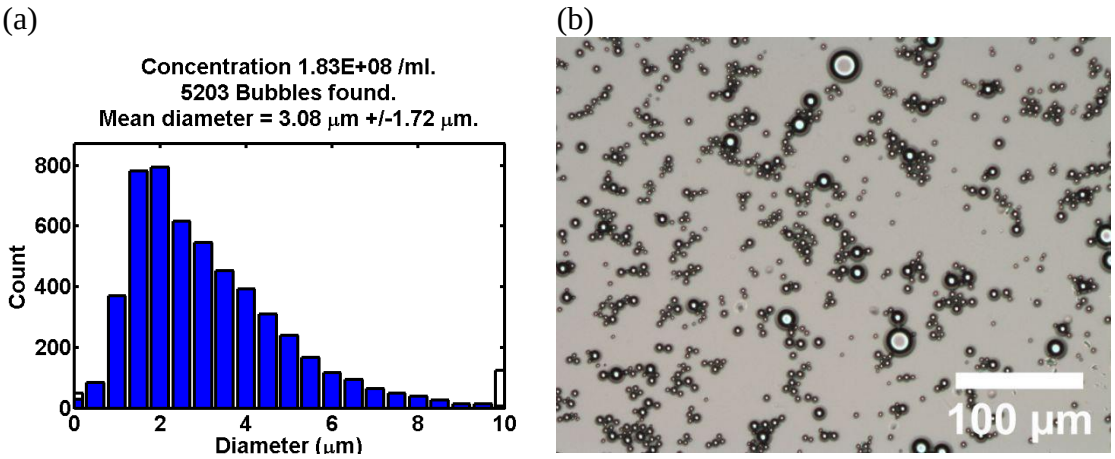


Figure 5.4: Microbubble sizing for DiI-MMB. (a) Size distribution plot obtained from 30 images of magnetic microbubbles using the image processing software. (b) Example brightfield image obtained at 20 × magnification.

### 5.3.1.2. Fluorescent labelling

Brightfield and fluorescence images of the same field of view of a sample of magnetic microbubbles are shown in Figure 5.5 (a-b). Comparison of the two images confirms that the lipophilic dye is attracted to the lipid-based microbubble shells, which are clearly visible against the background in the fluorescence image. In a cropped view taken with the same objective (c) distribution of the microbubble shell components appears visible on the larger microbubbles.

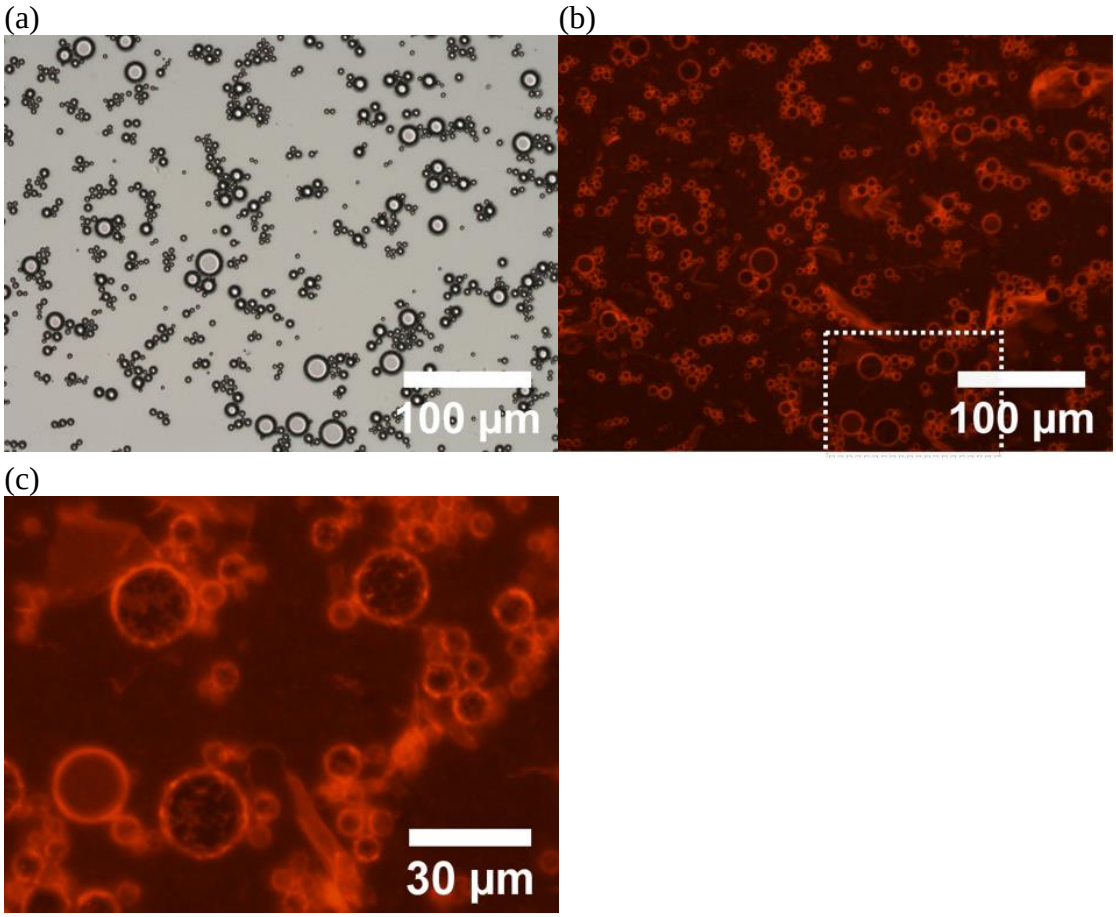


Figure 5.5: Microscope images of DiI-MMB (20 × objective). (a) Brightfield (33 ms exposure, 1 × gain) and (b) fluorescence (TRITC filter, 500 ms exposure, 1 × gain) images of the same field of view. (c) Cropped view of the area outlined in (b) from a second image.

### 5.3.1.3. Magnetic response

Microscope images showing DiI-MMB under the influence of a magnetic field are shown in Figure 5.6. Notably, the use of a coverslip on the microscope slide was found to impede microbubble motion, in contrast to previous work with magnetic microbubbles containing an oil-based ferrofluid (Chapter 3). It was hypothesised that this could be due to the lack of an oil layer in the new formulation resulting in more buoyant microbubbles. For this reason the microbubble sample was pipetted onto a slide and left in an approximately circular droplet, the microscope field of view being positioned towards one edge of the droplet. When a 1.5 T permanent magnet was brought close to the microscope slide, microbubbles were observed to move towards it and gather on this side of the droplet (Figure 5.6a). Observation of the same field of view under fluorescence (TRITC filter) showed strong emissions in the same region, which suggests successful colocalisation of magnetic particles and fluorescent dye within the microbubbles.

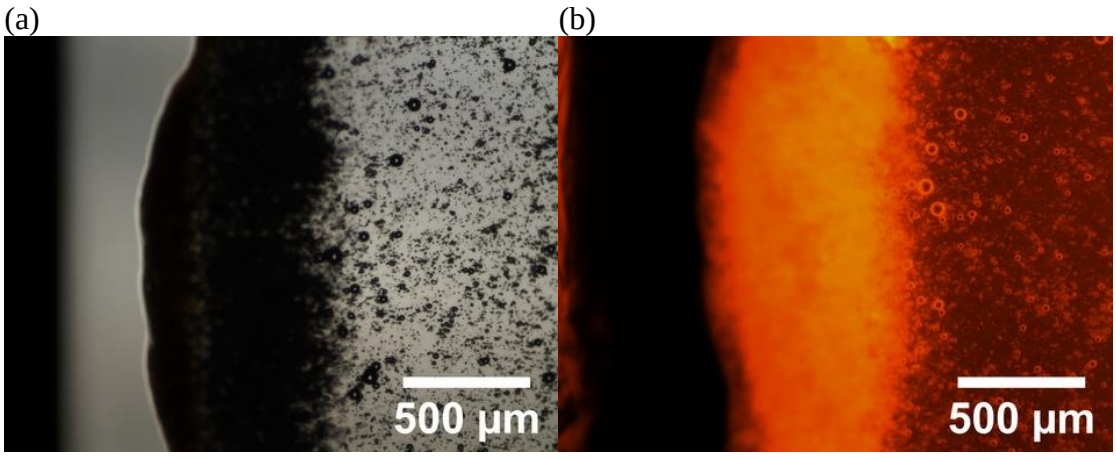


Figure 5.6: Microscope images showing DiI-MMB magnetic response. (a) Brightfield and (b) fluorescence (TRITC filter) microscope images of magnetic microbubbles (4 × objective) under influence of a magnet. Microbubbles were pipetted into a droplet without using a coverslip and the field of view was positioned towards one edge. A 1.5 T permanent magnet was held above the left side of the slide and is visible as the dark region to the left of the brightfield image. Microbubbles were observed to move towards the magnet and gather on the left side of the image under both brightfield and fluorescence imaging.

#### 5.3.1.3.1. Acoustic response

B-mode and PAM images for *in vitro* testing of the DiI-MMB in a sample holder are shown in Figure 5.7 and Figure 5.8 respectively.

The outline of the sample holder and reflections from the front and rear Mylar walls are clearly visible in the B-mode image for the sample holder containing water (Figure 5.7a), with negligible echo within the chamber. When 10 % DiI-MMB was added (Figure 5.7b) a strong increase in imaging contrast was observed within the sample chamber, which increased further with B-mode transmit voltage (Figure 5.7d) to around 24 times the baseline signal with water at a B-mode transmit voltage of 11.3 V (mean intensity 61,547 signal units vs. 2,534 signal units for water). Using 24 hour old DiI-MMB the increase in contrast was visibly slightly less pronounced (Figure 5.7c), this effect being more obvious when considering the mean signal intensity (Figure 5.7d) which fell by a factor of 3.6 compared to the fresh DiI-MMB sample (mean intensity 16,778 signal units at 11.3 V transmit voltage) but was still over 6 times that obtained with water.

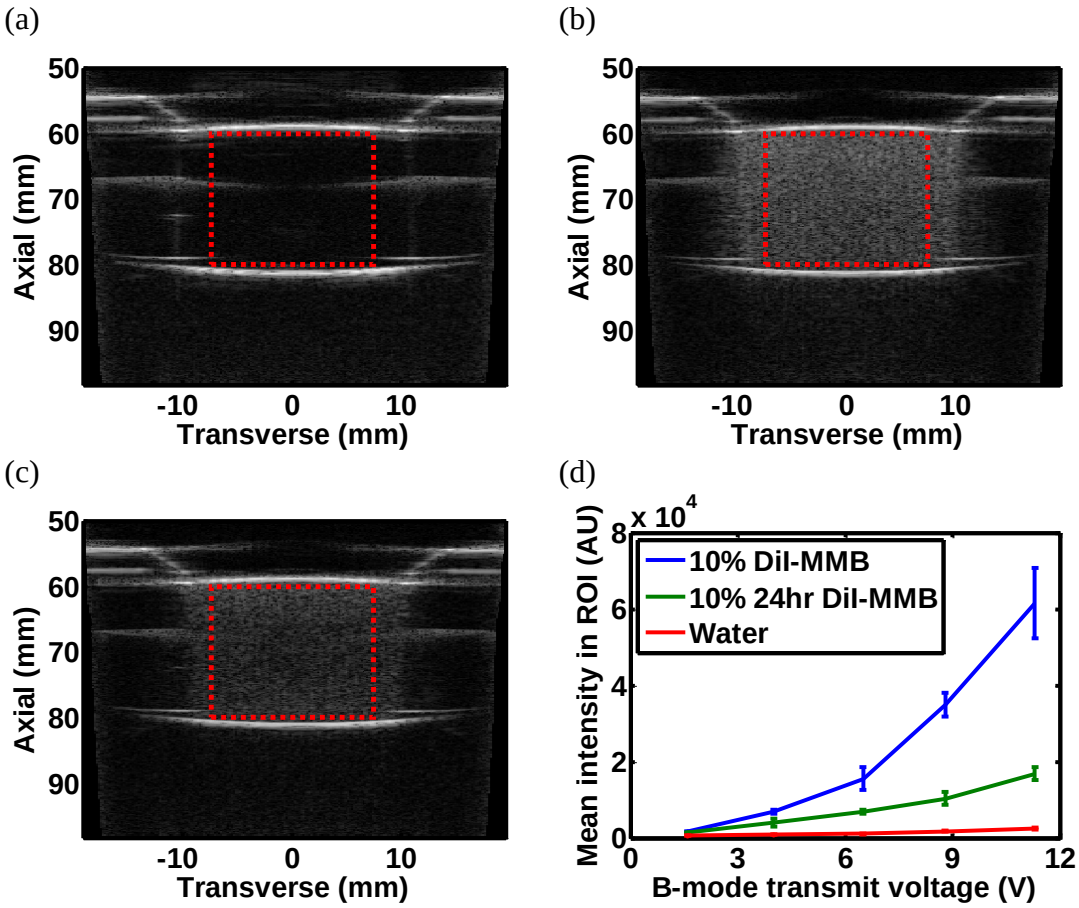


Figure 5.7: Acoustic testing of DiI-MMB under B-mode imaging. A region of interest (ROI) within the sample holder is shown by the red dotted box. (a-c) B-mode images for the sample holder containing (a) water, (b) 10 % by volume DiI-MMB and (c) 10 % by volume 24 hour old DiI-MMB (6.5 V B-mode transmit voltage). (d) Mean B-mode intensity in ROI vs. B-mode transmit voltage

When the 500 kHz focused transducer was activated and PAM data processed (Figure 5.8) only very low amplitude signals (corresponding to the electrical noise floor of the system) were observed using water (Figure 5.8a), with over 1000-fold increase in peak power when DiI-MMB were added (Figure 5.8b) (peak power 0.34 vs. 0.0002 W). The location of the peak in power in the maps correlates well with the previously measured focal point of the HIFU transducer, which was positioned in the centre of the sample chamber. When 24 hour old DiI-MMB was used (Figure 5.8c) the peak power fell by around 10 % (0.30 W) and cavitation appeared over a smaller area in the maps due to the lower concentration of microbubbles. When the ultrasound pressure was varied the maximum source power increased slightly between 1.2 and

1.6 MPa peak negative focal pressure (Figure 5.8d) but did not increase further at 2.0 MPa. In all cases time traces show a rapid rise to a peak power when the HIFU transducer was switched on, followed by decay due to lack of microbubble replenishment in this static setup. The decay in emissions was more rapid using the 24 hour old DiI-MMB which may indicate that the microbubbles were weaker as a result of storage for 24 hours and/or effects of the storage conditions (e.g. temperature change).

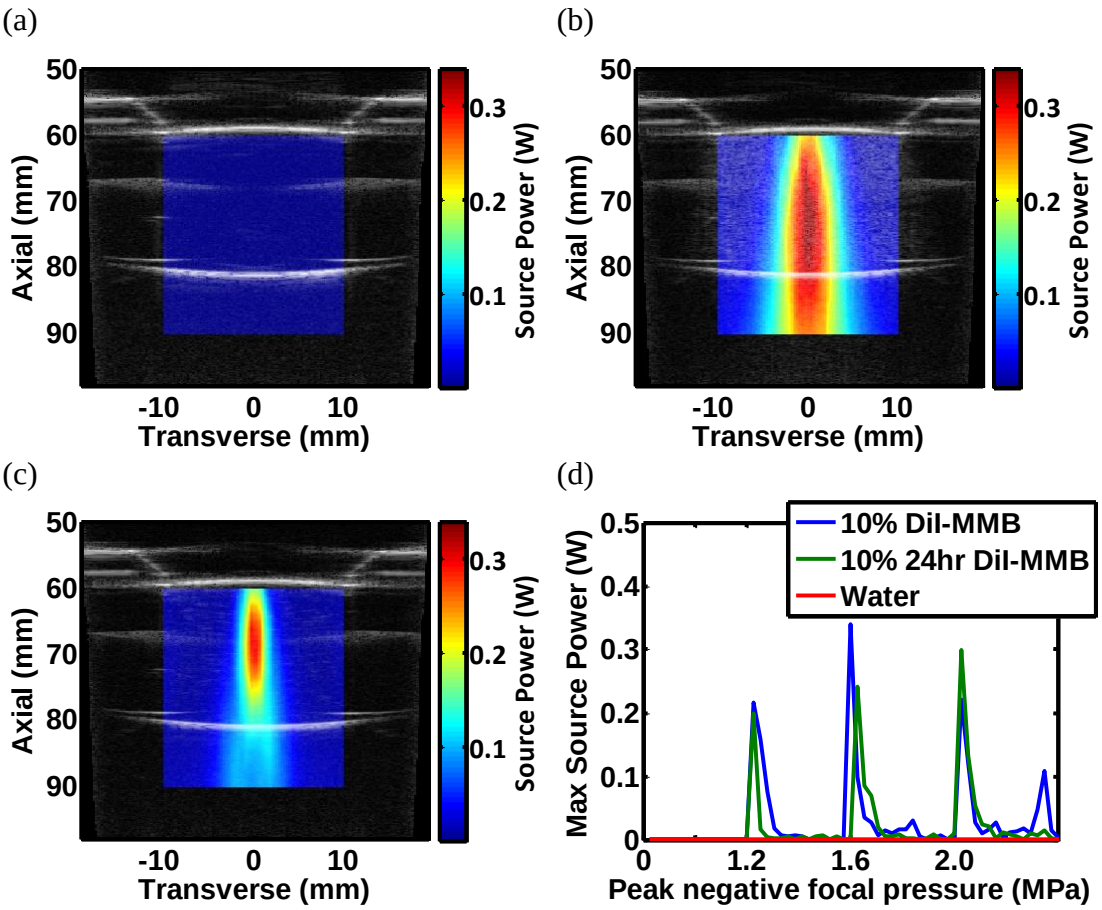


Figure 5.8: Acoustic testing of DiI-MMB under focused ultrasound excitation. (a-c) B-mode images (6.5 V transmit voltage) with PAM overlay showing maps of source power for (a) water, (b) 10 % by volume DiI-MMB and (c) 10 % by volume 24 hour old DiI-MMB (1.6 MPa peak negative focal pressure). (d) Maximum source power over time for 0, 1.2, 1.6, 2.0 MPa peak negative focal pressure. Each pressure shows 30 s of data at 0.5 Hz PRF.

#### 5.3.1.4. Fluorescence in blood

A chart showing the fluorescence measured for 100 µL samples consisting of PBS, mouse blood and known volumes of DiI-MMB is shown in Figure 5.9. The fluorescence intensity is shown against a 1 in 5 dilution curve of DiI-MMB on a logarithmic scale for both plasma samples and resuspended pellets after centrifugation. Background measurements (no DiI-MMB) were subtracted from the readings and all values are below the saturation level of the plate reader. DiI-MMB fluorescence was detectable in plasma down to 0.08 % by volume, which is many times lower than the total dose to be used *in vivo* (c. 10 % assuming 150 µL total injected: using 72 mL blood/kg mouse weight (Diehl *et al.*, 2001) gives a total blood volume of around 1.4 mL for a 20 g mouse). Both sets of samples showed a linear relationship between microbubble concentration and fluorescence intensity; these are plotted on the chart as dashed lines ($R^2$ values 0.98 and 0.99 respectively). In the resuspended pellets the fluorescence readings were lower by a factor of approximately 10 due to dilution as a result of the additional PBS added after centrifugation, and may be further reduced due to presence of insoluble components (e.g. red blood cells) in these samples. To maximise the signal to noise ratio, measurements in plasma were used for estimation of the DiI-MMB concentration in blood in the remainder of experiments.

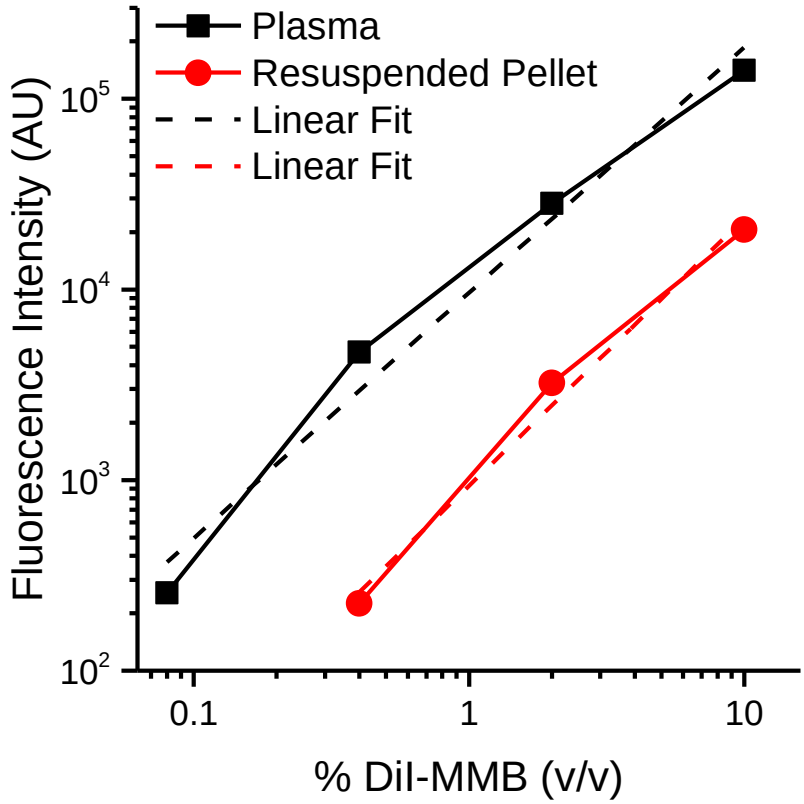


Figure 5.9: *In vitro* testing of fluorescence measurement of DiI-MMB in samples containing PBS and mouse blood (as per *in vivo* protocol) and known quantities of DiI-MMB. Fluorescence intensity measured using a plate reader (gain 2,500 ×) is shown against % DiI-MMB by volume in the samples for both plasma and resuspended pellets after centrifugation. Background measurements were subtracted from all readings. Linear fit for both samples is shown by the dashed lines ($R^2$ values 0.98 and 0.99 respectively).

## 5.3.2. Distribution of magnetic microbubbles *in vivo*

### 5.3.2.1. Fluorescence

The distribution of magnetic microbubbles in mice based on fluorescence measurements from the various organs after experiments is shown in Figure 5.10. Six mice were injected with magnetic microbubbles without therapeutic ultrasound exposure with either a magnet or nonmagnetic bar positioned close to the tumour. Fluorescence readings in blood and organ samples were converted to concentrations of microbubbles in the 100 µL samples tested with the plate reader by comparison with samples containing known quantities. Concentration measurements for blood were scaled up to obtain the total circulating volume based on the weight of each mouse and assuming 72 mL blood/kg mouse weight (Diehl *et al.*, 2001). Organ concentration measurements were scaled up to the total volume in each organ using the volume of buffer added to each (i.e. based on the measured mass of each organ) before homogenisation.

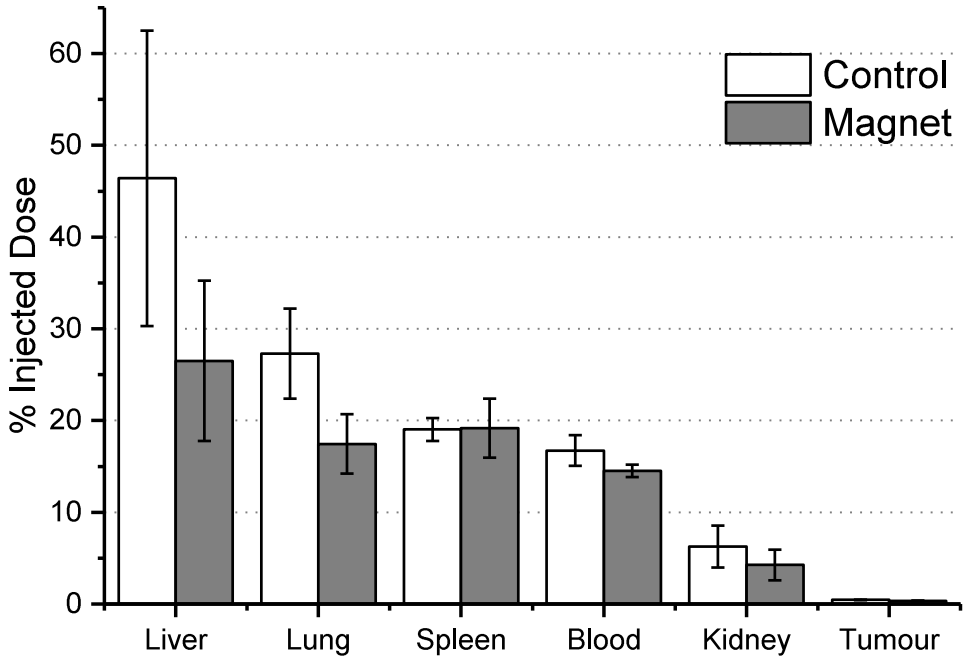


Figure 5.10: Percentage of injected dose in blood and organs of mice following experiments. Mice were injected with microbubbles while either a magnet (n = 3) or nonmagnetic bar (n = 3) were positioned close to the tumour. Mice were aligned with the magnet under B-mode guidance. Therapeutic excitation was not used. Values in the six samples studied may not add up to 100 % due to experimental uncertainties.

Fluorescence readings indicate that a DiI concentration corresponding to an average of 16 % (+/- 2 %) of the injected dose was still found in the blood after 15 minutes, with no significant difference between control and magnet runs ($p = 0.10$). This suggests that microbubble components were still present after several minutes which is a practical timescale for drug delivery applications – for example ultrasound-enhanced blood-brain barrier disruption has been demonstrated using treatments of 20 seconds (Hynynen *et al.*, 2006).

Within the major organs the highest uptake of DiI-MMB was seen in the liver (mean 36 % +/- 16 % of injected dose), with no significant difference between magnet and control runs ($p = 0.13$). This is in line with previous work using magnetic nanodroplets (Cheng *et al.*, 2013) and microbubbles (Barrefelt *et al.*, 2013) which showed high uptake of similar particles in the liver and is believed to involve capture by macrophages (in particular Kupffer cells) in the reticuloendothelial system. Strong uptake in the liver was also suggested by contrast from the iron content of the bubbles under MRI (see below).

The dose found in the lungs (mean 22 % +/- 7 % of injected dose) is encouragingly low (of a similar magnitude to that remaining in the blood after 15 minutes) as microbubbles were delivered via tail vein injection so would return to the heart and pass the lungs before reaching other organs via the systemic circulation – the lungs having been previously shown to trap microbubbles (Butler and Hills, 1979). A significant reduction ($p = 0.04$) was observed between control and magnet treated mice, which implies that magnetic targeting lowered the proportion of microbubbles trapped in the lungs, perhaps by retaining some of the larger microbubbles (which would be both most likely to be trapped in the lungs, and also contain the greatest quantity of magnetic material). Previous *in vivo* histological work using similar magnetic microbub-

bles showed that the concentration in the lungs is initially at its peak value before falling (while that in clearance organs such as the liver and spleen rises over time) (Barrefelt *et al.*, 2013).

The dose found in the spleen in these experiments was lower than that of the liver (mean 19 % +/- 2 % of injected dose) with no significant difference between experimental groups ($p = 0.94$). This is in agreement with previous work which found under histological analysis that the quantity of microbubbles in the spleen was initially low, reaching a peak value after 24 hours and declining thereafter as microbubbles remnants were cleared from circulation (Barrefelt *et al.*, 2013).

Only a small proportion of the injected dose was found in the kidney (mean 5 % +/- 2 %), which is in agreement with previous studies that found limited uptake of similar particles in this organ (Barrefelt *et al.*, 2013; Cheng *et al.*, 2013). Within the tumours only a very small (but detectable) average 0.39 % +/- 0.08 % of the injected dose was found. Therapeutic excitation was not used for this part of the experiments so this measurement represents the background volume of microbubbles or unbound dye retained in tumour vascularity.

Overall for the 6 mice it was possible to recover on average 99 % +/- 22 % of the injected dose. Due largely to reductions in the values for liver and lungs the total recovery was significantly lower (mean 83 % vs. 117 %, $p = 0.03$) in magnet-treated mice.

**5.3.2.2. Magnetic resonance imaging**

MRI images from DiI-MMB treated and saline control mice are shown in Figure 5.11 and Figure 5.12[36]. Slices showing the liver and tumour in each of the mice were selected and the borders of these regions outlined manually. Under T2* weighted imaging iron oxide content appears as negative contrast (Chavhan *et al.*, 2009; Na *et al.*, 2009). This is clearly seen in the liver of the treatment mouse (Figure 5.11a), which appears far darker than that of the control mouse (Figure 5.11b) at a given echo time. This negative contrast results in a lower mean image intensity within the liver and more pronounced decay with increasing echo time compared to the control mouse (Figure 5.11c), suggesting that a significant proportion of the magnetic material from the bubbles is captured by the liver. The standard deviation of the image intensity within the liver (Figure 5.11d) also declines with echo time (in contrast to the control mouse where it increases slightly) suggesting that the magnetic material was homogenously distributed throughout the organ (therefore masking the normally inhomogeneous appearance of the liver seen in the control mouse). These results are in agreement with previous work with PVA-based microbubbles containing iron oxide, which showed negative contrast in the liver under T2* weighted imaging as early as 10 minutes from injection (Barrefelt *et al.*, 2013). As outlined above significant fluorescence from the DiI-stained lipid was also observed in the liver.

Dark areas of negative contrast were visible over approximately one third of the area of the tumour in the treatment mouse (Figure 5.12a), while the control mouse tumour appears largely homogenous (Figure 5.12b). With increasing echo time the mean intensity in the tumour of the treatment mouse declined slightly compared to the control mouse (in which the mean intensity was approximately flat or slightly rising) (Figure 5.12c). The standard deviation of image intensity (Figure 5.12d) in the treat-

[36] MR imaging was conducted by Sean Smart

ment mouse was greater than that in the control mouse and increased with echo time due to the inhomogeneous distribution of magnetic particles. This implies that a detectable quantity of magnetic material from the microbubbles was retained in the tumour. Notably, the ultrasound duty cycle used in these experiments was very low (0.01 %), and the magnet was not applied to the tumour for 5 minutes between the end of experiments and mouse sacrifice. The inhomogeneous distribution of particles in the tumour and clustering around the centre are also notable as this coincides with the region exposed to both ultrasound and the magnetic field.

It is important to note that the primary aim of this part of the study was to establish whether MRI imaging of DiI-MMB was feasible at the concentrations used and subject to the constraints of these *in vivo* experiments[37]. As such only two mice at the extremes of the treatment options (one saline treated control, the other treated with DiI-MMB, focused ultrasound and magnet) were tested. The results in this section demonstrate that MR imaging is feasible under these conditions and show the expected negative contrast as a result of the iron oxide content of the microbubbles. Future studies should include additional controls (e.g. DiI-MMB + focused ultrasound without magnet) and multiple repeats per condition.

[37] Due to equipment limitations MR imaging was conducted at a separate facility post-mortem

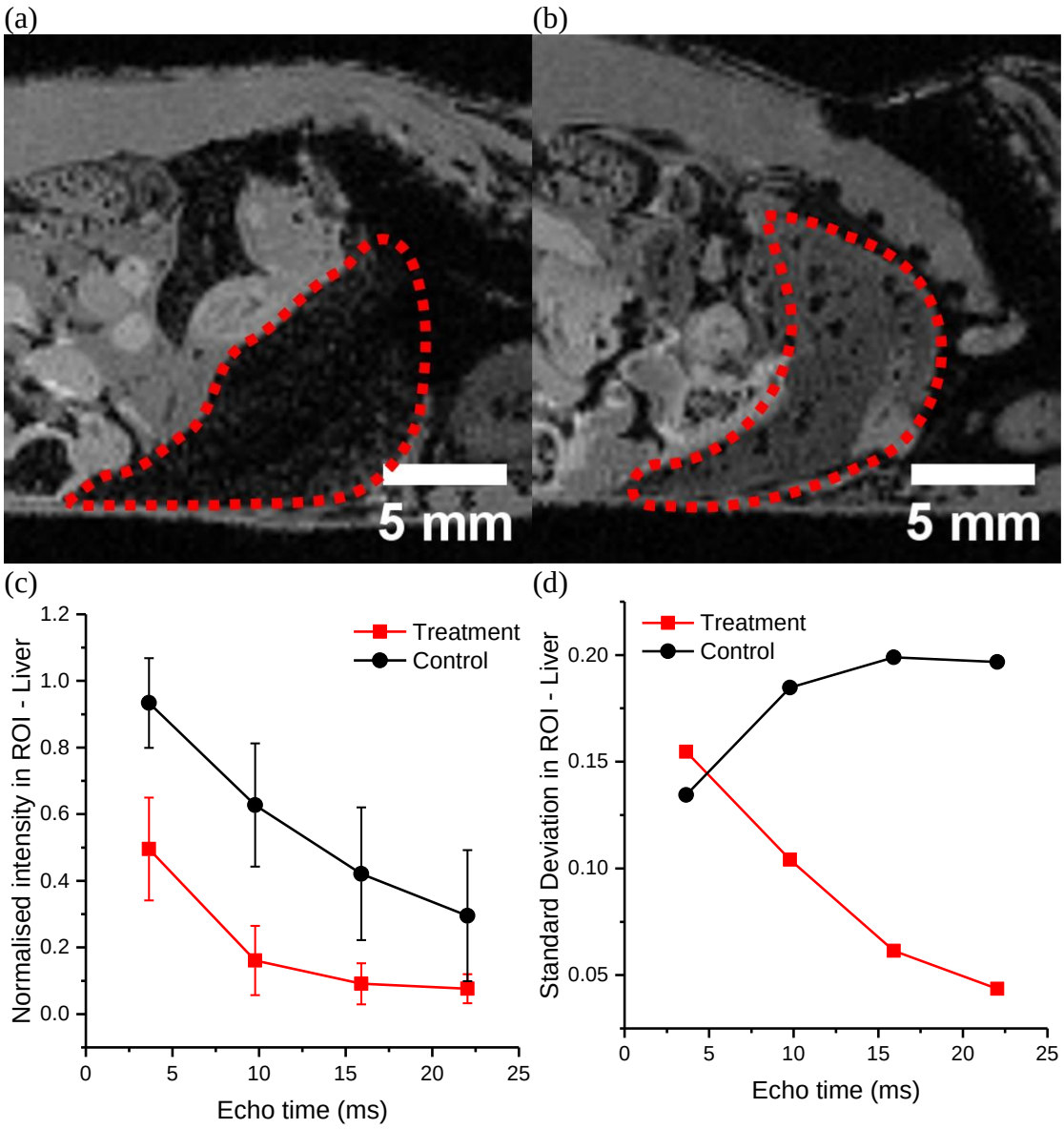


Figure 5.11: MRI images and analysis for liver of treatment (DiI-MMB, focused ultrasound + magnet) and control (saline) mouse. MRI images showing liver of (a) treated mouse and (b) control mouse (TE = 9.78 ms). Regions of interest (ROI) selected for analysis are highlighted by the red dotted outlines. For display purposes MRI images were cropped and enlarged by a factor of 5 using bicubic interpolation; analysis was performed on the raw images. Measurements were normalised using the mean intensity at each echo time in nearby regions of muscle. (c) Normalised intensity and (d) standard deviation in liver ROI for treatment and control mouse vs. echo time.

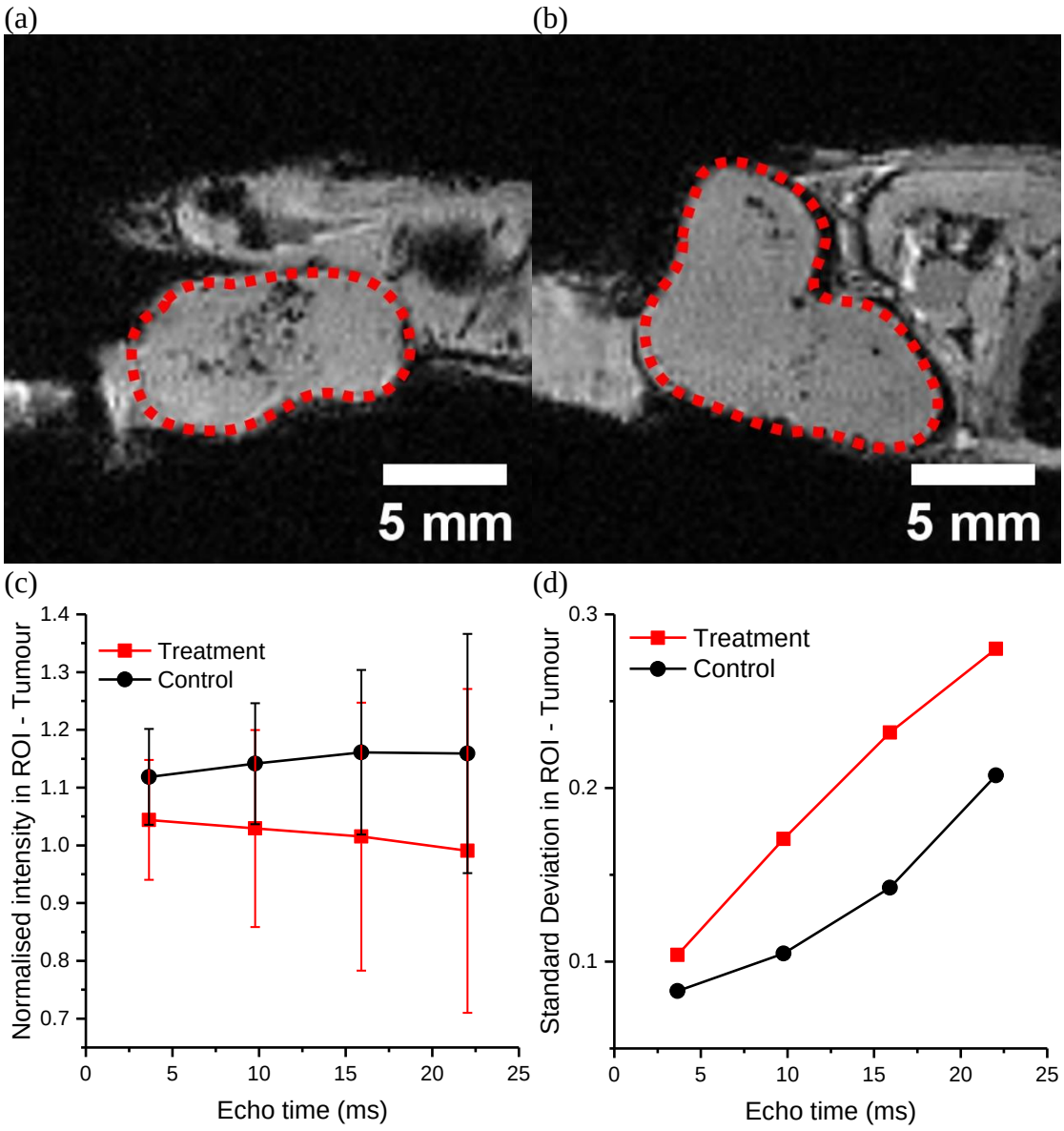


Figure 5.12: MRI images and analysis for tumour of treatment (DiI-MMB, focused ultrasound + magnet) and control (saline) mouse. MRI images showing tumour of (a) treated mouse and (b) control mouse (TE = 15.91 ms). Regions of interest (ROI) selected for analysis are highlighted by the red dotted outlines. For display purposes MRI images were cropped and enlarged by a factor of 5 using bicubic interpolation; analysis was performed on the raw images. Measurements were normalised using the mean intensity at each echo time in nearby regions of muscle. (c) Normalised intensity and (d) standard deviation in tumour ROI for treatment and control mouse vs. echo time.

### 5.3.3. *In vivo* cavitation threshold of magnetic microbubbles

B-mode and PAM data for the *in vivo* pressure ramp experiments are shown in Figure 5.13. At 1.2 MPa peak negative focal pressure (Figure 5.13a) some cavitation was observed within the tumour (peak power 29.2 mW). Over the duration of the experiment (Figure 5.13d, blue line) cavitation was sporadic, with minor peaks visible at the injection times (21.5, 10.8 and 1.5 mW at 1, 4 and 7 minutes respectively). Spectra of the received signal averaged over the duration of the experiment (Figure 5.13e, blue line) showed the 500 kHz excitation frequency and harmonics at 1 and 1.5 MHz only.

At 1.6 MPa peak negative focal pressure (Figure 5.13b) the amplitude of cavitation emissions was increased by a factor of 5 (peak power 152.9 mW) and clearly distinct peaks were visible at the injection times (Figure 5.13d, green line; peak values 152.9, 83.0, 48.7 mW at 1, 4 and 7 minutes). Spectra of the received signal (Figure 5.13e, green line) now showed a typical microbubble response (Leighton, 1994) with multiple harmonic peaks visible up to several MHz, smaller ultraharmonic peaks (commonly associated with stable cavitation), and an increase in the broadband signal level (associated with inertial cavitation).

Finally, at 2.0 MPa peak negative focal pressure (Figure 5.13c) multiple regions of cavitation were observed close to the ultrasound focus, with lower peak amplitude (peak power 81.1 mW) compared to that at 1.6 MPa. The evolution of this behaviour over time (Figure 5.13d, red line) shows that cavitation occurred immediately from the beginning of the experiment, even before microbubbles were injected, with some step changes visible at the points when the mouse was moved (3, 6 mins) thus placing a different region of tissue at the focus. The spectrum (Figure 5.13e, red line) was dominated by broadband noise.

The results for the three pressure steps may be summarised by extracting the cavitation power values from the time trace (Figure 5.13d) following each injection (i.e. at 1, 4 and 7 mins) and comparing this to the background cavitation 1 minute before each injection (0, 3, 6 mins). This is shown in Figure 5.13f. A large increase in the mean source power on injection was observed at 1.6 and 2.0 MPa compared to 1.2 MPa, however this was only above the background response at 1.6 MPa. These results are consistent with the *in vitro* tests (Section 5.2.2.4) and suggest that increasing the pressure from 1.2 to 1.6 MPa resulted in a higher amplitude response, probably due to a greater number (and area) of microbubbles being above the threshold for cavitation. At 2.0 MPa cavitation was initiated even without microbubble injection, which implies that the inertial cavitation threshold for tissue was exceeded. 2.0 MPa is therefore unsuitable for these experiments as the acoustic emissions are no longer correlated with microbubble injection. In order to maximise the signal to noise (and avoid endogenous cavitation) a 1.6 MPa peak negative focal pressure was selected for use in subsequent experiments. This is similar to that used previous studies at this frequency with SonoVue® (Choi *et al.*, 2014; Coviello *et al.*, 2015).

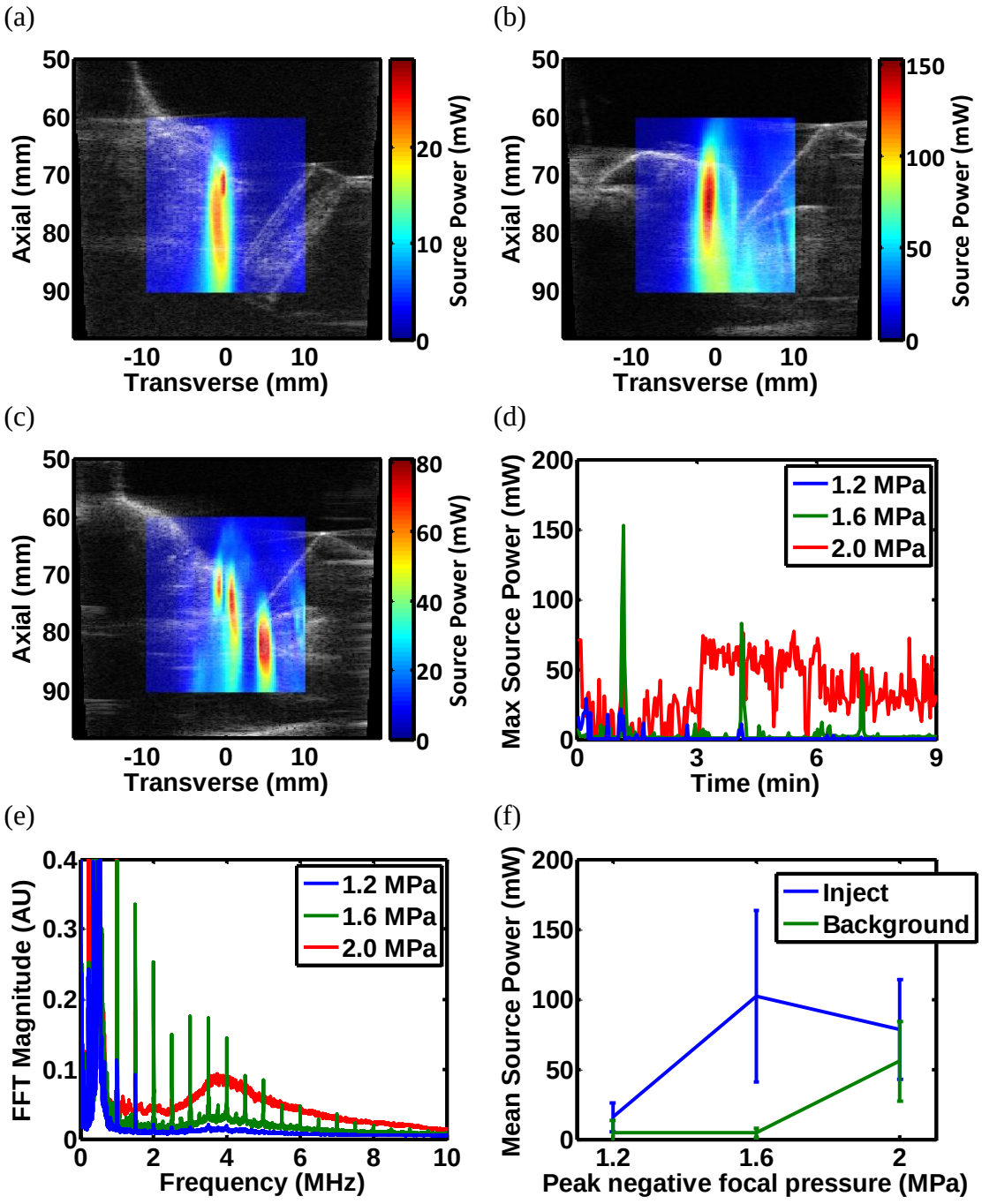


Figure 5.13: B-mode and PAM results for *in vivo* pressure ramp. (a-c) B-mode with PAM overlay showing peak source power for 1.2, 1.6 and 2.0 MPa peak negative focal pressures. The mouse body (left), tumour (centre) and nonmagnetic bar (right) are visible in the B-mode image. The rightmost area overlapping with the metal bar in (c) is an artefact caused by reflection against the metal surface. (d) Maximum source power over time. Mice were injected at 1, 4 and 7 mins and moved at 3 and 6 mins. (e) Averaged spectra for the 3 pressures, (f) Mean and standard deviation of source power at the 3 injection points (1, 4, 7 mins) and background cavitation 1 minute before each injection (0, 3, 6 mins).

### 5.3.4. Magnetic microbubbles compared to SonoVue® *in vivo*

B-mode and PAM data comparing the response of a new batch of DiI-MMB to freshly resuspended SonoVue® are shown in Figure 5.14. Spatial maps showing the maximum source power show a very similar response (Figure 5.14a-b) between the two agents. Over the duration of the experiment (Figure 5.14c) peaks in the maximum source power are clearly visible at the three injection points. The peak values for DiI-MMB were greater than those of SonoVue® by 5-10 % in 2/3 cases (peak values 291.4, 261.8, 216.8 for DiI-MMB; 318.3, 272.2, 155.9). The initial decline following the peak was rapid for both agents due to clearance of microbubbles from the circulation (Figure 5.14d), falling to 19 % (DiI-MMB) and 27 % (SonoVue®) of the peak value within 4 seconds. Following this initial rapid decay the amplitude of cavitation power fell more slowly, reaching the baseline level from before microbubble injection within approximately 30 s (DiI-MMB) and 60 s (SonoVue®).

These results suggest that DiI-MMB can be used to induce a similar cavitation response under focused ultrasound *in vivo* to SonoVue® in the absence of a magnetic field. The peaks in cavitation power for DiI-MMB were of comparable amplitude to SonoVue®, following which their response decayed slightly faster. However, cavitation effects tend to be threshold-dominated – for example Frenkel *et al.* (1999) examined the effects of ultrasound intensity and exposure duration on cavitation damage to skin, and found that no damage occurred at the lowest intensities regardless of exposure time (while at higher intensities damage increased with time). For this reason the longer duration of much lower-amplitude cavitation (less than 10 % of the peak value) observed with SonoVue® is likely to be of limited therapeutic relevance. The rapid decay in response for both agents compared to the phantom experiments (Chapter 3) suggests that biological clearance mechanisms (as well as other *in vivo* factors such as

elevated temperature and presence of whole blood) dominated over destruction of microbubbles by ultrasound: variation of the ultrasound conditions (e.g. increasing burst length and PRF over a shorter treatment duration) should be considered in future studies to optimise the effect of the microbubbles during their short circulation time.

Compared to SonoVue®, DiI-MMB thus promote overall similar cavitation behaviour *in vivo*, with the additional benefits of facilitating MRI contrast and payload delivery (in this case fluorescent dye). In the following section the effects of a magnetic field and reduced microbubble concentration on the cavitation response of DiI-MMB are evaluated.

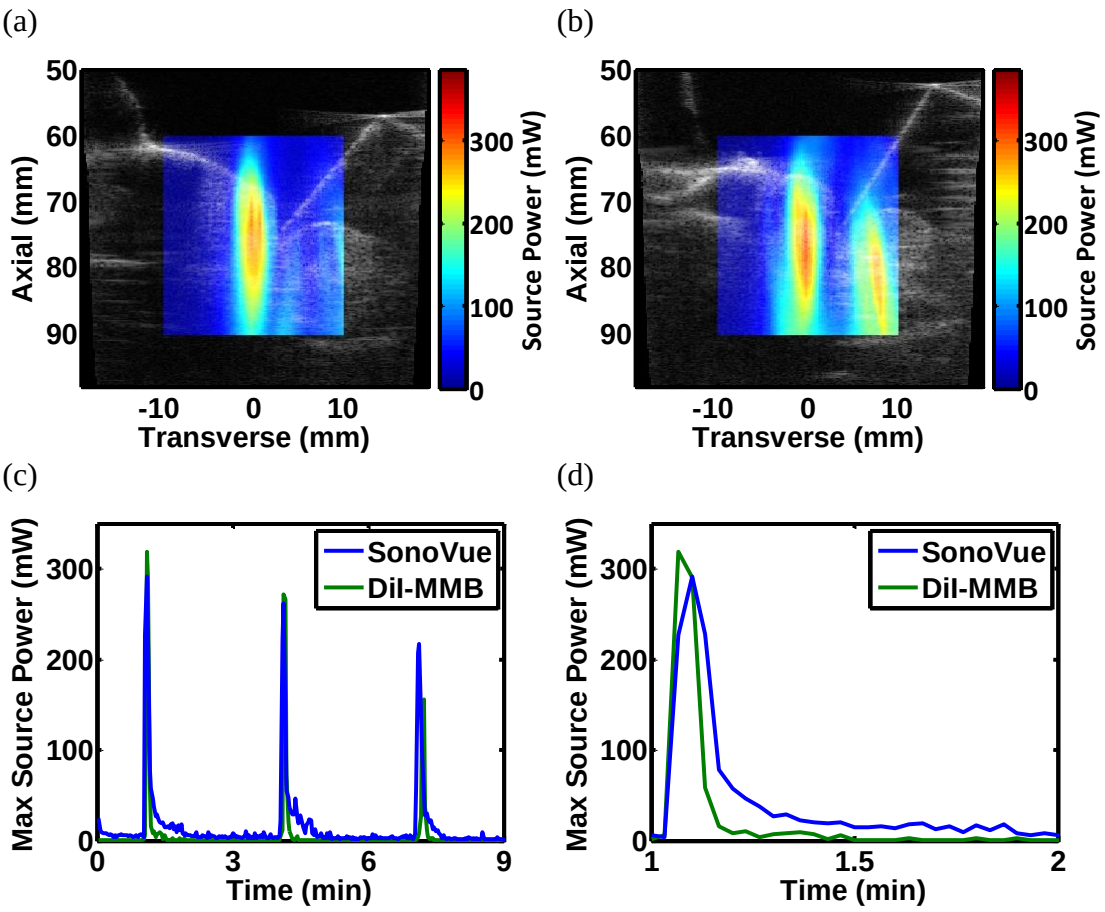


Figure 5.14: Comparison of DiI-MMB to SonoVue® *in vivo*. B-mode images with PAM overlay for (a) SonoVue® and (b) DiI-MMB; maximum source power over time for SonoVue® and DiI-MMB (c) over the whole 9 minute experiment and (d) for 1 minute following the first injection. The rightmost area overlapping with the metal bar in (b) is an artefact caused by reflection against the metal surface.

### 5.3.5. Effects of magnet and microbubble concentration *in vivo*

B-mode and PAM data showing the response of DiI-MMB *in vivo* with and without application of a magnet, and for a sample of DiI-MMB with depleted microbubble concentration is shown in Figure 5.15. Spatial maps showing the maximum source power for DiI-MMB in the presence of a magnet (Figure 5.15a) shows a more intense peak in the response compared to the case without magnet shown previously (Figure 5.14b) and with slightly higher peak amplitude (increase of 5.4 %; 335.5 vs. 318.3 mW). The depleted microbubble sample (Figure 5.15b) shows very little response as expected (peak power 16.5 mW), this run being used as a lower-cavitation control with otherwise similar chemical composition. Over the duration of the experiment (Figure 5.15c) peaks in the maximum source power were again clearly visible at the three injection points for DiI-MMB with and without the magnet, with negligible background cavitation in the depleted microbubble concentration control run. The peak values for DiI-MMB with a magnet was greater than those without on the first injection, which produced the highest response in both experiments, but was lower for the following 2 injections (peak values for DiI-MMB with magnet 335.5, 251.7, 86.6 mW; 318.3, 272.2, 155.9 mW without). The peak in response on injection (Figure 5.15d) persisted for approximately 15 % longer in the run with magnet (around 2 seconds over a peak of around 14 seconds duration). At 6 s from the start of the peak DiI-MMB with magnet was at 160.7 mW (47.9 % of peak) while DiI-MMB without magnet was at 59.0 mW (18.5 % of peak). The total time to return to the undisturbed background value before injection was ~30 s in both cases.

In these results the effect of magnetic targeting on the cavitation behaviour of DiI-MMB *in vivo* appears to be relatively minor, although small increases in the peak cavitation power and duration of activity were observed. This suggests that biological

clearance appears to dominate over retention of microbubbles by the magnetic field. However, increasing the pulse repetition frequency in future studies to optimise use of the microbubbles during their circulation time could increase the magnitude of any effect, as well as increasing the number of time points in the PAM data.

Nonetheless, even if the effect on cavitation is relatively small, due to their interaction with the magnetic field DiI-MMB could still result in increased bioeffects via mechanisms such as magnetofection (Section 2.3.2). To establish whether this holds in these experiments in the following section the cavitation response assessed from PAM data is compared with the fluorescence recorded in the tumours.

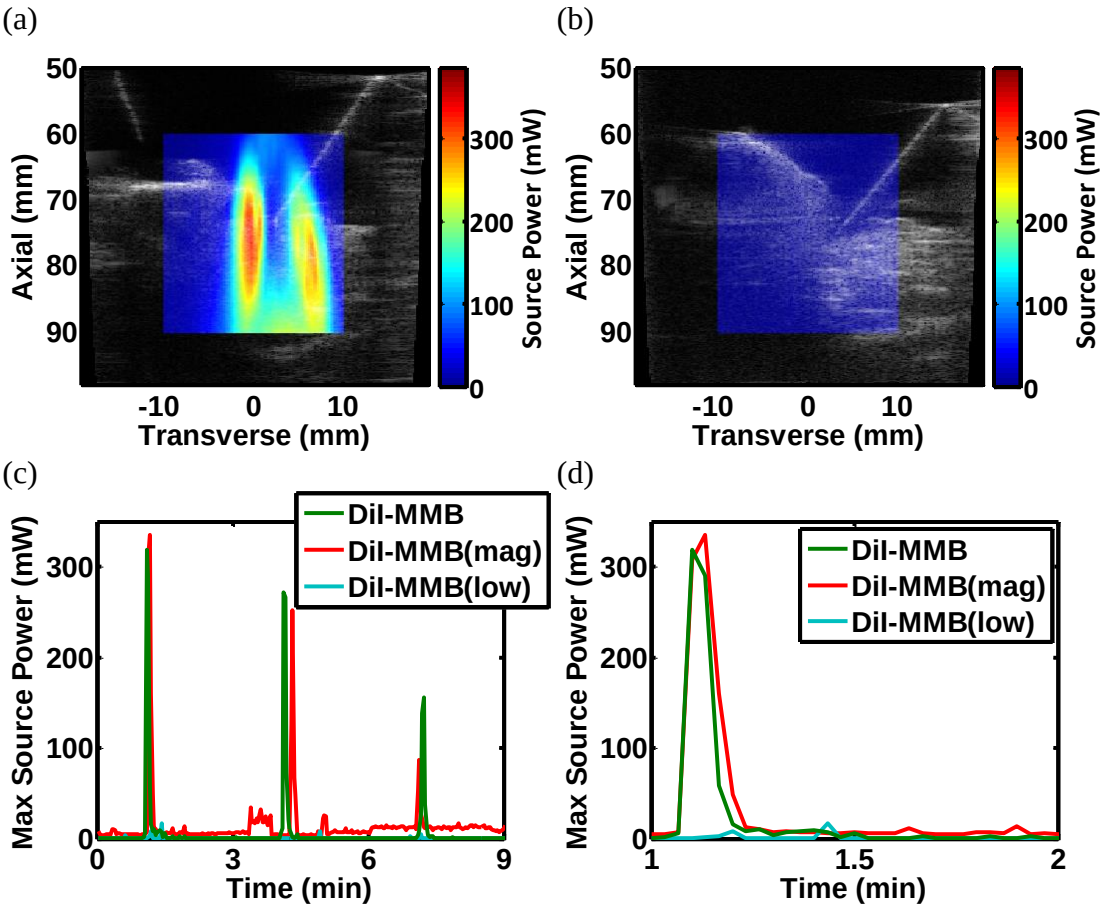


Figure 5.15: Effect of magnet and variation of DiI-MMB concentration *in vivo*. B-mode images with PAM overlay for (a) DiI-MMB with magnet and (b) depleted (24 hour old) DiI-MMB; maximum source power over time for DiI-MMB with and without magnet and at depleted concentration (c) over the whole 9 minute experiment and (d) for 1 minute following the first injection. The rightmost area overlapping with the magnet in (a) is an artefact caused by reflection against the metal surface.

### 5.3.6. Correlation between PAM and fluorescence in tumour *in vivo*

The maximum cavitation power from the PAM data and corresponding microbubble dose found in tumours from fluorescence measurements are shown in Figure 5.16. As per the experimental protocol (Section 5.2.6) the SonoVue® and three DiI-MMB data points each represent cavitation and fluorescence data from one mouse per condition. The mean and standard deviation of fluorescence readings from the six mice monitored with B-mode imaging only (cavitation source power = 0) in the distribution study (Section 5.3.2.1) are also shown for comparison.

The low level of cavitation observed in the depleted DiI-MMB sample resulted in a similarly low percentage of the injected dose being found in the tumour (0.30 % ± 0.04 %) which was within the range of the six mice monitored with B-mode imaging only (using a different batch of DiI-MMB) in the distribution study (0.39 % ± 0.08 %; Section 5.3.2.1). A significantly lower background fluorescence reading (corresponding to an implied DiI-MMB dose of 0.13 ± 0.01 %) was observed using SonoVue®. SonoVue® does not contain fluorescent dye so this value being non-zero may be due to minor variability in tissue autofluorescence between the treated mice and that used for preparation of standard curves. Using DiI-MMB without a magnet the mean cavitation power over the 3 injections was similar to that of SonoVue® (249 mW for DiI-MMB vs. 257 mW for SonoVue®). The standard deviation using DiI-MMB was greater than SonoVue® as the cavitation response on subsequent injections declined to a greater extent (as shown in Figure 5.14c-d), possibly due to effects such as settling of microbubbles in the syringe or tubing which could be remedied by small changes in the experimental protocol. Nonetheless, the dose in the tumour more than doubled compared to the depleted DiI-MMB sample to 0.63 % ± 0.02 %. The addition of a magnet was accompanied by a 19.5 % rise in fluorescence to a dose of 0.75 % ± 0.03

%, while the maximum cavitation power increased by 5.4 %. Note that the *mean* cavitation power fell (9.7 %) in the case with the magnet, due again to the decline in response on subsequent injections.

These results suggest that microbubble-induced cavitation resulted in a greater quantity of the fluorescent dye attached to the microbubbles being deposited in the tumour. Previous studies have attributed such effects to extravasation (Bazan-Peregrino *et al.*, 2013) and/or microscopic vessel damage (Hwang *et al.*, 2006) as a result of inertial cavitation: the spectra of cavitation emissions observed in these *in vivo* experiments was broadband in nature, suggesting this could be the dominant mechanism here. DiI-MMB resulted in cavitation with similar maximum amplitude to SonoVue®, and were associated with a significant (2-fold) increase in the fluorescence dose found in the tumour compared to samples injected with the same components but depleted bubble concentration. The addition of a magnet resulted in a small increase in the peak cavitation power and duration of activity, as discussed previously (Section 5.3.5). The rise in fluorescence under the influence of the magnet was larger than the effect on the acoustic signal, which may be due to the physical effects of the magnetic field (e.g. pulling bubbles closer to vessel walls) in a similar manner to magnetic-field mediated delivery to cells in the absence of ultrasound, i.e. magnetofection (Section 2.3.2).

It is important to note that the ultrasound conditions used in this study were particularly mild (100 cycles per burst at 0.5 Hz PRF, duty cycle 0.01 %) compared to duty cycles of 6-90 % employed in previous studies which aimed to promote extravasation (Bazan-Peregrino *et al.*, 2012). As the primary aim of this study was not extravasation but rather to establish whether the improved DiI-MMB formulation could promote cavitation *in vivo* in a localised manner (no active therapeutic was used at

this stage) this shorter burst length was intended to reduce microbubble destruction by ultrasound and therefore improve circulation time. However, the rapid decline in cavitation response still observed here *in vivo* (on the order of 30 seconds for DiI-MMB) and relatively similar response of SonoVue® in the same setup using 50,000 cycle pulses (Graham, 2015) compared to 100 cycles here suggest that biological clearance mechanisms are by far the dominant factor. These findings should be considered in the design of future drug delivery studies to maximise the impact of the microbubbles during their circulation time, for instance by increasing the burst length and/or PRF over a shorter total treatment time.

Nonetheless, even under the ultrasound conditions used here a significant increase in fluorescence in the tumour compared to control experiments suggests that ultrasound-induced cavitation of DiI-MMB did result in extravasation of fluorescent material from the bubbles (and that this may be further improved using magnetic targeting), while the discrete hypointense regions observed under MRI suggests the same is true of their iron content. Optimisation of the ultrasound conditions, addition of therapeutic drugs and investigation of the effects on distribution and treatment efficacy should be considered in future studies.

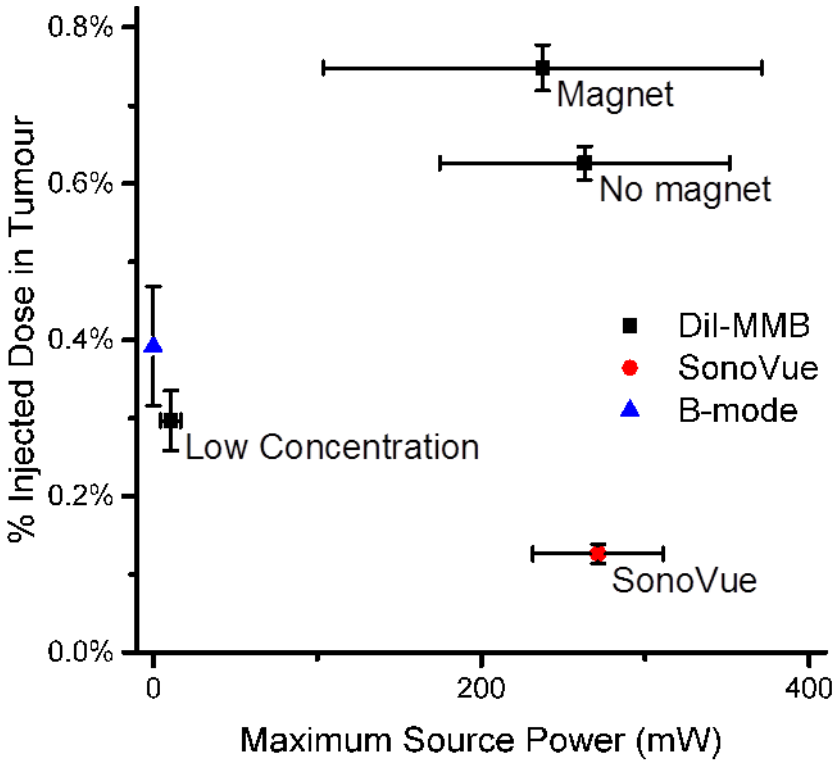


Figure 5.16: PAM vs. fluorescence in tumour. X-axis shows mean ± standard deviation of the maximum source power from 3 injections measured in real time during each experiment. Y-axis shows mean ± standard deviation of the percentage of injected dose found in each tumour derived from 3 tumour samples taken after completion of each experiment. Equivalent data for SonoVue®-treated and mice monitored with B-mode imaging only (no HIFU; cavitation source power = 0) are shown for comparison by the red and blue points respectively.

### 5.3.7. Limitations of the *in vivo* study

The study presented in this chapter has several limitations. In particular, the sample size was small (n = 1 mouse in some experiments). While multiple readings were taken (e.g. taking fluorescence measurements for several organ samples, or PAM following several injections) these cannot replace independent trials in several animals per condition. In the mice examined using MRI only two mice at the extremes of the experimental conditions (one saline-only control, the other treated with MMB, US and magnet) were included in this preliminary trial, which does not allow evaluation of the effects of any of these factors individually. Both MRI and fluorescence measurements were conducted at a single time point post-mortem, so cannot provide any temporal information on the distribution of microbubbles in a living animal, or distinguish between intact microbubbles and microbubble components. While the fluorescence protocol used here is clearly not compatible with multiple time points per animal (with the possible exception of blood), MRI could be used to study the distribution of magnetic components over time in a living animal. As a 'lower cavitation' control an aged sample of microbubbles was used (rather than diluted fresh bubbles) in order to retain a similar chemical composition, however this may not take into account other changes over time or effects of storage conditions. Finally, the PAM data suggest that microbubbles were cleared quickly from the circulation, such that the acoustic conditions used in the study were clearly not optimal. Nonetheless, the results presented here provides the first *in vivo* evidence for the effects of magnetic targeting on cavitation behaviour (and resulting deposition of material in tissue) which suggest that further study is warranted.

## 5.4. CONCLUSIONS

In this chapter the *in vivo* distribution and ability to promote cavitation of fluorescently labelled magnetic microbubbles (DiI-MMB) was investigated in a murine tumour model. It was shown that fluorescence from the microbubbles could be detected in blood and organs from treated mice, while their iron content was visible as negative contrast on MRI. Cavitation was observed using passive acoustic mapping under 0.5 MHz focused ultrasound excitation and found to be comparable to that produced by a commercial contrast agent, SonoVue®, with the additional benefits of facilitating MRI contrast and ability to carry a payload (here demonstrated using a fluorescent dye). Cavitation induced by the microbubbles and magnetic targeting were both found to be associated with increased fluorescence in the excised tumours. This provides evidence both for the magnetic microbubbles as a means of facilitating drug delivery *in vivo* and for PAM as a means of noninvasively monitoring this process.

CHAPTER 6

# CONCLUSIONS AND FUTURE WORK

The overall aim of this thesis was to combine two promising individual areas of research from the field of biomedical acoustics: magnetic microbubbles and passive acoustic mapping.

In this chapter the overall conclusions of the work are summarised and compared to the aims of the work outlined in Section 1.8.2. Limitations of the current work and other suggestions which warrant future investigation are identified.

## 6.1. CONCLUSIONS

In Chapter 2 previous work relevant to PAM and magnetic microbubbles was reviewed. The development of PAM was outlined from its roots in basic acoustics up to the more involved beamforming methods employed to improve performance. The range of previous applications suggested PAM could be a useful technique for monitoring of magnetic microbubbles. A review of the literature covered previous work with magnetic microbubbles and key design considerations which could be used to improve them, and identified several potential clinically relevant targets for their application. Notably, PAM had not been applied to monitor the effects of microbubble targeting, and there had been no investigation of the cavitation behaviour of magnetic microbubbles. A gap in knowledge and potentially novel clinical application were thus identified.

The experimental work of this thesis was contained in Chapters 3, 4 and 5, which included the application of PAM and magnetic microbubbles in tissue phantoms, *in vitro* treatment of cell lines and *in vivo* animal models respectively.

With respect to the five aims of the current work outlined in Section 1.8.2, Chapter 3 successfully addressed aims 1-3. The response of magnetic microbubbles to focused ultrasound excitation was investigated using PAM under controlled laboratory conditions in tissue phantoms. Magnetic localisation of microbubble-induced cavitation activity was successfully achieved and could be resolved using PAM (aim 1), where it manifested as shifts in the spatial distribution and increases in the intensity and sustainability of cavitation activity under the influence of a magnetic field (aim 2). Targeting efficacy was maintained under clinically relevant flow conditions, resulting in an increase in the energy of cavitation emissions on the order of 2-5 times

that without targeting – with similar effects as doubling the injected microbubble dose – both of which could be clinically useful for cavitation-enhanced therapies (aim 3).

In Chapter 4 the experimental methods were further refined and successfully applied to a number of *in vitro* models for enhancement and monitoring of drug delivery (aim 4). Initial results using a commercial parallel-plate cell culture device showed increased uptake of fluorescently tagged siRNA into cells treated with ultrasound, magnetic microbubbles and magnetic field, which could be correlated to their acoustic emissions using PAM. Marked improvements to the cell culture system, microbubble formulations and acoustic setup were made and subsequently used for further experiments involving siRNA transfection and paclitaxel delivery. Using a more robust siRNA model, fluorescence knockdown was achieved under the synergistic effects of ultrasound and the magnetic field and not in control experiments in which any of these components were omitted or using a scrambled siRNA control. In some of the siRNA experiments a significant loss in cell viability was observed, but this appeared to be associated to the action of the siRNA (and not the ultrasound or microbubbles).

With magnetic nanodroplets, improved efficacy of the chemotherapeutic drug paclitaxel was also demonstrated using the same model, while further investigation of the acoustic behaviour of the nanodroplets identified several possible avenues for improving their performance in future work. Comparing the biological results from each of these experiments with the corresponding PAM data clearly demonstrated the utility of PAM as a monitoring method for cavitation-enhanced therapies. Maps showing the total energy of cavitation emissions summed over the duration of each experiment were presented. The peak values of these maps – essentially a measure of the spatial peak, temporal average cavitation ‘dose’ for each experiment – was associated with greater therapeutic effect (fluorescence uptake, fluorescence knockdown, and cell-kill

respectively). In the experiments in which fluorescence distribution was also measured (Section 4.3.2) reasonable spatial match in fluorescence and PAM data was observed between the multiple treatment sites. The increase in cavitation dose was also evident in other parameters which can be obtained from the PAM data such as evolution of cavitation power over time and spectra of the emissions.

Finally, in Chapter 5 the techniques developed in the previous chapters were brought one step closer to clinical relevance by testing *in vivo* (aim 5). The improved magnetic microbubble formulation was tested for the first time in a tumour-bearing mouse model. Fluorescence from the labelled microbubbles was used to assess their distribution in the blood and organs of treated mice, while iron content from the microbubbles was also found to be visible as negative contrast on MRI. Cavitation behaviour of the microbubbles was found to be of similar magnitude to that of the commercial contrast agent SonoVue®, with the additional benefits of facilitating MRI contrast and payload delivery (in this case fluorescent dye). Cavitation induced by the microbubbles and magnetic targeting were both associated with increases in the fluorescence and MRI contrast found in tumours.

Overall, each of the aims of this thesis outlined in Section 1.8.2 has been met. It was shown for the first time that magnetic localisation of microbubble-induced cavitation could be achieved under focused ultrasound excitation and detected using PAM, manifesting as increased intensity and sustainability of cavitation activity. It was hypothesised that this enhanced cavitation could translate to therapeutically relevant benefits, and that PAM could be used to monitor this process. On the basis of several *in vitro* models both hypotheses appear to be supported, while numerous improvements were made to the microbubble formulations and experimental setup to push the system towards a viable tool for *in vivo* (and eventual clinical) use. In particular, PAM

was used to monitor therapy in real-time during the experiments, confirming that the agents used were acoustically active, cavitated under the therapeutic ultrasound conditions used, and that this cavitation activity took place in the desired treatment location. Increasing cavitation 'dose' – manifesting as greater total energy, higher maximum power and/or enhanced duration in the PAM data – was associated with enhanced bioeffects. Finally, new microbubble agents were tested for the first time *in vivo*, their distribution studied, and the *in vitro* findings tested in an animal model.

## 6.2. FUTURE WORK

As indicated throughout the thesis numerous areas for future work were identified over the duration of the project which are summarised below.

A major limitation which applies throughout the thesis concerns the magnets used to facilitate targeting, which were either single-element or relatively simple magnet arrays constructed from small permanent magnets. While the N52 grade neodymium magnets used are very strong (~1.5 T) their fields decay rapidly with distance (Appendix C): e.g. to around 0.1 T (~8 mm from the magnet surface) in the flow channel of Chapter 3. This limited the parameter space under which targeting could be effective in the characterisation experiments, and reduced the likelihood of success in those (e.g. *in vivo*) scenarios in which variables such as flow rate or depth of target were impractical or impossible to control. The small magnets used in this thesis were suitable for targets near the surface (<10mm depth) such as the tumour model employed in Chapter 5 – indeed, on the scale of a mouse small magnets were explicitly *required* for selective targeting – but are clearly unsuitable for deeper targets as would be required for clinical translation. Development of deep magnetic targeting systems on a human scale is clearly a nontrivial problem. It is important to note that the main challenge in achieving deep targeting is not so much achieving sufficient field *strength*

(for which there is established technology e.g. superconducting magnets for MRI), but achieving sufficient field *gradient*. However, examples in the literature such as the Stereotaxis magnetic navigation system (in which large permanent magnets are used to manipulate catheters within the body) (Kiemeneij *et al.*, 2008) or proof-of-concept studies with flowing particles in an MRI scanner (retrofitted with stronger gradient coils) (Mathieu and Martel, 2010) suggests this should be possible.

Concerning the magnetic microbubbles themselves, while the formulations used in the later chapters were vastly improved compared to those in the earlier work, stability and *in vivo* circulation time remain key issues which are yet to be fully resolved. The commercial contrast agent SonoVue® was observed to have slightly better stability than the magnetic microbubbles in the *in vivo* experiments, which suggests that further formulation improvements may be possible. That said, rapid clearance by filtration organs and destruction of microbubbles in the circulation is likely to be an unavoidable fact for any gas-based microbubble, and could be considered important for patient safety. Alternative agents such as the phase-change magnetic nanodroplets tested in Chapter 4 may provide stability and circulation time advantages, at the expense of requiring an additional vaporisation step which may influence the required acoustic conditions. While the *in vitro* results with magnetic nanodroplets in this thesis were encouraging, and some acoustic characterisation conducted, at the time of writing this particular formulation has not yet been tested *in vivo*.

Regardless of the agent under test, optimisation of parameters such as the acoustic conditions and concentrations of agents used for each therapeutic target is certainly required. In order to reduce the parameter space within the additional constraints imposed by cell work the acoustic conditions chosen in Chapter 4 were based on those found in the literature, while other parameters such as the concentration of siRNA rel-

ative to the bubble components were fixed. The results suggest several potential areas for optimisation: for example in some cases reducing the microbubble concentration appeared to improve results (by reducing shielding), while increasing the duty cycle in nanodroplet experiments gave more efficient conversion into microbubbles. Further testing is needed to establish whether these observations will translate (e.g. to an effect on cells) and to optimise the conditions for a given bioeffect.

While the *in vivo* experiments showed some promising results in terms of microbubble distribution and cavitation enhancement, these employed fluorescent marker molecules only and not active therapeutic agents. To establish whether these effects could translate into enhanced therapeutic efficacy would require incorporation of appropriate drugs (e.g. chemotherapeutics, siRNA, oncolytic viruses) either attached to or delivered alongside the microbubble agent. Such experiments would typically need to establish enhanced delivery of the agent under consideration (for instance using a fluorescently labelled drug) after which the goal of enhanced therapeutic efficacy could be tested. Further optimisation of the acoustic conditions for *in vivo* use – beyond the few variants tested here – is clearly necessary to maximise the effects of the relevant agents during their circulation time (for example increasing the burst length and/or pulse repetition frequency could provide more efficient use of microbubbles with a short circulation time).

Finally, with respect to the acoustic monitoring technique used, passive acoustic mapping was improved greatly during the course of this thesis from an offline post-processing technique into one which could be used for true real-time monitoring (within certain constraints). In order to facilitate this a relevantly simple algorithm was employed such that real-time calculation was feasible using conventional programming techniques on moderate hardware. The development of computational

methods to make improved beamforming methods practical for use in real time during experiments could allow more accurate and reliable mapping of cavitation behaviour. In addition, for compatibility with readily available equipment the PAM data presented in this thesis was captured using linear array ultrasound probes. The use of such probes means that the resulting maps are 2-dimensional, with a slice thickness based on the elevational focusing of the probe. For robust monitoring of cavitation in an arbitrary volume 3-dimensional PAM is required, which can be achieved by using 2-dimensional arrays. For interpretation of PAM data, further validation of the correlation between PAM and a desired therapeutic effect is crucial to development of the method into a viable tool for clinical use.

# APPENDICES

## APPENDIX A: HIFU TRANSDUCER CALIBRATION

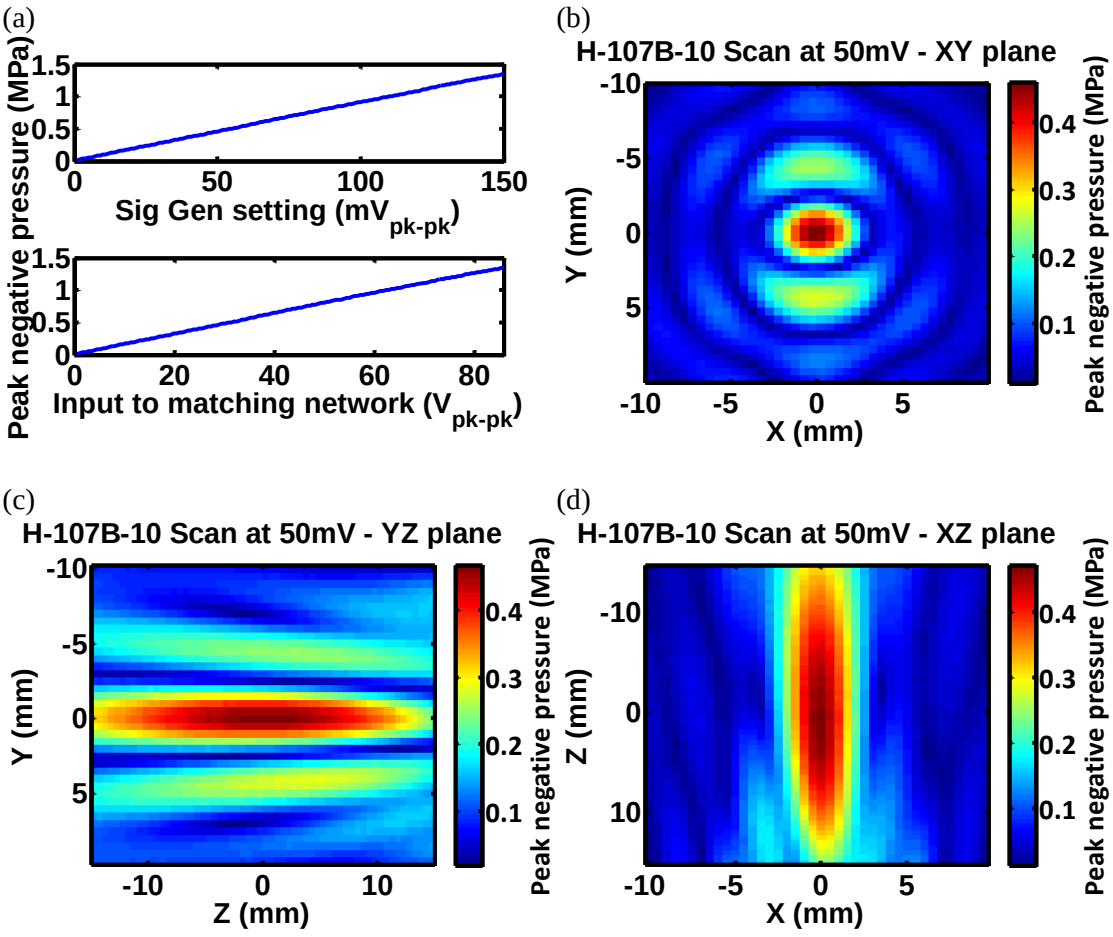


Figure A.1: 500 kHz rectangular cutout HIFU transducer calibration. (a) Absolute calibration showing peak negative focal pressure (MPa) vs. signal generator output voltage (mV) and input to transducer matching network (V). (a-c) Spatial scans for the three principal planes about the focal point. Colourbars represent pressure. X and Y axis are in plane of transducer (X axis along cutout), Z axis is in axial direction (towards transducer).

**Theoretical focus size for spherically focused transducer**

The theoretical focal width is (Sherman, 1962):

$$\Delta x_{-3dB} = 1.029\, F\lambda/D$$

For this transducer $F$ = 63 mm, $D$ = 64 mm and $\lambda$ = 3.08 mm (for a frequency of 500 kHz and speed of sound 1540 m/s), so $\Delta x_{-3dB}$ = 3.12 mm

The length of the focal zone may be estimated using (Olympus, 2006):

$$\Delta z_{-3dB} = NS_F^2[2/(1 + 0.5S_F)]$$

Where $N = D^2/4\lambda$ is the near-field distance and $S_F = F/N$ is the normalised focal length. Using the parameters from above yields $\Delta z_{-3dB}$ = 21.81 mm.

# APPENDIX B: ARRAY RECEIVE CALIBRATION

The L11-4v array was calibrated by comparison to the recordings from a needle hydrophone using a similar setup to (Gyöngy, 2010) in which the array and hydrophone were used to record a pulse produced by a focused transducer and then reflected to both from a metal wire. The frequency of the excitation pulse was varied (3-12 MHz, steps of 0.5 MHz) and the waveforms from the hydrophone and array recorded. By comparison of the peak-to-peak amplitude of the two recordings at each frequency a frequency-dependent calibration was obtained. For PAM a single sensitivity value based on the mean sensitivity in the specified 4-11 MHz range of the array ($7.5 \times 10^{-3}$ VSX units/Pa) was used. As in previous work this is a valid simplification assuming broadband cavitation sources (Gyöngy, 2010).

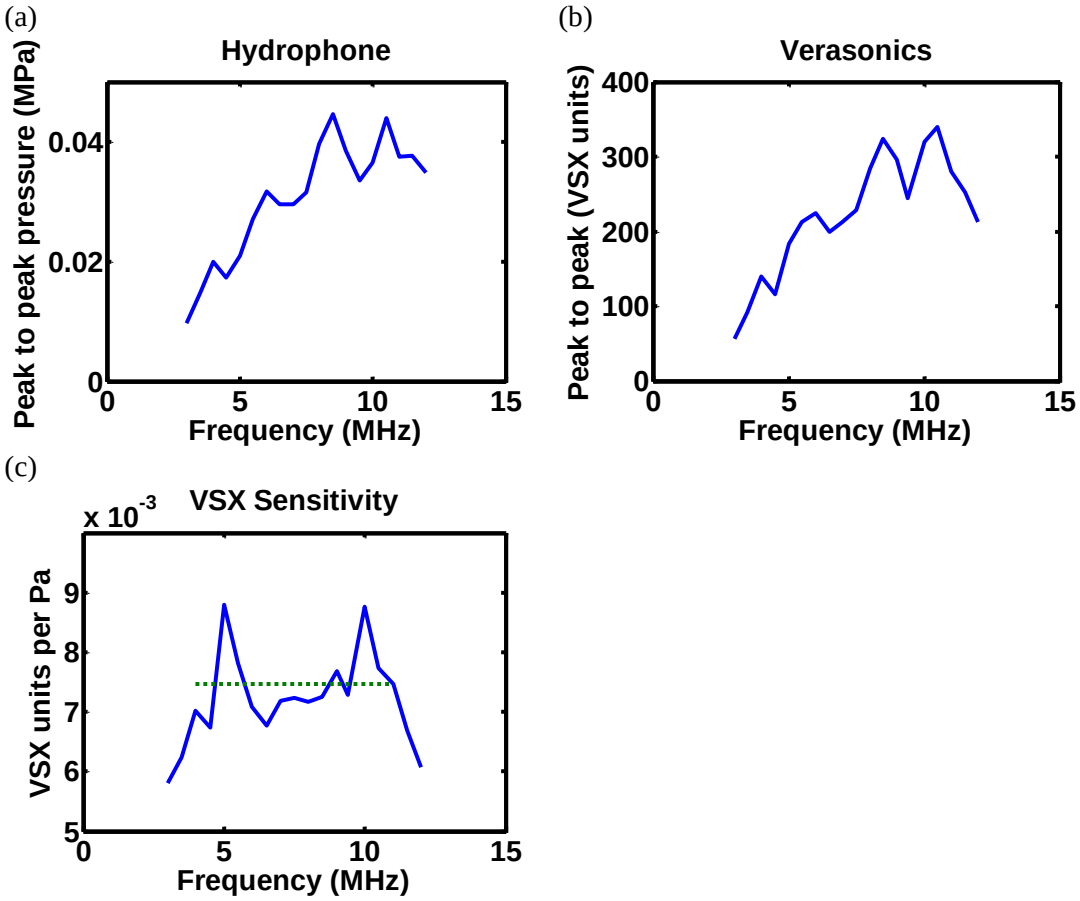


Figure B.1: L11-4v array and Verasonics system receive calibration. (a) Hydrophone peak-to-peak pressure vs. frequency. (b) L11-4v + Verasonics peak-to-peak (VSX units) vs. frequency. (c) Verasonics + L11-4v system sensitivity (VSX units/Pa).

# APPENDIX C: MAGNETIC FIELD CALIBRATION

The magnetic fields of the single magnet element and 5 magnet Halbach array were measured in air using a Hall-effect sensor IC (model A1302; Allegro MicroSystems, Worcester, MA, USA) mounted on a 3-axis automated positioning system. The sensor gave a DC output voltage proportional to the magnetic field. The sensor had a maximum range of 0.18 T so was saturated close to the magnet but was sufficient for characterisation of the field profile and decay in field strength with distance.

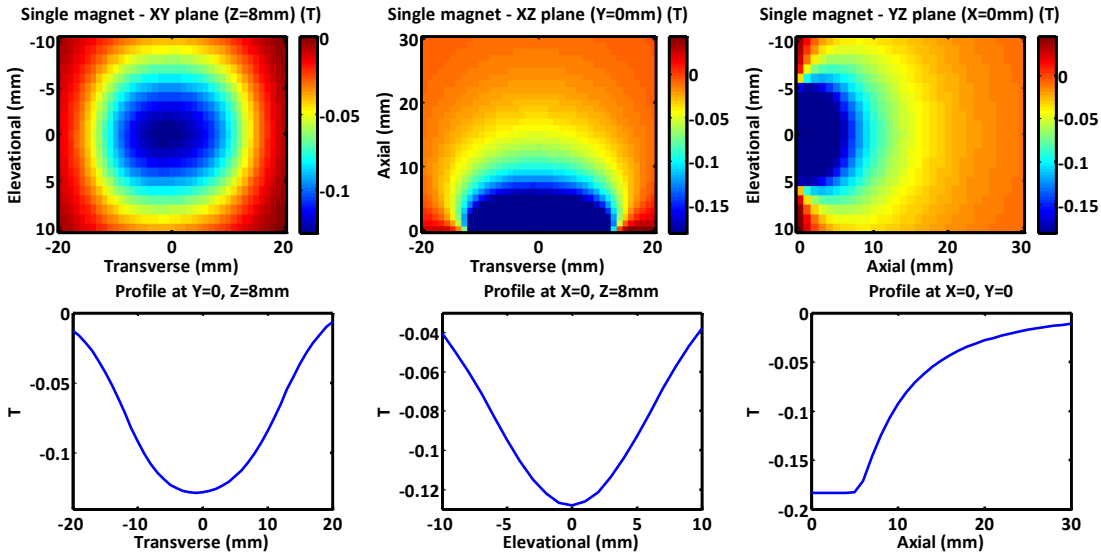


Figure C.1: Magnetic field calibration for single magnet (25 × 10 × 10 mm). Top row: spatial scans for the three principal planes; bottom row: profiles along centre lines of each plane. Axes: transverse along 25 mm, elevational along 10 mm, axial away from magnet.

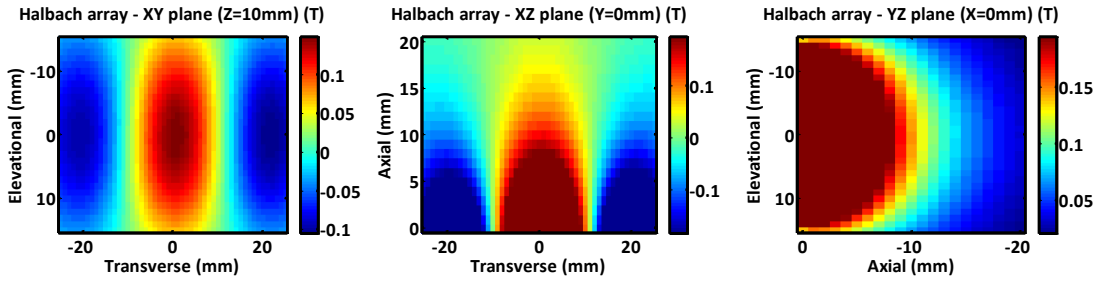


Figure C.2: Magnetic field calibration for Halbach array magnet (50 × 25 × 10 mm) constructed from 5 of the single magnets measured above. Spatial scans for the three principal planes are shown. Axes: transverse along 50 mm, elevational along 25 mm, axial away from magnet.

# APPENDIX D: CONSTRAINED OPTIMISATION PROBLEMS

A *constrained optimisation problem* such as that in Equation 2.19 may be solved using the method of Lagrange multipliers (Bertsekas, 1982). In order to minimise a function $f(x)$ subject to the constraint $h(x) = 0$, the expressions are combined into the *Lagrangian function* using a dummy variable $\lambda$ (the *Lagrange multiplier*):

$$L(x, \lambda) = f(x) + \lambda h(x) \tag{6.1}$$

From Equation 2.19 for the standard Capon beamformer the optimisation problem (dropping (**x**) terms for clarity) is:

$$\min_{\mathbf{w}} \mathbf{w}^T \mathbf{D} \mathbf{R}_s \mathbf{D} \mathbf{w} \qquad \text{subject to} \qquad \mathbf{w}^T \mathbf{a_0} = 1 \tag{6.2}$$

For which the Lagrangian function is:

$$L(x, \lambda) = \mathbf{w}^T \mathbf{D} \mathbf{R}_s \mathbf{D} \mathbf{w} + \lambda(\mathbf{w}^T \mathbf{a_0} - 1) \tag{6.3}$$

The minimum value occurs when the derivative with respect to $\mathbf{w}^T$ equals zero:

$$\frac{\partial L}{\partial \mathbf{w}^T} = \mathbf{D} \mathbf{R}_s \mathbf{D} \mathbf{w} + \lambda \mathbf{a_0} = 0 \tag{6.4}$$

In this case $\lambda$ may be found in terms of the other variables by substituting in the original constraint $\mathbf{w}^T \mathbf{a_0} = 1$, hence eliminating $\lambda$. The resulting expression for the weight terms **w** for the standard Capon beamformer as per (Coviello *et al.*, 2015) is:

$$\mathbf{w} = \frac{\mathbf{D}^{-1} \mathbf{R}_s^{-1} \mathbf{D}^{-1} \mathbf{a}_0}{\mathbf{a}_0^T \mathbf{D}^{-1} \mathbf{R}_s^{-1} \mathbf{D}^{-1} \mathbf{a}_0} \tag{6.5}$$

# APPENDIX E: DETAILED MMB MANUFACTURE PROTOCOLS

Detailed protocols for production of each of the microbubble formulations used in this thesis are included below. A summary is given in Table 2.1.

**DSPC-MMB Microbubbles**

**Protocol**

**Equip needed:**

1 DSPC powder - stored in -20 freezer (Avanti 850365P)
2 Ferrofluid - 10% v/v 10 nm spherical iron oxide in isoparaffin (Liquids Research WHJS1-B)
Stored in chemicals cupboard. Aliquot out a few mL into a glass vial
3 Plastic vial and lid
4 Surgical spirit - stored in flammables cupboard (Boots)
5 Scales and spatula for weighing powder
6 Probe sonicator (Misonix XL2000)
7 Deionised water or PBS (Life Technologies 14190-094)
8 Pipettes to measure 15 µL and 15 mL

**Steps**

1 Rinse vial by adding a few drops of surgical spirit and shaking. Dry with Kimwipe and allow to evaporate
2 Clean spatula and sonicator tip with DI water / ethanol and dry
3 Tare empty vial on scale. Weigh in 15 mg DSPC powder (touch scales/vial first to reduce static)
4 Add 15 mL DI water
5 Sonicate deep in liquid (power setting 4) to disperse the lipid for 30 s. Some clumps may remain
6 Move probe to air-liquid interface and tilt vial. Sonicate for 30 seconds. Bubbles should form.
7 Fit lid and shake vial vigorously for 30 seconds
8 Draw 15 µL ferrofluid into pipette. Wipe residue from outside of pipette with a Kimwipe
9 Pipette into vial and disperse by drawing up and down with pipette
10-12 Repeat steps 5-7. The solution should turn brown at the first sonication, and bubbles form at the second.

**Photos**

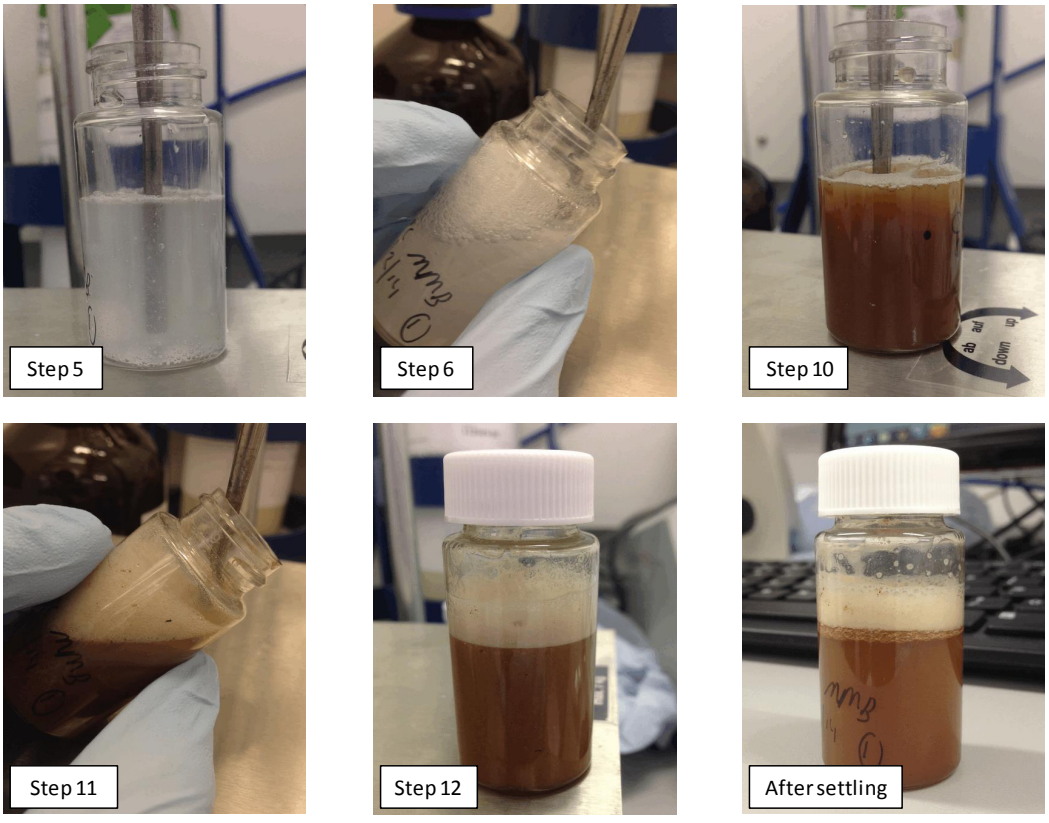


Table E.1: Protocol for DSPC-MMB manufacture used for phantom experiments (Chapter 3).

**Charged DSPC:PEG Microbubbles (F-MMB, K-MMB, S-MMB)**

**Protocol - Part 1**

**Equip needed:**

1 Solutions x4: prepare in advance, keep in freezer, take out 30 mins before
DSPC in chloroform (25 mg/ml, decant from supplied). Kept in freezer. Avanti order code 850365C.
DSEPC in chloroform (25 mg/ml, decant from supplied). Kept in freezer. Avanti order code 890703C.
- DSEPC has a positive charge so allows attachment of negatively charged payload (e.g. nucleic acids)
PEG 40 stearate: make solution of 10mg/ml in chloroform using bath sonicator. Chemicals cupboard. Sigma P3440
Chloroform for washing. Decant from supplied. Stock in flammables cupboard. Sigma C2432
2 Glass Hamilton syringes (chloroform may react with plastic) - 10 µL / 50 µL
3 Glass vial and lid
4 Parafilm
5 Hotplate / stirrer in fume hood

**Steps**

1 Wash syringe by drawing up ~0.1mL chloroform, draw through to end, shake around and expel. Repeat x3
2 Measure 60 µL DSPC (1.5mg), 29 µL DSEPC (0.7mg) and 18 µL PEG (0.2mg) into vial, washing syringe after each
3 Label vial, stretch Parafilm over the top (no lid), poke holes in film
4 Leave on hotplate in fume hood at 50 degrees overnight

**Protocol - Part 2**

**Equip needed:**

1 Chemicell Fluidmag lipid (50nm, 25mg/ml, in bubble fridge). Chemicell product 4119
2 siRNA: Fluorescent 'F-MMB' - BLOCK-iT (Life Technologies, lot no: 1477937; Alexa Fluorophore 647-tagged)
Knockdown 'K-MMB' - Ambion® Silencer® GFP (Life Technologies, product code AM4626)
Scrambled 'S-MMB' - Negative control for Ambion® Silencer® GFP (supplied with above)
3 Ice (get from first floor beside glass wash)
4 Probe sonicator (Misonix XL2000)
5 SF6 gas cylinder with regulator, tubing and needle on end
6 PBS with added glycerol and propylene glycol (80% PBS, 10% of each of the others)
PBS Life Technologies 14190-094, Glycerol Sigma 49781-1L, Propylene glycol Sigma W294004-1KG-K

**Steps: part B**

1 Add 1.5mL PBS/glycerol/propylene glycol mixture and stir bar
2 Leave on hotplate at 70 degrees with stirring for ~30 mins until cloudy
3 Take stir bar out, sonicate for ~1min on power setting ~2 deep in liquid until becomes clear
4 Add 15 µL ferrofluid solution and 20 µL of the chosen siRNA oligo, sonicate again
5 Move to air-water interface, power setting 15
6 Hold gas needle inside vial. Check inner gas regulator showing some pressure and valve on bottle closed
7 Turn on gas using regulator until needle starts to fall, turn on sonicator
8 When needle hits zero turn off, quickly put lid on vial and remove to ice
9 To refill gas close regulator and open and close valve on gas bottle
10 Optionally centrifuge (1000 RPM, 10 min) to remove unbound siRNA - may reduce bubble concentration

**Chemical quantities calculation**

| | | | | | | | | |
|---|---|---|---|---|---|---|---|---|
| **Solution volume** | | 1.5 | ml | **Avg Conc.** | 1.60 | mg/mL | **Total mass** | 2.40 mg |
| **Molar ratio:** | DSPC 100 | :DSEPC :44 | :PEG :4.5 | **FluidMag** | 0.25 | mg/mL | **Wgt avg MW** | 847.29 g/mol |

| | DSPC | | DSEPC | | PEG40S | | FluidMag | |
|---|---|---|---|---|---|---|---|---|
| **Molecular weight** | 790.15 | g/mol | 854.66 | g/mol | 2,045.00 | g/mol | **Stock concentration** | |
| **Stock conc** | 25.00 | mg/ml | 25.00 | mg/ml | 10.00 | mg/ml | 25.00 | mg/mL |
| **Required quantity** | 0.0019 | mMoles | 0.0008 | mMoles | 0.0001 | mMoles | **Required quantity** | |
| | 1.507 | mg | 0.717 | mg | 0.176 | mg | 0.375 | mg |
| | **60.3** | **µL** | **28.7** | **µL** | **17.6** | **µL** | **15.0** | **µL** |
| *molar ratio check:* | *100* | | *44* | | *4.5* | | | |

Table E.2: Protocol for F-MMB/K-MMB/S-MMB manufacture used for *in vitro* experiments (Chapter 4).

**Paclitaxel-Loaded Magnetic Nanodroplets (PTX-MND)**

**Protocol - Part 1**

**Equip needed:**

1 0.5% SDS solution: prepare in advance by dissolving SDS powder in DI water. Keep in fridge until use
2 Magnetic nanoparticles (MNP) in toluene (5 mg/ml) (Sigma 700312). Keep at room temperature
Evaporate toluene before using (heat to ~140 degrees C) and replace with chloroform
3 Human serum albumin (HSA) (Sigma A9511): make solution of 4mg in 1ml in DI water (stir for 10 mins, room temp)
4 bis-NHS-PEG (2000 Da, RAPP Polymere 112000-35) & Paclitaxel (Sigma T7191)
Make solution of 6mg bis-NHS-PEG & 0.5mg Paclitaxel in 100 µl chloroform. Stock in freezer
5 PFP (Apollo scientific): keep in fridge
6 Chloroform. Sigma C2432
7 Eppendorf tube 1.5mL
8 Glass vial and lid
9 Ultrasonic cell disruptor. XL 2000, Misonix Inc.
10 Rotary evaporator
11 Stirrer in fume hood

**Steps**

1 Mix 100µl of magnetic nanoparticles in chloroform and 100µl bis-NHS-PEG & Paclitaxel in chloroform
2 Add solution (1) to 1ml of HSA solution. Shake the mixture using vortex and then sonicate (power setting 2) for 30 sec in icy water
3 Transfer the prepared oil/water emulsion to a rotary evaporator
Evaporate the organic solvent under 100 mbar until emulsion turns transparent
4 Move solution (3) to 1.5mL Eppendorf tube
5 Add 50µl PFP and sonicate (power setting 1) for 10 sec.
6 Gently inject the emulsion (5) into 4mL of 0.5% SDS solution using a syringe (total solution volume now 5mL)
7 Leave the solution stirring for 5 min

**Chemical quantities calculation**

| | Albumin (HSA) | bis-NHS-PEG | Paclitaxel | PFP | |
|---|---|---|---|---|---|
| **Molecular weight** | 66,478 | 2,000 | 853.91 | 288.04 | g/mol |
| **Density** | | | | 1.63 | g/mL |

For cell chamber experiments described in Lee 2015 MND stock was diluted to give a final PTX concentration in the cell chambers of 0.5 µM by adding additional PBS. Based on calculation below 10mL PBS was added to bring the total volume of MND stock to 15 mL, following which 100 µL of diluted stock was added to each cell chamber

| MND Stock | | |
|---|---|---|
| **PTX mass** | 500.00 | µg |
| **PTX moles** | 0.59 | µmoles |
| **PBS added** | 10.00 | mL |
| **Diluted stock volume** | 15.00 | mL |
| **PTX conc. in stock** | 39.04 | µmoles/L (µM) |

| In cell chamber | | |
|---|---|---|
| **Diluted MND stock used** | 100.00 | µL |
| **PTX moles** | 0.004 | µmoles |
| **Cell chamber total volun** | 8.00 | mL |
| **Final PTX concentration** | 0.5 | µmoles/L (µM) |
| | *As per paper* | |

Table E.3: Protocol for PTX-MND manufacture as used for *in vitro* experiments (Chapter 4).

**DiI-MMB Microbubbles**

**Protocol - Part 1**

**Equip needed:**

1 Solutions x4: prepare in advance, keep in freezer, take out 30 mins before
DSPC in chloroform (25 mg/ml, decant from supplied). Kept in freezer. Avanti order code 850365C.
PEG 40 stearate: make solution of 10mg/ml in chloroform using bath sonicator. Chemicals cupboard. Sigma P3440
Chloroform for washing. Decant from supplied. Stock in flammables cupboard. Sigma C2432
DiI dye for fluorescent labelling. Made up to 2.5mg/mL in chloroform. Life Technologies D-282
2 Glass Hamilton syringes (chloroform may react with plastic) - 10 µL / 50 µL
3 Glass vial and lid
4 Parafilm
5 Hotplate / stirrer in fume hood

**Steps**

1 Wash syringe by drawing up ~0.1mL chloroform, draw through to end, shake around and expel. Repeat x3
2 Measure 61 µL DSPC (1.5mg) and 44 µL PEG (0.44mg) into vial, washing syringe as above after each
For fluorescent labelling add 20 µL of 2.5 mg/mL DiI solution
3 Label vial, stretch Parafilm over the top (no lid), poke holes in film
4 Leave on hotplate in fume hood at 50 degrees overnight

**Protocol - Part 2**

**Equip needed:**

1 Chemicell Fluidmag lipid (50nm, 25mg/ml, in bubble fridge). Chemicell product 4119
2 Ice (get from first floor beside glass wash)
3 Probe sonicator (Misonix XL2000)
4 SF6 gas cylinder with regulator, tubing and needle on end
5 PBS with added glycerol and propylene glycol (80% PBS, 10% of each of the others)
PBS Life Technologies 14190-094, Glycerol Sigma 49781-1L, Propylene glycol Sigma W294004-1KG-K

**Steps: part B**

1 Add 1.5mL PBS/glycerol/propylene glycol mixture and stir bar
2 Leave on hotplate at 70 degrees with stirring for ~30 mins until cloudy
3 Take stir bar out, sonicate for ~1min on power setting ~2 deep in liquid until becomes clear
4 Add 15 µL ferrofluid solution, sonicate again
5 Move to air-water interface, power setting 15
6 Hold gas needle inside vial. Check inner gas regulator showing some pressure and valve on bottle closed
7 Turn on gas using regulator until needle starts to fall, turn on sonicator
8 When needle hits zero turn off, quickly put lid on vial and remove to ice
9 To refill gas close regulator and open and close valve on gas bottle

**Chemical quantities calculation**

| | | | | | |
|---|---|---|---|---|---|
| **Solution volume** | 1.5 ml | **Avg Conc.** | 1.30 mg/mL | **Total mass** | 1.95 mg |
| **Molar ratio DSPC:PEG** | 9 :1 | **FluidMag** | 0.25 mg/mL | **Wgt avg MW** | 915.63 g/mol |

| **DSPC** | | | **PEG40S** | | | **FluidMag** | |
|---|---|---|---|---|---|---|---|
| **Molecular weight** | 790.15 | g/mol | **Molecular weight** | 2,045.00 | g/mol | **Stock concentration** | |
| **Stock concentration** | 25.00 | mg/ml | **Stock concentration** | 10.00 | mg/ml | 25.00 | mg/mL |
| **Required quantity** | 0.0019 | mMoles | **Required quantity** | 0.0002 | mMoles | **Required quantity** | |
| *molar ratio* | 1.514 | mg | | 0.436 | mg | 0.375 | mg |
| *check: 9.00* | **60.6** | **µL** | | **43.6** | **µL** | **15.0** | **µL** |

Table E.4: Protocol for DiI-MMB manufacture used for *in vivo* experiments (Chapter 5).

# REFERENCES


Aihara H and Miyazaki J-i 1998 Gene transfer into muscle by electroporation in vivo *Nat. Biotechnol.* **16** 867-70

Al-Mansour H A, Mulvagh S L, Pumper G M, Klarich K W and Foley D A 2000 Usefulness of harmonic imaging for left ventricular opacification and endocardial border delineation by optison *Am. J. Cardiol.* **85** 795-9

Alberts B, Johnson A, Lewis J, Raff M, Roberts K and Walter P 2002 *Molecular Biology of the Cell (4th edition)* (New York: Garland Science)

Alexandrov A V, Mikulik R, Ribo M, Sharma V K, Lao A Y, Tsivgoulis G, Sugg R M, Barreto A, Sierzenski P, Malkoff M D and Grotta J C 2008 A Pilot Randomized Clinical Safety Study of Sonothrombolysis Augmentation With Ultrasound-Activated Perflutren-Lipid Microspheres for Acute Ischemic Stroke *Stroke* **39** 1464-9

Alexiou C, Diehl D, Henninger P, Iro H, Rockelein R, Schmidt W and Weber H 2006 A High Field Gradient Magnet for Magnetic Drug Targeting *Applied Superconductivity, IEEE Transactions on* **16** 1527-30

Apfel R E 1998 Activatable infusable dispersions containing drops of a superheated liquid for methods of therapy and diagnosis, United States Patent (US 5840276 A).

Arvanitis C D, Bazan-Peregrino M, Rifai B, Seymour L W and Coussios C C 2011 Cavitation-Enhanced Extravasation for Drug Delivery *Ultrasound Med. Biol.* **37** 1838-52

Arvanitis C D, Clement G T and McDannold N 2015 Transcranial Assessment and Visualization of Acoustic Cavitation: Modeling and Experimental Validation *Medical Imaging, IEEE Transactions on* **34** 1270-81

Arvanitis C D, Livingstone M S and McDannold N 2013 Combined ultrasound and MR imaging to guide focused ultrasound therapies in the brain *Phys Med Biol* **58** 4749-61

Arvanitis C D and McDannold N 2013 Integrated ultrasound and magnetic resonance imaging for simultaneous temperature and cavitation

monitoring during focused ultrasound therapies *Med. Phys.* **40** 112901

Asen J P, Buskenes J I, Nilsen C-I C, Austeng A and Holm S 2014 Implementing capon beamforming on a GPU for real-time cardiac ultrasound imaging *Ultrasonics, Ferroelectrics, and Frequency Control, IEEE Transactions on* **61** 76-85

Asl B M and Mahloojifar A 2012 A low-complexity adaptive beamformer for ultrasound imaging using structured covariance matrix *Ultrasonics, Ferroelectrics, and Frequency Control, IEEE Transactions on* **59** 660-7

Barnsley L C, Carugo D, Owen J and Stride E 2015 Halbach arrays consisting of cubic elements optimised for high field gradients in magnetic drug targeting applications *Phys Med Biol* **60** 8303-27

Barrefelt Å, Saghafian M, Kuiper R, Ye F, Egri G, Klickermann M, Brismar T B, Aspelin P, Muhammed M, Dähne L and Hassan M 2013 Biodistribution, kinetics, and biological fate of SPION microbubbles in the rat *Int J Nanomedicine* **8** 3241-54

Bazan-Peregrino M, Arvanitis C D, Rifai B, Seymour L W and Coussios C-C 2012 Ultrasound-induced cavitation enhances the delivery and therapeutic efficacy of an oncolytic virus in an in vitro model *Journal of Controlled Release* **157** 235-42

Bazan-Peregrino M, Rifai B, Carlisle R C, Choi J, Arvanitis C D, Seymour L W and Coussios C C 2013 Cavitation-enhanced delivery of a replicating oncolytic adenovirus to tumors using focused ultrasound *Journal of Controlled Release* **169** 40-7

Bernstein E, Caudy A A, Hammond S M and Hannon G J 2001 Role for a bidentate ribonuclease in the initiation step of RNA interference *Nature* **409** 363-6

Bertsekas D P 1982 *Constrained optimization and Lagrange multiplier methods* (New York: Academic Press)

Bokor D, Chambers J B, Rees P J, Mant T G K, Luzzani F and Spinazzi A 2001 Clinical safety of SonoVue (TM), a new contrast agent for ultrasound imaging, in healthy volunteers and in patients with chronic obstructive pulmonary disease *Invest. Radiol.* **36** 104-9

Borden M A, Kruse D E, Caskey C F, Zhao S, Dayton P A and Ferrara K W 2005 Influence of lipid shell physicochemical properties on ultrasound-induced microbubble destruction *Ultrasonics, Ferroelectrics, and Frequency Control, IEEE Transactions on* **52** 1992-2002

Borden M A and Longo M L 2002 Dissolution behavior of lipid monolayer-coated, air-filled microbubbles: Effect of lipid hydrophobic chain length *Langmuir* **18** 9225-33

Borgiotti G V and Kaplan L J 1979 Superresolution of uncorrelated interference sources by using adaptive array techniques *Antennas and Propagation, IEEE Transactions on* **27** 842-5

Buckingham M J 1993 Theory of acoustic imaging in the ocean with ambient noise *J. Comput. Acoust* **1** 117-40

Buckingham M J, Berknout B V and Glegg S A L 1992 Imaging the ocean with ambient noise *Nature* **356** 327-9

Bulte J W M and Kraitchman D L 2004 Iron oxide MR contrast agents for molecular and cellular imaging *NMR Biomed.* **17** 484-99

Butler B D and Hills B A 1979 The lung as a filter for microbubbles *J. Appl. Physiol.* **47** 537-43

Campbell S, Warsof S L, Little D and Cooper D J 1985 Routine ultrasound screening for the prediction of gestational age *Obstet. Gynecol.* **65** 613-20

Capon J 1969 High-resolution frequency-wavenumber spectrum analysis *Proceedings of the IEEE* **57** 1408-18

Carlisle R, Choi J, Bazan-Peregrino M, Laga R, Subr V, Kostka L, Ulbrich K, Coussios C-C and Seymour L W 2013 Enhanced Tumor Uptake and Penetration of Virotherapy Using Polymer Stealthing and Focused Ultrasound *J. Natl. Cancer Inst.* **105** 1701-10

Carugo D, Owen J, Crake C, Lee J Y and Stride E 2015 Biologically and Acoustically Compatible Chamber for Studying Ultrasound-Mediated Delivery of Therapeutic Compounds *Ultrasound Med. Biol.* **41** 1927-37

Cella D, Peterman A, Hudgens S, Webster K and Socinski M A 2003 Measuring the side effects of taxane therapy in oncology *Cancer* **98** 822-31

Chavhan G B, Babyn P S, Thomas B, Shroff M M and Haacke E M 2009 Principles, Techniques, and Applications of T2*-based MR Imaging and Its Special Applications *Radiographics* **29** 1433-49

Chen C-E, Ali A M and Wang H 2006 Design and testing of robust acoustic arrays for localization and enhancement of several bird sources. In: *Proceedings of the 5th international conference on Information processing in sensor networks*, (Nashville, TN, USA: ACM) pp 268-75

Cheng X, Li H, Chen Y, Luo B, Liu X, Liu W, Xu H and Yang X 2013 Ultrasound-Triggered Phase Transition Sensitive Magnetic Fluorescent Nanodroplets as a Multimodal Imaging Contrast Agent in Rat and Mouse Model *PLoS ONE* **8** e85003

Choi J J, Carlisle R C, Coviello C, Seymour L and Coussios C-C 2014 Non-invasive and real-time passive acoustic mapping of ultrasound-mediated drug delivery *Phys. Med. Biol.* **59** 4861-77

Choi J J and Coussios C-C 2012 Spatiotemporal evolution of cavitation dynamics exhibited by flowing microbubbles during ultrasound exposure *J Acoust Soc Am* **132** 3538-49

Clark C W 1980 A real-time direction finding device for determining the bearing to the underwater sounds of

Southern Right Whales, Eubalaena australis *J Acoust Soc Am* **68** 508-11

Collin J, Coviello C, Lyka E, Leslie T and Coussios C C 2013 Real-time three-dimensional passive cavitation detection for clinical high intensity focussed ultrasound systems *Proc Meet Acoust* **19** 075023

Coussios C-C, Farny C H, ter Haar G and Roy R A 2007 Role of acoustic cavitation in the delivery and monitoring of cancer treatment by high-intensity focused ultrasound (HIFU) *Int J Hyperthermia* **23** 105-20

Coussios C-C and Roy R A 2008 Applications of Acoustics and Cavitation to Noninvasive Therapy and Drug Delivery *Annual Review of Fluid Mechanics* **40** 395-420

Coviello C, Kozick R, Choi J, Gyöngy M, Jensen C, Smith P P and Coussios C-C 2015 Passive acoustic mapping utilizing optimal beamforming in ultrasound therapy monitoring *J Acoust Soc Am* **137** 2573-85

Crake C, Coussios C C and Stride E 2014 Cavitation Dynamics of Magnetic Microbubbles using Passive Acoustic Mapping. In: *The 14th International Symposium on Therapeutic Ultrasound,* (Las Vegas, Nevada, USA: 2-5 April 2014)

Crake C, de Saint Victor M, Coviello C, Owen J, Coussios C C and Stride E 2013 Passive acoustic mapping of magnetic microbubbles in an in vitro flow model *Proc Meet Acoust* **19** 075025

Crake C, de Saint Victor M, Owen J, Coviello C, Collin J, Coussios C-C and Stride E 2015 Passive acoustic mapping of magnetic microbubbles for cavitation enhancement and localization *Phys. Med. Biol.* **60** 785-806

D'arrigo J S 1993 Method for the production of medical-grade lipid-coated microbubbles, paramagnetic labeling of such microbubbles and therapeutic uses of microbubbles, United States Patent (US 5215680 A).

Dalby B, Cates S, Harris A, Ohki E C, Tilkins M L, Price P J and Ciccarone V C 2004 Advanced transfection with Lipofectamine 2000 reagent: primary neurons, siRNA, and high-throughput applications *Methods* **33** 95-103

Datta S, Coussios C-C, Ammi A Y, Mast T D, de Courten-Myers G M and Holland C K 2008 Ultrasound-Enhanced Thrombolysis Using Definity® as a Cavitation Nucleation Agent *Ultrasound Med. Biol.* **34** 1421-33

de Boer A G and Gaillard P J 2007 Drug targeting to the brain *Annu. Rev. Pharmacol. Toxicol.* **47** 323-55

del Pino P, Munoz-Javier A, Vlaskou D, Rivera Gil P, Plank C and Parak W J 2010 Gene silencing mediated by magnetic liposphere tagged with small interfering RNA *Nano Lett.* **10** 3914-21

Delrue S, Van Den Abeele K, Blomme E, Deveugele J, Lust P and Matar O B 2010 Two-dimensional simulation of the single-sided air-coupled ultrasonic pitch-catch

technique for non-destructive testing *Ultrasonics* **50** 188-96

Dharmakumar R, Plewes D B and Wright G A 2003 Microbubble construct for sensitivity enhanced MR manometry, United States Patent (US 20030216638 A1).

Diehl K H, Hull R, Morton D, Pfister R, Rabemampianina Y, Smith D, Vidal J M and van de Vorstenbosch C 2001 A good practice guide to the administration of substances and removal of blood, including routes and volumes *J. Appl. Toxicol.* **21** 15-23

Dowling A P and Ffowcs Williams J E 1983 *Sound and sources of sound* (Chichester: E. Horwood)

Edelstein M L, Abedi M R and Wixon J 2007 Gene therapy clinical trials worldwide to 2007—an update *J Gene Med* **9** 833-42

European Medicines Agency 2014 SonoVue SUMMARY OF PRODUCT CHARACTERISTICS. http://www.ema.europa.eu/docs/en_GB/document_library/EPAR_-_Product_Information/human/000303/WC500055380.pdf.

Feinstein S B, Cheirif J, Ten Cate F J, Silverman P R, Heidenreich P A, Dick C, Desir R M, Armstrong W F, Quinones M A and Shah P M 1990 Safety and efficacy of a new transpulmonary ultrasound contrast agent: initial multicenter clinical results *Journal of the American College of Cardiology* **16** 316-24

Feldschuh J and Enson Y 1977 Prediction of the normal blood volume. Relation of blood volume to body habitus *Circulation* **56** 605-12

Felgner P L, Gadek T R, Holm M, Roman R, Chan H W, Wenz M, Northrop J P, Ringold G M and Danielsen M 1987 Lipofection: a highly efficient, lipid-mediated DNA-transfection procedure *PNAS* **84** 7413-7

Feshitan J A, Chen C C, Kwan J J and Borden M A 2009 Microbubble size isolation by differential centrifugation *J. Colloid Interface Sci.* **329** 316-24

Frenkel V, Kimmel E and Iger Y 1999 Ultrasound-induced cavitation damage to external epithelia of fish skin *Ultrasound Med. Biol.* **25** 1295-303

Fry W J and Fry F J 1960 Fundamental neurological research and human neurosurgery using intense ultrasound *IRE Transactions on Medical Electronics* **7** 166-81

Gad S C 2002 *Drug Safety Evaluation* (New York: Wiley)

Gateau J, Aubry J-F, Chauvet D, Boch A-L, Fink M and Tanter M 2011a In vivo bubble nucleation probability in sheep brain tissue *Phys. Med. Biol.* **56** 7001-15

Gateau J, Aubry J-F, Pernot M, Fink M and Tanter M 2011b Combined passive detection and ultrafast active imaging of cavitation events induced by short pulses of high-intensity ultrasound *IEEE Trans Ultrason Ferroelectr Freq Control* **58** 517-32

Gateau J, Marsac L, Pernot M, Aubry J F, Tanter M and Fink M 2010

Transcranial ultrasonic therapy based on time reversal of acoustically induced cavitation bubble signature *IEEE Trans. Biomed. Eng.* **57** 134-44

Gateau J, Taccoen N, Tanter M and Aubry J-F 2013 Statistics of Acoustically Induced Bubble-Nucleation Events in in Vitro Blood: A Feasibility Study *Ultrasound Med. Biol.* **39** 1812-25

Giesecke T and Hynynen K 2003 Ultrasound-mediated cavitation thresholds of liquid perfluorocarbon droplets in vitro *Ultrasound Med. Biol.* **29** 1359-65

Ginn S L, Alexander I E, Edelstein M L, Abedi M R and Wixon J 2013 Gene therapy clinical trials worldwide to 2012–an update *J Gene Med* **15** 65-77

Gormley G and Wu J 1998 Observation of acoustic streaming near Albunex® spheres *J. Acoust. Soc. Am.* **104** 3115-8

Graham S. 2015. *Ultrasound-triggered drug release from liposomes using nanoscale cavitation nuclei.* DPhil Thesis, University of Oxford.

Graham W J 1983 Analysis and synthesis of axial field patterns of focused apertures *Antennas and Propagation, IEEE Transactions on* **31** 665-8

Gramiak R, Shah P M and Kramer D H 1969 Ultrasound cardiography: contrast studies in anatomy and function *Radiology* **92** 939-48

Grayburn P 1997 Perflenapent Emulsion (EchoGen®): A New Long-Acting Phase-Shift Agent for Contrast Echocardiography *Clin. Cardiol.* **20** 12-8

Grayburn P A, Erickson J M, Escobar J, Womack L and Velasco C E 1995 Peripheral intravenous myocardial contrast echocardiography using a 2% dodecafluoropentane emulsion: identification of myocardial risk area and infarct size in the canine model of ischemia *Journal of the American College of Cardiology* **26** 1340-7

Greenleaf J F and Bahn R C 1981 Clinical imaging with transmissive ultrasonic computerized tomography *Biomedical Engineering, IEEE Transactions on* **BME-28** 177-85

Gyöngy M. 2010. *Passive Cavitation Mapping for Monitoring Ultrasound Therapy.* DPhil Thesis, University of Oxford.

Gyöngy M, Arora M, Noble J A and Coussios C C 2008 Use of passive arrays for characterization and mapping of cavitation activity during HIFU exposure. In: *IEEE Ultrasonics Symposium, 2008,* (Beijing: IEEE) pp 871-4

Gyöngy M and Coussios C-C 2010a Passive cavitation mapping for localization and tracking of bubble dynamics *J Acoust Soc Am* **128** EL175-EL80

Gyöngy M and Coussios C C 2010b Passive Spatial Mapping of Inertial Cavitation During HIFU Exposure *IEEE Trans. Biomed. Eng.* **57** 48-56

Hahn W R 1975 Optimum signal processing for passive sonar range and bearing estimation *J Acoust Soc Am* **58** 201-7

Haworth K J, Mast T D, Radhakrishnan K, Burgess M T, Kopechek J A, Huang S-L, McPherson D D and Holland C K 2012 Passive imaging with pulsed ultrasound insonations *J Acoust Soc Am* **132** 544-53

Haworth K J, Salgaonkar V A, Corregan N M, Holland C K and Mast T D 2015 Using Passive Cavitation Images to Classify High-Intensity Focused Ultrasound Lesions *Ultrasound Med. Biol.* **41** 2420-34

Hedrich H J 2012 *The Laboratory Mouse (Second Edition)* (London: Academic Press)

Heimburger R F, Fry F J, Franklin T D and Eggleton R C 1975 Ultrasound potentiation of chemotherapy for brain malignancy *Ultrasound in medicine* **1** 273-81

Herzenberg L A, Sweet R G and Herzenberg L A 1976 Fluorescence-activated cell sorting *Sci. Am.* **234** 108-17

Hoak J C 1964 Structure of thrombi produced by injections of fatty acids *Br. J. Exp. Pathol.* **45** 44-7

Holzbach T, Vlaskou D, Neshkova I, Konerding M A, Wörtler K, Mykhaylyk O, Gänsbacher B, Machens H G, Plank C and Giunta R E 2010 Non-viral VEGF165 gene therapy – magnetofection of acoustically active magnetic lipospheres ('magnetobubbles') increases tissue survival in an oversized skin flap model *J. Cell. Mol. Med.* **14** 587-99

Hosny N A, Mohamedi G, Rademeyer P, Owen J, Wu Y, Tang M-X, Eckersley R J, Stride E and Kuimova M K 2013 Mapping microbubble viscosity using fluorescence lifetime imaging of molecular rotors *PNAS* **110** 9225-30

Hua X, Liu P, Gao Y-H, Tan K-B, Zhou L-N, Liu Z, Li X, Zhou S-W and Gao Y-J 2010 Construction of thrombus-targeted microbubbles carrying tissue plasminogen activator and their in vitro thrombolysis efficacy: a primary research *J Thromb Thrombolysis* **30** 29-35

Hwang J H, Tu J, Brayman A A, Matula T J and Crum L A 2006 Correlation between inertial cavitation dose and endothelial cell damage in vivo *Ultrasound Med. Biol.* **32** 1611-9

Hynynen K, Darkazanli A, Unger E and Schenck J F 1993 MRI-guided noninvasive ultrasound surgery *Med. Phys.* **20** 107-15

Hynynen K, McDannold N, Vykhodtseva N and Jolesz F A 2001 Noninvasive MR Imaging–guided Focal Opening of the Blood-Brain Barrier in Rabbits *Radiology* **220** 640-6

Hynynen K, McDannold N, Vykhodtseva N, Raymond S, Weissleder R, Jolesz F A and Sheikov N 2006 Focal disruption of the blood-brain barrier due to 260-kHz ultrasound bursts: a method for molecular imaging and targeted drug delivery *Journal of neurosurgery* **105** 445-54

Illing R O, Kennedy J E, Wu F, ter Haar G R, Protheroe A S, Friend P J, Gleeson F V, Cranston D W, Phillips R R and Middleton M R

2005 The safety and feasibility of extracorporeal high-intensity focused ultrasound (HIFU) for the treatment of liver and kidney tumours in a Western population *Br. J. Cancer* **93** 890-5

Jackson J K, Pirmoradi F N, Wan C P L, Siu T, Chiao M and Burt H M 2011 Increased accumulation of paclitaxel and doxorubicin in proliferating capillary cells and prostate cancer cells following ultrasound exposure *Ultrasonics* **51** 932-9

Jagannathan J, Sanghvi N K, Crum L A, Yen C-P, Medel R, Dumont A S, Sheehan J P, Steiner L, Jolesz F and Kassell N F 2009 High-intensity focused ultrasound surgery of the brain: part 1-A historical perspective with modern applications *Neurosurgery* **64** 201-11

Jensen C R, Cleveland R O and Coussios C C 2013 Real-time temperature estimation and monitoring of HIFU ablation through a combined modeling and passive acoustic mapping approach *Phys Med Biol* **58** 5833-50

Jensen C R, Ritchie R W, Gyöngy M, Collin J R T, Leslie T and Coussios C-C 2012 Spatiotemporal Monitoring of High-Intensity Focused Ultrasound Therapy with Passive Acoustic Mapping *Radiology* **262** 252-61

Jones R M, O'Reilly M A and Hynynen K 2013 Transcranial passive acoustic mapping with hemispherical sparse arrays using CT-based skull-specific aberration corrections: a simulation study *Phys Med Biol* **58** 4981-5005

Kaczkowski P J and Daigle R E 2011 The Verasonics ultrasound system as a pedagogic tool in teaching wave propagation, scattering, beamforming, and signal processing concepts in physics and engineering *J Acoust Soc Am* **129** 2648

Kallel F, Stafford R J, Price R E, Righetti R, Ophir J and Hazle J D 1999 The feasibility of elastographic visualization of HIFU-induced thermal lesions in soft tissues *Ultrasound Med. Biol.* **25** 641-7

Kaufmann B A and Lindner J R 2007 Molecular imaging with targeted contrast ultrasound *Curr. Opin. Biotechnol.* **18** 11-6

Kawabata K-i, Asami R, Azuma T and Umemura S-i 2010 Acoustic response of microbubbles derived from phase-change nanodroplet *Japanese Journal of Applied Physics* **49** 07HF18

Khokhlova V A, Bailey M R, Reed J A, Cunitz B W, Kaczkowski P J and Crum L A 2006 Effects of nonlinear propagation, cavitation, and boiling in lesion formation by high intensity focused ultrasound in a gel phantom *J Acoust Soc Am* **119** 1834-48

Kiemeneij F, Patterson M S, Amoroso G, Laarman G and Slagboom T 2008 Use of the Stereotaxis Niobe® magnetic navigation system for percutaneous coronary intervention: Results from 350 consecutive patients *Catheter. Cardiovasc. Interv.* **71** 510-6

Kino G S 1987 *Acoustic waves: devices, imaging, and analog signal processing* (Englewood Cliffs, NJ: Prentice Hall)

Klibanov A L 2005 Ligand-carrying gas-filled microbubbles: ultrasound contrast agents for targeted molecular imaging *Bioconjug. Chem.* **16** 9-17

Kopechek J A, Park E, Mei C-S, McDannold N J and Porter T M 2013 Accumulation of phase-shift nanoemulsions to enhance MR-guided ultrasound-mediated tumor ablation in vivo *Journal of healthcare engineering* **4** 109-26

Kremkau F W 1979 Cancer therapy with ultrasound: a historical review *Journal of clinical ultrasound* **7** 287-300

Kripfgans O D, Fowlkes J B, Miller D L, Eldevik O P and Carson P L 2000 Acoustic droplet vaporization for therapeutic and diagnostic applications *Ultrasound Med. Biol.* **26** 1177-89

Lammers T, Kiessling F, Hennink W E and Storm G 2012 Drug targeting to tumors: principles, pitfalls and (pre-) clinical progress *Journal of Controlled Release* **161** 175-87

Layzer J M, McCaffrey A P, Tanner A K, Huang Z, Kay M A and Sullenger B A 2004 In vivo activity of nuclease-resistant siRNAs *RNA* **10** 766-71

Lee J Y, Carugo D, Crake C, Owen J, de Saint Victor M, Seth A, Coussios C and Stride E 2015 Nanoparticle-Loaded Protein-Polymer Nanodroplets for Improved Stability and Conversion Efficiency in Ultrasound Imaging and Drug Delivery *Adv. Mater.* **27** 5484-92

Leibacher I, Schatzer S and Dual J 2014 Impedance matched channel walls in acoustofluidic systems *Lab. Chip* **14** 463-70

Leighton T G 1994 *The Acoustic Bubble* (London: Academic Press)

Li J, Stoica P and Wang Z 2003 On robust Capon beamforming and diagonal loading *Signal Processing, IEEE Transactions on* **51** 1702-15

Liao A-H, Liu H-L, Su C-H, Hua M-Y, Yang H-W, Weng Y-T, Hsu P-H, Huang S-M, Wu S-Y, Wang H-E, Yen T-C and Li P-C 2012 Paramagnetic perfluorocarbon-filled albumin-(Gd-DTPA) microbubbles for the induction of focused-ultrasound-induced blood–brain barrier opening and concurrent MR and ultrasound imaging *Phys. Med. Biol.* **57** 2787-802

Lighthill J 2003 *Waves in Fluids* (Cambridge: Cambridge University Press)

Lin C-Y and Pitt W G 2013 Acoustic droplet vaporization in biology and medicine *BioMed research international* **2013** 404361

Lind S J 2014 On the dynamics of non-spherical magnetic microbubbles *Physics of Fluids (1994-present)* **26** 061901

Liu Z, Lammers T, Ehling J, Fokong S, Bornemann J, Kiessling F and Gätjens J 2011 Iron oxide nanoparticle-containing microbubble composites as contrast agents for MR and ultrasound dual-modality imaging *Biomaterials* **32** 6155-63

Loncar R, Zotz R B, Sucker C, Vodovnik A, Mihalj M and Scharf R E 2007 Platelet adhesion onto

immobilized fibrinogen under arterial and venous in-vitro flow conditions does not significantly differ between men and women *Thrombosis journal* **5** 5

Lorenz R G and Boyd S P 2005 Robust minimum variance beamforming *Signal Processing, IEEE Transactions on* **53** 1684-96

Lübbe A S, Bergemann C, Riess H, Schriever F, Reichardt P, Possinger K, Matthias M, Dörken B, Herrmann F, Gürtler R, Hohenberger P, Haas N, Sohr R, Sander B, Lemke A-J, Ohlendorf D, Huhnt W and Huhn D 1996 Clinical Experiences with Magnetic Drug Targeting: A Phase I Study with 4′-Epidoxorubicin in 14 Patients with Advanced Solid Tumors *Cancer Res* **56** 4686-93

Ludwig G D 1950 The velocity of sound through tissues and the acoustic impedance of tissues *J Acoust Soc Am* **22** 862-6

Lum A F H, Borden M A, Dayton P A, Kruse D E, Simon S I and Ferrara K W 2006 Ultrasound radiation force enables targeted deposition of model drug carriers loaded on microbubbles *Journal of Controlled Release* **111** 128-34

Magyar I, Schleidt W M and Miller B 1978 Localization of sound producing animals using the arrival time differences of their signals at an array of microphones *Experientia* **34** 676-7

Main M L, Goldman J H and Grayburn P A 2009 Ultrasound contrast agents: balancing safety versus efficacy *Expert Opin. Drug Saf.* **8** 49-56

Malich G, Markovic B and Winder C 1997 The sensitivity and specificity of the MTS tetrazolium assay for detecting the in vitro cytotoxicity of 20 chemicals using human cell lines *Toxicology* **124** 179-92

Mannell H, Pircher J, Räthel T, Schilberg K, Zimmermann K, Pfeifer A, Mykhaylyk O, Gleich B, Pohl U and Krötz F 2012 Targeted Endothelial Gene Delivery by Ultrasonic Destruction of Magnetic Microbubbles Carrying Lentiviral Vectors *Pharm Res* **29** 1282-94

Mata A, Fleischman A J and Roy S 2005 Characterization of polydimethylsiloxane (PDMS) properties for biomedical micro/nanosystems *Biomed Microdevices* **7** 281-93

Mathieu J B and Martel S 2010 Steering of aggregating magnetic microparticles using propulsion gradients coils in an MRI Scanner *Magn. Reson. Med.* **63** 1336-45

Maxwell A D, Cain C A, Hall T L, Fowlkes J B and Xu Z 2013 Probability of cavitation for single ultrasound pulses applied to tissues and tissue-mimicking materials *Ultrasound Med. Biol.* **39** 449-65

Meijering B D M, Henning R H, Van Gilst W H, Gavrilovic I, Van Wamel A and Deelman L E 2007 Optimization of ultrasound and microbubbles targeted gene delivery to cultured primary endothelial cells *J. Drug Target.* **15** 664-71

Meijering B D M, Juffermans L J M, van Wamel A, Henning R H, Zuhorn I S, Emmer M, Versteilen A M G, Paulus W J, van Gilst W H, Kooiman K, de Jong N, Musters R J

P, Deelman L E and Kamp O 2009 Ultrasound and microbubble-targeted delivery of macromolecules is regulated by induction of endocytosis and pore formation *Circ. Res.* **104** 679-87

Meltzer R S, Tickner E G, Sahines T P and Popp R L 1980 The source of ultrasound contrast effect *Journal of Clinical Ultrasound* **8** 121-7

Miller D L, Pislaru S V and Greenleaf J F 2002 Sonoporation: mechanical DNA delivery by ultrasonic cavitation *Somat. Cell Mol. Genet.* **27** 115-34

Mucci R A 1984 A comparison of efficient beamforming algorithms *Acoustics, Speech and Signal Processing, IEEE Transactions on* **32** 548-58

Mulvana H, Eckersley R J, Browning R, Hajnal J V, Stride E, Barrack T, Pankhurst Q, Tang M and Wells D 2010 Enhanced gene transfection in vivo using magnetic localisation of ultrasound contrast agents: Preliminary results. In: *2010 IEEE Ultrasonics Symposium (IUS),* (San Diego, CA: IEEE) pp 670-3

Mulvana H, Eckersley R J, Tang M-X, Pankhurst Q and Stride E 2012 Theoretical and Experimental Characterisation of Magnetic Microbubbles *Ultrasound Med. Biol.* **38** 864-75

Na H B, Song I C and Hyeon T 2009 Inorganic nanoparticles for MRI contrast agents *Advanced Materials* **21** 2133-48

Nacev A, Weinberg I N, Stepanov P Y, Kupfer S, Mair L O, Urdaneta M G, Shimoji M, Fricke S T and Shapiro B 2014 Dynamic inversion enables external magnets to concentrate ferromagnetic rods to a central target *Nano Lett.* **15** 359-64

Neppiras E A and Coakley W T 1976 Acoustic cavitation in a focused field in water at 1 MHz *Journal of Sound and Vibration* **45** 341-73

Newman C M, Lawrie A, Brisken A F and Cumberland D C 2001 Ultrasound gene therapy: on the road from concept to reality *Echocardiography* **18** 339-47

Nicolson P C and Vogt J 2001 Soft contact lens polymers: an evolution *Biomaterials* **22** 3273-83

Norton S J, Carr B J and Witten A J 2006 Passive imaging of underground acoustic sources *J Acoust Soc Am* **119** 2840-7

Norton S J and Won I J 2000 Time exposure acoustics *IEEE Transactions on Geoscience and Remote Sensing* **38** 1337-43

O'Reilly M A, Jones R M and Hynynen K 2014 Three-Dimensional Transcranial Ultrasound Imaging of Microbubble Clouds Using a Sparse Hemispherical Array *Biomedical Engineering, IEEE Transactions on* **61** 1285-94

Ogawa R, Kondo T, Honda H, Zhao Q L, Fukuda S and Riesz P 2002 Effects of dissolved gases and an echo contrast agent on ultrasound mediated in vitro gene transfection *Ultrasonics Sonochemistry* **9** 197-203

Olympus 2006 Ultrasonic transducers technical notes

http://www.olympus-ims.com/data/File/panametrics/UT-technotes.en.pdf.

Ophir J and Parker K J 1989 Contrast agents in diagnostic ultrasound *Ultrasound Med. Biol.* **15** 319-33

OUP 2015 *OED Online* (Web: Oxford University Press)

Owen J. 2015. *Magnetic microbubbles: investigation and design of new formulations for targeted therapy.* DPhil Thesis, University of Oxford.

Owen J, Grove P, Rademeyer P and Stride E 2014 The influence of blood on targeted microbubbles *Journal of The Royal Society Interface* **11** 20140622

Owen J, Pankhurst Q and Stride E 2012a Magnetic targeting and ultrasound mediated drug delivery: Benefits, limitations and combination *International Journal of Hyperthermia* **28** 362-73

Owen J, Zhou B, Rademeyer P, Tang M-X, Pankhurst Q, Eckersley R and Stride E 2012b Understanding the structure and mechanism of formation of a new magnetic microbubble formulation *Theranostics* **2** 1127-39

Park J I, Jagadeesan D, Williams R, Oakden W, Chung S, Stanisz G J and Kumacheva E 2010 Microbubbles loaded with nanoparticles: a route to multiple imaging modalities *ACS Nano* **4** 6579-86

Patil A V, Rychak J J, Klibanov A L and Hossack J A 2011 A real-time technique for improving molecular imaging and guiding drug delivery in large blood vessels: in vitro and ex vivo results *Mol Imaging* **10** 238-47

Plank C, Scherer F, Schillinger U, Anton M and Bergemann C 2002 Magnetofection: enhancing and targeting gene delivery by magnetic force *Eur Cells Mater* **3** 79-80

Plank C, Schillinger U, Vlaskou D and Mykhaylyk O 2007 *Biomedical Applications of Nanotechnology* (Hoboken, NJ: Wiley) pp 23-63

Plank C, Vlaskou D, Schillinger U, Mykhaylyk O, Brill T, Rudolph C, Huth S, Krötz F, Hirschberger J and Bergemann C 2005 Localized nucleic acid delivery using magnetic nanoparticles *Eur. Cell. Mater.* **10** 8

Plank C, Zelphati O and Mykhaylyk O 2011 Magnetically enhanced nucleic acid delivery. Ten years of magnetofection—Progress and prospects *Advanced Drug Delivery Reviews* **63** 1300-31

Potter J R 1994 Acoustic imaging using ambient noise: Some theory and simulation results *J Acoust Soc Am* **95** 21-33

Probst R, Lin J, Komaee A, Nacev A, Cummins Z and Shapiro B 2011 Planar steering of a single ferrofluid drop by optimal minimum power dynamic feedback control of four electromagnets at a distance *J Magn Magn Mater* **323** 885-96

Rabkin B A, Zderic V and Vaezy S 2005 Hyperecho in ultrasound images of HIFU therapy: involvement of cavitation *Ultrasound Med. Biol.* **31** 947-56

Rahim A, Taylor S L, Bush N L, ter Haar G R, Bamber J C and Porter C D 2006 Physical parameters affecting ultrasound/microbubble-mediated gene delivery efficiency in vitro *Ultrasound Med. Biol.* **32** 1269-79

Rand T A, Ginalski K, Grishin N V and Wang X 2004 Biochemical identification of Argonaute 2 as the sole protein required for RNA-induced silencing complex activity *PNAS* **101** 14385-9

Rand T A, Petersen S, Du F and Wang X 2005 Argonaute2 cleaves the anti-guide strand of siRNA during RISC activation *Cell* **123** 621-9

Rasor J S and Tickner E G 1984 Microbubble precursors and methods for their production and use, United States Patent (US 4442843 A).

Rifai B, Arvanitis C D, Bazan-Peregrino M and Coussios C-C 2010 Cavitation-enhanced delivery of macromolecules into an obstructed vessel *J Acoust Soc Am* **128** EL310-EL5

Rivens I, Shaw A, Civale J and Morris H 2007 Treatment monitoring and thermometry for therapeutic focused ultrasound *International Journal of Hyperthermia* **23** 121-39

Roberts W W, Hall T L, Ives K, Wolf Jr J S, Fowlkes J B and Cain C A 2006 Pulsed Cavitational Ultrasound: A Noninvasive Technology for Controlled Tissue Ablation (Histotripsy) in the Rabbit Kidney *The Journal of Urology* **175** 734-8

Sachs A B 1993 Messenger RNA degradation in eukaryotes *Cell* **74** 413-21

Salgaonkar V A, Datta S, Holland C K and Mast T D 2009 Passive cavitation imaging with ultrasound arrays *J Acoust Soc Am* **126** 3071-83

Scherer F, Anton M, Schillinger U, Henke J, Bergemann C, Krüger A, Gänsbacher B and Plank C 2002 Magnetofection: enhancing and targeting gene delivery by magnetic force in vitro and in vivo *Gene Ther.* **9** 102-9

Schneider M 1999 Characteristics of SonoVue™ *Echocardiography* **16** 743-6

Schutt E G, Klein D H, Mattrey R M and Riess J G 2003 Injectable microbubbles as contrast agents for diagnostic ultrasound imaging: the key role of perfluorochemicals *Angewandte Chemie International Edition* **42** 3218-35

Schwarz D S, Tomari Y and Zamore P D 2004 The RNA-induced silencing complex is a Mg 2+-dependent endonuclease *Curr. Biol.* **14** 787-91

Sennoga C A, Mahue V, Loughran J, Casey J, Seddon J M, Tang M and Eckersley R J 2010 On sizing and counting of microbubbles using optical microscopy *Ultrasound Med. Biol.* **36** 2093-6

Senyei A, Widder K and Czerlinski G 1978 Magnetic guidance of drug-carrying microspheres *Journal of Applied Physics* **49** 3578-83

Sheeran P S and Dayton P A 2014 Improving the performance of

phase-change perfluorocarbon droplets for medical ultrasonography: current progress, challenges, and prospects *Scientifica* **2014** 579684

Sheeran P S, Matsunaga T O and Dayton P A 2013 Phase-transition thresholds and vaporization phenomena for ultrasound phase-change nanoemulsions assessed via high-speed optical microscopy *Phys. Med. Biol.* **58** 4513-34

Sherman J W 1962 Properties of focused apertures in the Fresnel region *Antennas and Propagation, IRE Transactions on* **10** 399-408

Shpak O, Verweij M, Vos H J, de Jong N, Lohse D and Versluis M 2014 Acoustic droplet vaporization is initiated by superharmonic focusing *PNAS* **111** 1697-702

Sia S K and Whitesides G M 2003 Microfluidic devices fabricated in poly (dimethylsiloxane) for biological studies *Electrophoresis* **24** 3563-76

Smith M D, Kwan O L, Reiser H J and DeMaria A N 1984 Superior intensity and reproducibility of SHU-454, a new right heart contrast agent *Journal of the American College of Cardiology* **3** 992-8

Soetanto K and Watarai H 2000 Development of magnetic microbubbles for drug delivery system (DDS) *Japanese Journal of Applied Physics* **39** 3230-2

Soutschek J, Akinc A, Bramlage B, Charisse K, Constien R, Donoghue M, Elbashir S, Geick A, Hadwiger P, Harborth J, John M, Kesavan V, Lavine G, Pandey R K, Racie T, Rajeev K G, Rohl I, Toudjarska I, Wang G, Wuschko S, Bumcrot D, Koteliansky V, Limmer S, Manoharan M and Vornlocher H-P 2004 Therapeutic silencing of an endogenous gene by systemic administration of modified siRNAs *Nature* **432** 173-8

Spiesberger J L and Fristrup K M 1990 Passive localization of calling animals and sensing of their acoustic environment using acoustic tomography *Am. Nat.* **135** 107-53

Steinkamp J A 1984 Flow cytometry *Rev. Sci. Instrum.* **55** 1375-400

Stoica P and Moses R 2005 *Spectral analysis of signals* (Upper Saddle River, NJ: Prentice Hall)

Stride E 2009 Physical principles of microbubbles for ultrasound imaging and therapy *Cerebrovascular Diseases* **27 (Suppl 2)** 1-13

Stride E and Edirisinghe M 2008 Novel microbubble preparation technologies *Soft matter* **4** 2350-9

Stride E, Porter C, Prieto A G and Pankhurst Q 2009 Enhancement of Microbubble Mediated Gene Delivery by Simultaneous Exposure to Ultrasonic and Magnetic Fields *Ultrasound Med. Biol.* **35** 861-8

Szabo T L 2004 *Diagnostic Ultrasound Imaging: Inside Out* (Burlington, MA: Elsevier Science)

Takalkar A M, Klibanov A L, Rychak J J, Lindner J R and Ley K 2004 Binding and detachment dynamics of microbubbles targeted to P-selectin under controlled shear flow

*Journal of Controlled Release* **96** 473-82

Talu E, Hettiarachchi K, Nguyen H, Lee A P, Powell R L, Longo M L and Dayton P A 2006 P2A-8 lipid-stabilized monodisperse microbubbles produced by flow focusing for use as ultrasound contrast agents. In: *Ultrasonics Symposium, 2006. IEEE,* (Vancouver, BC: IEEE) pp 1568-71

Taylor R C, Cullen S P and Martin S J 2008 Apoptosis: controlled demolition at the cellular level *Nature reviews Molecular cell biology* **9** 231-41

Thurber G M, Schmidt M M and Wittrup K D 2008 Antibody tumor penetration: transport opposed by systemic and antigen-mediated clearance *Advanced Drug Delivery Reviews* **60** 1421-34

Tranquart F, Grenier N, Eder V and Pourcelot L 1999 Clinical use of ultrasound tissue harmonic imaging *Ultrasound Med. Biol.* **25** 889-94

Uchida M, Li X W, Mertens P and Alpar H O 2009 Transfection by particle bombardment: delivery of plasmid DNA into mammalian cells using gene gun *Biochimica et Biophysica Acta (BBA)-General Subjects* **1790** 754-64

Unger E C, McCreery T P, Sweitzer R H, Caldwell V E and Wu Y 1998 Acoustically Active Lipospheres Containing Paclitaxel: A New Therapeutic Ultrasound Contrast Agent *Invest. Radiol.* **33** 886-92

Van Veen B D and Buckley K M 1988 Beamforming: A versatile approach to spatial filtering *ASSP Magazine, IEEE* **5** 4-24

Villanueva F S, Jankowski R J, Klibanov S, Pina M L, Alber S M, Watkins S C, Brandenburger G H and Wagner W R 1998 Microbubbles targeted to intercellular adhesion molecule-1 bind to activated coronary artery endothelial cells *Circulation* **98** 1-5

Vlaskou D, Mykhaylyk O, Krötz F, Hellwig N, Renner R, Schillinger U, Gleich B, Heidsieck A, Schmitz G, Hensel K and Plank C 2010a Magnetic and acoustically active lipospheres for magnetically targeted nucleic acid delivery *Advanced Functional Materials* **20** 3881-94

Vlaskou D, Pradhan P, Bergemann C, Klibanov A L, Hensel K, Schmitz G, Plank C and Mykhaylyk O 2010b Magnetic Microbubbles: Magnetically Targeted and Ultrasound-Triggered Vectors for Gene Delivery in Vitro *AIP Conference Proceedings* **1311** 485-94

Vorobyov S A, Gershman A B and Luo Z-Q 2003 Robust adaptive beamforming using worst-case performance optimization: A solution to the signal mismatch problem *Signal Processing, IEEE Transactions on* **51** 313-24

Vovk U, Pernus F and Likar B 2007 A review of methods for correction of intensity inhomogeneity in MRI *Medical Imaging, IEEE Transactions on* **26** 405-21

Walker R A 1963 Some Intense, Low-Frequency, Underwater Sounds of Wide Geographic Distribution,

Apparently of Biological Origin *J Acoust Soc Am* **35** 1816-24

Wang J, Lu Z, Wientjes M G and Au J L-S 2010 Delivery of siRNA therapeutics: barriers and carriers *AAPS J* **12** 492-503

Wang T H, Wang H S and Soong Y K 2000 Paclitaxel-induced cell death *Cancer* **88** 2619-28

Wang X, Hagemeyer C E, Hohmann J D, Leitner E, Armstrong P C, Jia F, Olschewski M, Needles A, Peter K and Ahrens I 2012 Novel single-chain antibody-targeted microbubbles for molecular ultrasound imaging of thrombosis: validation of a unique noninvasive method for rapid and sensitive detection of thrombi and monitoring of success or failure of thrombolysis in mice *Circulation* **125** 3117-26

Wani M C, Taylor H L, Wall M E, Coggon P and McPhail A T 1971 Plant antitumor agents. VI. Isolation and structure of taxol, a novel antileukemic and antitumor agent from Taxus brevifolia *J. Am. Chem. Soc.* **93** 2325-7

Ward M, Wu J and Chiu J-F 2000 Experimental study of the effects of optison® concentration on sonoporation in vitro *Ultrasound Med. Biol.* **26** 1169-75

Watkins W A and Schevill W E 1971 *Four hydrophone array for acoustic three-dimensional location* (Woods Hole, MA: Woods Hole Oceanographic Institution)

Whitehead K A, Langer R and Anderson D G 2009 Knocking down barriers: advances in siRNA delivery *Nature reviews Drug discovery* **8** 129-38

Whitmore R L 1967 The flow behaviour of blood in the circulation *Nature* **215** 123-6

Wood B J, Yanof J, Frenkel V, Viswanathan A, Dromi S, Oh K, Kruecker J, Bauer C, Seip R, Kam A and Li K C P 2006 CT and Ultrasound Guided Stereotactic High Intensity Focused Ultrasound (HIFU) *AIP Conference Proceedings* **829** 122-6

Wood R W and Loomis A L 1927 XXXVIII. The physical and biological effects of high-frequency sound-waves of great intensity *The London, Edinburgh, and Dublin philosophical magazine and journal of science* **4** 417-36

Wu J, Leong-Poi H, Bin J, Yang L, Liao Y, Liu Y, Cai J, Xie J and Liu Y 2011 Efficacy of Contrast-enhanced US and Magnetic Microbubbles Targeted to Vascular Cell Adhesion Molecule–1 for Molecular Imaging of Atherosclerosis *Radiology* **260** 463-71

Xia H, Mao Q, Paulson H L and Davidson B L 2002 siRNA-mediated gene silencing in vitro and in vivo *Nat. Biotechnol.* **20** 1006-10

Yang F, Li Y, Chen Z, Zhang Y, Wu J and Gu N 2009 Superparamagnetic iron oxide nanoparticle-embedded encapsulated microbubbles as dual contrast agents of magnetic resonance and ultrasound imaging *Biomaterials* **30** 3882-90

Zaloga G P, Malcolm D, Holaday J and Chernow B 1987 Verapamil

reverses calcium cardiotoxicity *Annals of Emergency Medicine* **16** 637-9

Zhang P and Porter T 2010 An in vitro study of a phase-shift nanoemulsion: a potential nucleation agent for bubble-enhanced HIFU tumor ablation *Ultrasound Med. Biol.* **36** 1856-66

Zhao S, Borden M, Bloch S H, Kruse D, Ferrara K W and Dayton P A 2004 Radiation-force assisted targeting facilitates ultrasonic molecular imaging *Mol Imaging* **3** 135-48